University of Warsaw

Małgorzata Niemiec

Studies of the Three-Dimensional Structure of the Nucleon at the COMPASS Experiment at CERN

Doctoral thesis

The thesis written under the supervision
of prof. dr hab. Barbara Badełek

Warsaw, October 2025

To my mother Marzena

A man can control only what he comprehends,
and comprehend only what he is able to put into words.
The unexpressed is incomprehensible.

— Stanisław Lem, The Futurological Congress

Abstract

Understanding the structure of the nucleon remains one of the central challenges in modern hadron physics. The aim of this thesis is to experimentally study the three-dimensional structure of the nucleon in terms of Transverse-Momentum Dependent (TMD) Parton Distribution Functions (PDFs). Experimental validation of the TMD framework has been significantly advanced by data from semi-inclusive deep inelastic scattering experiments. To achieve a more universal understanding of TMD PDFs, it is essential to study them in complementary processes, with the Drell–Yan process playing a particularly important role.

This thesis presents an analysis of Transverse-Spin Dependent Azimuthal Asymmetries in the Drell–Yan process, $\pi^- + \mathrm{p}^\uparrow \to \gamma^* + \mathrm{X} \to \mu^+ + \mu^- + \mathrm{X}$, based on data collected by the Common Muon and Proton Apparatus for Structure and Spectroscopy (COMPASS) Collaboration in 2015 and 2018. The data were obtained using a 190 GeV negative pion beam scattered off transversely polarised NH_3 target.

A key aspect of the analysis is the introduction of a novel weighting method, where asymmetries are weighted by powers of the transverse momentum of the dimuon pair relative to the beam direction. The method of weighted asymmetries has proven to be a powerful tool for probing the transverse structure of the nucleon, allowing direct access to specific k_T^2 moments of the TMD PDFs. In this work, the first k_T^2 moments of the Sivers and Boer–Mulders functions have been extracted. These results represent one of the most significant experimental contributions to the study of TMD physics in recent years, and are expected to remain a key reference until future measurements from facilities such as the EIC and LHCspin become available.

Streszczenie

Dziesięciolecia eksperymentów umożliwiły szczegółowe poznanie struktury nukleonu, opisanej ilościowo przez kolinearne rozkłady pędów partonów. Opis ten nie jest jednak wystarczający, co pociąga za sobą konieczność rozważenia funkcji rozkładu partonów zależnych od ich poprzecznego pędu i opisujących korelacje spinowo-orbitalne (ang. Transverse-Momentum Dependent Parton Distribution Functions, TMD PDFs). Mogą być one zbadane za pomocą semi-inkluzywnego rozpraszania głęboko nieelastycznego leptonów o wysokich energiach na nukleonach albo w reakcji rozpraszania Drella-Yana, w której na nukleonie rozpraszany jest szybki hadron.

W pracy przedstawiono analizę azymutalnych asymetrii zależnych od spinu poprzecznego w procesie Drella–Yana $\pi^- + \mathrm{p}^\uparrow \to \gamma^* + \mathrm{X} \to \mu^+ + \mu^- + \mathrm{X}$, opartą na danych zebranych w eksperymencie COMPASS (ang. Common Muon and Proton Apparatus for Structure and Spectroscopy) w latach 2015 i 2018. Dane uzyskano przy użyciu ujemnej wiązki pionów o energii 190 GeV, rozpraszającej się na poprzecznie spolaryzowanej tarczy NH_3.

Kluczowym elementem analizy jest zastosowanie nowej metody wyznaczania asymetrii poprzez ich ważenie potęgami poprzecznego pędu (względem kierunku wiązki) pary mionów. Metoda umożliwia bezpośrednie wyznaczenie funkcji TMD PDFs i ich momentów w zmiennej k_T^2, w tym pierwszych momentów funkcji Siversa i Boer-Muldersa, uzyskanych i opisanych w niniejszej pracy. Wyniki te pozostaną cennym odniesieniem w dziedzinie fizyki spinowej, aż do momentu, gdy pomiary z przyszłych eksperymentów, takich jak EIC i LHCspin, staną się dostępne.

Preface

The following work is the culmination of four years of my research in spin physics, one of the most memorable and rewarding experiences.

My deepest gratitude goes to my supervisor, *Prof. Barbara Badełek*, who gave me the opportunity to work within the COMPASS experiment despite my initial lack of experience, and who trusted that I could rise to the challenge. I will always remember all that I have learned from her, not only in science but also in life.

This work would not have been possible without the invaluable contributions of two COMPASS members. I am especially grateful to *Dr. Jan Matoušek*, the first person I worked with in the COMPASS collaboration, who patiently guided me through my initial steps in analysis. I cannot forget to thank *dr Bakur Parsamyan*, whose exceptional attention to detail and and insightful advice opened my research to new perspectives. Despite his strong personality, I will never forget his willingness to help and his ability to provide support even in challenging situations.

Pragnę również podziękować moim rodzicom, *Marzenie* i *Krzysztofowi*, za niezachwianą wiarę w moje marzenia, zawsze dając mi znacznie więcej, niż kiedykolwiek mogłam zasłużyć. Obserwując ich jako dziecko, wiedziałam, że pewnego dnia chciałabym stać się człowiekiem tak dobrym jak oni.

List of Acronyms

ADC Analog-To-Digital Converter
BMS Beam Momentum Station
CAMERA COMPASS Apparatus for Measurement of Exclusive Reactions
CASTOR CERN Advanced STORage manager
CATCH COMPASS Accumulate, Transfer and Control Hardware
CEDAR Cerenkov Differential counter with Achromatic Ring
CERN Conseil Européen pour la Recherche Nucléaire
CDF Collider Detector at Fermilab
CMS Compact Muon Solenoid
CM center-of-mass
COMPASS Common Muon and Proton Apparatus for Structure and Spectroscopy
COOOL COMPASS Object-Oriented OnLine tool
CORAL COMPASS reconstruction and analysis
CS Collins-Sopper
DAQ Data Acquisition System
DC Drift Chamber
DCS Detector Control System
DESY Deutsches Elektronen-Synchrotron
DGLAP Dokshitzer–Gribov–Lipatov–Altarelli–Parisi
DIS Deep Inelastic Scattering
DNP Dynamic Nuclear Polarisation
DVCS Deeply Virtual Compton Scattering
DY Drell–Yan
ECAL Electromanetic Calorimeter
EIC Electron-Ion Collider
EMC European Muon Collaboration
Fermilab Fermi National Accelerator Laboratory
FF Fragmentation Function

FI Scintillating Fiber

FPGA Field-Programmable Gate Array

Gandalf Generic Advanced Numerical Device for Analog and Logic Functions

GEM Gas Electron Multiplier

GEANT4 Geometry And Tracking

GPD Generalised Parton Distributions

HCAL Hadronic Calorimeter

HGeSiCA Hot GEM and Silicon Control and Acquisition

IT Inner Trigger

JLab Thomas Jefferson National Accelerator Facility

LAS Large Angle Spectrometer

LAST Large-Angle Trigger

LAT Large Area Tracker

LHAPDF Les Houches Accord PDFs

LHC Large Hadron Collider

LHCb Large Hadron Collider beauty

LO Leading Order

LT Ladder Trigger

MC Monte Carlo

MDT Multiwire Drift Tube

MF Muon Filter

MicroMega Micromesh Gaseous Structure Detector

MT Middle-Angle Trigger

mDST mini Data Summary Tape

MW Muon Wall

MWPC Multi-Wire Proportional Chamber

NLO Next-to-Leading Order

NNLO Next-to-Next-to Leading Order

OT Outer-Angle Trigger

PDF Parton Distribution Function

PHAST Physics Analysis Software tools

PID Particle Identification

PV Primary Vertex

PVSS Prozessvisualisierungs und Steuerungssystem

QCD Quantum Chromodynamics

RHIC Relativistic Heavy Ion Collider

RICH Ring Imaging Cherenkov

RT Random Trigger

RW Rich Wall

SAS Small Angle Spectrometer

SAT Small Area Tracker

SCADA Supervisory Control and Data Acquisition

SIDIS Semi-Inclusive Deep Inelastic Scattering

SI Silicon Microstrip

SLAC Stanford Linear Accelerator Center

SM Spectrometer Dipole Magnet

SPS Super Proton Synchrotron

STAR Solenoidal Tracker at Relativistic Heavy Ion Collider

ST Straw Tube

TDC Time-to-Digital Converter Chip

TMD Transverse-Momentum Dependent

TMD PDF Transverse-Momentum Dependent Parton Distribution Function

TSA Transverse-Spin Dependent Azimuthal Asymmetry

VETO Beam Halo Veto

VSAT Very Small Area Tracker

W45 Large Size Drift Chamber

WTSA Transverse-Momentum Weighted Transverse-Spin Dependent Azimuthal Asymmetry

RT Random Trigger

QPM Quark Parton Model

PHENIX Pioneering High Energy Nuclear Interaction eXperiment

pQCD perturbative QCD

SMOG System for Measuring Overlap with Gas

Contents

Chapter 1

Introduction

Well begun is half done.

—Old Proverb

This chapter provides an overview of the theoretical framework and experimental progress in the study of nucleon structure. Sec. 1.1 presents a historical perspective on particle physics, emphasizing key discoveries that shaped our understanding of the nucleon substructure. Sec. 1.2 introduces the deep inelastic scattering process, which serves as the basis for the structure functions and Parton Distribution Functions (PDFs) described in Sec. 1.3 and 1.4, respectively.

1.1 Brief History of Hadron Physics

In the early 20th century, the understanding of the structure of matter was profoundly redefined, beginning with E. Rutherford discovery of the atomic nucleus in 1911 [1]. The atomic model advanced further with J. Chadwick's observation of the neutron in 1932 [2], providing the final key piece for the nuclear model of the atom. At that stage, protons and neutrons were regarded as elementary particles, the fundamental building blocks of all nuclei.

Cosmic-ray studies in the 1930s-1950s revealed a variety of previously unknown particles, which were subsequently reproduced and studied in detail once accelerators reached higher collision energies. This growing "particle zoo" in the late 1950s and early 1960s raised fundamental questions about which particles are truly elementary building blocks of matter. The internal structure of the nucleon was described by model proposed independently by M. Gell-Mann [3] and G. Zweig [4] in 1964. According to this concept, all then known hadrons could be understood as combinations of three quarks or a quark-antiquark pair. At that time, only three types of quarks, up, down, and strange, were required to account for all the hadrons observed. Since then, the quark model has been expanded, and six quark flavours are now known: up (u), down (d), strange (s), charm (c), bottom (b), and top (t).

The first experimental indications of a substructure within the nucleon were obtained at SLAC in the late 1960s [5]. Building on these observations, R. Feynman proposed the Parton Model [6], in which the nucleon is described as being composed of point-like constituents called partons. Soon after, this framework evolved into the Quark Parton Model (QPM) [7], which identified the partons with quarks.

Further refinements of the model have assumed that the nucleon is composed not only of three valence quarks, but also of a dynamic background of sea quark–antiquark pairs and electrically neutral, spin-1 bosons, known as gluons, which mediate the strong interaction [8]. Initially, it was assumed that the entire nucleon spin originates from its constituent quarks. Accounting for relativistic effects the fraction of the nucleon spin carried by the quarks is reduced to $\Delta\Sigma \approx 0.6$ [9].

The EMC experiment at CERN [10, 11], which studied polarised muons scattering off a polarised proton target, was initially expected to confirm earlier SLAC [12, 13] measurements. The results came as a suprose to the community, as the measured fraction of the proton spin carried by quarks was only $\Delta\Sigma = 0.12 \pm 0.10$ (stat.) $\pm$ 0.14 (sys.) [10], suggesting thet not only quarks contribute to its spin. This unexpected result became known as the proton "spin crisis" and significantly influenced the direction of spin physics research over the following two decades, leading to a new generation of high-precision experiments such as SMC at CERN [14], HERMES at DESY [15], and several programs at JLab [16–18].

Building on these findings, the nucleon spin can be described as the sum of the first moment of the quark and antiquark helicity, $\Delta\Sigma$, the first moment of helicity of gluons, $\Delta\mathrm{G}$, as well as the orbital angular momenta of quarks L_q and gluons L_g:

$$\frac{1}{2} = \frac{1}{2}\Delta\Sigma + \Delta\mathrm{G} + L_\mathrm{q} + L_\mathrm{g}. \tag{1.1}$$

Nearly three decades have passed since the emergence of the "spin puzzle", yet it remains unresolved. Experimental efforts continue to investigate all components of the nucleon spin, but this analysis focuses primarily on the first two contributions, $\Delta\Sigma$ and $\Delta\mathrm{G}$. Following the pioneering EMC experiment, multiple studies have measured $\Delta\Sigma$, establishing that quark spins account for roughly 30% of the nucleon spin [19]. Measurements of $\Delta\mathrm{G}$ have also been attempted, and current results suggest that the gluon spin contribution is likely small [20], but the uncertainties of the experiments are still large.

In recent years, significant progress has been made in understanding the nucleon multi-dimensional structure. These efforts focus particularly on the study of Transverse-Momentum Dependent Parton Distribution Functions (TMD PDF) and Generalised Parton Distributionss (GPDs), which provide deeper insight into the internal dynamics and spatial structure of the nucleon. The three-dimensional parton structure of hadrons in momentum space is encoded in Transverse-Momentum Dependent Parton Distribution Functions (TMD PDFs), each describing different correlations between parton spins and their transverse momenta. These correlations reveal important aspects of partonic dynamics and spin-orbit interactions within the nucleon. In parallel, GPDs play a fundamental role in characterizing the spatial distribution of partons inside hadrons. Moreover, the second moments of specific GPDs are directly related to the total angular momentum carried by quarks and gluons, offering a promising path toward resolving the spin puzzle. GPDs and TMD PDFs provide complementary perspectives on partonic structure, enabling a multidimensional description of the nucleon. fistr

While a comprehensive account of the nucleon structure is beyond the reach of this study, the analysis presented herein concentrates on TMD PDFs, offering valuable insight and making a meaningful contribution to the understanding of hadronic structure.

1.2 Deep Inelastic Scattering

Deep inelastic lepton–nucleon scattering is a powerful probe of the nucleon partonic structure, described by structure functions that reflect quark and antiquark distribution functions. Let us consider a lepton ℓ with four-momentum $l = (E, \boldsymbol{l})$ scattering off a nucleon N with initial four-momentum $P = (M, \mathbf{0})$ at rest. The resulting in a final state is composed of a scattered lepton with four-momentum $l' = (E', \boldsymbol{l'})$ and a hadronic system X with total four-momentum P_{X}. The initial state of the reaction is characterized by the square of the center-of-mass (CM) energy, $s = (l + P)^2$, or equivalently, by the incident lepton energy, E.

$$\ell(l) + \mathrm{N}(P) \to \ell(l') + \mathrm{X}(P_{\mathrm{X}})$$

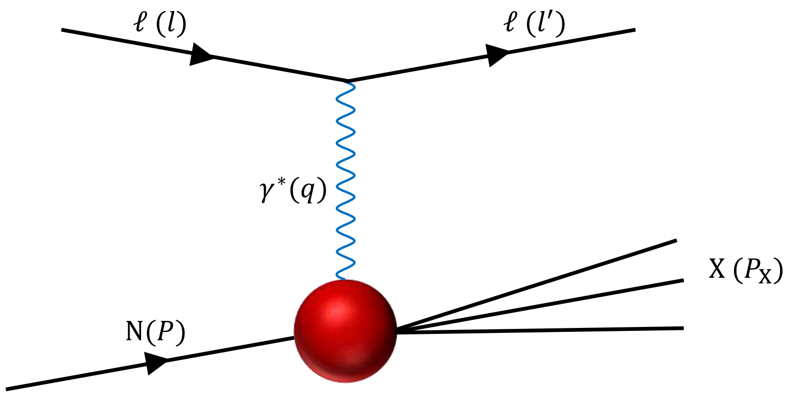

Figure 1.1: A schematic diagram of the deep inelastic scattering process at leading order (one-photon exchange) and CM energy (no Z^0 exchange).

At low CM energies, charged-lepton scattering is dominated by a pure electromagnetic interaction, which can be accurately described by one-photon exchange. In this picture, the incoming and outgoing leptons are of the same type, and the process is mediated entirely through the exchange of a virtual photon $\gamma^{\star}$, as illustrated in Fig. 1.2. This mechanism remains the leading contribution even at higher energies and low-to-moderate momentum transfer Q^2 making the one-photon approximation a natural starting point for theoretical analysis. [21].

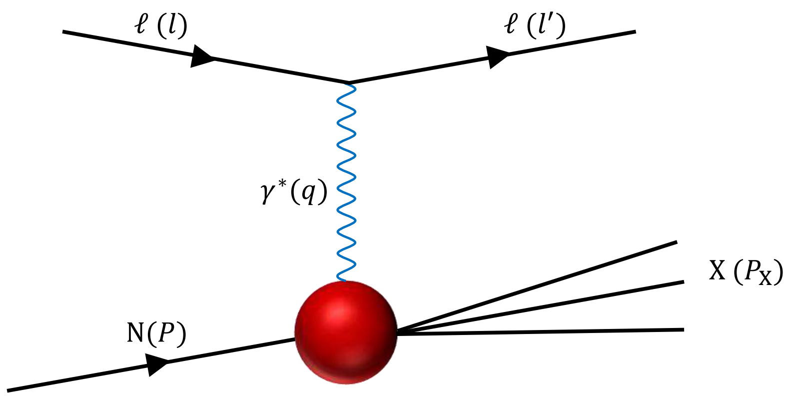

Figure 1.2: A schematic diagram of the deep inelastic scattering process at leading order (one-photon exchange) and CM energy (no Z^0 exchange).

The final state is typically characterized by relativistic invariants:

$$Q^2 = -q^2 = (l - l')^2 \tag{1.2}$$

$$\nu = \frac{Pq}{M} \overset{\text{lab}}{=} E - E' \tag{1.3}$$

$$y = \frac{qP}{lP} \overset{\text{lab}}{=} \frac{\nu}{E} \tag{1.4}$$

$$x = \frac{Q^2}{2P \cdot q} \overset{\text{lab}}{=} \frac{Q^2}{2M\nu} \tag{1.5}$$

$$W^2 = (P + q)^2 \overset{\text{lab}}{=} M^2 + Q^2 \left(\frac{1}{x} - 1\right) \tag{1.6}$$

Here, the negative four-momentum transfer Q^2 is related to the wavelength of the

Table 1.1: Definition of the kinematic variables used in Deep Inelastic Scattering (DIS).

Kinematic variable	Definition
E	Energy of the incident lepton
E'	Energy of the scattered lepton
l	Four-momentum of the incident lepton
l'	Four-momentum of the scattered lepton
q	Four-momentum of the virtual photon γ^*
P	Four-momentum of the target nucleon
Q^2	Virtuality of the photon
ν	Lepton energy transfer to the γ^*
y	Fraction of the lepton energy transferred to the γ^*
x	Bjorken scaling variable
W^2	Squared invariant mass of the hadronic final state

virtual photon, while ν represents the energy of the virtual photon in the laboratory frame. The fraction of the incoming lepton energy carried by the photon is denoted as

y. The Bjorken scaling variable, x, carries a particularly insightful interpretation, originally proposed by Feynman [6]. In the infinite momentum frame of the nucleon, where transverse momenta are negligible, it represents the fraction of the nucleon momentum carried by the parton involved in the interaction. Finally, W^2 denotes the invariant mass squared of the hadronic final state. The variables used to describe DIS are also summarised in Tab. 1.1.

The kinematic domain of DIS is characterized by $Q^2 \gtrsim 1$ GeV^2, ensuring that the photon wavelength is short enough to probe the internal structure of the nucleon and that the strong coupling constant α_S is small enough for perturbative Quantum Chromodynamics (QCD) to be applicable. Additionally, $W^2 \gtrsim 5$ GeV^2 is imposed to avoid the nucleon resonance region.

The DIS cross section is defined as [22]:

$$\frac{\mathrm{d}\sigma}{\mathrm{d}E'\mathrm{d}\Omega} = \frac{e^4}{16\pi^2 Q^4}\left(\frac{E'}{ME}\right) L_{\mu\nu} W^{\mu\nu}. \tag{1.7}$$

The tensors $L^{\mu\nu}$ and $W^{\mu\nu}$ can be decomposed into two distinct components: a symmetric part, which accounts for the spin-independent contribution to the scattering, and an antisymmetric part, which captures the spin-dependent scattering. The decompositions are given by:

$$L_{\mu\nu} = L^{\mathrm{S}}_{\mu\nu}(l, l') + iL^{\mathrm{A}}_{\mu\nu}(l, s_\ell, l'), \tag{1.8}$$

$$W^{\mu\nu} = W^{\mu\nu}_{\mathrm{S}}(q, P) + iW^{\mu\nu}_{\mathrm{A}}(q, P, S), \tag{1.9}$$

where the indices S and A denote the symmetric and antisymmetric parts, while S and s_ℓ represent the spin of the nucleon or incoming lepton, respectively. The $L^{\mathrm{S}}_{\mu\nu}$ and $L^{\mathrm{A}}_{\mu\nu}$ can be calculated within Quantum Electrodynamics (QED) [22]:

$$L^{\mathrm{S}}_{\mu\nu}(l, l') = 2\left[l_\mu l'_\nu + l'_\nu l_\mu - g_{\mu\nu}\left(l \cdot l' - m_\ell^2\right)\right], \tag{1.10}$$

$$L^{\mathrm{A}}_{\mu\nu}(l, s_\ell, l') = -2\epsilon_{\mu\nu\alpha\beta}\, q^\alpha s_\ell^\beta. \tag{1.11}$$

where $\epsilon_{\mu\nu\alpha\beta}$ is the fully antisymmetric Levi-Civita tensor defined by $\epsilon_{1234} = 1$ and $g_{\mu\nu}$ is the diagonal metric tensor. Unlike the $L_{\mu\nu}$, the hadronic tensor $W^{\mu\nu}$ cannot be obtained from QCD because of the non-perturbative dynamics of the strong interaction.Instead, $W^{\mu\nu}$ can be expressed in a general form that satisfies Lorentz invariance, parity and time-reversal symmetry, as well as the conservation of the electromagnetic current. For polarized DIS on a spin-1/2 target, this general form of $W^{\mu\nu}$ can be written as [22]:

$$W^{\mu\nu}_{\mathrm{S}} = -g^{\mu\nu} f_1^{\mathrm{q}} + \frac{F_2}{P \cdot q} P^\mu P^\nu, \tag{1.12}$$

$$W^{\mu\nu}_{\mathrm{A}} = \frac{g_1}{\nu}\epsilon^{\mu\nu\alpha\beta} q_\alpha S_\beta + \frac{g_2}{\nu^2}\epsilon^{\mu\nu\alpha\beta} q_\alpha \left(P \cdot q S_\beta - S \cdot q P_\beta\right). \tag{1.13}$$

The symmetric part, which governs unpolarised scattering, is expressed in terms of the structure functions f_1^{q} and F_2. In contrast, the antisymmetric part, sensitive to the spin orientations of the lepton and the target, introduces the spin–dependent structure functions g_1 and g_2. All of them depend on both x and Q^2. The unpolarised structure functions f_1^{q} and F_2 can be measured with an unpolarised beam and target. For spin-1/2 targets, accessing g_1 and g_2 requires both the beam and target to be polarised. For higher-spin targets, the symmetric part of $W^{\mu\nu}$ becomes sensitive to the target polarization, allowing measurements even with an unpolarised beam.

1.3 Nucleon Structure Functions

The structure functions f_1^{q}, F_2, g_1 and g_2, introduced in the preceding section, are non-perturbative quantities. Consequently, they cannot be calculated directly using perturbative QCD (pQCD) and must instead be determined experimentally. The available experimental results for proton F_2^{p} are presented in Fig. 1.3a, while analogical results for g_1^{p} are shown in Fig. 1.3b.

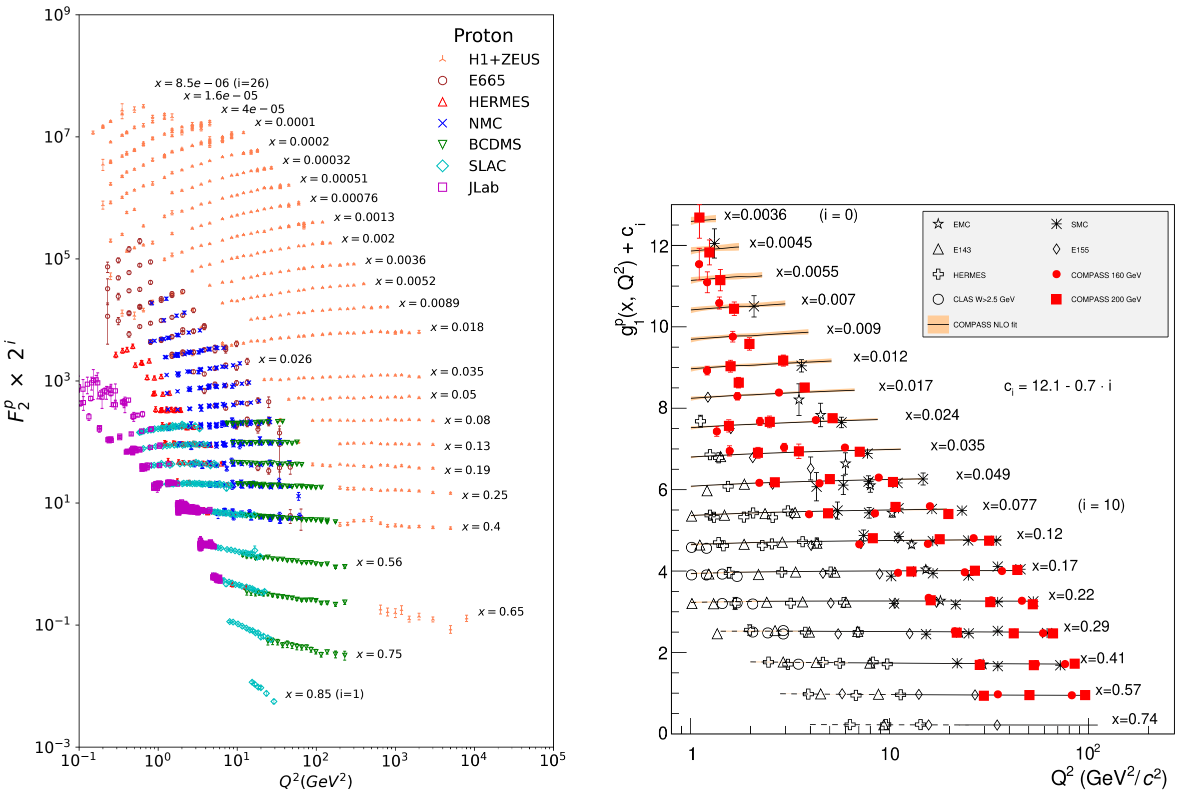

(a) (b)

Figure 1.3: The world data of the proton structure functions as functions of Q^2 for various x values: (a) F_2^{p} and (b) g_1^{p} [23].

At Leading Order (LO) QCD the structure functions F_2 and g_1 and can be expressed in terms of the quark distribution functions f_1^{q}:

$$F_2 = \frac{1}{2}\sum_{\mathrm{q}} e_{\mathrm{q}}^2\, x\, f_1^{\mathrm{q}} = \frac{1}{2}\sum_{\mathrm{q}} e_{\mathrm{q}}^2\, x\, \left(f_1^{\mathrm{q}} + f_1^{\bar{\mathrm{q}}}\right), \tag{1.14}$$

$$g_1 = \frac{1}{2}\sum_{\mathrm{q}} e_{\mathrm{q}}^2 \Delta f_1^{\mathrm{q}} = \frac{1}{2}\sum_{\mathrm{q}} e_{\mathrm{q}}^2 \left(\Delta f_1^{\mathrm{q}} + \Delta f_1^{\bar{\mathrm{q}}}\right). \tag{1.15}$$

Here, e_q denotes the electric charge of a quark (q) or antiquark ($\bar{\mathrm{q}}$), while f_1^{q} represents the probability density of finding a q ($\bar{\mathrm{q}}$) carrying a fraction x of the nucleon momentum.[1]. The f_1^{q} is called quark number density, also known as the unpolarised PDF. In turn, Δf_1^{q}, also called $g_{1\mathrm{L}}^{\mathrm{q}}$, is the longitudinal polarisation (helicity) distribution of

[1] For completeness, the antiquark distributions $f_1^{\bar{\mathrm{q}}}$ are also included, as they are analogous to the quark distributions.

quarks. In what follows, the superscript q is not displayed on the PDFs for clarity[2]. In contrast to F_2, the structure function g_1 is measure much less precisely.

In the "naive" QPM proposed by Feynman [6], the nucleon is composed of partons, point-like constituents that do not interact with each other. As highlighted in Sec. 1.1, this framework is formulated in the infinite momentum frame, where the nucleon carries an asymptotically large momentum and the transverse motion of partons can be neglected. An important feature of the QPM is the scaling of the structure functions. In the Bjorken limit, where $Q^2 \to \infty$ and $\nu \to \infty$ with x held fixed, these functions depend only on x, i.e. $F_2(x, Q^2) \to F_2(x)$ [24]. To a good approximation, the Callan–Gross relation is fulfilled [25]. $F_2(x) \approx 2x\, f_1^q(x)$. Additionally, within this model, the structure function g_2 has no direct physical interpretation and is predicted to vanish.

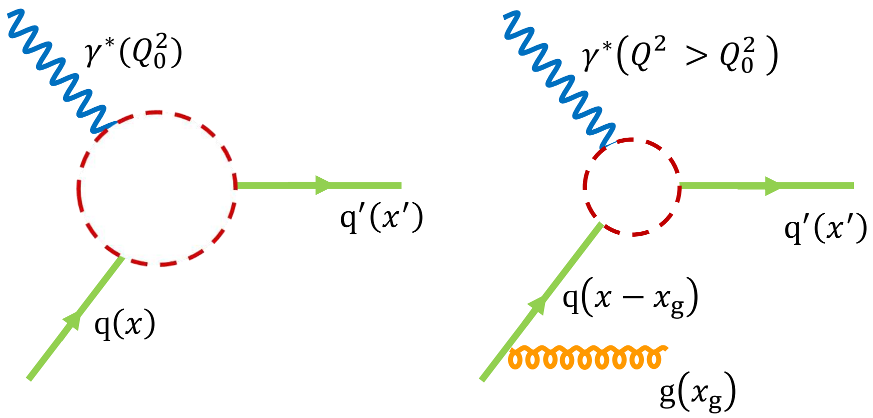

Figure 1.4: llustration of how virtual photons with increasing Q^2 probe the quark distribution more finely, resolving gluon emission and leading to a reduction of the quark momentum fraction.

It is worth emphasizing that the simple QPM, in which structure functions depend solely on the scaling variable x, provides only a first approximation. As Q^2 increases, the measurements become sensitive to more subtle aspects of the nucleon structure, revealing gluon dynamics that the naive model cannot account for. In this approximation the strong coupling constant α_s vanishes, and quarks behave as free, non-interacting constituents. When $Q^2 \gg M^2$, the α_s becomes small but remains non-zero. This motivated the introduction of the QCD-improved parton model. In this regime, pQCD can be applied to extend the naive parton model by including gluonic degrees of freedom, which introduce non-zero transverse momenta for quarks The inclusion of QCD dynamics introduces a non-trivial dependence of the nucleon structure functions on the probing scale Q^2. Quarks can radiate gluons, gluons can split into quark–antiquark pairs, and the resulting quarks may in turn emit additional gluons. As Q^2 increases, the virtual photon becomes capable of resolving gluon emissions from quarks. Consequently, the effective momenta of the observed quarks are reduced, as part of their momentum is carried away by radiated gluons. This mechanism, schematically illustrated in Fig. 1.4, demonstrates how the nucleon at higher resolution appears not as a

[2]It should be emphasized that the PDFs are still defined separately for each quark flavour.

collection of static quarks, but as a dynamic system in which quarks and gluons continuously branch and redistribute momentum. This effect, known as the violation of Bjorken scaling, is supported by experimental evidence, as shown in Fig.1.3a. For fixed values of x, the dependence of quark and gluon distribution functions on Q^2 is governed by the Dokshitzer–Gribov–Lipatov–Altarelli–Parisi (DGLAP) equations [26–28]. These equations describe the evolution of parton densities with respect to Q^2 at fixed x. The predictive power of the DGLAP framework lies in its ability to connect PDFs across different energy scales, thereby offering a unified description of the nucleon internal structure over a wide kinematic range.

1.4 Parton Distribution Functions

In Sec. 1.3, two PDFs, the quark number density and helicity, have been introduced. In addition to these, one also defines the transversity distribution, h_1, which describes the difference between quarks whose transverse spin is aligned or anti-aligned with the transverse polarization of the nucleon. These three distributions define the so-called collinear formalism of QCD, in which the spins of the partons are neglected. Within this approach, QCD has proven highly successful in describing a wide range of experimental data. However, since the pioneering European Muon Collaboration (EMC) measurements at CERN [10], it has become clear that the spin carried by the valence quarks alone cannot account for the total nucleon spin.

Table 1.2: Twist-2 TMD PDFs for longitudinally, transversely, and unpolarised quarks and nucleons. Purple, yellow, and red arrows indicate the nucleon spin, quark spin, and quark transverse momentum, respectively.

		Quark Polarisation		
		Unpolarised (U)	Logitudinally Polarised (L)	Transversely Polarised (T)
Nucleon Polarisation	U	number density $f_1\ (x, Q^2, \boldsymbol{k}_\mathbf{T})$		Boer−Mulders $h_1^\perp(x, Q^2, \boldsymbol{k}_\mathbf{T})$
	L		helicity $g_{1\mathrm{L}}(x, Q^2, \boldsymbol{k}_\mathbf{T})$	worm−gear L $h_{1\mathrm{L}}^\perp(x, Q^2, \boldsymbol{k}_\mathbf{T})$
	T	Sivers $f_{1\mathrm{T}}^\perp(x, Q^2, \boldsymbol{k}_\mathbf{T})$	worm−gear T $g_{1\mathrm{T}}(x, Q^2, \boldsymbol{k}_\mathbf{T})$	pretzelosity $h_{1\mathrm{T}}^\perp(x, Q^2, \boldsymbol{k}_\mathbf{T})$ transversity $h_1\ (x, Q^2, \boldsymbol{k}_\mathbf{T})$

To fully describe nucleon structure, let us now consider transverse motion of partons. In inclusive deep inelastic scattering, only the final-state lepton is detected, while the details of the hadronic final state are not observed. As a result, the transverse momentum of the struck parton is not measured, and the inclusive DIS cross-section effectively integrates over all possible transverse momenta of the partons. This integration implies that inclusive DIS lacks sensitivity to the parton transverse momentum distributions. For this reason, processes such as Drell–Yan and Semi-Inclusive Deep Inelastic Scattering (SIDIS) are employed, as they are sensitive to the internal transverse momentum of partons.

At leading twist, the nucleon structure is described in terms of eight TMD PDFs, each depending on the longitudinal momentum fraction x, the hard scale Q^2, and the transverse parton momentum $\boldsymbol{k}_\mathrm{T}$[3]. In Tab. 1.2 the so-called Amsterdam (also known as Jaffe–Ji–Mulders) notation is introduced. An analogous classification can be formulated for gluon leading twist TMD PDFs [29, 30].

Along the diagonal of Tab. 1.2 lie the only three TMD PDFs that survive integration over the transverse momentum $\boldsymbol{k}_\mathrm{T}$, reducing to their corresponding collinear PDFs. These are the unpolarised (number density) distribution $f_1^\mathrm{q}(x, \boldsymbol{k}_\mathrm{T})$, the helicity distribution $g_{1\mathrm{L}}^\mathrm{q}(x, \boldsymbol{k}_\mathrm{T})$, and the transversity distribution $h_1^\mathrm{q}(x, \boldsymbol{k}_\mathrm{T})$.

For example, the unpolarised distribution satisfies the relation:

$$f_1^\mathrm{q}(x) = \int d^2\boldsymbol{k}_\mathrm{T}\, f_1^\mathrm{q}(x, \boldsymbol{k}_\mathrm{T}). \tag{1.16}$$

Analogous expressions hold for the helicity and transversity PDFs. In contrast, the remaining five leading-twist TMD PDFs vanish in the collinear limit; that is, their integrals over $\boldsymbol{k}_\mathrm{T}$ are zero. These distributions therefore do not contribute to the collinear PDFs and encapsulate purely transverse momentum-dependent phenomena.

The quark Sivers function $f_{1\mathrm{T}}^{\perp\mathrm{q}}(x, \boldsymbol{k}_\mathrm{T})$, originally proposed to explain the unexpectedly large spin-dependent asymmetries observed in polarised nucleon scattering [31], describes the correlation between the intrinsic transverse momentum of unpolarised quarks and the transverse polarization of the nucleon. A nonzero Sivers function implies a preferred transverse momentum direction of quarks in a polarised nucleon, which necessarily originates from partonic orbital angular momentum. Since partonic orbital motion is a key missing piece in resolving how the nucleon constituents generate its overall spin, the Sivers function provides crucial experimental access to this component, making it central to addressing the nucleon spin puzzle.

The Boer–Mulders TMD PDF, $h_1^{\perp\mathrm{q}}(x, \boldsymbol{k}_\mathrm{T})$, introduced in 1998 [32], describes a correlation between the transverse momentum and the transverse spin of quarks inside an unpolarised hadron. It represents the difference in distributions of quarks with opposite transverse spin orientations for a given transverse momentum, leading to a net quark transverse polarization even in an unpolarised nucleon. A nonzero Boer–Mulders function signifies a net transverse quark polarization oriented orthogonally to the plane spanned by $\boldsymbol{k}_\mathrm{T}$ and the nucleon momentum.

While parton distribution functions are generally considered process-independent, the "naive" time-reversal odd Sivers and Boer–Mulders functions are predicted to change sign when measured in SIDIS compared to Drell–Yan (DY) processes. This bso-called limited universality is expressed mathematically as

$$h_1^{\perp\mathrm{q}}(x, \boldsymbol{k}_\mathrm{T})\Big|_\mathrm{SIDIS} = -h_1^{\perp\mathrm{q}}(x, \boldsymbol{k}_\mathrm{T})\Big|_\mathrm{DY} \tag{1.17}$$

$$f_{1\mathrm{T}}^{\perp\mathrm{q}}(x, \boldsymbol{k}_\mathrm{T})\Big|_\mathrm{SIDIS} = -f_{1\mathrm{T}}^{\perp\mathrm{q}}(x, \boldsymbol{k}_\mathrm{T})\Big|_\mathrm{DY} \tag{1.18}$$

[3]For clarity, the Q^2 dependence is omitted in the notation.

The sign reversal arises from the different color interactions involved, since in SIDIS the struck quark undergoes final-state interactions with the target remnants, whereas in DY initial-state interactions occur before the hard scattering.

The two worm-gear functions [33], $g_{1\mathrm{T}}^{\mathrm{q}}(x, \boldsymbol{k}_{\mathrm{T}})$ and $h_{1\mathrm{L}}^{\perp\mathrm{q}}(x, \boldsymbol{k}_{\mathrm{T}})$, characterize the distributions of longitudinally polarised quarks in a transversely polarised nucleon ($g_{1\mathrm{T}}^{\mathrm{q}}(x, \boldsymbol{k}_{\mathrm{T}})$) and transversely polarised quarks in a longitudinally polarised nucleon ($h_{1\mathrm{L}}^{\perp\mathrm{q}}(x, \boldsymbol{k}_{\mathrm{T}})$), respectively.

The transversity distribution, $h_{1}^{\mathrm{q}}(x, \boldsymbol{k}_{\mathrm{T}})$, is the transverse polarization analog of the helicity distribution, $g_{1\mathrm{L}}^{\mathrm{q}}(x, \boldsymbol{k}_{\mathrm{T}})$. It describes the difference between the number of quarks polarised transversely parallel to the parent hadron spin and those polarised antiparallel. This function was first introduced in 1979 in the context of Drell–Yan production with polarised beams [34].

Finally, the pretzelosity distribution, $h_{1\mathrm{T}}^{\perp\mathrm{q}}(x, \boldsymbol{k}_{\mathrm{T}})$, describes the correlation between the transverse polarization of partons and their intrinsic transverse momentum within a transversely polarised nucleon. It has been linked to the spatial structure of the nucleon, where a nonzero value of $h_{1\mathrm{T}}^{\perp\mathrm{q}}(x, \boldsymbol{k}_{\mathrm{T}})$ would imply that the nucleon deviates from a perfectly spherical shape [35]. Moreover, in simple quark models, such as the MIT bag model, the difference between helicity and transversity distributions—often regarded as a measure of relativistic effects in the nucleon—is directly related to the pretzelosity distribution [36].

Perturbative QCD can be used to describe many high energy scattering processes. If hadrons in the final state are identified, the non-perturbative functions describing the formation of these colorless bound final states are called fragmentation function. At leading twist, eight Transverse-Momentum Dependent (TMD) Fragmentation Functions (FFs) are defined. Measurements of these functions have been performed by the BELLE [37, 38], BABAR [39, 40], and BESIII [41]. A detailed discussion of TMD FF is beyond the scope of this work and is therefore only briefly mentioned here for completeness.

Chapter 2

Drell–Yan Process

With four parameters I can fit an elephant,
and with five I can make him wiggle his trunk.
— John von Neumann

The following chapter focuses on the Drell–Yan process, which is the main subject of this thesis. Sec. 2.1 introduces the process and the coordinate systems used to describe it, laying the foundation for the cross section derivation in Sec. 2.2. Sec. 2.3 then discusses how transverse-momentum weighted structure functions relate to the corresponding TMD PDFs.

2.1 Introduction

The Drell–Yan dilepton production has played an important role in pinning down parton distributions of hadrons. A general expression of this process is given by:

$$\mathrm{H}_a(P_a, S_a) + \mathrm{H}_b(P_b, S_b) \to \gamma^*/\mathrm{Z}^0(q) + \mathrm{X} \to \ell^-(l^-) + \ell^+(l^+) + \mathrm{X}.$$

where the four-momentum vectors of hadrons are denoted as P_a and P_b, while their spin four-vectors as S_a and S_b. At leading order, a $\mathrm{q}\bar{\mathrm{q}}$ pair annihilates into a virtual photon γ^* or a neutral weak boson Z^0, which subsequently convert into a lepton pair, as illustrated in Fig. 2.1.

In the Common Muon and Proton Apparatus for Structure and Spectroscopy (COMPASS) experiment, a negative pion beam[1] interacts with three targets, a polarised NH_3[2] and unpolarized Al and W. Moreover, the DY process proceeds predominantly via γ^* exchange, the contribution from Z^0 production is strongly suppressed.

The CM energy. $\sqrt{s}$, cenergy can be expressed in terms of the hadronic four-momenta as:

$$s = (P_a + P_b)^2 \tag{2.1}$$

The four-momentum of the exchanged boson is given by:

$$q = l^- + l^+, \tag{2.2}$$

[1]Hence, the spin four-vector of the beam is $S_a = (0, 0, 0, 0)$.
[2]The analysis presented in this work is based on data collected with the polarized NH_3 target.

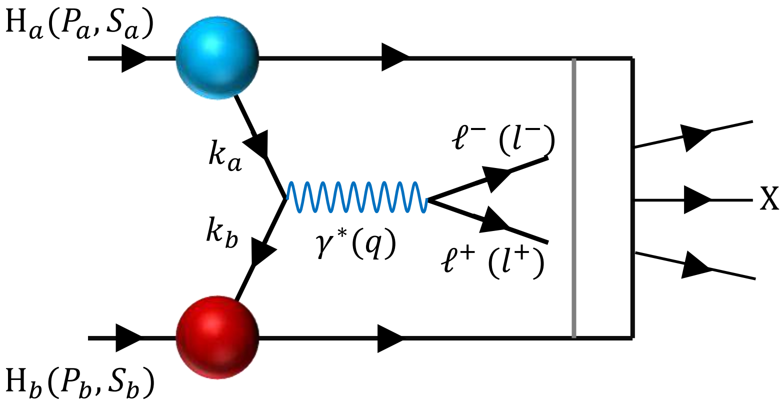

Figure 2.1: Leading order Feynman diagram for Drell-Yan process in the general case, where the virtual neutral boson is a virtual photon, where both hadrons are polarised.

with $l^{\pm}$ denoting the four-momenta of the produced leptons. The partonic four-momenta, k_a and k_b, are related to the hadronic four-momenta via x_a and x_b:

$$\begin{cases} k_a = x_a P_a, \\ k_b = x_b P_b, \end{cases} \qquad \text{with} \quad x_{a,b} = \frac{Q^2}{2P_{a,b} \cdot q}. \tag{2.3}$$

A summary of the variables used to describe the DY process is given in Tab. 2.1.

Table 2.1: Definition of the kinematic variables relevant for the DY process.

Kinematic variable	Definition
$s = (P_a + P_b)^2$	Total centre-of-mass energy squared
$x_{a(b)} = q^2/2P_{a(b)} \cdot q$	Momentum fraction carried by a parton from $H_{a(b)}$
$x_F = x_a - x_b$	Feynman variable
$M^2_{\ell\bar{\ell}} = Q^2 = q^2 = s\, x_a x_b$	Invariant mass squared of the dilepton, virtuality of the photon
P_a, P_b	Beam and target four-momenta
l^-, l^+	Lepton and antilepton four-momenta
$\boldsymbol{S_T}$	Transverse (w.r.t. $\hat{\boldsymbol{z}}_{\mathrm{TF}}$) part of the target polarisation
$\boldsymbol{q_T}$	Transverse (w.r.t. $\hat{\boldsymbol{z}}_{\mathrm{TF}}$) part of $\boldsymbol{q} = \boldsymbol{k_a} + \boldsymbol{k_b}$
φ_S	Azimuthal angle between $\boldsymbol{S_T}$ and $\boldsymbol{q_T}$ in target rest frame
$\theta_{CS}, \varphi_{CS}$	Polar and azimuthal angles in Collin–Sopper frame

Target Rest Frame

In the target rest frame (Fig. 2.2), $\hat{\boldsymbol{z}}_{\mathrm{TF}}$ is chosen along the beam hadron momentum, $\hat{\boldsymbol{x}}_{\mathrm{TF}}$ along the transverse component of the virtual photon four-momentum $\boldsymbol{q}_{\mathrm{T}}$, and $\hat{\boldsymbol{y}}_{\mathrm{TF}}$

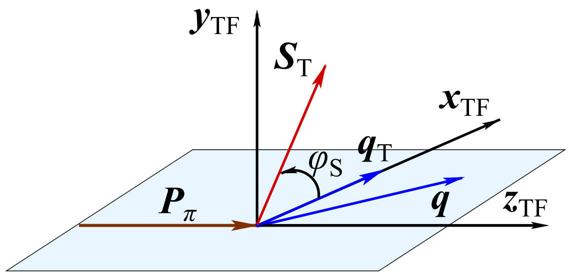

Figure 2.2: Definition of the azimuthal angle φ_{S} of transverse target spin S_{T} in the target rest frame.

is defined by $\hat{\boldsymbol{y}}_{\mathrm{TF}} = \hat{\boldsymbol{z}}_{\mathrm{TF}} \times \hat{\boldsymbol{x}}_{\mathrm{TF}}$. The four-vectors in this reference frame are defined as follows:

$$\begin{cases} q = (q_0, q_{\mathrm{T}}, 0, q_{\mathrm{L}}), \\ S_b = (0, S_{\mathrm{T}} \cos\varphi_{\mathrm{S}}, S_{\mathrm{T}} \sin\varphi_{\mathrm{S}}, S_{\mathrm{L}}), \end{cases} \tag{2.4}$$

where the polarisation vector is normalised as $S_b^2 = -1$.

The Collins–Soper Frame

The Collins-Sopper (CS) frame is defined as the rest frame of the virtual photon. It is obtained from the target rest frame through a sequence of Lorentz boosts: first along the $\hat{\boldsymbol{z}}_{\mathrm{CS}}$-axis, followed by a boost along the $\hat{\boldsymbol{x}}_{\mathrm{CS}}$-axis. These transformations ensure that both the longitudinal and transverse momenta of the virtual photon vanish (see Fig. 2.3). In the CS frame, and under the assumption that the lepton mass is negligible,

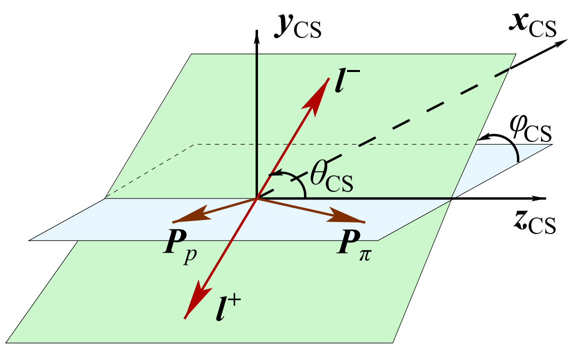

Figure 2.3: Definition of polar and azimuthal angles θ_{CS} and φ_{CS} of transverse target spin S_{T} of the lepton momenta in the Collins–Soper frame.

the four-momenta of the lepton and antilepton take the following form:

$$\begin{cases} l^- = \frac{q}{2}\left(1, \sin\theta_{\mathrm{CS}} \cos\varphi_{\mathrm{CS}}, \sin\theta_{\mathrm{CS}} \sin\varphi_{\mathrm{CS}}, \cos\theta_{\mathrm{CS}}\right), \\ l^+ = \frac{q}{2}\left(1, -\sin\theta_{\mathrm{CS}} \cos\varphi_{\mathrm{CS}}, -\sin\theta_{\mathrm{CS}} \sin\varphi_{\mathrm{CS}}, -\cos\theta_{\mathrm{CS}}\right). \end{cases} \tag{2.5}$$

2.2 Drell–Yan cross section

2.2.1 Single Polarised Drell–Yan Process

When summing over the polarizations of the produced leptons, the LO differential cross section for pion-induced Drell–Yan production on a transversely polarised nucleon can be expressed as [42][3]:

$$\begin{aligned}\frac{d\sigma_{\mathrm{DY}}}{d^4q\,d\Omega} = \frac{\alpha^2}{CQ^2}\Bigg\{&(1+\cos^2\theta_{\mathrm{CS}})F_{\mathrm{U}}^1 + (1-\cos^2\theta_{\mathrm{CS}})F_{\mathrm{U}}^2\\
&+\sin 2\theta_{\mathrm{CS}}\cos\varphi_{\mathrm{CS}}F_{\mathrm{U}}^{\cos\varphi_{\mathrm{CS}}} + \sin^2\theta_{\mathrm{CS}}\cos 2\varphi_{\mathrm{CS}}F_{\mathrm{U}}^{\cos 2\varphi_{\mathrm{CS}}}\\
&+|S_{\mathrm{T}}|\Big[\sin\varphi_{\mathrm{S}}\Big((1+\cos^2\theta_{\mathrm{CS}})F_{\mathrm{T}}^1 + (1-\cos^2\theta_{\mathrm{CS}})F_{\mathrm{T}}^2\Big)\\
&+\sin 2\theta_{\mathrm{CS}}\Big(\sin(\varphi_{\mathrm{CS}}+\varphi_{\mathrm{S}})F_{\mathrm{T}}^{\sin(\varphi_{\mathrm{CS}}+\varphi_{\mathrm{S}})} + \sin(\varphi_{\mathrm{CS}}-\varphi_{\mathrm{S}})F_{\mathrm{T}}^{\sin(\varphi_{\mathrm{CS}}-\varphi_{\mathrm{S}})}\Big)\\
&+\sin^2\theta_{\mathrm{CS}}\Big(\sin(2\varphi_{\mathrm{CS}}+\varphi_{\mathrm{S}})F_{\mathrm{T}}^{\sin(2\varphi_{\mathrm{CS}}+\varphi_{\mathrm{S}})} + \sin(2\varphi_{\mathrm{CS}}-\varphi_{\mathrm{S}})F_{\mathrm{T}}^{\sin(2\varphi_{\mathrm{CS}}-\varphi_{\mathrm{S}})}\Big)\Big]\Bigg\}\end{aligned} \tag{2.6}$$

where θ_{CS} and φ_{CS} represent the polar and azimuthal angles of the $\boldsymbol{l}^-$ in the CS frame shown in 2.3, while φ_{S} is defined as the angle q_{T} and $\boldsymbol{S}_{\mathrm{T}}$ in target frame (Fig. 2.2). Finally, the kinematic factor C is expressed as $C = 4\sqrt{(\boldsymbol{P}_a\cdot\boldsymbol{P}_b)^2 - M_a^2M_b^2}$, where $\boldsymbol{P}_a$ and $\boldsymbol{P}_b$ represent the momenta of the particles a and b, and M_a and M_b are their respective masses.

The differential cross section on the left-hand side is expressed in terms of six variables, namely the four components of the momentum transfer q together with two angular variables that specify the lepton direction:

$$d\Omega = d\cos\theta_{\mathrm{CS}}d\varphi_{\mathrm{CS}}. \tag{2.7}$$

The four-momentum of the virtual photon q can be conveniently decomposed in the target rest frame, where it takes the form $q = (q_0, q_{\mathrm{T}}\sin\varphi_{\mathrm{S}}, q_{\mathrm{T}}\cos\varphi_{\mathrm{S}}, q_{\mathrm{L}})$. Thus, the differential four-momentum element d^4q becomes $d^4q = \frac{1}{2}dq_0dq_{\mathrm{L}}dq_{\mathrm{T}}^2\,d\varphi_{\mathrm{S}}$. Then, the elements q_0 and q_{L} can be reformulated using the Bjorken variables x_a and x_b:

$$\begin{aligned}\frac{d\sigma_{\mathrm{DY}}}{dx_a\,dx_b\,dq_{\mathrm{T}}^2\,d\varphi_{\mathrm{S}}\,d\cos\theta_{\mathrm{CS}}\,d\varphi_{\mathrm{CS}}} &= \frac{J(x_a,x_b,P_a,P_b)}{2}\frac{d\sigma_{\mathrm{DY}}}{d^4q\,d\Omega}\\
&= C_0(x_a,x_b,P_a,P_b)\left\{(1+\cos^2\theta_{\mathrm{CS}})F_{\mathrm{U}}^1(x_a,x_b,q_{\mathrm{T}}) + \dots\right\},\end{aligned} \tag{2.8}$$

The coefficient $C_0 = \alpha^2 J(x_a,x_b,P_a,P_b)/\,(2CQ^2)$, where for massless hadrons the Jacobian reduces to $J(x_a,x_b,P_a,P_b) = s/2$ [42], while in the general case it takes a more complicated form.

2.2.2 Lam–Tung Relation

Integrating the transversely polarised DY cross section given in Eq. (2.6) over φ_{S} yields the unpolarised angular distribution, expressed in terms of the coefficients

[3]Presented structure functions depend on Q^2, x, and transverse momenta of quarks, $\boldsymbol{k}_{a\mathrm{T}}$ and $\boldsymbol{k}_{b\mathrm{T}}$, which have been omitted here for clarity of notation.

(λ, μ, ν) [42]:

$$\frac{1}{\sigma_0}\frac{d\sigma_{\rm DY}}{d\Omega} = \frac{3}{4\pi}\left[1 + \lambda\cos^2\theta_{\rm CS} + \mu\sin 2\theta_{\rm CS}\cos\varphi_{\rm CS} + \frac{\nu}{2}\sin^2\theta_{\rm CS}\cos 2\varphi_{\rm CS}\right], \tag{2.9}$$

where σ_0 represents the total Drell–Yan cross section obtained by integrating over the angular $\varphi_{\rm CS}$ distribution. The parameters (λ, μ, ν) are the unpolarised Drell–Yan angular coefficients expressed as:

$$\lambda = \frac{F_{\rm U}^1 - F_{\rm U}^2}{F_{\rm U}^1 + F_{\rm U}^2}, \quad \mu = \frac{F_{\rm U}^{\cos\varphi_{\rm CS}}}{F_{\rm U}^1 + F_{\rm U}^2}, \quad \nu = \frac{2F_{\rm U}^{\cos 2\varphi_{\rm CS}}}{F_{\rm U}^1 + F_{\rm U}^2}. \tag{2.10}$$

At LO "naive" Drell–Yan model the angular coefficients are predicted to be $\lambda = 1$, and $\mu = 0$, $\nu = 0$. Beyond this simple description, higher-order QCD contributions must be considered, such as gluon emission, qG Compton scattering. The virtual photon is not restricted to purely transverse polarization, and the angular coefficients μ, ν become nonzero. At Next-to-Leading Order (NLO) pQCD, the Lam–Tung relation is expected to remain satisfied [42]:

$$\lambda + 2\nu = 1. \tag{2.11}$$

The Lam–Tung relation has been experimentally tested in pion-induced Drell–Yan processes by the NA10 Collaboration at CERN [43, 44] and E615 Collaboration in Fermilab [45]. A significant violation of this relation was observed, sparking extensive theoretical investigations. As demonstrated by D. Boer [46], the discrepancy can be traced back to the Boer–Mulders function, a transverse-momentum dependent structure function previously omitted, which generates spin-momentum correlations in the quark distributions. The E866 Collaboration reported no significant deviation from the Lam–Tung relation for pd [47] and pp [48] interactions at 800 GeV/c. This result remains consistent with the explanation involving the Boer–Mulders function, as the antiquarks in these reactions originate primarily from the sea, whereas in π^-A Drell–Yan, valence antiquarks play a dominant role. In 2011 and 2015, the CDF [49] and CMS [50] Collaborations reported new results on the Lam–Tung relation. While CDF found good agreement, CMS observed a clear violation. Studies of angular distributions in Z-boson production [51] provided new perspectives, and comparisons of CMS and CDF data suggest a dependence on the q$\bar{\rm q}$ and qG production fractions. Despite extensive efforts, the interpretation of the Lam–Tung violation remains an open question, and new fixed-target experiments, such as COMPASS and E906/SeaQuest [52], are expected to provide valuable insights.

2.2.3 Structure Functions in the TMD Approach

This section systematically describes structure functions, concentrating on the kinematic region where the virtual photon transverse momentum, $q_{\rm T}$, is of the order of a typical hadronic scale, yet much smaller than the hard scale q. To compute leading-twist observables present in Eq. (2.6) the notation for the convolution of TMD PDFs in the transverse momentum space is used[4]:

$$\mathcal{C}[w(\boldsymbol{k}_{a\mathrm{T}},\boldsymbol{k}_{b\mathrm{T}})f_a f_b] = \frac{1}{N_c}\sum_{\mathrm{q}} e_{\mathrm{q}}^2 \int \mathrm{d}^2\boldsymbol{k}_{a\mathrm{T}}\,\mathrm{d}^2\boldsymbol{k}_{b\mathrm{T}}\,\delta^{(2)}(\boldsymbol{q}_{\mathrm{T}}-\boldsymbol{k}_{a\mathrm{T}}-\boldsymbol{k}_{b\mathrm{T}}) \\ \times w(\boldsymbol{k}_{a\mathrm{T}},\boldsymbol{k}_{b\mathrm{T}})\left[f_a^{\mathrm{q}}(x_a,k_{a\mathrm{T}}^2)f_b^{\bar{\mathrm{q}}}(x_b,k_{b\mathrm{T}}^2)+f_a^{\bar{\mathrm{q}}}(x_a,k_{a\mathrm{T}}^2)f_b^{\mathrm{q}}(x_b,k_{b\mathrm{T}}^2)\right], \tag{2.12}$$

where N_c is the number of colors. The TMD PDFs depend not only on $x_{a,b}$, the fractions of the parent hadron momenta carried by the quarks in the TMD approach, and the transverse momenta $\boldsymbol{k}_{a\mathrm{T}},\boldsymbol{k}_{b\mathrm{T}}$, but also on the QCD scale Q^2, which is not explicitly indicated. The structure functions from Eq. (2.6) in the LO QCD and TMD factorisation can be written as[5]:

$$F_{\mathrm{U}}^1 = \mathcal{C}\left[f_{1,a}f_{1,b}\right], \tag{2.13}$$

$$F_{\mathrm{U}}^2 = 0, \tag{2.14}$$

$$F_{\mathrm{U}}^{\cos\varphi_{\mathrm{CS}}} = 0, \tag{2.15}$$

$$F_{\mathrm{U}}^{\cos 2\varphi_{\mathrm{CS}}} = \mathcal{C}\left[\frac{2(\boldsymbol{q}_{\mathrm{T}}\cdot\boldsymbol{k}_{a\mathrm{T}})(\boldsymbol{q}_{\mathrm{T}}\cdot\boldsymbol{k}_{b\mathrm{T}})-\boldsymbol{q}_{\mathrm{T}}^2(\boldsymbol{k}_{a\mathrm{T}}\cdot\boldsymbol{k}_{b\mathrm{T}})}{q_{\mathrm{T}}^2 M_a M_b}h_{1,a}^{\perp}h_{1,b}^{\perp}\right], \tag{2.16}$$

$$F_{\mathrm{T}}^2 = 0, \tag{2.17}$$

$$F_{\mathrm{T}}^{\cos(\varphi_{\mathrm{CS}}\pm\varphi_{\mathrm{S}})} = 0, \tag{2.18}$$

$$F_{\mathrm{T}}^1 = F_{\mathrm{T}}^{\sin\varphi_{\mathrm{S}}} = -\mathcal{C}\left[\frac{\boldsymbol{q}_{\mathrm{T}}\cdot\boldsymbol{k}_{b\mathrm{T}}}{q_{\mathrm{T}}M_b}f_{1,a}f_{1\mathrm{T},b}^{\perp}\right], \tag{2.19}$$

$$F_{\mathrm{T}}^{\sin(2\varphi_{\mathrm{CS}}+\varphi_{\mathrm{S}})} = -\mathcal{C}\left[\frac{(\boldsymbol{q}_{\mathrm{T}}\cdot\boldsymbol{k}_{b\mathrm{T}})\left[2(\boldsymbol{q}_{\mathrm{T}}\cdot\boldsymbol{k}_{a\mathrm{T}})(\boldsymbol{q}_{\mathrm{T}}\cdot\boldsymbol{k}_{b\mathrm{T}})-\boldsymbol{q}_{\mathrm{T}}^2(\boldsymbol{k}_{a\mathrm{T}}\cdot\boldsymbol{k}_{b\mathrm{T}})\right]}{q_{\mathrm{T}}^3 M_a M_b^2} \\ -\frac{\boldsymbol{k}_{b\mathrm{T}}^2(\boldsymbol{q}_{\mathrm{T}}\cdot\boldsymbol{k}_{a\mathrm{T}})}{2q_{\mathrm{T}}M_a M_b^2}\right]h_{1,a}^{\perp}h_{1\mathrm{T},b}^{\perp}, \tag{2.20}$$

$$F_{\mathrm{T}}^{\sin(2\varphi_{\mathrm{CS}}-\varphi_{\mathrm{S}})} = -\mathcal{C}\left[\frac{\boldsymbol{q}_{\mathrm{T}}\cdot\boldsymbol{k}_{a\mathrm{T}}}{q_{\mathrm{T}}M_a}h_{1,a}^{\perp}h_{1,b}\right]. \tag{2.21}$$

[4]The TMD PDFs also depend on Q^2, this dependence has been omitted in the notation for clarity.

[5]For clarity of notation, the dependence on $x_{a(b)}$, $\boldsymbol{k}_{a(b)\mathrm{T}}$, and $\mathrm{q}(\bar{\mathrm{q}})$ in the superscript have been omitted when possible.

Given that certain structure functions vanish under the assumptions made, the cross section from Eq. (2.6) simplifies to:

$$\begin{aligned}\frac{d\sigma_{\mathrm{DY}}}{dx_a\,dx_b\,dq_{\mathrm{T}}^2\,d\varphi_{\mathrm{S}}\,d\cos\theta_{\mathrm{CS}}\,d\varphi_{\mathrm{CS}}} = C_0\Big\{&(1+\cos^2\theta_{\mathrm{CS}})F_{\mathrm{U}}^1 + \sin^2\theta_{\mathrm{CS}}\cos 2\varphi_{\mathrm{CS}}\,F_{\mathrm{U}}^{\cos 2\varphi_{\mathrm{CS}}}\\ &+|S_{\mathrm{T}}|\Big[(1+\cos^2\theta_{\mathrm{CS}})\sin\varphi_{\mathrm{S}}\,F_{\mathrm{T}}^{\sin\varphi_{\mathrm{S}}}\\ &+\sin^2\theta_{\mathrm{CS}}\sin(2\varphi_{\mathrm{CS}}+\varphi_{\mathrm{S}})\,F_{\mathrm{T}}^{\sin(2\varphi_{\mathrm{CS}}+\varphi_{\mathrm{S}})}\\ &+\sin^2\theta_{\mathrm{CS}}\sin(2\varphi_{\mathrm{CS}}-\varphi_{\mathrm{S}})\,F_{\mathrm{T}}^{\sin(2\varphi_{\mathrm{CS}}-\varphi_{\mathrm{S}})}\Big]\Big\}.\end{aligned} \tag{2.22}$$

Because spin effects are very subtle, precise measurement of the azimuthal distributions of outgoing particles is challenging. To address this, the so-called Transverse-Spin Dependent Azimuthal Asymmetrys (TSAs) are introduced, defined as:

$$A_{\mathrm{X}}^{\mathrm{Y}}(x_a, x_b) = \frac{F_{\mathrm{X}}^{\mathrm{Y}}}{F_{\mathrm{U}}^1}, \tag{2.23}$$

where $F_{\mathrm{X}}^{\mathrm{Y}}$ epresents the relevant structure function: X = U for unpolarised case and X = T for the transversely polarised case.

2.3 TMD Expressions via Momentum Weighting

Extraction of the TMD parton distribution functions from a TSA requires accounting for the convolution over the intrinsic transverse momenta of partons. While the unpolarised structure function F_{U}^1 in the Drell–Yan process can be integrated analytically over transverse momentum, this is not generally possible for modulated terms, which involve angular dependencies. In such cases, the convolution integrals cannot be solved exactly without introducing strong model assumptions [53, 54]. It has been demonstrated [55–57] that these convolutions can be effectively disentangled if the cross section is weighted appropriately with functions of the transverse momentum. This approach also relies on certain assumptions, but it significantly reduces the model dependence. In the following, the principle of so-called Transverse-Momentum Weighted Transverse-Spin Dependent Azimuthal Asymmetry (WTSA) in the Drell–Yan process with a transversely polarised target is outlined.

2.3.1 Constant Term in Transverse Momentum Weighting

In the simplest case of F_{U}^{1}, the integration over q_{T} is straightforward. Using Eqs 2.12 and 2.13, one finds:

$$\begin{aligned}\int \mathrm{d}^2\boldsymbol{q}_{\mathrm{T}}\, F_{\mathrm{U}}^{1} &= \int \mathrm{d}^2\boldsymbol{q}_{\mathrm{T}}\, \mathcal{C}\left[f_{1,a} f_{1,b}\right] \\ &= \int \mathrm{d}^2\boldsymbol{q}_{\mathrm{T}}\, \frac{1}{N_c}\sum_{\mathrm{q}} e_{\mathrm{q}}^2 \int \mathrm{d}^2\boldsymbol{k}_{a\mathrm{T}}\, \mathrm{d}^2\boldsymbol{k}_{b\mathrm{T}}\, \delta^{(2)}(\boldsymbol{q}_{\mathrm{T}} - \boldsymbol{k}_{a\mathrm{T}} - \boldsymbol{k}_{b\mathrm{T}}) \\ &\quad \times \left[f_{1,a}^{\bar{\mathrm{q}}}(x_a, k_{a\mathrm{T}}^2) f_{1,b}^{\mathrm{q}}(x_b, k_{b\mathrm{T}}^2) + f_{1,a}^{\mathrm{q}}(x_a, k_{a\mathrm{T}}^2) f_{1,b}^{\bar{\mathrm{q}}}(x_b, k_{b\mathrm{T}}^2)\right] \\ &= \frac{1}{N_c}\sum_{\mathrm{q}} e_{\mathrm{q}}^2 \left[f_{1,a}^{\mathrm{q}}(x_a) f_{1,b}^{\bar{\mathrm{q}}}(x_b) + f_{1,a}^{\bar{\mathrm{q}}}(x_a) f_{1,b}^{\mathrm{q}}(x_b)\right]. \end{aligned} \tag{2.24}$$

In the case of other structure functions (Eqs.(2.15–2.21)), the main difficulty arises from the presence of $q_{\mathrm{T}} = |\boldsymbol{q}_{\mathrm{T}}|$ in the denominator of the integration weight. This can be addressed by using a carefully chosen weight that removes the q_{T} dependence, and in some cases, additional multiplicative factors are introduced to obtain more compact or analytically convenient expressions.

2.3.2 Structure function arising from the Sivers Effect

Integration of the structure function $F_{\mathrm{T}}^{\sin\varphi_{\mathrm{S}}}$ over $\boldsymbol{q}_{\mathrm{T}}$ with a weight q_{T}/M_b yields:

$$\begin{aligned}\int \mathrm{d}^2\boldsymbol{q}_{\mathrm{T}}\, \frac{q_{\mathrm{T}}}{M_b}\, F_{\mathrm{T}}^{\sin\varphi_{\mathrm{S}}} &= -\int \mathrm{d}^2\boldsymbol{q}_{\mathrm{T}}\, \frac{q_{\mathrm{T}}}{M_b}\, \mathcal{C}\left[\frac{\boldsymbol{q}_{\mathrm{T}}\cdot\boldsymbol{k}_{b\mathrm{T}}}{q_{\mathrm{T}} M_b} f_{1,a} f_{1\mathrm{T},b}^{\perp}\right] \\ &= -\sum_{\mathrm{q}} e_{\mathrm{q}}^2 \int \frac{\mathrm{d}^2\boldsymbol{k}_{a\mathrm{T}}\, \mathrm{d}^2\boldsymbol{k}_{b\mathrm{T}}}{N_c M_b^2}\, (\boldsymbol{k}_{a\mathrm{T}} + \boldsymbol{k}_{b\mathrm{T}})\cdot\boldsymbol{k}_{b\mathrm{T}} \\ &\quad \times \left[f_{1,a}^{\bar{\mathrm{q}}}(x_a, k_{a\mathrm{T}}^2)\, f_{1\mathrm{T},b}^{\mathrm{q}\perp}(x_b, k_{b\mathrm{T}}^2) + (\mathrm{q} \leftrightarrow \bar{\mathrm{q}})\right]. \end{aligned} \tag{2.25}$$

The presence of the q_{T}/M_b weight in Eq. (2.25) cancels the q_{T} in the denominator. It follows that only contributions even in $\boldsymbol{k}_{a\mathrm{T}}$ remain after integration, as any integrand that is odd under $\boldsymbol{k}_{a\mathrm{T}} \to -\boldsymbol{k}_{a\mathrm{T}}$ integrates to zero:

$$\int \mathrm{d}^2\boldsymbol{k}_{a\mathrm{T}} (\boldsymbol{k}_{a\mathrm{T}}\cdot\boldsymbol{k}_{b\mathrm{T}}) f(x, k_{a\mathrm{T}}^2) = 0. \tag{2.26}$$

Final expression for the integral of the $F_{\mathrm{T}}^{\sin\varphi_{\mathrm{S}}}$ over $\boldsymbol{q}_{\mathrm{T}}$ reads:

$$\int \mathrm{d}^2\boldsymbol{q}_{\mathrm{T}}\, \frac{q_{\mathrm{T}}}{M_b}\, F_{\mathrm{T}}^{\sin\varphi_{\mathrm{S}}} = -\frac{2}{N_c}\sum_{\mathrm{q}} e_{\mathrm{q}}^2 \left[f_{1,a}^{\bar{\mathrm{q}}}(x_a)\, f_{1\mathrm{T},b}^{\perp(1)\mathrm{q}}(x_b) + (\mathrm{q} \leftrightarrow \bar{\mathrm{q}})\right], \tag{2.27}$$

This formula provides direct access to the unpolarised parton distribution function and the first transverse moment of the Sivers function. The general form of n-th transverse moment (k_{T}^2 moment) of a TMD PDF $f(x)$ is given by:

$$f^{(n)}(x) = \int \mathrm{d}^2\boldsymbol{k}_{\mathrm{T}} \left(\frac{k_{\mathrm{T}}^2}{2M^2}\right)^n f(x, k_{\mathrm{T}}^2), \tag{2.28}$$

and M stands for the hadron mass.

2.3.3 Transversity and Boer–Mulders Contributions to Structure Functions

The structure function $F_{\mathrm{T}}^{\sin(2\varphi_{\mathrm{CS}}-\varphi_{\mathrm{S}})}$, arising from the convolution of the transversity distribution with the Boer–Mulders function, has a form analogous to that of the Sivers-related structure function. The integration over the transverse momentum $\boldsymbol{q}_{\mathrm{T}}$, weighted by q_{T}/M_a, leads to a simplified form:

$$\int \mathrm{d}^2\boldsymbol{q}_{\mathrm{T}}\, \frac{q_{\mathrm{T}}}{M_a} F_{\mathrm{T}}^{\sin(2\varphi_{\mathrm{CS}}-\varphi_{\mathrm{S}})} = \int \mathrm{d}^2\boldsymbol{q}_{\mathrm{T}}\, \frac{q_{\mathrm{T}}}{M_a}\, \mathcal{C}\left[\frac{\boldsymbol{q}_{\mathrm{T}}\cdot\boldsymbol{k}_{\mathrm{aT}}}{q_{\mathrm{T}}M_a}\, h_1^{\perp}\, h_1\right]. \tag{2.29}$$

Employing the delta function within the convolution operator allows one to carry out the integration explicitly, yielding:

$$\begin{aligned}&\int \mathrm{d}^2\boldsymbol{q}_{\mathrm{T}}\, \frac{q_{\mathrm{T}}}{M_a} F_{\mathrm{T}}^{\sin(2\varphi_{\mathrm{CS}}-\varphi_{\mathrm{S}})} = \\ &-\sum_{\mathrm{q}} e_{\mathrm{q}}^2 \int \mathrm{d}^2\boldsymbol{k}_{\mathrm{aT}}\mathrm{d}^2\boldsymbol{k}_{\mathrm{bT}} \frac{(\boldsymbol{k}_{\mathrm{aT}}+\boldsymbol{k}_{\mathrm{bT}})\cdot\boldsymbol{k}_{\mathrm{aT}}}{N_c M_a^2}\left[h_1^{\perp\,\bar{\mathrm{q}}}(x_a,k_{\mathrm{aT}}^2)\, h_1^{\mathrm{q}}(x_b,k_{\mathrm{bT}}^2) + (\mathrm{q}\leftrightarrow\bar{\mathrm{q}})\right].\end{aligned} \tag{2.30}$$

After performing the angular integration and taking the first transverse moment of the Boer–Mulders function, $h_1^{\perp(1)\mathrm{q}/\bar{\mathrm{q}}}(x_a)$, the weighted structure function reduces to:

$$\int \mathrm{d}^2\boldsymbol{q}_{\mathrm{T}}\, \frac{q_{\mathrm{T}}}{M_a} F_{\mathrm{T}}^{\sin(2\varphi_{\mathrm{CS}}-\varphi_{\mathrm{S}})} = -\frac{2}{N_c}\sum_{\mathrm{q}} e_{\mathrm{q}}^2 \left[h_1^{\perp(1)\mathrm{q}/\bar{\mathrm{q}}}(x_a)\, h_1^{\mathrm{q}}(x_b) + (\mathrm{q}\leftrightarrow\bar{\mathrm{q}})\right]. \tag{2.31}$$

The unpolarised structure function $F_{\mathrm{U}}^{\cos 2\varphi_{\mathrm{CS}}}$ can be analysed in a similar manner, as it receives contributions from the convolution of two Boer–Mulders distributions. For this scenario, the weight factor $q_{\mathrm{T}}^2/(4M_aM_b)$ is applied, leading to the following expression:

$$\int \mathrm{d}^2\boldsymbol{q}_{\mathrm{T}}\, \frac{q_{\mathrm{T}}^2}{4M_aM_b} F_{\mathrm{U}}^{\cos 2\varphi_{\mathrm{CS}}} = \int \mathrm{d}^2\boldsymbol{q}_{\mathrm{T}}\, \frac{q_{\mathrm{T}}^2}{4M_aM_b}\, \mathcal{C}\left[\frac{2(\boldsymbol{q}_{\mathrm{T}}\cdot\boldsymbol{k}_{\mathrm{aT}})(\boldsymbol{q}_{\mathrm{T}}\cdot\boldsymbol{k}_{\mathrm{bT}}) - q_{\mathrm{T}}^2(\boldsymbol{k}_{\mathrm{aT}}\cdot\boldsymbol{k}_{\mathrm{bT}})}{q_{\mathrm{T}}^2 M_a M_b}\, h_1^{\perp}\, h_1^{\perp}\right]. \tag{2.32}$$

After performing the $\boldsymbol{q}_{\mathrm{T}}$-integration using the delta function, the numerator reduces to:

$$\begin{aligned}&2(\boldsymbol{k}_{\mathrm{aT}}+\boldsymbol{k}_{\mathrm{bT}})\cdot\boldsymbol{k}_{\mathrm{aT}}\,(\boldsymbol{k}_{\mathrm{aT}}+\boldsymbol{k}_{\mathrm{bT}})\cdot\boldsymbol{k}_{\mathrm{bT}} - \boldsymbol{k}_{\mathrm{aT}}\cdot\boldsymbol{k}_{\mathrm{bT}}\cdot(\boldsymbol{k}_{\mathrm{aT}}+\boldsymbol{k}_{\mathrm{bT}})^2 \\ &\quad = 2k_{\mathrm{aT}}^2k_{\mathrm{bT}}^2 + (k_{\mathrm{aT}}^2+k_{\mathrm{bT}}^2)(\boldsymbol{k}_{\mathrm{aT}}\cdot\boldsymbol{k}_{\mathrm{bT}}).\end{aligned} \tag{2.33}$$

Substituting this into the full expression and retaining only terms even in $\boldsymbol{k}_{\mathrm{aT}}$ and $\boldsymbol{k}_{\mathrm{bT}}$, the final result is:

$$\begin{aligned}\int \mathrm{d}^2\boldsymbol{q}_{\mathrm{T}}\, \frac{q_{\mathrm{T}}^2}{4M_aM_b} F_{\mathrm{U}}^{\cos 2\varphi_{\mathrm{CS}}} &= -\sum_{\mathrm{q}} e_{\mathrm{q}}^2 \int \mathrm{d}^2\boldsymbol{k}_{\mathrm{aT}}\mathrm{d}^2\boldsymbol{k}_{\mathrm{bT}}\, \frac{2k_{\mathrm{aT}}^2k_{\mathrm{bT}}^2 + (k_{\mathrm{aT}}^2+k_{\mathrm{bT}}^2)(\boldsymbol{k}_{\mathrm{aT}}\cdot\boldsymbol{k}_{\mathrm{bT}})}{4M_a^2M_b^2} \\ &\quad\times\left[h_1^{\perp(1)\bar{\mathrm{q}}}(x_a,k_{\mathrm{aT}}^2)\, h_1^{\perp(1)\mathrm{q}}(x_b,k_{\mathrm{bT}}^2) + (\mathrm{q}\leftrightarrow\bar{\mathrm{q}})\right].\end{aligned} \tag{2.34}$$

which evaluates to:

$$\int \mathrm{d}^2\boldsymbol{q}_{\mathrm{T}}\, \frac{q_{\mathrm{T}}^2}{4M_aM_b} F_{\mathrm{U}}^{\cos 2\varphi_{\mathrm{CS}}} = \frac{2}{N_c}\sum_{\mathrm{q}} e_{\mathrm{q}}^2 \left[h_1^{\perp(1)\bar{\mathrm{q}}}(x_a)\, h_1^{\perp(1)\mathrm{q}}(x_b) + (\mathrm{q}\leftrightarrow\bar{\mathrm{q}})\right]. \tag{2.35}$$

The structure function $F_{\mathrm{T}}^{\sin(2\varphi_{\mathrm{CS}}-\varphi_{\mathrm{S}})}$ provides direct access to the transversity distribution of the target hadron multiplied by the first transverse moment of the Boer–Mulders function of the beam hadron. On the other hand, $F_{\mathrm{U}}^{\cos 2\varphi_{\mathrm{CS}}}$ encodes the product of the first moments of the Boer–Mulders functions of both hadrons. These results highlight the role of transverse momentum-dependent distributions in describing azimuthal asymmetries in unpolarised and polarised scattering processes.

2.3.4 Pretzelosity Contribution to the Structure Function

The structure function $F_{\mathrm{T}}^{\sin(2\varphi_{\mathrm{CS}}+\varphi_{\mathrm{S}})}$ originates from the convolution of the Boer–Mulders TMD PDF, $h_1^{\perp}$, and the pretzelosity TMD PDF, $h_{1\mathrm{T}}^{\perp}$, making it the most complicated among all leading-twist structure functions. Given the complexity of the formulas and calculations involved, the derivations are presented step by step, including even the seemingly trivial substitutions.

This structure function is integrated over $\boldsymbol{q}_{\mathrm{T}}$ with the weight $q_{\mathrm{T}}^3/(2M_aM_b^2)$. By applying the delta function, the convolution simplifies to:

$$\int \mathrm{d}^2\boldsymbol{q}_{\mathrm{T}}\, \frac{q_{\mathrm{T}}^3}{2M_aM_b^2}\, F_{\mathrm{T}}^{\sin(2\varphi_{\mathrm{CS}}+\varphi_{\mathrm{S}})} = \tag{2.36}$$

$$\int \mathrm{d}^2\boldsymbol{q}_{\mathrm{T}}\, \frac{q_{\mathrm{T}}^3}{2M_aM_b^2}\, \mathcal{C}\left[\frac{(\boldsymbol{q}_{\mathrm{T}}\cdot\boldsymbol{k}_{b\mathrm{T}})\,(2(\boldsymbol{q}_{\mathrm{T}}\cdot\boldsymbol{k}_{a\mathrm{T}})(\boldsymbol{q}_{\mathrm{T}}\cdot\boldsymbol{k}_{b\mathrm{T}}) - \boldsymbol{q}_{\mathrm{T}}^2(\boldsymbol{k}_{a\mathrm{T}}\cdot\boldsymbol{k}_{b\mathrm{T}}))}{q_{\mathrm{T}}^3M_aM_b^2} - \frac{\boldsymbol{k}_{b\mathrm{T}}^2(\boldsymbol{q}_{\mathrm{T}}\cdot\boldsymbol{k}_{a\mathrm{T}})}{2q_{\mathrm{T}}M_aM_b^2}\right] h_{1,a}^{\perp}\, h_{1\mathrm{T},b}^{\perp}. \tag{2.37}$$

Upon expanding the expression above, one obtains:

$$\begin{aligned}\int \mathrm{d}^2\boldsymbol{q}_{\mathrm{T}}\, \frac{q_{\mathrm{T}}^2}{2M_aM_b^2}\, F_{\mathrm{T}}^{\sin(2\varphi_{\mathrm{CS}}+\varphi_{\mathrm{S}})} &= -\frac{1}{N_c}\sum_{\mathrm{q}} e_{\mathrm{q}}^2 \int \mathrm{d}^2\boldsymbol{k}_{a\mathrm{T}}\,\mathrm{d}^2\boldsymbol{k}_{b\mathrm{T}}\,\delta^{(2)}(\boldsymbol{q}_{\mathrm{T}}-\boldsymbol{k}_{a\mathrm{T}}-\boldsymbol{k}_{b\mathrm{T}})\\ &\times \frac{2(\boldsymbol{q}_{\mathrm{T}}\cdot\boldsymbol{k}_{b\mathrm{T}})\,[2(\boldsymbol{q}_{\mathrm{T}}\cdot\boldsymbol{k}_{a\mathrm{T}})(\boldsymbol{q}_{\mathrm{T}}\cdot\boldsymbol{k}_{b\mathrm{T}}) - \boldsymbol{q}_{\mathrm{T}}^2(\boldsymbol{k}_{a\mathrm{T}}\cdot\boldsymbol{k}_{b\mathrm{T}})] - \boldsymbol{q}_{\mathrm{T}}^2\boldsymbol{k}_{b\mathrm{T}}^2(\boldsymbol{q}_{\mathrm{T}}\cdot\boldsymbol{k}_{a\mathrm{T}})}{4\,M_a^2\,M_b^4}\\ &\times\left[h_{1,\pi}^{\bar{\mathrm{q}}\perp}(x_a,k_{a\mathrm{T}}^2)\,h_{1\mathrm{T},b}^{\mathrm{q}\perp}(x_b,k_{b\mathrm{T}}^2) + (\bar{\mathrm{q}}\leftrightarrow q)\right].\end{aligned} \tag{2.38}$$

The integration over $\boldsymbol{q}_{\mathrm{T}}$ is performed first, using the momentum conservation condition $\boldsymbol{q}_{\mathrm{T}} = \boldsymbol{k}_{a\mathrm{T}} + \boldsymbol{k}_{a\mathrm{T}}$. To improve readability, let us define $\boldsymbol{a} \equiv \boldsymbol{k}_{b\mathrm{T}}$ and $\boldsymbol{b} \equiv \boldsymbol{k}_{b\mathrm{T}}$. In this new notation, the expression takes the form:

$$\begin{aligned}2(\boldsymbol{q}_{\mathrm{T}}\cdot\boldsymbol{k}_{b\mathrm{T}})\left[2(\boldsymbol{q}_{\mathrm{T}}\cdot\boldsymbol{k}_{a\mathrm{T}})(\boldsymbol{q}_{\mathrm{T}}\cdot\boldsymbol{k}_{b\mathrm{T}}) - \boldsymbol{q}_{\mathrm{T}}^2(\boldsymbol{k}_{a\mathrm{T}}\cdot\boldsymbol{k}_{b\mathrm{T}})\right] - \boldsymbol{q}_{\mathrm{T}}^2\boldsymbol{k}_{b\mathrm{T}}^2(\boldsymbol{q}_{\mathrm{T}}\cdot\boldsymbol{k}_{a\mathrm{T}}) &=\\ 2\left[(\boldsymbol{a}+\boldsymbol{b})\cdot\boldsymbol{b}\right]\left[2(\boldsymbol{a}+\boldsymbol{b})\cdot\boldsymbol{a}(\boldsymbol{a}+\boldsymbol{b})\cdot\boldsymbol{b} - (\boldsymbol{a}+\boldsymbol{b})^2(\boldsymbol{a}\cdot\boldsymbol{b})\right] - (\boldsymbol{a}+\boldsymbol{b})^2b^2(\boldsymbol{a}+\boldsymbol{b})\cdot\boldsymbol{a} &=\\ 2\left[(\boldsymbol{a}+\boldsymbol{b})\cdot\boldsymbol{b}\right]B(\boldsymbol{a},\boldsymbol{b}) - C(\boldsymbol{a},\boldsymbol{b}) = A(\boldsymbol{a},\boldsymbol{b}).&\end{aligned} \tag{2.39}$$

Next, let us determine $B(\boldsymbol{a},\boldsymbol{b})$ and $C(\boldsymbol{a},\boldsymbol{b})$ separately:

$$\begin{aligned}B(\boldsymbol{a},\boldsymbol{b}) &= \left[2(\boldsymbol{a}+\boldsymbol{b})\cdot\boldsymbol{a}\,(\boldsymbol{a}+\boldsymbol{b})\cdot\boldsymbol{b} - (\boldsymbol{a}+\boldsymbol{b})^2\boldsymbol{a}\cdot\boldsymbol{b}\right] = \left[2a^2b^2 + (a^2+b^2)\,\boldsymbol{a}\cdot\boldsymbol{b}\right]\\ C(\boldsymbol{a},\boldsymbol{b}) &= (\boldsymbol{a}+\boldsymbol{b})^2b^2(\boldsymbol{a}+\boldsymbol{b})\cdot\boldsymbol{a} = b^2\left[a^4 + (3a^2+b^2)\,\boldsymbol{a}\cdot\boldsymbol{b} + a^2b^2 + 2(\boldsymbol{a}\cdot\boldsymbol{b})^2\right].\end{aligned} \tag{2.40}$$

Putting this together, the expression simplifies to:

$$A(\boldsymbol{a},\boldsymbol{b}) = 3a^2b^4 - a^4b^2 + 3a^2b^2\,\boldsymbol{a}\cdot\boldsymbol{b} + 2a^2(\boldsymbol{a}\cdot\boldsymbol{b})^2. \tag{2.41}$$

The third term in Eq. (2.41), $3a^2b^2\,\boldsymbol{a}\cdot\boldsymbol{b}$, is clearly odd under the exchange of $\boldsymbol{a}$ and $\boldsymbol{b}$, so by symmetry, its contribution vanishes after integration.

To evaluate the contribution of the last term, $2a^2(\boldsymbol{a}\cdot\boldsymbol{b})^2$, note that

$$\int_{-\infty}^{\infty} \mathrm{d}a_1\,\mathrm{d}a_2\,a_i^2 f(a^2) = \frac{1}{2}\int_{-\infty}^{\infty} \mathrm{d}a_1\,\mathrm{d}a_2\,a^2 f(a^2), \tag{2.42}$$

where $i = 1, 2$ and $\boldsymbol{a} = (a_1, a_2)$. Therefore,

$$\begin{aligned}\int_{-\infty}^{\infty} \mathrm{d}^2\boldsymbol{a}\,\mathrm{d}^2\boldsymbol{b}\,a^2(\boldsymbol{a}\cdot\boldsymbol{b})^2 f(a^2)g(b^2) &= \int_{-\infty}^{\infty} \mathrm{d}^2\boldsymbol{a}\,\mathrm{d}^2\boldsymbol{b}\,a^2\Big(a_1^2b_1^2 + 2a_1a_2b_1b_2 + a_2^2b_2^2\Big) f(a^2)g(b^2)\\ &= \frac{1}{2}\int_{-\infty}^{\infty} \mathrm{d}^2\boldsymbol{a}\,\mathrm{d}^2\boldsymbol{b}\,a^4b^2 f(a^2)g(b^2).\end{aligned} \tag{2.43}$$

This follows from the application of Eq. (2.42) and the observation that the term linear in a_i vanishes upon integration, as it is odd under inversion. Then, the integral of $A(\boldsymbol{a},\boldsymbol{b})$ over the transverse plane is given by:

$$\int_{-\infty}^{\infty} \mathrm{d}^2\boldsymbol{a}\,\mathrm{d}^2\boldsymbol{b}\;A(\boldsymbol{a},\boldsymbol{b})\,f(a^2)\,g(b^2) = \int_{-\infty}^{\infty} \mathrm{d}^2\boldsymbol{a}\,\mathrm{d}^2\boldsymbol{b}\;a^2b^4 f(a^2)\,g(b^2). \tag{2.44}$$

Finally, coming back to Eq. (2.38), the following expression is obtained:

$$\int \mathrm{d}^2\boldsymbol{q}_{\mathbf{T}}\,\frac{q_{\mathrm{T}}^3}{2M_aM_b^2}F_{\mathrm{T}}^{\sin(2\varphi_{\mathrm{CS}}+\varphi_{\mathrm{S}})} = -\frac{6}{N_{\mathrm{c}}}\sum_{\mathrm{q}} e_{\mathrm{q}}^2\Big[h_{1,a}^{\perp(1)\bar{\mathrm{q}}}(x_a)\,h_{1\mathrm{T},b}^{\perp(2)\mathrm{q}}(x_b) + (q \leftrightarrow \bar{q})\Big], \tag{2.45}$$

structure function $F_{\mathrm{T}}^{\sin(2\varphi_{\mathrm{CS}}+\varphi_{\mathrm{S}})}$ grants an access to the second transverse moment of the pretzelosity distribution of the target hadron, multiplied by the first transverse moment of the Boer–Mulders function of the beam hadron.

2.3.5 Transverse-Momentem Weighted Asymmetries

The calculations yield the following expressions for the transverse-momentum weighted integrals of the structure functions, expressed as products of TMD PDFs or their corresponding transverse moments, defined in Eq. (2.28):

$$\int \mathrm{d}^2\boldsymbol{q}_{\mathrm{T}}\,F_{\mathrm{U}}^1 = \frac{1}{N_c}\sum_{\mathrm{q}} e_{\mathrm{q}}^2\left[f_{1,a}^{\bar{\mathrm{q}}}(x_a)f_{1,b}^{\mathrm{q}}(x_b) + (\mathrm{q}\leftrightarrow\bar{\mathrm{q}})\right], \tag{2.46}$$

$$\int \mathrm{d}^2\boldsymbol{q}_{\mathrm{T}}\,\frac{q_{\mathrm{T}}^2}{4M_aM_b}F_{\mathrm{U}}^{\cos 2\varphi_{\mathrm{CS}}} = \frac{2}{N_c}\sum_{\mathrm{q}} e_{\mathrm{q}}^2\left[h_{1,a}^{\perp(1)\bar{\mathrm{q}}}(x_a)h_{1,b}^{\perp(1)\mathrm{q}}(x_b) + (\mathrm{q}\leftrightarrow\bar{\mathrm{q}})\right], \tag{2.47}$$

$$\int \mathrm{d}^2\boldsymbol{q}_{\mathrm{T}}\,\frac{q_{\mathrm{T}}}{M_b}F_{\mathrm{T}}^{\sin\varphi_{\mathrm{S}}} = -\frac{2}{N_c}\sum_{\mathrm{q}} e_{\mathrm{q}}^2\left[f_{1,a}^{\bar{\mathrm{q}}}(x_a)f_{1\mathrm{T},b}^{\perp(1)\mathrm{q}}(x_b) + (\mathrm{q}\leftrightarrow\bar{\mathrm{q}})\right], \tag{2.48}$$

$$\int \mathrm{d}^2\boldsymbol{q}_{\mathrm{T}}\,\frac{q_{\mathrm{T}}^3}{2M_aM_b^2}F_{\mathrm{T}}^{\sin(2\varphi_{\mathrm{CS}}+\varphi_{\mathrm{S}})} = -\frac{6}{N_c}\sum_{\mathrm{q}} e_{\mathrm{q}}^2\left[h_{1,a}^{\perp(1)\bar{\mathrm{q}}}(x_a)h_{1\mathrm{T},b}^{\perp(2)\mathrm{q}}(x_b) + (\mathrm{q}\leftrightarrow\bar{\mathrm{q}})\right], \tag{2.49}$$

$$\int \mathrm{d}^2\boldsymbol{q}_{\mathrm{T}}\,\frac{q_{\mathrm{T}}}{M_a}F_{\mathrm{T}}^{\sin(2\varphi_{\mathrm{CS}}-\varphi_{\mathrm{S}})} = -\frac{2}{N_c}\sum_{\mathrm{q}} e_{\mathrm{q}}^2\left[h_{1,a}^{\perp(1)\bar{\mathrm{q}}}(x_a)h_{1,b}^{\mathrm{q}}(x_b) + (\mathrm{q}\leftrightarrow\bar{\mathrm{q}})\right]. \tag{2.50}$$

For completeness, one may introduce the weighted asymmetries (WTSA), analogous to the TSA in Eq. (2.23):

$$A_{\mathrm{X}}^{\mathrm{Y}W_{\mathrm{Y}}} = \frac{\int \mathrm{d}^2\boldsymbol{q}_{\mathrm{T}}\, W_{\mathrm{Y}} F_{\mathrm{X}}^{\mathrm{Y}}}{\int \mathrm{d}^2\boldsymbol{q}_{\mathrm{T}}\, F_{\mathrm{U}}^{1}} = \frac{F_{\mathrm{X}}^{\mathrm{Y}\,W_{\mathrm{Y}}}}{F_{\mathrm{U}}^{1}}, \tag{2.51}$$

where structure function $F_{\mathrm{X}}^{\mathrm{Y}}$ is as defined in Eq. (2.23), while W_{Y} indicates the corresponding weight in Eqs (2.46–2.50).

For the Sivers weighted asymmetry, the following result is obtained:

$$A_{\mathrm{T}}^{\sin\varphi_{\mathrm{S}}\frac{q_{\mathrm{T}}}{M_b}} = \frac{\int \mathrm{d}^2\boldsymbol{q}_{\mathrm{T}}\, \frac{q_{\mathrm{T}}}{M_b}\, F_{\mathrm{T}}^{\sin\varphi_{\mathrm{S}}}}{\int \mathrm{d}^2\boldsymbol{q}_{\mathrm{T}}\, F_{\mathrm{U}}^{1}} = -2\frac{\sum_{\mathrm{q}} e_{\mathrm{q}}^2 \left[f_{1,a}^{\bar{\mathrm{q}}}(x_a) f_{1\mathrm{T},b}^{\perp(1)\mathrm{q}}(x_b) + (\mathrm{q} \leftrightarrow \bar{\mathrm{q}})\right]}{\sum_{\mathrm{q}} e_{\mathrm{q}}^2 \left[f_{1,a}^{\bar{\mathrm{q}}}(x_a) f_{1,b}^{\mathrm{q}}(x_b) + (\mathrm{q} \leftrightarrow \bar{\mathrm{q}})\right]}. \tag{2.52}$$

The so-called transversity WTSA is given by:

$$A_{\mathrm{T}}^{\sin(2\varphi_{\mathrm{CS}}-\varphi_{\mathrm{S}})\frac{q_{\mathrm{T}}}{M_a}} = -2\frac{\sum_{\mathrm{q}} e_{\mathrm{q}}^2 \left[h_{1,a}^{\perp(1)\bar{\mathrm{q}}}(x_a) h_{1,b}^{\mathrm{q}}(x_b) + (\mathrm{q} \leftrightarrow \bar{\mathrm{q}})\right]}{\sum_{\mathrm{q}} e_{\mathrm{q}}^2 \left[f_{1,a}^{\bar{\mathrm{q}}}(x_a) f_{1,b}^{\mathrm{q}}(x_b) + (\mathrm{q} \leftrightarrow \bar{\mathrm{q}})\right]} \tag{2.53}$$

Finally, for the pretzelosity WTSA can be expressed as:

$$A_{\mathrm{T}}^{\sin(2\varphi_{\mathrm{CS}}+\varphi_{\mathrm{S}})\frac{q_{\mathrm{T}}^3}{2M_a M_b^2}}(x_a, x_b) = -6\,\frac{\sum_{\mathrm{q}} e_{\mathrm{q}}^2 \left[h_{1,a}^{\perp(1)\bar{\mathrm{q}}}(x_a)\, h_{1\mathrm{T},b}^{\perp(2)\mathrm{q}}(x_b) + (\mathrm{q} \leftrightarrow \bar{\mathrm{q}})\right]}{\sum_{\mathrm{q}} e_{\mathrm{q}}^2 \left[f_{1,a}^{\bar{\mathrm{q}}}(x_a)\, f_{1,b}^{\mathrm{q}}(x_b) + (\mathrm{q} \leftrightarrow \bar{\mathrm{q}})\right]}. \tag{2.54}$$

Using this weighted asymmetry approach, one can extract the TMD PDFs directly, eliminating the need for k_{T}-dependence assumptions required in TSA analyses. The extraction of the first k_{T}^2 moment of the Sivers function from the Sivers WTSA, as well as the first k_{T}^2 moment of the Boer–Mulders function from the transversity WTSA, will be discussed in detail in Chapter 6[6]

[6]In this work, the extraction of TMD PDFs from the pretzelosity WTSA is not addressed.

Chapter 3

Parton Distribution Functions: Experimental Framework

We can judge our progress
by the courage of our questions
and the depth of our answers,
our willingness to embrace what is true...

— Carl Sagan

In this chapter, experimental results related to PDFs will be presented. It begins with Sec. 3.1, which outlines the processes and the kinematic coverage of experimental data used in global QCD analyses. Since the collinear PDFs discussed in Sec. 3.2 are well known, the emphasis here is placed on the TMD PDFs described in Sec. 3.3.

3.1 Processes in Global QCD Analyses

Decades of experimental exploration in high-energy physics have led to significant improvements in constraining PDFs of quarks and gluons within hadrons. Building on this, Tab. 3.1 provides an overview of the processes relevant to current global QCD analyses. The dataset for unpolarised proton scattering is significantly larger and more diverse than for polarised or nuclear reactions. This is mainly due to technical challenges, particularly the difficulty of polarising nucleons and, in some cases accelerating them. The following sections present results for both unpolarised and polarised processes.

3.2 Collinear Approximation

Within the collinear approach, where the transverse momenta of partons within hadrons are neglected, pQCD has proven highly successful in describing experimental observations. A clear example is provided by measurements of pion production cross sections in $\mathrm{p}+\mathrm{p}$ collisions at mid-rapidity for $\sqrt{s} = 200$ GeV, shown in Fig. 3.1. The results exhibit good agreement with pQCD predictions across a broad kinematic range, motivating the study of collinear PDFs in this section. The unpolarised PDFs, have

Table 3.1: Main processes used for parton distribution function (PDF) determinations. For each reaction, the subprocess, the probed parton flavors, and the availability of data in unpolarised (U), spin-dependent (so-called polarised, P), and nuclear (N) cases are indicated [58].

Process	**Subprocess**	**Probed Partons**	**U**	**P**	**N**
Fixed Target DIS					
$\ell^\pm\{\mathrm{p},\mathrm{n}\} \to \ell^\pm + \mathrm{X}$	$\gamma^*\mathrm{q} \to \mathrm{q}$	$\mathrm{q}^+, \mathrm{q}, \bar{\mathrm{q}}, \mathrm{g}$	✓	✓	✓
$\ell^\pm\{\mathrm{n},\mathrm{A}\}/\mathrm{p} \to \ell^\pm + \mathrm{X}$	$\gamma^*\mathrm{d}/\mathrm{u} \to \mathrm{d}/\mathrm{u}$	d/u	✓		✓
$\nu(\bar{\nu})\mathrm{A} \to \mu^-(\mu^+) + \mathrm{X}$	$\mathrm{W}^*\mathrm{q} \to \mathrm{q}'$	$\mathrm{q}, \bar{\mathrm{q}}$	✓		✓
$\nu\mathrm{A} \to \mu^-\mu^+ + \mathrm{X}$	$\mathrm{W}^*\mathrm{s} \to \mathrm{c}$	s	✓		✓
$\bar{\nu}\mathrm{A} \to \mu^+\mu^- + \mathrm{X}$	$\mathrm{W}^*\bar{\mathrm{s}} \to \bar{\mathrm{c}}$	$\bar{\mathrm{s}}$	✓		✓
Collider DIS					
$e^\pm\mathrm{p} \to e^\pm + \mathrm{X}$	$\gamma^*\mathrm{q} \to \mathrm{q}$	$\mathrm{g}, \mathrm{q}, \bar{\mathrm{q}}$	✓		
$e^+\mathrm{p} \to \bar{\nu} + \mathrm{X}$	$\mathrm{W}^+\{\mathrm{d},\mathrm{s}\} \to \{\mathrm{u},\mathrm{c}\}$	d, s	✓		
$e^\pm\mathrm{p} \to e^\pm\mathrm{c}\bar{\mathrm{c}} + \mathrm{X}$	$\gamma^*\mathrm{c} \to \mathrm{c}, \gamma^*\mathrm{g} \to \mathrm{c}\bar{\mathrm{c}}$	c, g	✓		
$e^\pm\mathrm{p} \to (\text{di-jets}) + \mathrm{X}$	$\gamma^*\mathrm{g} \to \mathrm{q}\bar{\mathrm{q}}$	g	✓		
Fixed Target SIDIS					
$\ell^\pm\{\mathrm{p},\mathrm{d}\} \to \ell^\pm + \mathrm{h} + \mathrm{X}$	$\gamma^*\mathrm{q} \to \mathrm{q}$	$\mathrm{u}, \bar{\mathrm{u}}, \mathrm{d}, \bar{\mathrm{d}}, \mathrm{g}$	✓	✓	
$\ell^\pm\{\mathrm{p},\mathrm{d}\} \to \ell^\pm\mathrm{c}\bar{\mathrm{c}} \to \ell^\pm\mathrm{D} + \mathrm{X}$	$\gamma^*\mathrm{g} \to \mathrm{c}\bar{\mathrm{c}}$	g	✓		
Fixed Target DY					
$\mathrm{pp} \to \mu^+\mu^- + \mathrm{X}$	$\mathrm{u}\bar{\mathrm{u}}, \mathrm{d}\bar{\mathrm{d}} \to \gamma^*$	$\bar{\mathrm{q}}$	✓		
$\mathrm{p}\{\mathrm{n},\mathrm{A}\}/\mathrm{pp} \to \mu^+\mu^- + \mathrm{X}$	$(\mathrm{u}\bar{\mathrm{d}})/(\mathrm{u}\bar{\mathrm{u}}) \to \gamma^*$	$\bar{\mathrm{d}}/\bar{\mathrm{u}}$	✓	✓	
Collider DY					
$\mathrm{p}\bar{\mathrm{p}} \to (\mathrm{W}^\pm \to \ell^\pm\nu) + \mathrm{X}$	$\mathrm{ud} \to \mathrm{W}^+, \bar{\mathrm{u}}\bar{\mathrm{d}} \to \mathrm{W}^-$	$\mathrm{u}, \mathrm{d}, \bar{\mathrm{u}}, \bar{\mathrm{d}}$	✓		
$\mathrm{p}\{\mathrm{p},\mathrm{A}\} \to (\mathrm{W}^\pm \to \ell^\pm\nu) + \mathrm{X}$	$\mathrm{u}\bar{\mathrm{d}} \to \mathrm{W}^+, \mathrm{d}\bar{\mathrm{u}} \to \mathrm{W}^-$	$\mathrm{u}, \mathrm{d}, \bar{\mathrm{u}}, \bar{\mathrm{d}}$	✓	✓	✓
$\mathrm{p}\bar{\mathrm{p}}(\mathrm{p}\{\mathrm{p},\mathrm{A}\}) \to (Z \to \ell^+\ell^-) + \mathrm{X}$	$\mathrm{uu}, \mathrm{dd}(\mathrm{u}\bar{\mathrm{u}}, \mathrm{d}\bar{\mathrm{d}}) \to Z$	$\mathrm{u}, \mathrm{d}, \mathrm{g}$	✓	✓	✓
$\mathrm{pp} \to (W + \mathrm{c}) + \mathrm{X}$	$\mathrm{gs} \to \mathrm{W}^-\mathrm{c}, \mathrm{g}\bar{\mathrm{s}} \to \mathrm{W}^+\bar{\mathrm{c}}$	$\mathrm{s}, \bar{\mathrm{s}}, \mathrm{g}$	✓		
$\mathrm{pp} \to (\gamma^* \to \ell^+\ell^-)\mathrm{X}$	$\mathrm{u}\bar{\mathrm{u}}, \mathrm{d}\bar{\mathrm{d}} \to \gamma^*, \mathrm{u}\gamma, \mathrm{d}\gamma \to \gamma^*$	$\bar{\mathrm{q}}, \mathrm{g}, \gamma$	✓		
Jet and Hadron Production					
$\mathrm{p}\bar{\mathrm{p}}(\mathrm{p}\{\mathrm{p},\mathrm{A}\}) \to (\text{di-jets}) + \mathrm{X}$	$\mathrm{gg}, \mathrm{qg}, \mathrm{qq} \to \text{jets}$	g, q	✓	✓	✓
$\mathrm{p}\bar{\mathrm{p}}(\mathrm{pp}) \to \mathrm{h} + \mathrm{X}$	$\mathrm{gg}, \mathrm{qg}, \mathrm{qq} \to \pi, K, \mathrm{D}$	g, q	✓	✓	
Top Production					
$\mathrm{pp} \to \mathrm{t}\bar{\mathrm{t}} + \mathrm{X}$	$\mathrm{gg} \to \mathrm{t}\bar{\mathrm{t}}$	g	✓		
$\mathrm{pp} \to \mathrm{t} + \mathrm{X}$	$\mathrm{W}^*\mathrm{q} \to \mathrm{q}'$	$\mathrm{q}, \bar{\mathrm{q}}$	✓		

been characterized, mainly owing to the insights gained from measurement processes such as DIS, unpolarised SIDIS, and the Drell-Yan process as shown in Tab. 3.1. As can be seen in Fig. 3.2, the recent extractions are characterized by a very high level of accuracy. For helicity PDFs shown in Fig. 3.3, data exists for a more restricted range of Q^2 and x and have lower precision. In recent years, more experimental data have become available for determining longitudinally polarised PDFss These include SIDIS in fixed-target experiments [64–66], one- or two-hadron and open-charm production in lepton-nucleon (ℓN) scattering [67–69], as well as semi-inclusive production [70–72], jet production [73–75] and parity-violating $\mathrm{W}^\pm$ boson production [76, 77] in polarised proton-proton (pp) collisions.

To fully describe the collinear structure at leading-twist, the transversity PDF is required. Due to its chiral-odd nature, it cannot be directly accessed through inclu-

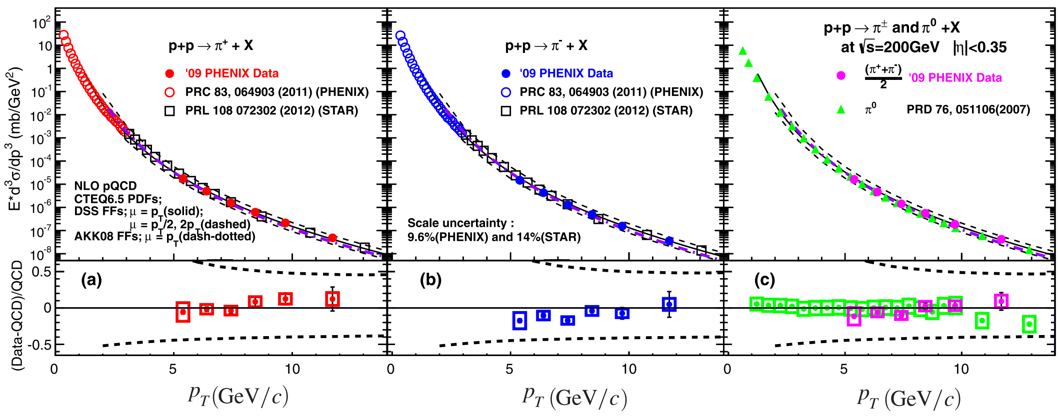

Figure 3.1: Charged-pion cross sections in p+p collisions at $\sqrt{s} = 200$ GeV measured by PHENIX Collaboration at high pion transverse momentum (p_{T}), compared with pQCD predictions [59]. Top panels show a comparison with low-p_{T} data from PHENIX [60] and STAR [61], the bottom panels show data-theory ratios.

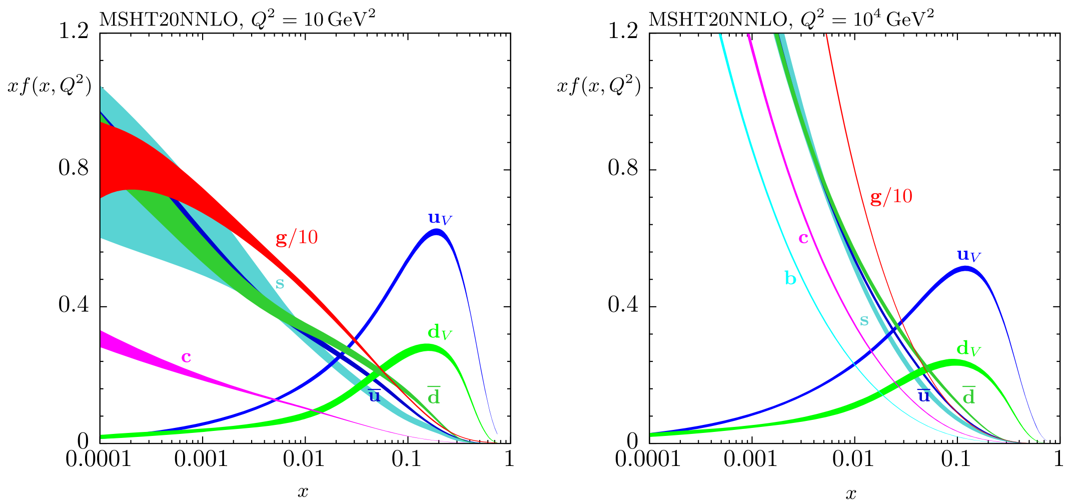

Figure 3.2: Results of a recent global fit of the number density PDFs obtained in the NNLO MSHT20 global analysis at $Q^2 = 10$ GeV^2 (left) and $Q^2 = 10^4$ GeV^2 (right) [62], (b) helicity distributions obtained from global analyses at NLO and NNLO, and from the NLO BDSSV22 fit [63].

sive DIS, making its experimental determination challenging. The first experimental indications of this PDF were reported in 2005 by HERMES in electron-proton ($e^-p^\uparrow$) SIDIS [78] and by COMPASS [79] in muon-deuteron ($\mu^+d^\uparrow$) SIDIS. A detailed discussion of transversity results is presented in Sec. 3.3.

3.3 Transverse Momentum Dependent Approach

While the collinear framework described in Sec. 3.2 provides a solid starting point for pQCD, several experimental observations cannot be fully explained within this approximation. Large single-transverse spin asymmetries (A_{N}) in pion production, first observed in fixed-target experiments [81–84] and later confirmed at RHIC collider en-

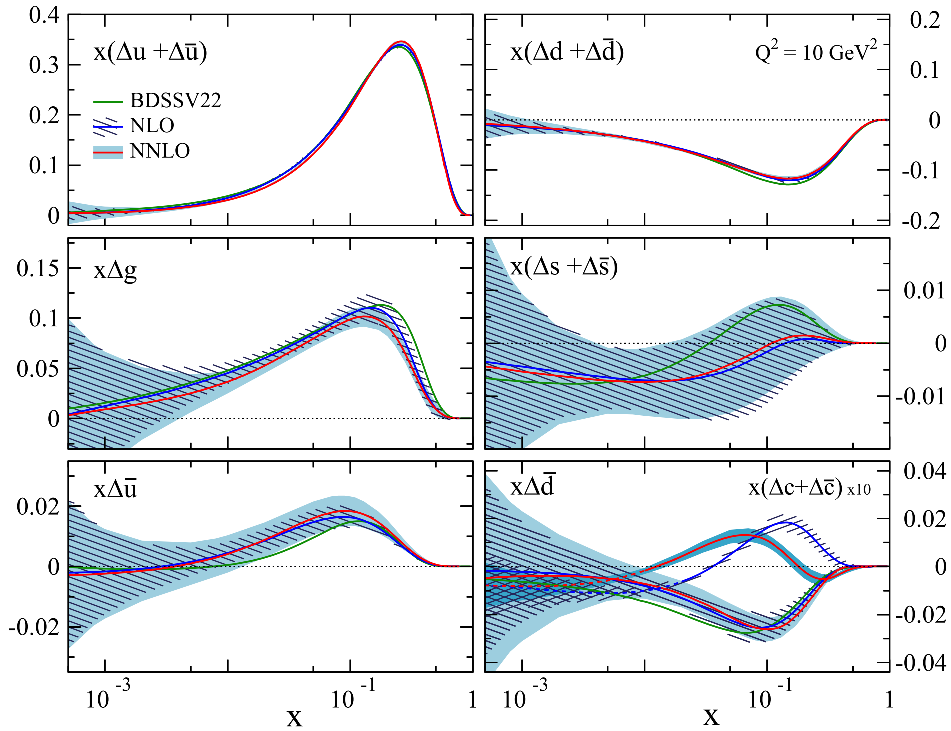

Figure 3.3: Results of a recent global fit of the helicity PDFs obtained from global analyses at NLO and NNLO, and from the NLO BDSSV22 fit [63].

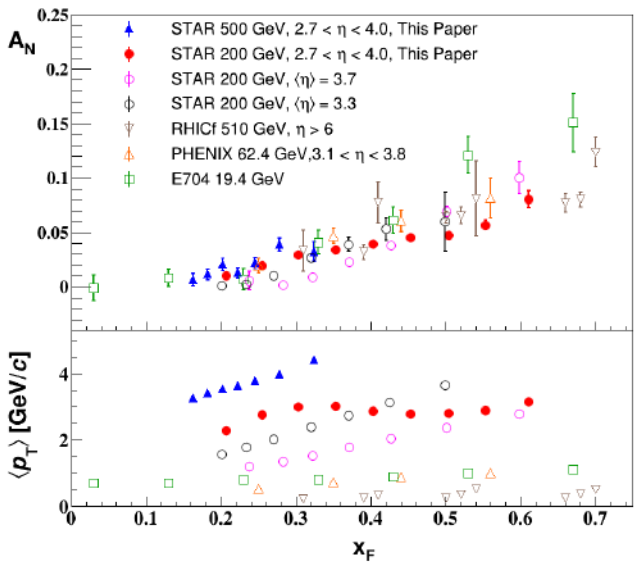

Figure 3.4: Transverse single-spin asymmetry A_{N} for π^0 production in $\mathrm{p}^{\uparrow}p$ collisions as a function of x_{F}. The top panel compares the results with measurements at $\sqrt{s} = 19.5 - 510$ GeV, while the bottom panel shows the average $\langle p_{\mathrm{T}} \rangle$ of π^0 for each x_{F} bin [80].

ergies [85, 86], persist over a wide range of $\sqrt{s}$ (Fig. 3.4). Such asymmetries cannot be accommodated within the leading-twist collinear framework alone, indicating the necessity of an extended approach to describe parton dynamics. When considering non-zero quark transverse momenta, the nucleon structure at leading-twist is characterized by eight PDFs (see Sec. 1.4). This section provides an overview of measurements relevant for extracting TMD PDFs[1], focusing on observables directly related to this work.

3.3.1 Sivers function

Among the TMD PDFs, the naive T-odd Sivers function, $f_{1T}^{\perp}$, has attracted considerable attention from both experimental and phenomenological perspectives. Important input comes from SIDIS data on $\pi^{\pm}$ and $K^{\pm}$ production, collected off a polarised proton target at HERMES [87] and COMPASS [88], as well as off a deuterium target at COMPASS [89, 90]. Parallel studies have also been carried out at JLab, where the asymmetry was investigated using a ^{3}He target [91, 92]. PHENIX Collaboration at RHIC has carried out measurements of forward neutron production [93], providing complementary insights into particle production mechanisms in hadronic collisions. Sivers-related asymmetries from pion-induced DY at COMPASS [94] are shown in Fig. 3.5a, while the corresponding COMPASS analysis of SIDIS using a longitudinally polarised muon beam on a transversely polarised NH_3 target [95] is presented in Fig. 3.5b. Results from STAR Collaboration in π^0 [96] and $W^{\pm}/Z^0$ [97] production are depicted in Figs 3.6a and 3.6b, respectively.

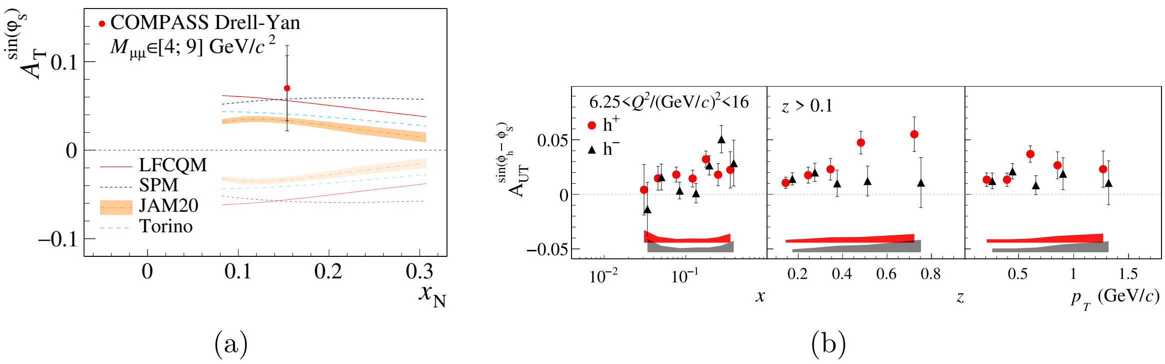

Figure 3.5: COMPASS results for the Sivers asymmetries in: (a) $\pi^{-}p^{\uparrow}$ DY as a function of proton Bjorken x_N [94] compared with theoretical predictions from different models and Q^2 evolution schemes [98] and (b) SIDIS off $p^{\uparrow}$ as a function of Bjorken x, fractional energy z, and transverse momentum relative to the virtual photon p_T for positive and negative hadrons [90].

3.3.2 Boer–Mulders function

Another naive T-odd TMD PDF, the Boer–Mulders function $h_1^{\perp}$, describes the correlation between the transverse momentum and transverse polarisation of a struck quark inside an unpolarised nucleon. In SIDIS, it contributes to the spin-independent asymmetry $A_{UU}^{\cos(2\phi_h)}$ measured by HERMES [99] and COMPASS [100]. The COMPASS results for the $\cos(2\phi_h)$ amplitude are shown in Fig. 3.7a. The Boer-Mulders function

[1]All presented TMD PDFs depend on x, $\boldsymbol{k}_T$, and Q^2. These arguments have been omitted for clarity.

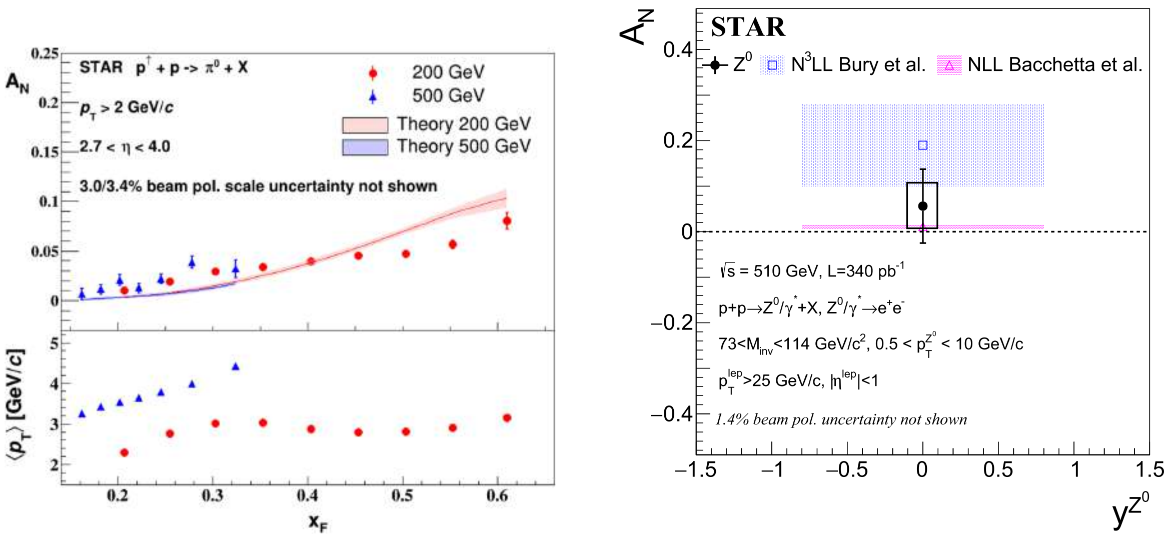

(a) (b)

Figure 3.6: STAR results for the Sivers asymmetries in transversely polarised pp collisions at RHIC: (a) π^0 production [96] as a function of x_{F}, and (b) Z^0 production [97] as a function of rapidity y^{Z^0}.

can be studied in Drell–Yan through the angular coefficient $\nu = 2A_{\mathrm{U}}^{\cos(2\varphi_{\mathrm{CS}})}$, which characterizes the unpolarised part of the cross section. Measurements from NA10 at CERN and E615 at Fermilab, along with preliminary COMPASS results [101], show consistent trends and agree with NNLO pQCD predictions, as illustrated in Fig. 3.7b. The Boer–Mulders TMD PDF for the pion can also be determined via azimuthal asymmetries $A_{\mathrm{T}}^{\sin(2\varphi_{\mathrm{CS}}-\varphi_{\mathrm{S}})}$ in the DY process. The resulting amplitude is shown in Fig. 3.8a. An attempt to extract $h_1^{\perp}$ is one of the topics addressed in this work and will be discussed in detail in Chapter 9.

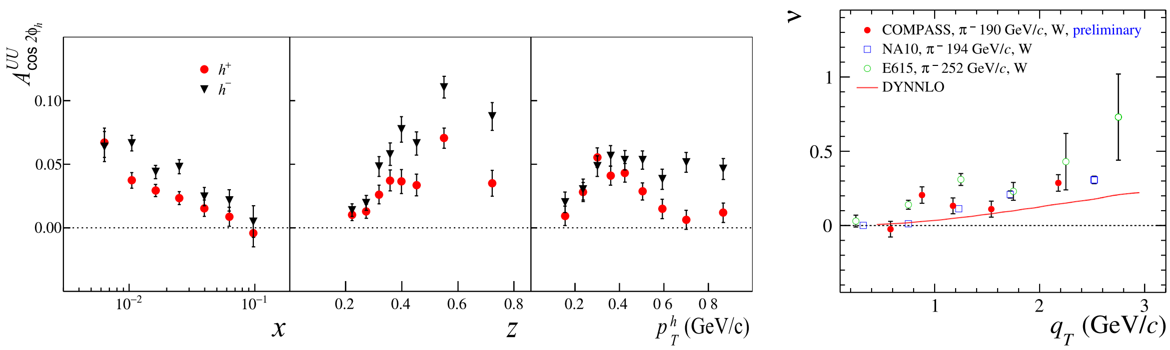

(a) (b)

Figure 3.7: COMPASS results for the Boer–Mulders effect: (a) $A_{\mathrm{UU}}^{\cos(2\phi_h)}$ from SIDIS off deuterons as a function of x, z, and p_{T} for positive and negative hadrons [100], (b) $\pi^-\mathrm{p}^{\uparrow}$ DY angular coefficient ν as a function of q_{T}, compared with the NA10 and E615 data, as well as NLO pQCD calculations [101].

3.3.3 Transversity function

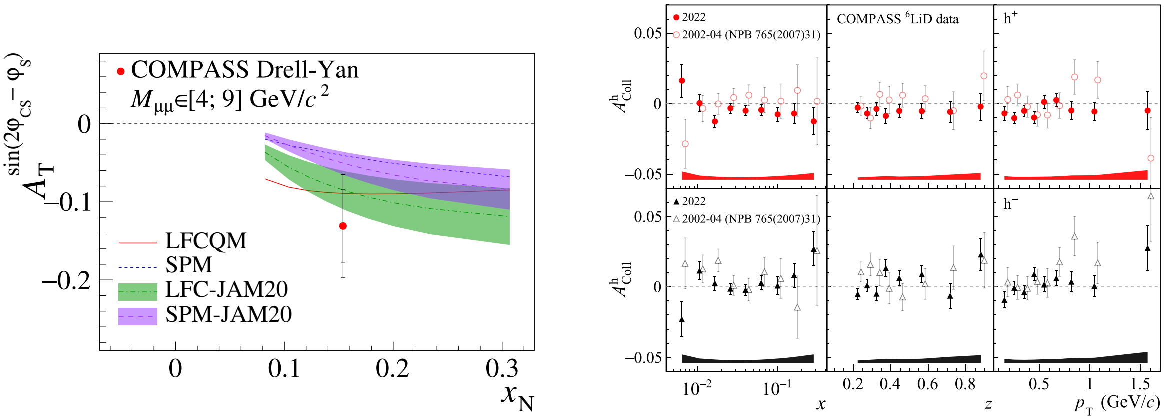

(a) (b)

Figure 3.8: COMPASS results: (a) transveristy TSAs as function of x_N in $\pi^-p^\uparrow$ DY process [94] with the theoretical predictions for different Q^2 evolution schemes from different models [98], (b) SIDIS Collins asymmetries for deuterons as a function of x, z and p_T for positive and negative hadrons [90].

The transversity distribution h_1 describes the correlation between the transverse spin of a quark and the transverse polarization of the parent hadron. The possibility of accessing transversity in double polarised Drell-Yan process and a careful study of its properties and sum rules was explored by Jaffe and Ji in Ref. [102]. Being chiral-odd, h_1 cannot be directly accessed in DIS, as another chiral-odd function is needed to form a chiral even observable. To form a chiral-even observable, h_1 must couple to another chiral-odd function. In SIDIS, this role is played by the Collins fragmentation function $H_1^\perp$[103], which describes the correlation between the transverse polarisation of a quark and the transverse momentum of the resulting unpolarised hadron. This spin–momentum correlation generates an asymmetry in the azimuthal distribution of hadrons produced from transversely polarised quarks, known as the Collins asymmetry $A_{\mathrm{Coll}}^{\mathrm{h}}$. Measurements of $A_{\mathrm{Coll}}^{\mathrm{h}}$ in the SIDIS process have been performed by HERMES [87], COMPASS [88–90, 95], and JLab [91, 92]. The Collins asymmetry, measured by HERMES in SIDIS from a transversely polarised proton target for charged pion production [87], is shown in Fig. 3.9a. Fig. 3.9b shows a corresponding measurement from STAR, which observed the Collins asymmetry in the distribution of charged pions within jets produced in pp collisions [104]. Transversity can also be probed through the measurement of specific azimuthal asymmetries in the Drell–Yan process, as studied by the COMPASS experiment using a transversely polarised target [94, 105]. The resulting transversity-related asymmetries in the $\pi^-p^\uparrow$ Drell–Yan reaction [94], along with the Collins asymmetries extracted from $\mu^+d^\uparrow$ SIDIS [90], are illustrated in Figs 3.8b and 3.8a.

3.3.4 Pretzelosity function

The chiral-odd pretzelosity distribution function, $h_{1T}^\perp$, describes the correlation between transverse polarization and transverse momentum of a parton inside a transversely-

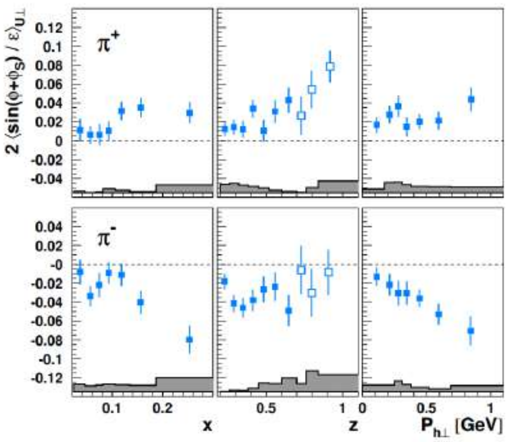

(a)

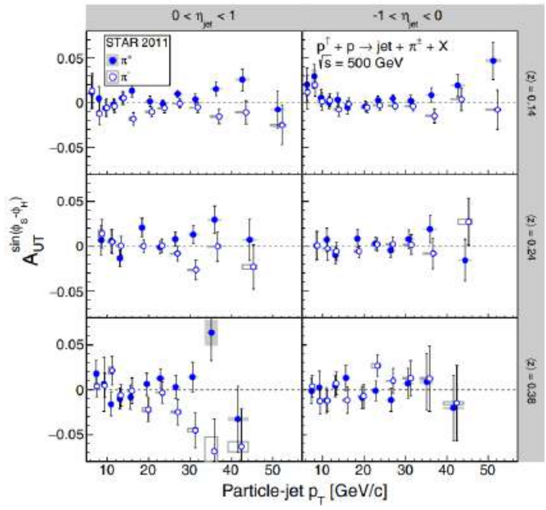

(b)

Figure 3.9: Collins asymmetries: (a) HERMES results from SIDIS off trasnversely-polarised proton target as a function of x, z, and hadron transverse momentum $P_{h\mathrm{T}}$ [87], and (b) STAR results as a function of particle-jet p_{T} in charged pion production in pp collisions [104].

polarized hadron. It can be probed in SIDIS through its coupling to the chiral-odd Collins fragmentation function $H_1^{\perp}$, appearing in the $\sin(3\phi - \phi_S)$ modulation of the cross section. The corresponding amplitude $A_{\mathrm{UT}}^{\sin(3\phi-\phi_S)}$ has been measured by HERMES [87], COMPASS [106], and JLab [107]. Conversely, in the Drell–Yan process, $h_{1\mathrm{T}}^{\perp}$ is convoluted with another polarised PDF, the Boer–Mulders function. This effect has been investigated in the COMPASS experiment using transversely polarised protons [94]. A comparison of the measured asymmetries in SIDIS and DY is presented in Figs 3.10a and 3.10b.

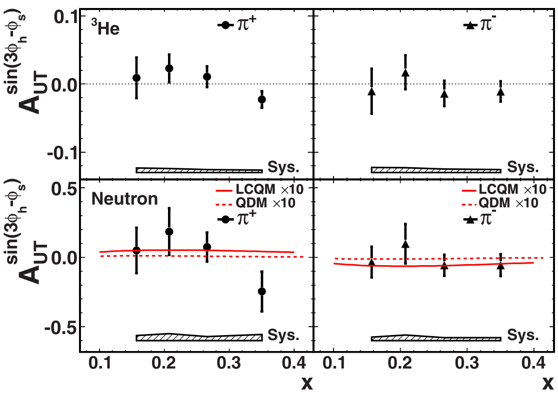

(a)

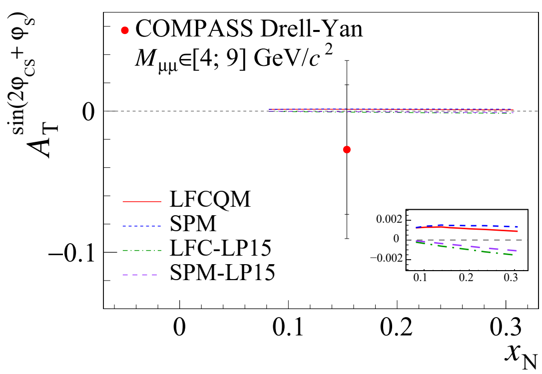

(b)

Figure 3.10: Pretzelosity asymmetries extracted from: (a) SIDIS on ^{3}He nucleon (top) and on the neutron (botton) [107] as a function of x, (b) $\pi^-\mathrm{p}^{\uparrow}$ DY as as function of x_{N} [94] with the theoretical predictions for different Q^2 evolution schemes from different models [98].

In summary, current knowledge of TMD PDFs remains limited. Upcoming experiments, such as LHCSpin and the Electron-Ion Collider (EIC), will extend the accessible (Q^2, x) range and provide new insights. This work presents key results on the Sivers, transversity, and pretzelosity asymmetries, the so-called WTSAs (Sec. 2.3), in the $\pi^-\mathrm{p}^\uparrow$ DY process for dimuon masses $M_{\mu\mu}$ between 4 and 9 GeV/c^2 in the valence quark region ($x_\mathrm{N} \approx 0.2$, $x_\pi \approx 0.5$).

Chapter 4

The COMPASS experiment

Knowledge is of no value
unless you put it into practice.
— Anton Chekhov

While the previous chapters focused on the theoretical background of TMD PDFs and current understanding of nucleon structure, this chapter turns to the experimental side, specifically the Common Muon and Proton Apparatus for Structure and Spectroscopy (COMPASS, NA58) experiment, which provides the data for this work. The COMPASS experiment is a fixed-target apparatus located along the M2 beamline of the Super Proton Synchrotron (SPS) at Conseil Européen pour la Recherche Nucléaire (CERN). Designed as a versatile facility for hadron physics, the 60-meter-long spectrometer has supported a wide range of studies on hadron structure and spectroscopy.

The COMPASS experiment operated in two main phases: COMPASS I (2002-2011) [108] and COMPASS II (2012–2022) [109]. In the first phase, the spin structure of nucleons was studied through DIS and SIDIS with longitudinally polarised targets, focusing on the helicity distributions of quarks [19, 110, 111] and gluons [20, 112, 113]. Complementary SIDIS measurements with transversely polarised targets probed the nucleon transverse spin and momentum structure [79, 114, 115]. In the second phase, Deeply Virtual Compton Scattering (DVCS) with a muon beam was studied to access nucleon GPDs [116], while the Drell–Yan process with a pion beam and a transversely polarised ammonia target was used to test TMD PDFs universality [94, 105]. Additional measurements with unpolarised tungsten and aluminia targets enabled cross-section and nuclear-effect studies.

The present chapter outlines the COMPASS setup used during the Drell–Yan measurements in 2015 and 2018. A detailed description of the full apparatus and its components is available in Refs. [117, 118]. The dedicated beamline and polarised targets are discussed in Secs. 4.1 and 4.2, respectively. Sec. 4.3 describes the spectrometer tracking detectors and calorimeters, followed by the trigger system in Sec. 4.4. The data acquisition system is described in Sec. 4.5, while Sec. 4.6 covers the software for event reconstruction, data analysis, and Monte Carlo simulations.

4.1 Beamline and Target Area

4.1.1 M2 Beamline

The COMPASS experiment is located at the end of the M2 beam line, illustrated in Fig. 4.1, of the CERN SPS accelerator complex. It operates with either a secondary hadron beam, composed primarily of pions or protons, with momenta up to 280 GeV/c, or with a tertiary muon beam reaching energies up to 200 GeV/c. These beams are produced by directing the primary 400 GeV/c proton beam from the SPS, delivering approximately 10^{13} protons in a typical 5 s spill during a 17 s supercycle, onto a beryllium production target, denoted T6. The interaction at T6 generates a secondary

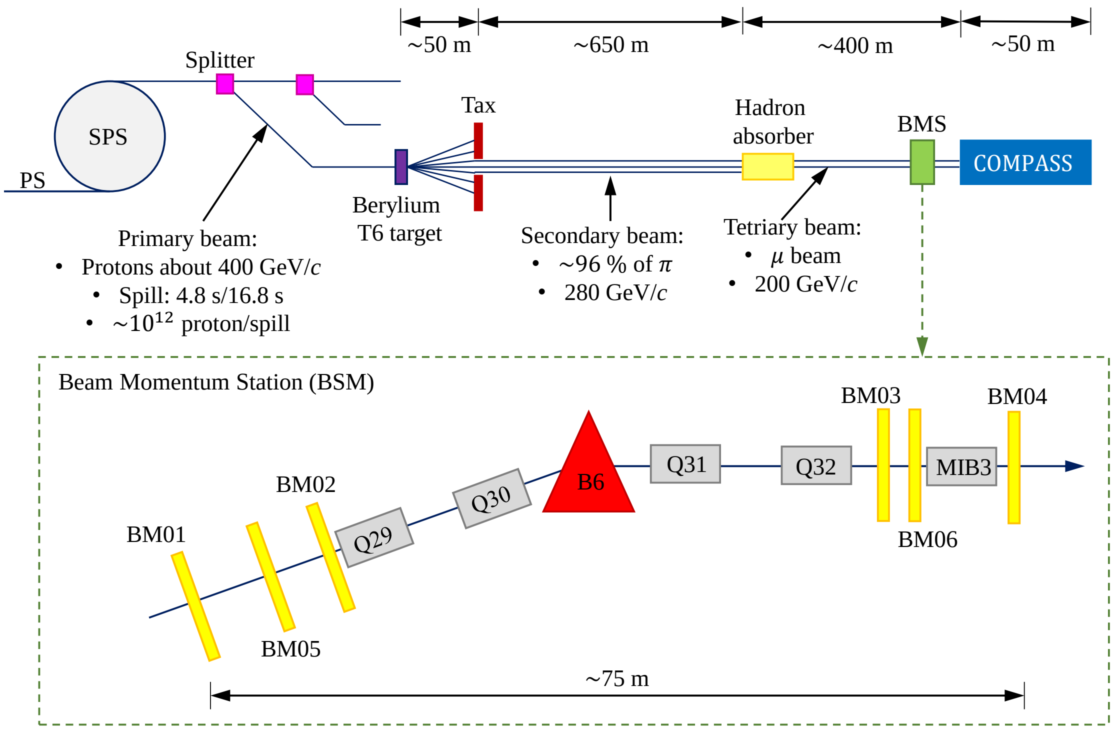

Figure 4.1: Simplified sketch of the M2 beam line of the SPS for the COMPASS experiment, highlighting the beam momentum station with quadrupole magnets (grey), tracking detectors (yellow), and B6 magnets that bend the beam horizontally. For a detailed layout, see Ref. [117].

beam containing a mixture of protons, antiprotons, pions, and kaons. The thickness of the T6 target is adjustable, allowing a control over an intensity of the secondary beam. The momentum of secondary hadrons are selected by passing through an array of quadruples and dipoles magnets (Tax, see Fig. 4.1). The negative hadron beam used during the 2015 and 2018 COMPASS Drell–Yan data taking campaigns consisted predominantly of π^-, with small contributions from K^-, $\bar{p}$, and other hadrons. The exact composition varies with beam momentum; at 190 GeV/c, the beam contained approximately 95% π^-, 4.5% K^-, and 0.5% $\bar{p}$ [117]. The beam was delivered at high intensity, with a rate of about 6×10^7 particles per spill. The CERN SPS delivers various beam types, supporting a diverse physics programme. While the muon beam is relatively pure, the hadron beam—comprising pions, kaons, and protons—requires particle identification. For this purpose, a Cerenkov Differential counter with Achromatic Ring (CEDAR) [118] is installed 30 m upstream of the target. Although effective in hadron spectroscopy, its time resolution is insufficient for reliable particle tagging in the high-intensity Drell–Yan experiment.

4.1.2 Beam Momentum Station

The most upstream component of the COMPASS setup is the Beam Momentum Station (BMS), located approximately 100 m upstream of the target region. The BMS comprises four scintillator hodoscopes (BM01-BM04), two scintillating fibre detectors (BM05 and BM06), a system of quadrupole magnets for momentum selection, and a sequence of three dipole magnets (B6) that bend the beam horizontally, redirecting it upwards towards the surface level. This station is primarily employed to determine the momentum of incoming muons. During hadron beam operation, however, the BMS is removed from the M2 beam line to reduce the material budget along the beam path.

4.2 Target Station

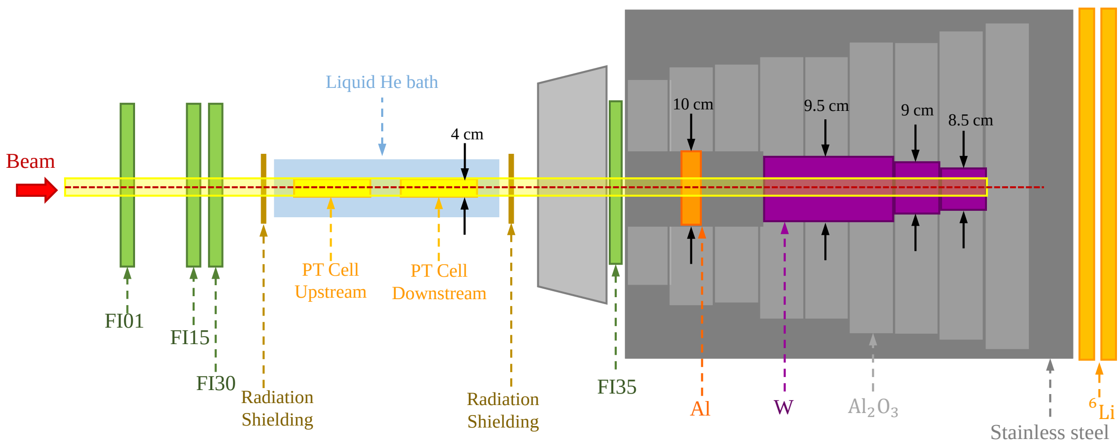

Figure 4.2: Top view of the polarised target (PT) and the hadron absorber including the Al and W targets. The scintillating fibers (FI), described in Sec.4.3.1, are included for completeness.

During the COMPASS Drell–Yan data taking, three distinct types of targets were utilized: polarised NH_3, Al, and W targets. A schematic top view of the target region is shown in Fig. 4.2. The polarised NH_3 target consists of two cylindrical cells, each 55 cm in length and 2 cm in diameter, separated by a 20 cm longitudinal gap. Downstream of the polarised targets are a 7 cm long Al target and a 120 cm long W target, the latter serving also as a beam dump, which accounts for its significant length.

4.2.1 Polarised Target

The NH_3 target is polarised via the Dynamic Nuclear Polarisation (DNP) technique [119], which transfers the high electron polarisation to the nucleons. The target material is cooled to approximately 60 mK in a liquid helium bath (10% ^{3}He / 90% ^{4}He) and placed in a homogeneous 2.5 T magnetic field generated by a superconducting solenoid. Microwave radiation at about 70 GHz induces hyperfine transitions, enabling efficient spin transfer from electrons to nucleons. To preserve the achieved polarisation, the target cells are placed in a dilution refrigerator, known as the polarised target cryostat. Operating in the so-called frozen-spin mode at a temperature of about 50 mK extends the polarisation relaxation time to several months. The target spin is then rotated from the longitudinal to the transverse orientation using a superconducting dipole magnet providing a 0.63 T transverse field. The transverse polarisation cannot be permanently maintained because the applied magnetic field is relatively weak, resulting in an exponential decay of the polarisation over time. n the 2015 and 2018 DY campaigns, the transverse polarisation exhibited a relaxation time of roughly 1000 hours, with an average level of about 73%.

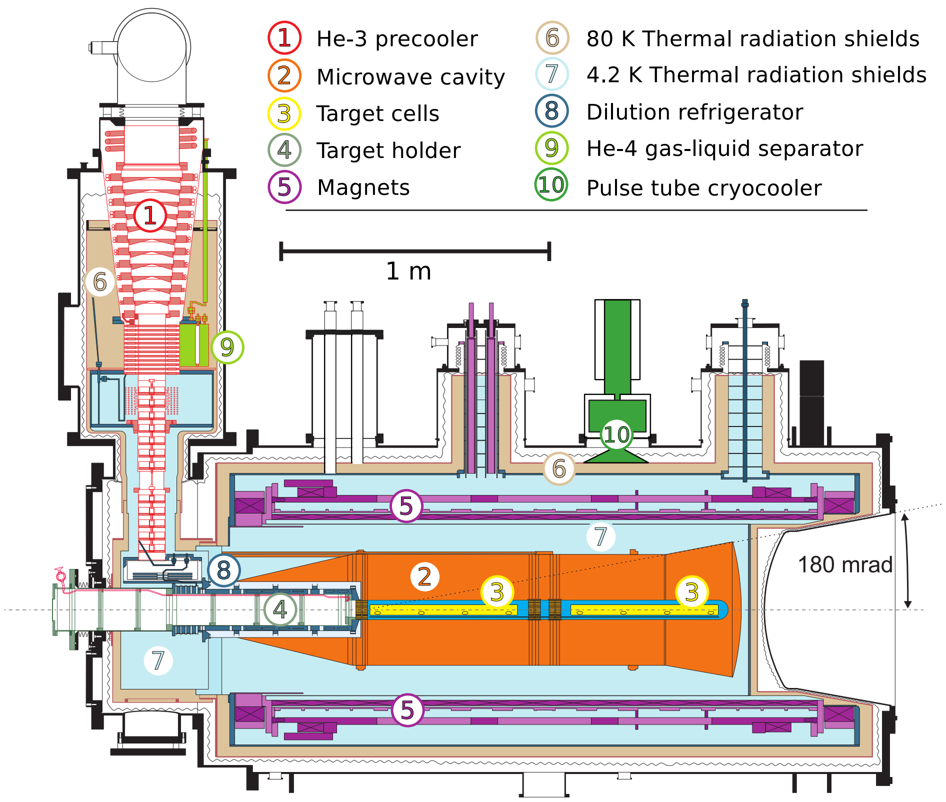

Figure 4.3: The polarised target system. Beam enters from the left (fine dashed line) and passes through two oppositely polarised cells filled with polarised material (yellow). The cells are enclosed in the refrigerator mixing chamber (cyan), the microwave cavity for Dynamic Nuclear Polarisation (DNP) (orange), and the magnet with its cryostat.

4.2.2 Hadron Absorber

During the 2015 and 2018 Drell–Yan data taking, the primary interest was a detection of muons originating from the hard scattering, while the accompanying hadrons were not relevant for the analysis. To suppress this undesired hadronic background, a dedicated hadron absorber was installed downstream of the polarised target. The absorber is constructed from alumina tiles (Al_2O_3) enclosed within a stainless-steel frame, with an upstream section made of aluminum and lithium plates mounted at the bottom to mitigate radiation levels. Although the absorber effectively suppresses hadrons, it also causes multiple scattering and energy loss, which reduces their spatial resolution.

4.3 Spectrometer

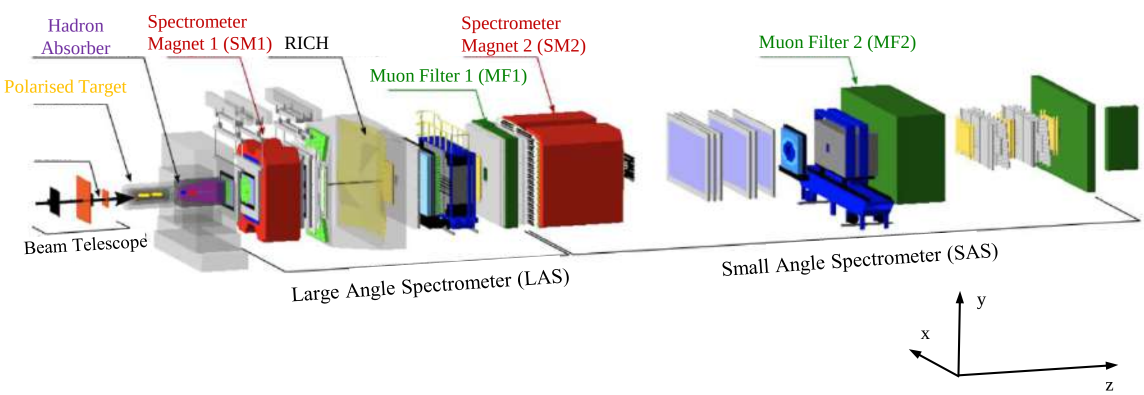

Figure 4.4: A schematic view of the COMPASS setup for the Drell–Yan programme, with labelled key components.

The DY COMPASS spectrometer configuration, illustrated in Fig. 4.4, provides broad angular coverage: from 25 to 165 mrad in the Large Angle Spectrometer (LAS) and from 8 to 45 mrad in the Small Angle Spectrometer (SAS). The first stage of the setup includes one of the two Spectrometer Dipole Magnets (SMs). The SM1 provides a vertical magnetic field with an integrated field strength of 1 Tm. Its large aperture ($\pm$180 mrad) matches the target angular acceptance and enables momentum measurements up to several tens of GeV/c. The second stage, SAS, includes the SM2 magnet with a vertical field of integrated strength of 4.4 Tm. It detects particles with momenta between 5 GeV/c and several hundred GeV/c within a forward cone of 30 mrad.

4.3.1 Trackers

The COMPASS spectrometer is designed to provide extensive angular coverage, enabling precise tracking of particles over a wide phase space. To achieve this, a combination of tracking detectors, optimized for different acceptance regions, is employed and grouped into three main tracking regions: Very Small Area Trackers (VSATs), Small Area Trackers (SATs), and Large Area Trackers (LATs). VSATs are located closest to the beam axis and required to operate reliably under extremely high particle rates, reaching up to $5{\times}10^7$ Hz. SATs, positioned between approximately 2.5 cm and 40 cm from the beam axis, is characterised by high spatial resolution and low material budget. LATs, situated at even larger radial distances, are optimized for maximum spatial coverage. The active areas, as well as the spatial and time resolutions of all VSAT, SAT, and LAT trackers, are summarized in Tab. 4.1 and briefly described below.

Table 4.1: Definition of the three angular regions used to segment the acceptance of the COMPASS spectrometer. Parameters δ_x and δ_t denote the spatial and time resolutions, respectively [117].

Very small area trackers (max flux: 5×10^7 Hz/cm^2)			
Detector	Number of detectors	δ_x (μm)	δ_t (ns)
Silicon Microstrips	23	120–210	0.35–0.45
Scintillatinf Fibers	6	8–11	2.5
Small area trackers (max flux: 3×10^5 Hz/cm^2)			
Detector	Number of detectors	δ_x (μm)	δ_t (ns)
MicroMegas	12	90	9
GEM	22	70	12
Large area trackers (max flux: 1×10^4 Hz/cm^2)			
Detector	Number of detectors	δ_x (μm)	δ_t (ns)
Drift Chambers	3	190	–
Straw Tubes	9	190	–
MWPC	14	1600	–

Silicon Multistrips

Silicon Microstrips (SIs) are placed upstream and downstream of the target. The silicon tracking stations have an active area of 5×7 cm^2 and provide an excellent spatial resolution of 10 μm combined with a time resolution of 2.5 ns. Each detector station consists of two identical detectors mounted back-to-back, with one rotated by 5° to improve spatial resolution. The detectors are operated at low temperatures (approximately 130 K) to minimize electronic noise. However, their long-term operation in a high-rate hadron beam is limited by radiation damage, which led to the removal of all SIs for the DY data taking.

Scintillating Fibres

Scintillating Fibers (FIs) are designed to track incoming and scattered beam particles, as well as other charged reaction products, particularly in the region close to the primary beam axis. The setup includes five stations with active areas ranging from 3.9×3.9 to 5.4×5.4 cm^2. Each station includes at least two coordinate projections, oriented along the vertical and horizontal axes. Three stations feature an additional inclined projection to enhance spatial resolution. To ensure sufficient photoelectron yield—at least ∼20 per minimum ionising particle—multiple fibre layers are stacked per projection, with each layer offset relative to the next as shown in the Fig. 4.5.

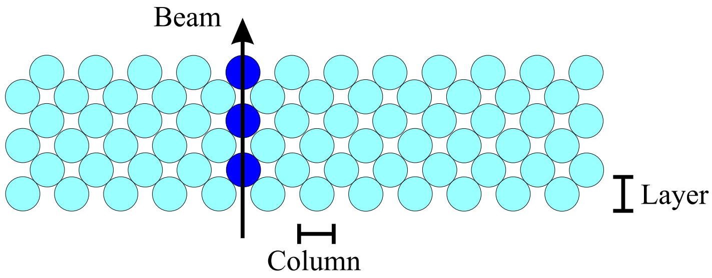

Figure 4.5: Fibre configuration of a FI plane [117].

Micromesh Gaseous Structure Detectors

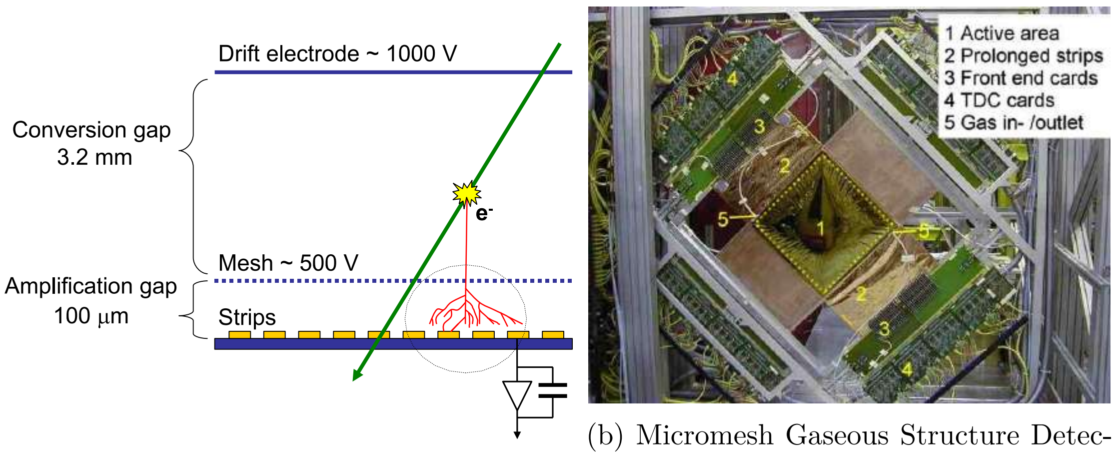

(a) Schematic of the amplification process.

(b) Micromesh Gaseous Structure Detectors (MicroMegas) doublet layers.

Figure 4.6: Illustration of a MicroMega detector [117].

Between the absorber and the SM1 magnet, three MicroMegas stations are installed, each composed of four projection planes. Their active areas consist of a pixelized region complemented by a 40×40 cm^2 standard section [117]. MicroMegas operate as gaseous tracking devices utilizing a two-stage amplification process, as illustrated in Fig. 4.6a. In this setup, ionisation electrons produced in the conversion gap drift toward a micromesh, which acts as a boundary between the initial conversion and the subsequent amplification regions. The stron electric field (∼50 kV/cm) creates an electron avalanche, which is collected by readout strips. The amplification region is only 100 μm wide, keeping the avalanche narrow and enabling a spatial resolution of about 110 μm. The nominal timing resolution of the micromegas is 9 ns.

Gas Electron Multipliers

Gas Electron Multipliers (GEMs), shown in the Fig. 4.7, are micro-pattern gaseous detectors that employ a cascade of amplification stages to detect ionizing particles with high spatial resolution. Each stage consists of a 50 μm thick polyimide foil, coated with copper on both sides and perforated with a dense array of microscopic holes of approximately 50 μm diameter. A voltage difference of about 100 V is applied across each foil, creating a strong electric field inside the holes. Primary ionization electrons generated in the drift region are directed into these holes, where they undergo avalanche multiplication due to the intense field. In COMPASS, GEMs with an active area of 32×32 cm^2 are employed, achieving a spatial resolution of around 110 μm. Additionally, two pixelized GEMs with smaller active areas of 10×10 cm^2 are used for tracking particles at small angles, offering the same spatial resolution.

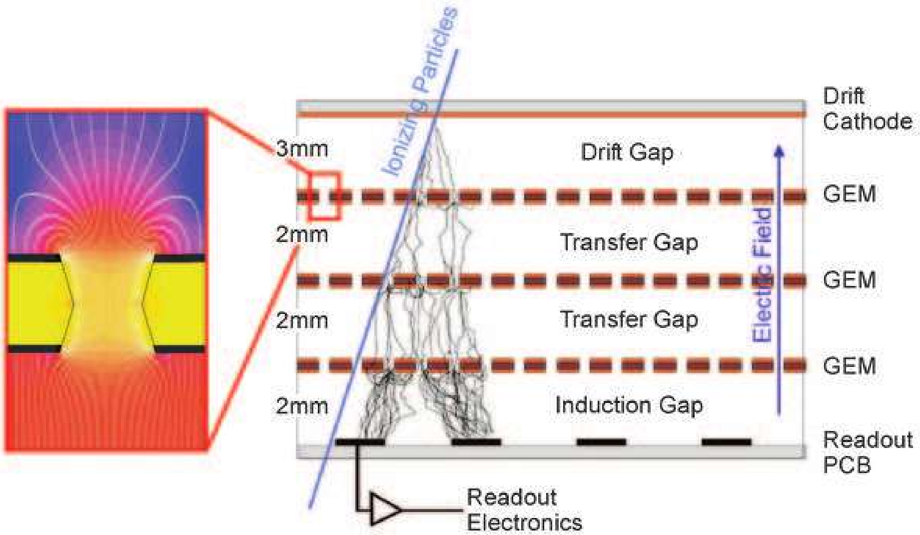

Figure 4.7: Schematic cross section of a triple Gas Electron Multiplier (GEM) detector. The left-hand side schematic illustrates the typical electric field in a GEM gap [117].

Rich Wall

The Rich Wall (RW) detector is a large-area tracking station with an active region of 5.27×3.91 m^2, excluding a central inactive zone of 1.02×0.51 m^2 [118]. It is composed of eight layers of Multiwire Drift Tubes (MDTs), arranged to provide up to four position measurements per track in both the vertical and horizontal projections. A schematic view of the MDT module layout is shown in Fig. 4.8. The nominal spatial resolution is 600 μm per plane.

MultiWire Proportional Chambers

The Multi-Wire Proportional Chambers (MWPCs) of the COMPASS spectrometer are used to track particles emitted at large angles in the SAS. When a charged particle traverses the detector volume, it ionizes the filling gas along its path, producing primary electrons. The electrons, driven by the uniform electric field, move toward the closely packed anode wires. Near the wires, the strong electric field initiates an avalanche, amplifying the primary ionisation signal. This signal is collected by 1-meter-long wires, 20 μm-diameter wires spaced by 2 mm. This amplified signal is then collected by the anode wires and processed by the readout electronics.

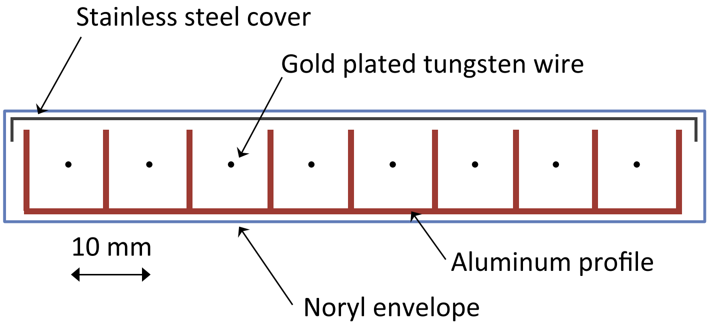

Figure 4.8: Sketch of a Multiwire Drift Tube (MDT) module [118].

Straw Tubes

Straw Tubes (STs) [120] are gaseous detectors used in COMPASS for tracking charged particles at large scattering angles in the large angle spectrometer. A gold-plated tungsten anode wire (30 μm diameter) runs along the center of each tube, while the aluminum-coated inner surface serves as the cathode. When a charged particle traverses a tube, it ionizes the gas, initiating an electron avalanche collected by the central wire. The typical spatial resolution reaches 200 μm. Three detector stations, each comprising three individual detectors with an active area of 323×280 cm^2, are installed downstream of SM1.

Drift Chambers

The acpDC detect charged particles by measuring the time it takes for ionization electrons, produced along a particle path, to drift toward thin anode wires in a gas-filled volume under an electric field. By combining timing information with the known geometry of the wire planes, the particle position can be reconstructed with high spatial resolution. A sketch of the operating principle is shown in Fig. 4.9. Each Drift Chamber (DC) module contains parallel wire layers between two cathode foils, with 20 μm anode wires alternated with 100 μm field wires held at 0 V and -1700 V, respectively, creating an electric field that directs ionization electrons to the anodes.

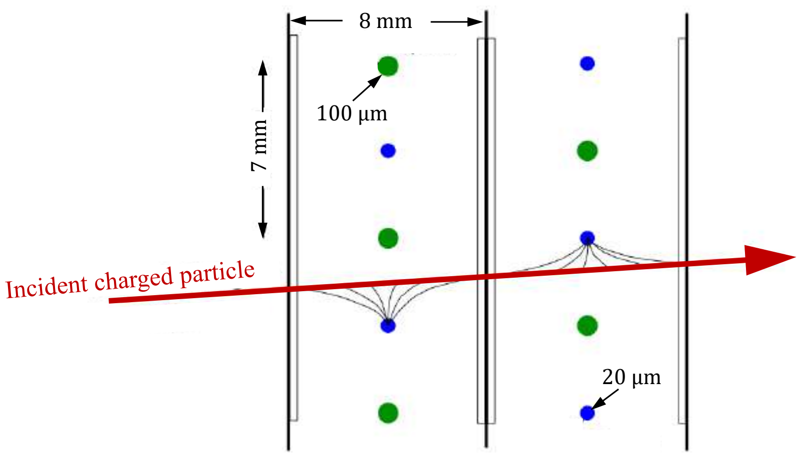

Figure 4.9: The principle of operation of the Drift Chamber (DC) [117].

Large Size Drift Chamber

The Large Size Drift Chamber (W45) consists of six stations, each comprising two coordinate projections. Each projection is equipped with a double wire layer that covers an active area of 520×260 cm^2 with a central dead zone of either 50 or 100 cm in diameter. The sensitive wires are arranged with a 4 cm pitch. During the 2015 and 2018 data taking periods, the detector achieved a typical spatial resolution of 500-600 μm.

4.3.2 Particle Identification

Accurate Particle Identification (PID) is a crucial requirement for most of the COMPASS physics programme. To accomplish this, COMPASS utilizes a combination of specialized detectors spanning a wide kinematic range. The Ring Imaging Cherenkov (RICH), located in the LAS, plays a key role in distinguishing between pions, kaons, and protons, up to momenta of about 43 GeV/c. The setup includes two Electromanetic Calorimeters (ECALs) and two Hadronic Calorimeters (HCALs), one of each in the LAS and SAS. Photon and electron energies are measured with ECALs, whereas hadron energies are measured with HCALs. The calorimeter material absorbs the incoming particles, creating electromagnetic or hadronic showers that are recorded by photomultiplier tubes to determine their energy. Additionally, the CAMERA detector supports the reconstruction of exclusive events, which is particularly important in studies of DVCS. For the Drell–Yan programme, precise identification of muon pairs is of particular importance. This capability is provided by the dedicated muon detection system, comprising the Muon Walls (MWs) and Muon Filters (MFs). These systems ensure efficient separation of muons from the hadronic background over a wide angular range, enabling reliable reconstruction of dimuon final states.

Muon Filters

The spectrometer is equipped with two MFs, which serve as absorbers that stop most particles while allowing muons to pass. MF1, located at the end of the LAS before SM2, consists of a 60 cm thick iron absorber. In contrast, MF2, positioned near the end of the SAS before W45, is built from a 2.4 m thick concrete absorber.

Muon Walls

The Muon Walls (MWs) were the primary particle identification detectors during the DY runs. Each wall, MW1 and MW2, contained 16 tracking planes arranged symmetrically, with 8 located upstream and 8 downstream of their respective muon filters (MF1 and MF2). Despite their similar design, the two MWs are installed in different regions of the spectrometer and serve different purposes. MW1, located in the LAS, covers an active area of 480×410 cm^2 with a central aperture of 140×80 cm^2 for the beam. MW2, placed in the SAS, combines MDT planes downstream of MF2 with the W45 detector upstream, providing efficient tracking over a wide acceptance.

4.4 Triggering System

The trigger system plays a crucial role in reducing the load on the Data Acquisition System (DAQ) while enabling the selection of specific kinematic regions through dedicated configurations. It also provides a common timing reference for the entire detector readout and DAQ. Trigger decisions are typically based on fast, precisely timed signals from scintillator counters or hodoscopes.

During the Drell–Yan data taking, a dedicated dimuon triggers were employed to select events containing two muon tracks approximately pointing back to the target region. The logic behind the dimuon trigger relies on combinations of single-muon triggers presented in Sec. 4.4.1, with the exact coincidence conditions concisely outlined in Sec. 4.4.2. Additionally, a Beam Halo Veto (VETO) system located upstream of the target and a Random Trigger (RT) outside the spectrometer region are implemented. Their operation is detailed in Secs 4.4.3 and 4.4.4, respectively. An overview of the relevant trigger and veto hodoscopes used during the Drell–Yan data taking is presented in Fig. 4.10.

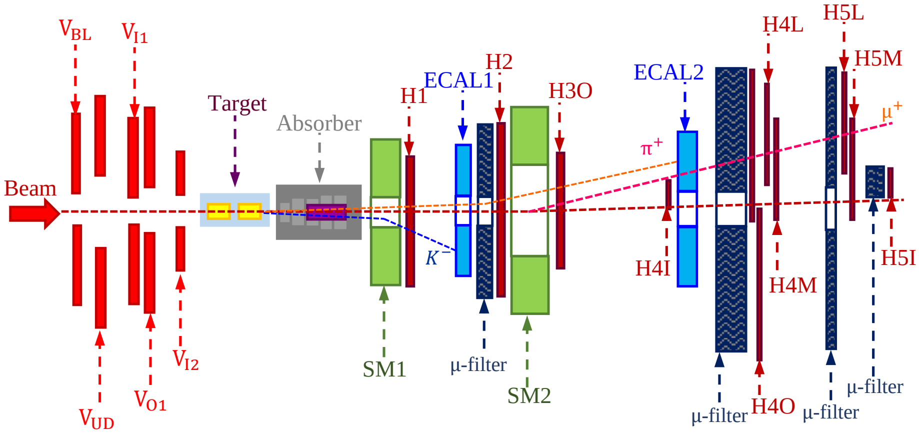

Figure 4.10: Top view of the hodoscopes in the COMPASS Drell–Yan data taking in 2015 and 2018. The VETO hodoscope V_{ud} was not used during data collection, it remained present in the experimental setup.

4.4.1 Single Muon Triggers

Target-Pointing Triggers

Muon detection relies on three hodoscope subsystems: Large-Angle Trigger (LAST), Outer-Angle Trigger (OT), and Middle-Angle Trigger (MT). Each consists of horizontal scintillating slabs placed at different locations along the spectrometer and is used to identify single-muon trajectories. Due to their geometry, these hodoscopes have reduced sensitivity to deflections caused by the magnetic field, particularly near the edges of their acceptance. The trigger logic is based on the target pointing technique, illustrated in Fig. 4.11a, in which a signal is generated and recorded when a particle simultaneously

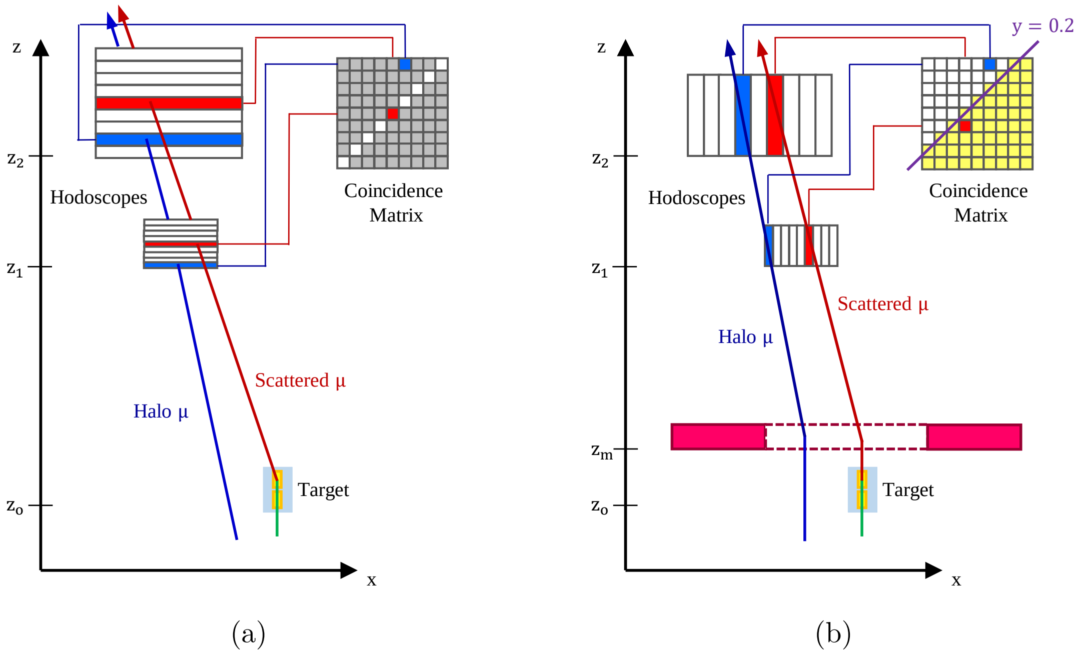

Figure 4.11: Illustration of techniques employed for single muon triggers: (a) target-pointing, (b) energy loss. The accepted pixels of the trigger matrix are shown in white. Following the coincidence logic, a flip-flop gate ensures the generation of a single trigger pulse. The red signal represents the trigger pulse that is transmitted to the front-end electronics and the data acquisition system.

crosses both planes of a hodoscope, as determined by a coincidence matrix. The three main single muon trigger subsystems are:

1. **Large-Angle Trigger (LAST), hodoscope planes H1 and H2:** Located between the SM1 and SM2 magnets, it consists of one single-part and one split hodoscope, designed to optimize spatial coverage in the LAS region.

2. **Outer-Angle Trigger (OT), hodoscope planes H3O and H4O:** Positioned further downstream, it incorporates hodoscopes located at the end of the LAS and within the SAS region, enabling efficient detection for angles greater than 5 mrad.

3. **Middle-Angle Trigger (MT), hodoscope planes H4M and H5M:** Fully situated within the SAS region, the MT trigger enhances coverage across the range of 0.5 to 5 mrad.

Energy Loss Triggers

At small scattered muon angles, the target pointing becomes insufficiently precise. In such cases, the trigger decision is based on the energy loss of the muon candidate. As illustrated in Fig. 4.11b, this is implemented using two vertical scintillator hodoscopes, where all possible combinations of hits form a triangular coincidence matrix. This method is employed in the following trigger systems:

1. **Inner Trigger (IT), hodoscope planes VI1 and VI2:** Located near the target station and forming part of the VETO logic described in Sec.4.4.3.

2. **Ladder Trigger (LT), planes H4L and H5L:** Positioned behind the muon filters, close to the rear end of the spectrometer covering small muon scattering angles.

4.4.2 Dimuon Triggers

The dimuon trigger is constructed as the logical coincidence of two independent single-muon trigger signals. Each single muon trigger is based on hodoscope planes positioned downstream of the spectrometer magnets. A logical coincidence (denoted by $\otimes$) between two such triggers ensures that two muon candidates are detected within the same event window.

In 2015 and 2018, three distinct dimuon triggers were utilized:

$$\big(\mathrm{LAST} \otimes \mathrm{LAST}\big), \quad \big(\mathrm{LAST} \otimes \mathrm{OT}\big), \quad \big(\mathrm{LAST} \otimes \mathrm{MT}\big).$$

Kinematic $M_{\mu\mu} - x_{\mathrm{F}}$ coverage is presented in Fig. 4.12. Dimuon events reconstructed with LAST $\otimes$ LAST, LAST $\otimes$ OT, and LAST $\otimes$ MT are concentrated at high mass/low x_{F}, intermediate, and low mass/high x_{F}, respectively.

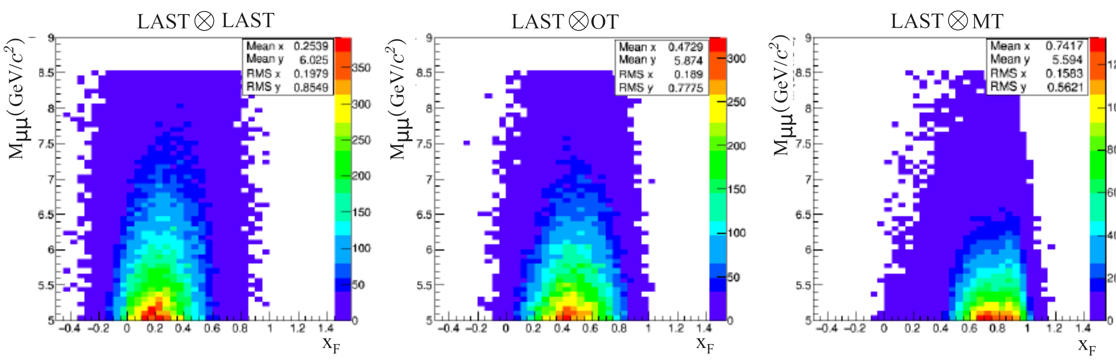

Figure 4.12: Kinematic coverage of dimuon trigger in terms of $M_{\mu\mu}$ and x_{F} from the real data in 2018 DY data taking [121].

4.4.3 Beam Halo Veto Tiggers

The VETO trigger is designed to suppress halo muons originating from beam decays upstream of the target. The reduced momentum of these muons leads to the formation of a peripheral halo around the hadron beam. This trigger utilizes hodoscopes positioned outside the nominal beam line to identify and reject events associated with the muon halo, thereby improving the overall signal purity.

4.4.4 Random Trigger

The RT provides an uncorrelated event sample, independent of the beam and detector activity. It is generated by signals from a radioactive source located outside the spectrometer area. In the 2015 DY data taking, this trigger was primarily employed for beam flux studies and for validating trigger system performance by providing an unbiased reference sample.

4.5 Data Acquisition and Detector Control

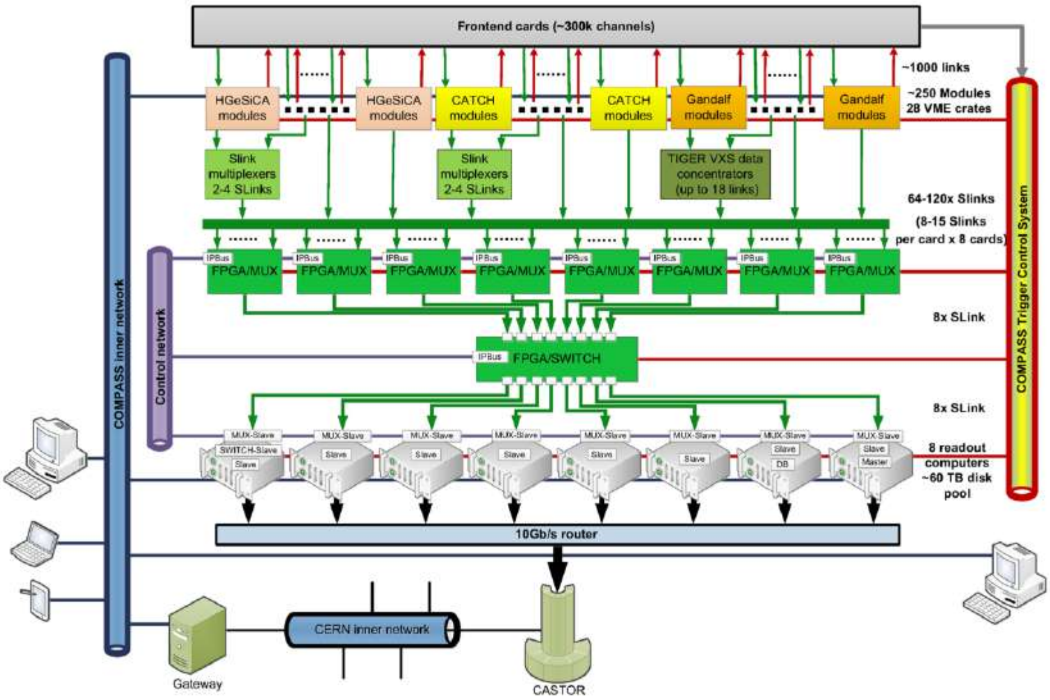

Figure 4.13: Sketch of COMPASS Data Acquisition System (DAQ) [122].

Data acquisition (DAQ), encompassing the collection, processing, and storage of detector signals, is schematically shown in Fig. 4.13. In COMPASS, data taking is organized into runs, each consisting of a sequence of consecutive spills. A typical run lasts up to 30 minutes and, by convention, contains around 200 SPS spills.

The analog signals from each detector are first processed by front-end cards, where they are digitized using either Analog-To-Digital Converters (ADCs) or Time-to-Digital Converter Chips (TDCs). These digitizers may be integrated directly on the front-end cards or implemented on dedicated readout modules such as Generic Advanced Numerical Device for Analog and Logic Functions (Gandalf), Hot GEM and Silicon Control and Acquisition (HGeSiCA), or COMPASS Accumulate, Transfer and Control Hardware (CATCH). These digitized signals are then transmitted via optical fibers (using the S-Link protocol) to Field-Programmable Gate Array (FPGA) based multiplexing cards. From there, the data is routed through an FPGA switch to multiple slave computers. These online computers assemble the raw data into complete events, which are then transferred to the CERN Advanced STORage manager (CASTOR) storage system.

The data taking conditions and apparatus stability are continuously monitored throughout data collection using two software systems: the Detector Control System (DCS) and the COMPASS Object-Oriented OnLine tool (COOOL). The primary purpose of the DCS [123] is to monitor and control all essential parameters of the COMPASS setup during data taking. This encompasses the operation of high-voltage and low-voltage power supplies, gas distribution systems, as well as electronic racks and crates. In addition, the DCS continuously monitors slowly varying environmental parameters such as pressure, temperature, and humidity. The system is built on a commercial Supervisory Control and Data Acquisition (SCADA) platform known as PVSS. It is routinely used by data taking shift crews and detector experts to ensure stable and safe operation of the experiment. The stability of COMPASS detectors is monitored using the COOOL software, which performs online, run-by-run decoding of selected raw data from the DAQ. Among the outputs are various histograms, particularly those depicting detector plane profiles, which are instrumental in quickly identifying anomalies such as voltage failures, single-channel issues, or signal disruptions at the front-end stage.

4.6 Reconstruction Chain

The COMPASS data analysis workflow is supported by three dedicated software packages, designed for event simulation, detector reconstruction, and physics analysis. The raw data from the DAQ consist of digitized timing information from tracking detectors and energy measurements from calorimeters. CORAL [124] is a C++ based software framework used to convert detector output into physical quantities. Timing, calibration, and alignment data are first combined to reconstruct particle hit positions within the detectors. The recorded hits are linked into continuous tracks using a Kalman Filter algorithm, which determines straight trajectories. This process is typically repeated multiple times, with each iteration incorporating refinements in detector calibration, alignment, beam tracking, and other preprocessing steps. The reconstructed data generated by CORAL are stored in mini Data Summary Tapes (mDSTs) files. These files are subsequently analyzed using Physics Analysis Software tools (PHAST) [125], a dedicated C++-based physics analysis framework.

Data Simulations

The COMPASS physics programme relies extensively on Monte Carlo (MC) simulations for determining the spectrometer acceptance and evaluating background contributions. This MC framework consists of four components: PYTHIA, TGEANT, CORAL, and PHAST. The event generator PYTHIA [126] provides the initial kinematic conditions for simulated processes, such as dimuon production via Drell–Yan process. These events are generated according to the calculated differential cross-sections of the respective interactions, forming the starting point of the full detector simulation and reconstruction chain. Subsequently, TGEANT [127], a C++ MC package based on GEANT4, simulates the detector response to the generated physics processes and determines which detectors register hits. This simulation accounts for the full experimental setup, including detectors and targets, and determines whether particles from the generated events produce detectable signals. This workflow ensures that simulated events undergo the same processing chain as experimental data, enabling consistent studies of detector performance, acceptance, and background contributions.

Chapter 5

General Aspects of Drell-Yan Data Analysis

Polarisation data has often been the graveyard of fashionable theories.
If theorists had their way, they might well ban
such measurements altogether out of self-protection.

— James Bjorken

In Chapter 2, the Drell–Yan reaction is introduced as one of the fundamental processes used to probe the partonic structure of hadrons. This chapter presents the analysis of the single-polarised Drell–Yan process measured by COMPASS Collaboration in 2015 and 2018[1]:

$$\pi^- + \mathrm{p} \to \gamma^* + \mathrm{X} \to \mu^+ + \mu^- + X.$$

The study considers two dimuon mass intervals of particular interest:

$$M_{\mu\mu} \in (4.3,\, 8.5)\,\mathrm{GeV}/c^2 \quad \text{and} \quad M_{\mu\mu} \in (4.0,\, 9.0)\,\mathrm{GeV}/c^2.$$

The event selection criteria are described in Sec. 5.1, while Sec. 5.2 introduces the definitions of the two mass intervals used throughout the analysis. The binning strategy and related technical considerations for each mass range are discussed in Sec.5.3. Additionally, Sec.5.4 introduces the dilution factor, which plays a central role in determining asymmetries in subsequent chapters. As these initial steps are largely consistent across both intervals, they are presented here in a comparative manner. The extraction of asymmetries for each mass interval are discussed separately in Chapters. 7 and 8.

5.1 Event Selection

Identifying DY candidates requires a dedicated multi-step event selection procedure, designed to suppress background contributions and ensure the consistency of the final dataset. In this study, the selection criteria closely follow those employed in the TSA

[1] The superscript symbols a and b, previously used in Chapter 2 to describe the general DY process (e.g., x_a and x_b), are here replaced by π and N (e.g., x_π and x_N) referring specifically to π^-p DY dimuon production.

analysis reported in [94], ensuring consistency with previous work. The applied selection steps are summarised below.

1. **Stability Requirements**: Data quality is ensured by requiring that both the spill and the run pass stability criteria, which are described in detail in Sec. 5.1.1.

2. **Muon Identification**: Each event must contain a muon pair, with each track satisfying:
$$\frac{X}{X_0} > 30,$$
where X is the material thickness traversed in the spectrometer and X_0 is the radiation length. This requirement ensures reliable muon identification. Further details are given in Sec. 5.1.2.

3. **Primary Vertex Selection**: The best Primary Vertex (PV) associated with the muon pair is selected according to the procedure described in Sec. 5.1.2.

4. **Charge and Mass Selection**: Only muon pairs with opposite charges and a dimuon mass of:
$$M_{\mu\mu} > 1.5 \text{ GeV}/c^2$$
are considered for the analysis.

5. **Trigger Conditions**: Events must pass:
$$(\text{LAST} \otimes \text{LAST or LAST} \otimes \text{OT}) \text{ and not } (\text{LAST} \otimes \text{MT}),$$
where the LAST $\otimes$ MT signal serves as a veto to suppress beam-decay muons. For details, see Sec. 5.1.3.

6. **Trigger Validation**: A dedicated study validating the trigger conditions is presented in Sec. 5.1.4.

7. **Track Quality Requirements**: Accurate muon identification is ensured by selecting tracks with:
$$Z_{\text{first}} < 300 \text{ cm} \quad \text{and} \quad Z_{\text{last}} > 1500 \text{ cm},$$
corresponding to positions upstream of SM1 and downstream of MF1, respectively.

8. **Track Fit Quality**: Tracks must meet the condition:
$$\frac{\chi^2}{\text{ndf}} < 3.2,$$
which is tighter than the threshold of 10 used in previous analyses. Applying this cut improves consistency between the early (spring and summer) and late (autumn) data-taking periods within the 2015 and 2018 datasets.

9. **Timing Consistency**: The absolute time difference between the mean hit times of the two muon tracks is required to be:
$$|\Delta t| \leqslant 5\,\text{ns}.$$

10. **Dimuon Mass Range**: The invariant mass of the dimuon system is restricted to lie within the ranges:

$$M_{\mu\mu} \in (4.3, 8.5)\ \mathrm{GeV}/c^2 \quad \text{or} \quad M_{\mu\mu} \in (4.0, 9.0)\ \mathrm{GeV}/c^2$$

.

11. **Energy Conservation**: In the target frame, the sum of the muon momenta must satisfy:

$$l^+ + l^- < 190\ \mathrm{GeV}/c \quad \text{target frame.}$$

12. **Transverse Momentum Constraint**: The transverse momenta of both muons in the target frame must not exceed:

$$l_\mathrm{T}^\pm < 7\ \mathrm{GeV}/c \quad \text{target frame.}$$

13. **Kinematic Validity**: The Bjorken variables x_N and x_π, as well as the Feynman variable x_F, are required to lie within their physically meaningful ranges:

$$x_\mathrm{N},\ x_\pi \in [0,\ 1] \quad \text{and} \quad x_\mathrm{F} \in [-1,\ 1].$$

14. **Primary Vertex Position**: The longitudinal position of the primary vertex, Z_vert, must lie within one of the two NH_3 target cell intervals:

$$Z_\mathrm{vert} \in [-294.5, -239.4]\,\mathrm{cm} \quad \text{or} \quad Z_\mathrm{vert} \in [-219.1, -163.9]\,\mathrm{cm}.$$

15. **Radial Vertex Constraint**: The radial position of the primary vertex, R_vert, is required to satisfy

$$R_\mathrm{vert} \leqslant 1.9\,\mathrm{cm},$$

given that the target cell radius is 2 cm.

5.1.1 Spill and Run Stability

To ensure data quality, this analysis uses the lists of excluded spills and runs provided by the TSA study [94]. These lists are generated via standard monitoring software, which evaluates macroscopic variables on a spill-by-spill basis, following methodologies established in previous DY and SIDIS measurements. Spills with anomalous behavior are flagged and removed, and the stability of key kinematic variables is checked run-by-run to identify and discard unreliable runs

5.1.2 Selection of the Dimuon Pair and Primary Vertex

Both particle tracks are required to traverse at least 30 radiation lengths beyond the hadron absorber, ensuring their identification as muons rather than hadrons or electrons. All such track pairs within an event are considered, and a common primary vertex is reconstructed for each pair. Since multiple vertices may be associated with a single pair, mainly differing in the set of tracks assigned, a selection procedure is applied to determine the optimal primary vertex for each muon pair [94]:

1. When possible, the vertex identified by PHAST as the best primary vertex of the event[2] is selected.

2. If no such vertex is designated, the vertex with the lowest χ^2 value[3] is chosen.

Multiple muon pairs can, in principle, originate from the same primary vertex within a single interaction, but no such cases are observed within the selected mass range.

5.1.3 Dimuon Trigger Configuration

The dimuon trigger, briefly introduced in Sec. 4.4.2, is designed to select events containing two muon tracks originating approximately from the target region. It is implemented as the logical coincidence of two independent single-muon trigger signals. Originally, the trigger condition is defined as

$$\Big(\mathrm{LAST} \otimes \mathrm{LAST}\Big) \;\text{ or }\; \Big(\mathrm{LAST} \otimes \mathrm{OT}\Big) \;\text{ or }\; \Big(\mathrm{LAST} \otimes \mathrm{MT}\Big),$$

where each term represents the logical AND of two single muon triggers based on different hodoscope systems. Subsequent studies demonstrated that events recorded by the LAST $\otimes$ MT condition are dominated by combinatorial background. To suppress such background contributions, the trigger logic is refined to

$$\Big(\mathrm{LAST} \otimes \mathrm{LAST}\Big) \;\text{ or }\; \Big(\mathrm{LAST} \otimes \mathrm{OT}\Big),$$

with all events triggered solely by $\Big(\mathrm{LAST} \otimes \mathrm{MT}\Big)$ excluded.

5.1.4 Trigger Validation

To validate the trigger, it is necessary to confirm that at least one of the dimuon triggers that fired corresponds to the reconstructed muon tracks. This is achieved by propagating each reconstructed track through the spectrometer using the detector geometry. From the reconstructed trajectory, the intersected hodoscope planes are identified, enabling the determination of the trigger conditions potentially satisfied[4]. Trigger logic is based on requiring coincident signals in specific pairs of hodoscope planes belonging to three distinct detector subsystems:

1. **LAST** hodoscopes: planes **HG01** and **HG02**,

2. **OT** hodoscopes: planes **HO03** and **HO04**,

3. **MT** hodoscopes: planes **HM04** and **HM05**.

The selection criterion is met if any of the fired dimuon triggers corresponds to the specific hodoscope intersections of the reconstructed muon tracks. For example, if the event is triggered exclusively by $\Big(\mathrm{LAST} \otimes \mathrm{LAST}\Big)$, then both muon tracks are required to traverse the HG01 and HG02 hodoscope planes.

[2]The best PV is identified by the `PaEvent::iBestPrimaryVertex()` in PHAST.
[3]The χ^2 is accessed via PHAST `PaVertex::Chi2()`.
[4]Validation is performed via `PaTrack::Extrapolate()` and `PaDetect::InActive()` in PHAST.

5.2 Selection Criteria for Transverse Momentum Distributions

In the standard TSA analysis [94], the transverse momentum q_{T} is restricted to values above 0.4 GeV/c to ensure adequate resolution of the azimuthal angles φ_{S} and φ_{CS}. For the weighted analysis, however, the full q_{T} range must be included, as the cross section is nonzero throughout, meaning no q_{T} cut can be applied[5]. Removing the cut reveals a long high-q_{T} tail. Although this tail contains few events, they can significantly influence certain weighted observables, including the $2\varphi_{\mathrm{CS}} + \varphi_{\mathrm{S}}$ asymmetry, and their statistical uncertainties. To mitigate this effect, a selection is applied on the combined muon momenta in the target frame, $l^- + l^+ < 190$ GeV/c, effectively limiting the dimuon energy below the initial-state energy while neglecting the beam momentum spread and the μ, π, and proton masses.

Even after this cut, events with relatively large q_{T} remain. The reconstructed vertices deviate from the inclusive sample, clustering predominantly at the upstream end of the upstream cell and, to a lesser extent, within the absorber region ($Z_{\mathrm{v}} \in [-80, 0]$cm)[128]. These characteristics are not consistent with genuine signal events and suggest background contamination. In order to suppress this contribution, each muon is required to have a transverse momentum $l_{\mathrm{T}}^{\pm}$ below 7 GeV/c in the target frame. Events at high q_{T} often feature an asymmetric momentum configuration, with one muon carrying very little transverse momentum and the other exhibiting a large l_{T}, which poses challenges for accurate event reconstruction.

Despite the applied cutoffs, some reconstruction artifacts persist. Their impact on the asymmetry extraction within the standard mass range is negligible. However, in the extended mass range, the new extraction procedure requires that these events be taken into account. This will be discussed in detail in Chapter 8.

Mass Range Definition and Background Separation

The COMPASS DY data are commonly divided into four ranges of Q^2[6] as presented in Fig. 5.1 [105]:

- $M_{\mu\mu} \in (1,\ 2)(\mathrm{GeV}/c^2)$: low-mass region with significant background contributions,
- $M_{\mu\mu} \in (2,\ 2.5)(\mathrm{GeV}/c^2)$: intermediate-mass region,
- $M_{\mu\mu} \in (2.5,\ 4.3)(\mathrm{GeV}/c^2)$: charmonium region (J/$\psi$, Ψ'(2S)),
- $M_{\mu\mu} \in (4.3,\ 8.5)(\mathrm{GeV}/c^2)$: high-mass region dominated by DY process.

The corresponding $M_{\mu\mu}$ distribution, with contributions from different channels disentangled, is shown in Fig. 5.2 [105].[7]

[5]In Chapter 8, the analysis is limited to the TMD region with a q_{T} cut, intentionally excluding part of the phase space.

[6]For Drell–Yan events, Q refers to the dimuon invariant mass $M_{\mu\mu}$

[7]The contributions are determined from Monte Carlo simulations based on the PYTHIA8 event generator [126], with particle transport handled by `TGEANT` and data reconstruction performed using `CORAL`.

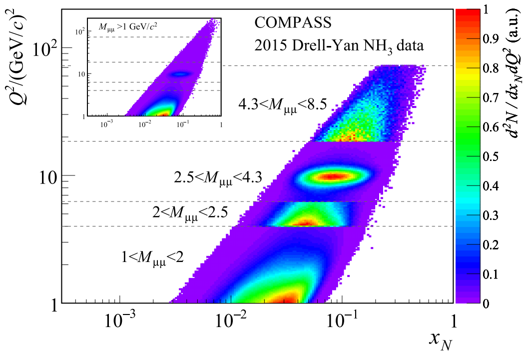

Figure 5.1: Kinematic coverage of the 2015 DY data in (x_{N}, Q^2) [105].

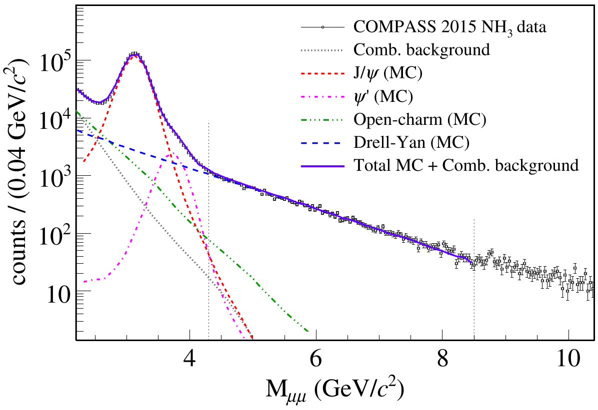

Figure 5.2: Invariant dimuon mass spectrum with background contributions estimated from MC simulations [105].

The background contribution reaches approximately 30% in the lowest bin ($M_{\mu\mu} \in (4.0, 4.36)$ GeV/c^2) due to the tail of the $\Psi'(2S)$ resonance, but gradually decreases to around 10% across the extended mass range. Recent COMPASS results indicate small, statistically insignificant asymmetries in resonance regions [94], with a precision of 0.5–2%, allowing the background to be treated as a dilution effect.

Two dimuon invariant mass intervals are defined[8]:

- Standard range: $M_{\mu\mu} \in (4.3, 8.5)$ GeV/c^2, which suppresses contributions from Υ resonances and limits the background below 4%.
- Extended range: $M_{\mu\mu} \in (4.0, 9.0)$ GeV/c^2, chosen to improve statistical precision and ensure consistency with the TSA analysis [94].

In both ranges, TMD factorization ($q_{\mathrm{T}} \ll M_{\mu\mu}$) is satisfied, and SIDIS and DY cross sections are dominated by valence u-quark nucleon TMD PDFs, providing favorable conditions to study the predicted Sivers sign change [129, 130].

5.3 Binning Strategy

The analysis is performed within specific kinematic ranges of four key variables describing DY process: x_π, x_{N}, x_{F}, and $M_{\mu\mu}$, as defined in Chapter 2. Additionally, a single integrated bin is considered to provide an overall reference for the differential studies.

The binning scheme is summarized in the Tabs 5.1a and 5.1b. The bin ranges are selected to ensure comparable statistics across binning intervals, which results in different binning for the standard and extended dimuon mass ranges. In particular, for $M_{\mu\mu}$, the first bin is defined to include all events below the previous lower mass limit, ensuring a consistent event distribution across the two mass ranges.

In Figs 5.3a and 5.3b, the distributions of specific powers of the transverse momentum q_{T}, used in the weighting procedure, are shown for the dimuon invariant mass

[8] In the following chapters, $M_{\mu\mu} \in (4.3, 8.5)$ GeV/c^2 is referred to as the standard range, and $M_{\mu\mu} \in (4.0, 9.0)$ GeV/c^2 as the extended range.

Table 5.1: Binning schemes for two dimuon pair mass ranges: (a) $M_{\mu\mu} \in (4.3,\, 8.5)$ GeV/c^2, (b) $M_{\mu\mu} \in (4.0,\, 9.0)$ GeV/c^2.

(a)

x_{N}	x_π	x_{F}	$M_{\mu\mu}$ (GeV/c^2)
0.00	0.00	-1.00	4.30
0.13	0.40	0.21	4.75
0.19	0.56	0.41	5.50
1.00	1.00	1.00	8.50

(b)

x_{N}	x_π	x_{F}	$M_{\mu\mu}$ (GeV/c^2)
0.00	0.00	-1.00	4.00
0.13	0.365	0.21	4.36
0.19	0.52	0.41	5.12
1.00	1.00	1.00	9.00

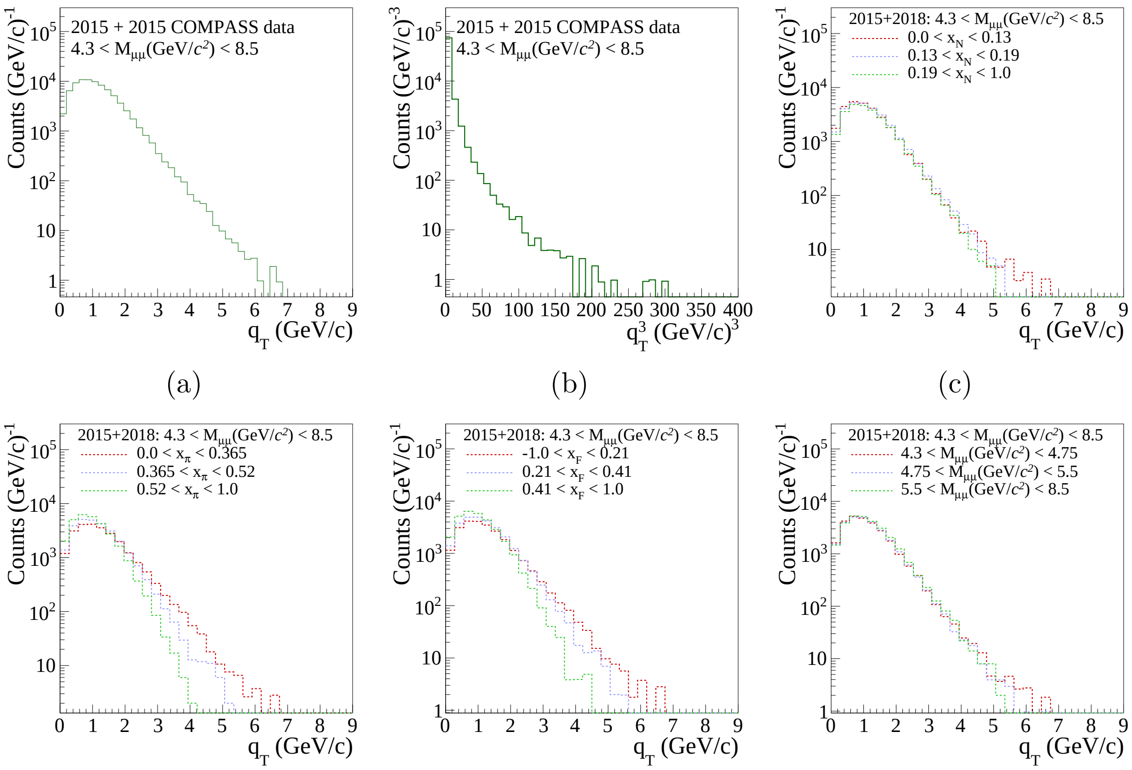

(a) (b) (c)

(d) (e) (f)

Figure 5.3: Transverse momentum distributions of dimuon pairs q_{T} for the mass range $M_{\mu\mu} \in (4.3,\, 8.5)$ GeV/c^2 after applying all analysis cuts: (a) q_{T} distribution normalized to event counts, (b) q_{T}^3 distribution used for pretzelosity weighting, (c) q_{T} in bins of x_{N}, (d) q_{T} in bins of x_π, (e) q_{T} in bins of x_F, (f) q_{T} in different $M_{\mu\mu}$ intervals.

range $M_{\mu\mu} \in (4.3,\, 8.5)$ GeV/c^2. Corresponding distributions for the extended mass range $M_{\mu\mu} \in (4.0,\, 9.0)$ GeV/c^2 are presented in Figs. 5.4a and 5.4b. In each interval, a small fraction of very high q_{T} values can influence the analysis by skewing the distribution and affecting the weighting procedure. The correlation between x_π and x_{N} is shown in Fig. 5.5a for the standard mass range and in Fig. 5.5b for the extended mass range, indicating that both the nucleon and pion are probed in the valence region.

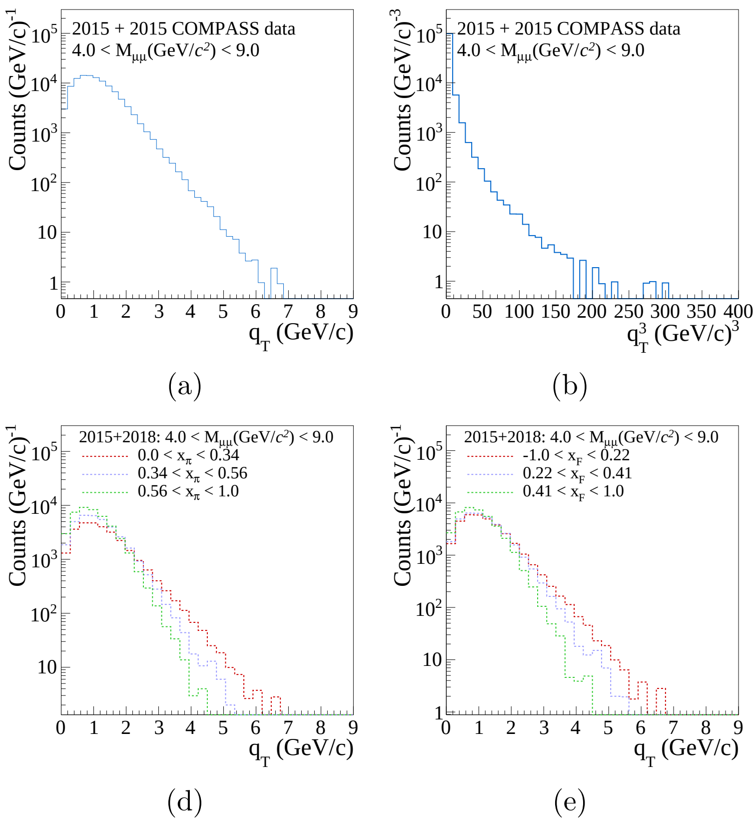

Figure 5.4: Transverse momentum distributions of dimuon pairs q_{T} for the mass range $M_{\mu\mu} \in (4.0,\, 9.0)$ GeV$/c^2$ after applying all analysis cuts: (a) q_{T} distribution normalized to event counts, (b) q_{T}^3 distribution used for pretzelosity weighting, (c) q_{T} in bins of x_{N}, (d) q_{T} in bins of x_π, (e) q_{T} in bins of x_F, (f) q_{T} in different $M_{\mu\mu}$ intervals.

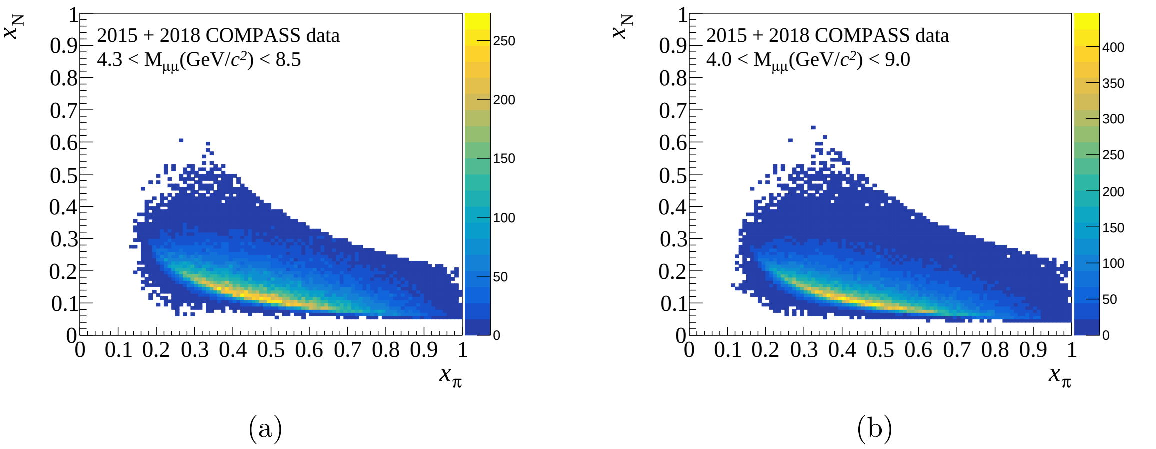

Figure 5.5: Correlation of the nucleon momentum fraction x_{N} with x_π after all analysis cuts for the two mass ranges: (a) $M_{\mu\mu} \in (4.3, 8.5)$ GeV$/c^2$, (b) $M_{\mu\mu} \in (4.0, 9.0)$ GeV$/c^2$.

5.4 Polarisation Dilution Effect

Determining the transverse component of the nucleon spin requires accounting for several factors, among which the target composition and its effective polarisation, expressed through the dilution factor, are of particular importance. During the 2015 and 2018 data taking, as described in Sec. 4.2, a polarised ammonia target is employed, in which only the protons can be polarised. For an NH_3, a naive estimate gives a value close to 3/17, reflecting the ratio of polarisable protons to the total number of nucleons.

The dilution factor which is actually used in the analysis is defined as [131, 132]:

$$f_{\mathrm{dil}} = \frac{n_{\mathrm{p}}^{\mathrm{tot}}}{\sum_{\mathrm{A}\in\mathrm{target}} n_{\mathrm{A}} \sigma_{\mathrm{A}}^{\mathrm{tot}}}, \tag{5.1}$$

where $n_{\mathrm{p}}^{\mathrm{tot}}$ is the total number of protons, n_{A} is the number of nucleons of type A in the target, and $\sigma_{A}^{\mathrm{tot}}$ denotes the total cross section of the considered process on nucleons of type A. The total cross sections, $\sigma_{\mathrm{A}}^{\mathrm{tot}}$, are computed using the parton-level Monte Carlo program MCFM [133], which is adapted to include a pion beam. The reliability of these calculations is confirmed through comparison with the E615 πW Drell–Yan cross section measurements [134]. To account for nuclear effects such as shadowing, antishadowing, and the EMC effect, PDF correction factors from the EKS group [135] are applied. These corrections, which describe modifications of parton densities in bound nucleons relative to free nucleons, are validated using the E772 πA Drell–Yan data [136].

5.4.1 Dilution Due to Cell Migration

Event migration between the target cells, resulting from event reconstruction, is accounted for by applying correction factors to the dilution factors of events originating from each cell. These corrections ensure that the measured asymmetries properly reflect the true event distribution. The correction factor for a given cell c is defined as

$$f_{\mathrm{mig}} = r_{c\to c} - r_{\bar{c}\to c}, \tag{5.2}$$

where $r_{c\to c}$ represents the fraction of events correctly reconstructed in their original cell, and $r_{\bar{c}\to c}$ denotes the fraction of events migrating from the other cell $\bar{c}$ due to misreconstruction. The correction factors are determined using a full COMPASS detector simulation performed with TGEANT MC. For the upstream cell, the correction factor is found to be 0.95, while for the downstream cell, it is 0.91. The dilution factor, corrected for cell migration effects, is defined as:

$$f = f_{\mathrm{dil}} \times f_{\mathrm{mig}}, \tag{5.3}$$

where f_{dil} is the nominal dilution factor defined in Eq. (5.1), and f_{mig} corrects for target cell migration. The resulting transverse nucleon polarization is calculated as:

$$\langle S_{\mathrm{T}} \rangle = \langle P \rangle \times \langle f \rangle, \tag{5.4}$$

where $\langle P \rangle$ denotes the average target polarization and $\langle f \rangle$ the average dilution factor. Both P and f are evaluated on an event-by-event basis and subsequently averaged over the entire data-taking period.

The analysis presented above serves as a preliminary step toward the extraction of asymmetries in the two dimuon mass ranges. The weighted asymmetries, discussed in Sec. 2.3, are determined using the so-called modified double ratio method, which is described in detail in the following chapter.

Chapter 6

Extraction of the Transverse Spin Asymmetries

Nothing in life is to be feared, it is only to be understood.
Now is the time to understand more, so that we may fear less.
— Maria Skłodowska–Curie

Spin-dependent effects are subtle, making precise measurements of azimuthal distributions challenging. Such measurements require careful characterization of the experimental acceptance, which depends on detector geometry and component efficiencies throughout the data-taking period. Determining acceptance corrections with high precision can introduce significant systematic uncertainties. To mitigate this, the extraction of asymmetries employs the so-called modified double ratio method, which takes advantage of frequent target polarization reversal and two oppositely polarized target cells. This method effectively suppresses effects from luminosity fluctuations and detector acceptance asymmetries by combining the number of unweighted and weighted events from both cells, as described in Chapter 4.

In this chapter, the extraction of weighted asymmetries from the measured observables is described. Sec. 6.1 introduces the key quantities for azimuthal asymmetries, Secs 6.2 and 6.3 present the full extraction procedure, and Sec. 6.4 discusses the differences between the two dimuon mass regions.

6.1 Azimuthal Asymmetry Observables

At leading twist, within the TMD framework, the measured cross section can be expressed as a sum of independent angular modulations, each associated with a distinct physical mechanism. By selecting appropriate integration variables, a given modulation can be isolated, enabling the direct extraction of individual asymmetry observables, such as the event counts determined.

For the parameterization of the azimuthal dependence of the Drell–Yan cross section (Eq. (2.6)), a set of azimuthal angles is introduced, constructed as linear combinations of φ_S and φ_CS:

$$\Phi = \varphi_\mathrm{S}, 2\varphi_\mathrm{CS}+\varphi_\mathrm{S}, 2\varphi_\mathrm{CS}-\varphi_\mathrm{S}, \text{and } \Xi = \begin{cases} \varphi_\mathrm{CS} & \text{if } \Phi = \varphi_\mathrm{S}, \\ \varphi_\mathrm{CS}+\varphi_\mathrm{S} & \text{if } \Phi = 2\varphi_\mathrm{CS}+\varphi_\mathrm{S}, \\ \varphi_\mathrm{CS}-\varphi_\mathrm{S} & \text{if } \Phi = 2\varphi_\mathrm{CS}-\varphi_\mathrm{S}. \end{cases} \tag{6.1}$$

These definitions are chosen to align the azimuthal structure of the experimental observables with the theoretical decomposition of the cross section. In particular, they ensure that each modulation can be treated independently when performing integrations over uncorrelated angular variables.

6.1.1 Event Counts and Azimuthal Integrals

To determine the azimuthal asymmetries in the DY process, the number of observed events is considered for each bin defined by Φ, target cell c, and subperiod p. The event count in these conditions is described by:

$$\begin{aligned} \frac{\mathrm{d}N_{cp}}{\mathrm{d}\Phi} = {} & L_{cp} \int \mathrm{d}^2 q_\mathrm{T} \int_0^1 \mathrm{d}x_\pi \int_0^1 \mathrm{d}x_\mathrm{N} \int_{-1}^1 \mathrm{d}\cos\theta_\mathrm{CS} \int_0^{2\pi} \mathrm{d}\Xi \\ & \times a_{cp}\Big(q_\mathrm{T}, x_\pi, x_\mathrm{N}, \cos\theta_\mathrm{CS}, \Phi, \Xi\Big) \frac{\mathrm{d}\sigma_\mathrm{DY}}{\mathrm{d}q_\mathrm{T}\,\mathrm{d}x_\pi\,\mathrm{d}x_\mathrm{N}\,\mathrm{d}\Xi\,\mathrm{d}\cos\theta_\mathrm{CS}\,\mathrm{d}\Phi}\,. \end{aligned} \tag{6.2}$$

where L_{cp} denotes the integrated luminosity for target cell c and subperiod p, and a_{cp} represents the corresponding detector acceptance. The variables x_π and x_N are the Bjorken scaling variables of the beam pion and target nucleon, respectively, θ_CS is the polar angle in the Collins–Soper frame.

Based on the angular definitions introduced in Eq. (6.1), three distinct cases are considered, corresponding to $\Phi = \varphi_\mathrm{S}$, $\Phi = 2\varphi_\mathrm{CS}+\varphi_\mathrm{S}$, and $\Phi = 2\varphi_\mathrm{CS}-\varphi_\mathrm{S}$, each paired with its respective conjugate variable Ξ. These cases are treated separately in the subsequent sections, allowing the integrations to be performed analytically for each configuration.

Integration over Ξ

Before integrating over the angle Ξ, the acceptance $a_{cp}(q_\mathrm{T}, x_\pi, x_\mathrm{N}, \cos\theta_\mathrm{CS}, \Phi, \Xi)$ is taken into account. Assuming the acceptance is flat in Ξ, its dependence on this angle can be neglected, allowing it to be factored out of the integral. The integration over Ξ is then performed for each modulation independently, with acceptance effects consistently included in the results.

Case 1: $\Phi = \varphi_\mathrm{S}$, $\Xi = \varphi_\mathrm{CS}$

$$\begin{aligned} \int_0^{2\pi} \mathrm{d}\Xi \frac{\mathrm{d}\sigma_\mathrm{DY}}{\mathrm{d}q_\mathrm{T}\,\mathrm{d}x_\pi\,\mathrm{d}x_\mathrm{N}\,\mathrm{d}\Xi\,\mathrm{d}\cos\theta_\mathrm{CS}\,\mathrm{d}\Phi} = {} & C_0 \Big\{ 2\pi F_\mathrm{U}^1 + 2|\boldsymbol{S}_\mathrm{T}|\pi F_\mathrm{T}^{\sin\Phi}\sin\Phi \\ & + 2\pi\cos^2\theta_\mathrm{CS}\left(F_\mathrm{U}^1 + |\boldsymbol{S}_\mathrm{T}|F_\mathrm{T}^{\sin\Phi}\sin\Phi\right) \\ & + \sin^2\theta_\mathrm{CS}\Big(F_\mathrm{U}^{\cos(2\Xi)} + |\boldsymbol{S}_\mathrm{T}|\,F_\mathrm{T}^{\sin(2\Xi+\Phi)} \\ & + |\boldsymbol{S}_\mathrm{T}|\,F_\mathrm{T}^{\sin(2\Xi-\Phi)}\Big)\Big\} \end{aligned} \tag{6.3}$$

Case 2: $\Phi = 2\varphi_{\mathrm{CS}} + \varphi_{\mathrm{S}}$, $\Xi = \varphi_{\mathrm{CS}} + \varphi_{\mathrm{S}}$

$$
\begin{aligned}
\int_0^{2\pi} \mathrm{d}\Xi \frac{\mathrm{d}\sigma_{\mathrm{DY}}}{\mathrm{d}q_{\mathrm{T}}\,\mathrm{d}x_\pi\,\mathrm{d}x_{\mathrm{N}}\,\mathrm{d}\Xi\,\mathrm{d}\cos\theta_{\mathrm{CS}}\,\mathrm{d}\Phi} = \frac{1}{2}C_0 \Big\{ & 4\pi F_{\mathrm{U}}^1 + 4\pi|\boldsymbol{S}_{\mathrm{T}}|F_{\mathrm{T}}^{\sin(\Phi)} \sin\Phi \sin^2\theta_{\mathrm{CS}} \\
& + 2\sin(2\pi)\sin^2\theta_{\mathrm{CS}} F_{\mathrm{U}}^{\cos(2\Phi-2\Xi)} \cos(2\Phi - 2\pi) \\
& - 2|\boldsymbol{S}_{\mathrm{T}}|\sin(2\pi) F_{\mathrm{T}}^{\sin(2\Xi-\Phi)} \sin(\Phi - 2\pi) \\
& + \cos^2\theta_{\mathrm{CS}} \left[4\pi F_{\mathrm{U}}^1 - 2\sin(2\pi) F_{\mathrm{T}}^{\sin(2\Xi-\Phi)} \sin(\Phi - 2\pi)\right] \\
& + 2\sin(2\pi)|\boldsymbol{S}_{\mathrm{T}}|\sin^2\theta_{\mathrm{CS}} F_{\mathrm{T}}^{\sin(3\Phi-4\Xi)} \sin(3\Phi - 4\pi) \Big\}.
\end{aligned} \tag{6.4}
$$

Case 3: $\Phi = 2\varphi_{\mathrm{CS}} - \varphi_{\mathrm{S}}$, $\Xi = \varphi_{\mathrm{CS}} - \varphi_{\mathrm{S}}$

$$
\begin{aligned}
\int_0^{2\pi} \mathrm{d}\Xi \frac{\mathrm{d}\sigma_{\mathrm{DY}}}{\mathrm{d}q_{\mathrm{T}}\,\mathrm{d}x_\pi\,\mathrm{d}x_{\mathrm{N}}\,\mathrm{d}\Xi\,\mathrm{d}\cos\theta_{\mathrm{CS}}\,\mathrm{d}\Phi} = \frac{1}{2}C_0 \Big\{ & 4\pi F_{\mathrm{U}}^1 + 4\pi|\boldsymbol{S}_{\mathrm{T}}|F_{\mathrm{T}}^{\sin(\Phi)} \sin\Phi \sin^2\theta_{\mathrm{CS}} \\
& + 2\sin(2\pi)\sin^2\theta_{\mathrm{CS}} F_{\mathrm{U}}^{\cos(2\Phi-2\Xi)} \cos(2\Phi - 2\pi) \\
& + 2|\boldsymbol{S}_{\mathrm{T}}|\sin(2\pi) F_{\mathrm{T}}^{\sin(\Phi-2\Xi)} \sin(\Phi - 2\pi) \\
& + \cos^2\theta_{\mathrm{CS}} \left[4\pi F_{\mathrm{U}}^1 - 2\sin(2\pi) F_{\mathrm{T}}^{\sin(\Phi-2\Xi)} \sin(\Phi - 2\pi)\right] \\
& + 2\sin(2\pi)|\boldsymbol{S}_{\mathrm{T}}|\sin^2\theta_{\mathrm{CS}} F_{\mathrm{T}}^{\sin(3\Phi-4\Xi)} \sin(3\Phi - 4\pi) \Big\}
\end{aligned} \tag{6.5}
$$

The right-hand sides of Eqs (6.3–6.5) contain terms with $\sin(2\pi) = 0$.[1] Consequently, all contributions involving linear combinations of Ξ and Φ vanish, reducing the expressions to the following simplified form:

$$
\begin{aligned}
& \int_0^{2\pi} \mathrm{d}\Xi \frac{\mathrm{d}\sigma_{\mathrm{DY}}}{\mathrm{d}q_{\mathrm{T}}\,\mathrm{d}x_\pi\,\mathrm{d}x_{\mathrm{N}}\,\mathrm{d}\Xi\,\mathrm{d}\cos\theta_{\mathrm{CS}}\,\mathrm{d}\Phi} = \\
& \qquad 2\pi C_0 \left\{(1+\cos^2\theta_{\mathrm{CS}})F_{\mathrm{U}}^1 + |\boldsymbol{S}_{\mathrm{T}}|F_{\mathrm{T}}^{\sin(\Phi)}(1 \pm \cos^2\theta_{\mathrm{CS}})\sin\Phi\right\},
\end{aligned} \tag{6.6}
$$

where $1 + \cos^2\theta_{\mathrm{CS}}$ applies for $\Phi = \varphi_{\mathrm{S}}$, and $1 - \cos^2\theta_{\mathrm{CS}}$ for $\Phi = 2\varphi_{\mathrm{CS}} \pm \varphi_{\mathrm{S}}$.

After performing the integration over Ξ, the expression for the number of events reduces to:

$$
\begin{aligned}
\frac{\mathrm{d}N_{cp}}{\mathrm{d}\Phi} = & 2\pi C_0 L_{cp} \int \mathrm{d}^2 q_{\mathrm{T}} \int_0^1 \mathrm{d}x_\pi \int_0^1 \mathrm{d}x_{\mathrm{N}} \int_{-1}^1 \mathrm{d}\cos\theta_{\mathrm{CS}}\, a_{cp}(q_{\mathrm{T}}, x_\pi, x_{\mathrm{N}}, \cos\theta_{\mathrm{CS}}, \Phi) \\
& \times \left[(1+\cos^2\theta_{\mathrm{CS}})F_{\mathrm{U}}^1 + |\boldsymbol{S}_{\mathrm{T}}|F_{\mathrm{T}}^{\sin(\Phi)}(1 \pm \cos^2\theta_{\mathrm{CS}})\sin\Phi\right].
\end{aligned} \tag{6.7}
$$

Integration over $\cos\theta_{\mathrm{CS}}$

The acceptance a_{cp} generally depends on multiple kinematic variables, including x_π, x_{N}, the polar angle $\cos\theta_{\mathrm{CS}}$, and the azimuthal angle Φ. In order to simplify the

[1] These terms are explicitly included in the equations to ensure clarity in the reasoning.

integration over $\cos\theta_{\mathrm{CS}}$, it is commonly assumed that the acceptance can be factorized into separate functions of $\cos\theta_{\mathrm{CS}}$ and the remaining variables, i.e.,

$$a_{cp}(q_{\mathrm{T}}, x_\pi, x_{\mathrm{N}}, \cos\theta_{\mathrm{CS}}, \Phi) = a_{cp}(q_{\mathrm{T}}, x_\pi, x_{\mathrm{N}}, \Phi) \times a_{cp}(\cos\theta_{\mathrm{CS}}). \tag{6.8}$$

This factorization implies that any correlations between $\cos\theta_{\mathrm{CS}}$ and the other variables in the acceptance are negligible or sufficiently small.

In the presence of detector acceptance, angular functions $g(\cos\theta_{\mathrm{CS}}) = 1 \pm \cos\theta_{\mathrm{CS}}$ are integrated over $\cos\theta_{\mathrm{CS}}$. This leads to the introduction of an acceptance-weighted average, defined as:

$$\langle g(\cos\theta_{\mathrm{CS}})\rangle \equiv \int_{-1}^{1} \mathrm{d}\cos\theta_{\mathrm{CS}} a_{cp}(\cos\theta_{\mathrm{CS}}) g(\cos\theta_{\mathrm{CS}}), \tag{6.9}$$

which effectively incorporates acceptance effects into the angular term and simplifies subsequent expressions involving such integrals.

With this notation, the expression for $\mathrm{d}N_{cp}/\mathrm{d}\Phi$ becomes:

$$\begin{aligned}\frac{\mathrm{d}N_{cp}}{\mathrm{d}\Phi} = 2\pi C_0 L_{cp} \int \mathrm{d}^2 q_{\mathrm{T}} \int_0^1 \mathrm{d}x_\pi \int_0^1 \mathrm{d}x_{\mathrm{N}}\ a_{cp}(q_{\mathrm{T}}, x_\pi, x_{\mathrm{N}}, \Phi)\Big[&\langle 1+\cos^2\theta_{\mathrm{CS}}\rangle F_{\mathrm{U}}^{1} \\ &+ |\boldsymbol{S}_{\mathrm{T}}| F_{\mathrm{T}}^{\sin\Phi} \langle 1 \pm \cos^2\theta_{\mathrm{CS}}\rangle \sin\Phi\Big].\end{aligned} \tag{6.10}$$

Integration over q_{T}

At higher values of q_{T}, the acceptance exhibits non-uniformity, increasing due to bin-to-bin migration effects arising from the finite resolution in q_{T}. For simplicity, the acceptance is treated as constant in q_{T}, leading to the expression:

$$\begin{aligned}\frac{\mathrm{d}N_{cp}}{\mathrm{d}\Phi} = 2\pi C_0 L_{cp} \int_0^1 \mathrm{d}x_\pi \int_0^1 \mathrm{d}x_{\mathrm{N}}\, a_{cp}(x_{\mathrm{N}}, x_\pi, \Phi)\Big[&\langle 1+\cos^2\theta_{\mathrm{CS}}\rangle F_{\mathrm{U}}^{1} \\ &+ |\boldsymbol{S}_{\mathrm{T}}| F_{\mathrm{T}}^{\sin\Phi} \langle 1 \pm \cos^2\theta_{\mathrm{CS}}\rangle \sin\Phi\Big].\end{aligned} \tag{6.11}$$

Integration over x_π and x_{N}

Given the limited variation of the kinematic variables x_π and x_{N}, the acceptance is approximated as constant. This approximation simplifies the integration over these variables, resulting in the following final expression:

$$\frac{\mathrm{d}N_{cp}}{\mathrm{d}\Phi} = 2\pi C_0 L_{cp}\, a_{cp}(\langle x_{\mathrm{N}}\rangle, \langle x_\pi\rangle, \Phi)\Big[\langle 1+\cos^2\theta_{\mathrm{CS}}\rangle F_{\mathrm{U}}^{1} + |\boldsymbol{S}_{\mathrm{T}}| F_{\mathrm{T}}^{\sin\Phi} \langle 1 \pm \cos^2\theta_{\mathrm{CS}}\rangle \sin\Phi\Big]. \tag{6.12}$$

Here, the structure functions F_{U}^{1} and $F_{\mathrm{T}}^{\sin\Phi}$ are evaluated at the mean values of the kinematic variables within each analysis bin. For consistency with the notation introduced in the introduction, they can be expressed in a compact form as $F_{\mathrm{X}}^{\mathrm{Y}}$, defined as:

$$F_{\mathrm{X}}^{\mathrm{Y}} \equiv F_{\mathrm{X}}^{\mathrm{Y}}\Big(\langle x_{\mathrm{N}}\rangle, \langle x_\pi\rangle\Big). \tag{6.13}$$

As introduced in Eq. (2.51) (Chapter 2) and recalled here for clarity, in the single-polarised Drell–Yan case the index X denotes either the transverse-polarisation or unpolarised contribution of the nucleon to the cross section, while Y specifies the angular modulation. This compact notation, which retains the dependence on the bin-averaged kinematic variables, is adopted throughout the following discussion for brevity.

6.1.2 Event Counts weighted by Dilution and Kinematic Factors

In the previous section, the analysis was based on simple (unweighted) event counts. However, it is also possible and often essential to apply weights to individual events. A crucial weighting factor employed in the subsequent analysis combines the dilution factor $f_{cp}(x_\pi, x_\mathrm{N})$ with a kinematic factor $D = 1 \pm \cos^2\theta_\mathrm{CS}$.

For convenience, this combined factor will be denoted as:

$$W_\mathrm{Y}(f_{cp}D) = f_{cp}(x_\pi, x_\mathrm{N}) \times D. \tag{6.14}$$

The specific form of the kinematic factor depends on the azimuthal modulation under consideration:

$$D = \begin{cases} 1 + \cos^2\theta_\mathrm{CS} & \text{for } \Phi = \varphi_S, \\ 1 - \cos^2\theta_\mathrm{CS} & \text{for } \Phi = 2\varphi_\mathrm{CS} \pm \varphi_S. \end{cases} \tag{6.15}$$

In the following sections, the structure functions will be modified accordingly by these weighting factors. In order to clearly identify weighted functions, a superscript denoting the corresponding weight will be used, $F_\mathrm{X}^{\mathrm{Y}W_\mathrm{Y}}$, distinguishing them from unweighted functions.

Integration over Ξ

The weighting factors introduced in Eqs (6.14) and (6.15), are independent of Ξ. As a result, the integration over this angle follows the same procedure as that used for the unweighted event count presented in Sec. 6.1.1. Consequently, the integrals take the same form as given in Eqs (6.3–6.5), modified only by the presence of the weighting factors. The presence of the $\sin(2\pi)$ term causes most contributions to vanish after integration, ensuring that the resulting expression closely parallels that of Eq. (6.7):

$$\begin{aligned} \int_0^{2\pi} \mathrm{d}\Xi \frac{\mathrm{d}\sigma_\mathrm{DY}^{W_\mathrm{Y}(f_{cp}D)}}{\mathrm{d}q_\mathrm{T}\,\mathrm{d}x_\pi\,\mathrm{d}x_\mathrm{N}\,\mathrm{d}\Xi\,\mathrm{d}\cos\theta_\mathrm{CS}\,\mathrm{d}\Phi} &= 2\pi C_0 L_{cp} \int \mathrm{d}^2q_\mathrm{T} \int_0^1 \mathrm{d}x_\pi \int_0^1 \mathrm{d}x_\mathrm{N} \int_{-1}^1 \mathrm{d}\cos\theta_\mathrm{CS} \\ &\times f_{cp}(x_\pi, x_\mathrm{N})\,(1 \pm \cos^2\theta_\mathrm{CS}) \\ &\times a_{cp}(q_\mathrm{T}, x_\pi, x_\mathrm{N}, \cos\theta_\mathrm{CS}, \Phi) \\ &\times \Big[(1 + \cos^2\theta_\mathrm{CS})\,F_\mathrm{U}^{1\,W_\mathrm{Y}(f_{cp}D)} \\ &+ |\boldsymbol{S}_\mathrm{T}|\,F_\mathrm{T}^{\sin\Phi\,W_\mathrm{Y}(f_{cp}D)}\,(1 \pm \cos^2\theta_\mathrm{CS})\,\sin\Phi\Big]. \end{aligned}$$

Integration over $\cos\theta_\mathrm{CS}$, q_T, x_N, and x_π

The inclusion of additional weighting factors introduces a higher level of complexity to the integration strategy. In particular, the modulation-dependent form of the kinematic factor $D = 1 \pm \cos\theta_\mathrm{CS}$, as presented in Eq. (6.15), takes two distinct forms depending on the modulation, necessitating separate integration treatments for each case. Consequently, the analysis is divided into separate calculations corresponding to the modulations φ_S and $2\varphi_\mathrm{CS} \pm \varphi_\mathrm{S}$.

It is important to emphasize that the acceptance assumptions outlined in Eqs (6.8) and (6.9) remain valid, since the weighting procedure does not alter these characteristics. In particular, the acceptance retains its flat behavior in Ξ and continues to factorize into independent components, allowing the previously established simplifications to hold.

Case 1: $\Phi = \varphi_{\mathrm{S}}$

Here, applying the weights f_{cp} and $1+\cos^2\theta_{\mathrm{CS}}$ yields the final form of the weighted event count for the φ_S modulation:

$$\begin{aligned}
\frac{\mathrm{d}N_{cp}^{W_{\mathrm{Y}}(f_{cp}D)}}{\mathrm{d}\Phi} &= 2\pi C_0 L_{cp}\int \mathrm{d}^2 q_{\mathrm{T}}\int_0^1 \mathrm{d}x_\pi \int_0^1 \mathrm{d}x_{\mathrm{N}}\int_{-1}^1 \mathrm{d}\cos\theta_{\mathrm{CS}}\\
&\times f_{cp}(x_\pi x_{\mathrm{N}})\, a_{cp}(x_\pi x_{\mathrm{N}},\cos\theta_{\mathrm{CS}},\varphi_{\mathrm{S}})\\
&\times\left[(1+\cos^2\theta_{\mathrm{CS}})^2 F_{\mathrm{U}}^{1W_{\mathrm{Y}}(f_{cp}D)} + |\boldsymbol{S}_{\mathrm{T}}| F_{\mathrm{T}}^{\sin(\varphi_{\mathrm{S}})W_{\mathrm{Y}}(f_{cp}D)}(1+\cos^2\theta_{\mathrm{CS}})^2\sin\varphi_{\mathrm{S}}\right]\\
&= 2\pi C_0 L_{cp}\, f_{cp}(\langle x_{\mathrm{N}}\rangle,\langle x_\pi\rangle)\, a_{cp}(\langle x_{\mathrm{N}}\rangle,\langle x_\pi\rangle,\varphi_{\mathrm{S}})\,\langle(1+\cos^2\theta_{\mathrm{CS}})^2\rangle\\
&\times\left[F_{\mathrm{U}}^{1W_{\mathrm{Y}}(f_{cp}D)} + |\boldsymbol{S}_{\mathrm{T}}| F_{\mathrm{T}}^{\sin(\varphi_{\mathrm{S}})W_{\mathrm{Y}}(f_{cp}D)}\sin\varphi_{\mathrm{S}}\right].
\end{aligned} \tag{6.16}$$

Case 2: $\Phi = 2\varphi_{\mathrm{CS}} \pm \varphi_{\mathrm{S}}$

In contrast to the φ_S case, the $2\varphi_{\mathrm{CS}} \pm \phi_S$ modulation introduces the factor $1-\cos^2\theta_{\mathrm{CS}}$, which makes the calculation considerably more challenging. Accordingly, the integration is carried out in sequence, beginning with $\cos\theta_{\mathrm{CS}}$ followed by q_{T}, x_π and x_{N}.

$$\begin{aligned}
\frac{\mathrm{d}N_{cp}^{W_{\mathrm{Y}}(f_{cp}D)}}{\mathrm{d}\Phi} &= \int_{-1}^1 \mathrm{d}\cos\,\theta_{\mathrm{CS}}\,\frac{\mathrm{d}\sigma_{\mathrm{DY}}^{W_{\mathrm{Y}}(f_{cp}D)}}{\mathrm{d}q_{\mathrm{T}}\ \mathrm{d}x_\pi\ \mathrm{d}x_{\mathrm{N}}\ \mathrm{d}\cos\theta_{\mathrm{CS}}\ \mathrm{d}2\varphi_{\mathrm{CS}}\pm\varphi_{\mathrm{S}}}\\
&= \int_{-1}^1 \mathrm{d}\cos\,\theta_{\mathrm{CS}}\, a_{cp}(\cos\theta_{\mathrm{CS}})(1-\cos^2\theta_{\mathrm{CS}})\Big[(1+\cos^2\theta_{\mathrm{CS}})\,F_{\mathrm{U}}^{1W_{\mathrm{Y}}(f_{cp}D)}\\
&\quad+|\boldsymbol{S}_{\mathrm{T}}|\,F_{\mathrm{T}}^{\sin(2\varphi_{\mathrm{CS}}\pm\varphi_{\mathrm{S}})W_{\mathrm{Y}}(f_{cp}D)}\,(1-\cos^2\theta_{\mathrm{CS}})\,\sin(2\varphi_{\mathrm{CS}}\pm\varphi_{\mathrm{S}})\Big]\\
&= \int_{-1}^1 \mathrm{d}\cos\,\theta_{\mathrm{CS}}\, a_{cp}(\cos\theta_{\mathrm{CS}})\times\Big[(1-\cos^4\theta_{\mathrm{CS}})\,F_{\mathrm{U}}^{1W_{\mathrm{Y}}(f_{cp}D)}\\
&\quad+|\boldsymbol{S}_{\mathrm{T}}|\,(1-\cos^2\theta_{\mathrm{CS}})^2\,F_{\mathrm{T}}^{\sin(2\varphi_{\mathrm{CS}}\pm\varphi_{\mathrm{S}})W_{\mathrm{Y}}(f_{cp}D)}\,\sin(2\varphi_{\mathrm{CS}}\pm\varphi_{\mathrm{S}})\Big]\\
&= \langle 1-\cos^4\theta_{\mathrm{CS}}\rangle\,F_{\mathrm{U}}^{1W_{\mathrm{Y}}(f_{cp}D)}\\
&\quad+|\boldsymbol{S}_{\mathrm{T}}|\,\langle(1-\cos^2\theta_{\mathrm{CS}})^2\rangle\,F_{\mathrm{T}}^{\sin(2\varphi_{\mathrm{CS}}\pm\varphi_{\mathrm{S}})W_{\mathrm{Y}}(f_{cp}D)}\,\sin(2\varphi_{\mathrm{CS}}\pm\varphi_{\mathrm{S}})
\end{aligned} \tag{6.17}$$

Subsequently, the integrals over q_{T}, x_π, and x_{N} are evaluated using the same methodology as for unweighted event counts, yielding the following expression:

$$\begin{aligned}\frac{\mathrm{d}N_{cp}^{W_{\mathrm{Y}}(f_{cp}D)}}{\mathrm{d}\Phi} &= 2\pi C_0\, f_{cp}\Big(\langle x_{\mathrm{N}}\rangle, \langle x_\pi\rangle\Big)\, L_{cp}\, a_{cp}\Big(\langle x_{\mathrm{N}}\rangle, \langle x_\pi\rangle, 2\varphi_{\mathrm{CS}} \pm \varphi_{\mathrm{S}}\Big) \\ &\times \Big[\langle 1-\cos^4\theta_{\mathrm{CS}}\rangle\, F_{\mathrm{U}}^{1W_{\mathrm{Y}}(f_{cp}D)} \\ &+ |\boldsymbol{S}_{\mathrm{T}}|\,\langle (1-\cos^2\theta_{\mathrm{CS}})^2\rangle\, F_{\mathrm{T}}^{\sin(2\varphi_{\mathrm{CS}}\pm\varphi_{\mathrm{S}})\,W_{\mathrm{Y}}(f_{cp}D)}\,\sin\Big(2\varphi_{\mathrm{CS}}\pm\varphi_{\mathrm{S}}\Big)\Big].\end{aligned} \tag{6.18}$$

For convenience in subsequent calculations, let us define the following notations:

$$f_{cp}(\langle x_{\mathrm{N}}\rangle, \langle x_\pi\rangle) = f_{cp}, \quad a_{cp}(\langle x_{\mathrm{N}}\rangle, \langle x_\pi\rangle, \Phi) = a_{cp}(\Phi). \tag{6.19}$$

6.1.3 Event Counts Additionally Weighted by Transverse Momentum of Dimuon Pair

As described in Sec. 2.3, weighting by specific powers of the transverse momentum of the dilepton pair allows one to avoid the convolution of TMD PDFs in structure functions, reducing them to simple products. For this reason, a weighting procedure is applied to the event counts. The explicit form of the applied weights is given below:

$$W_{\mathrm{Y}}(q_{\mathrm{T}}) = \begin{cases} \frac{q_{\mathrm{T}}}{M_{\mathrm{N}}} & \text{for } \Phi = \varphi_{\mathrm{S}}, \\ \frac{q_{\mathrm{T}}^3}{2M_{\mathrm{N}}^2 M_\pi} & \text{for } \Phi = 2\varphi_{\mathrm{CS}} + \varphi_{\mathrm{S}}, \\ \frac{q_{\mathrm{T}}}{M_\pi} & \text{for } \Phi = 2\varphi_{\mathrm{CS}} - \varphi_{\mathrm{S}}. \end{cases} \tag{6.20}$$

The calculation of event counts follows the same procedure as in Secs. 6.1.1 and 6.1.2, but here the integration over the dimuon transverse momentum q_{T} is performed with the appropriate weight, yielding the weighted structure functions $F_{\mathrm{X}}^{\mathrm{Y}W_{\mathrm{Y}}(q_{\mathrm{T}})}$ and $F_{\mathrm{X}}^{\mathrm{Y}W_{\mathrm{Y}}(f_{cp}Dq_{\mathrm{T}})}$.

6.2 Modified Double Ratio Method

Having determined both the weighted and unweighted event counts, one can construct observables that serve as the foundation for the subsequent analysis. Among these, the modified double ratio method plays a central role. Originally developed in the context of SIDIS [137], this approach was later adapted for use in the Drell–Yan process. Due to methodological differences in distinct kinematic regions, the analysis is performed separately for two dimuon mass intervals.

The standard mass range, $M_{\mu\mu} \in (4.3, 8.5)\,\mathrm{GeV}/c^2$, features a high Drell–Yan signal purity (approximately 96%), allowing asymmetries to be extracted directly from the measured event counts without additional corrections.

In the extended mass range, $M_{\mu\mu} \in (4.0, 9.0)\,\mathrm{GeV}/c^2$, background contributions become non-negligible. In this case, each event is weighted by the dilution factor and the kinematic factor to account for these effects.

The primary advantage of the modified double ratio lies in its ability to suppress effects stemming from luminosity fluctuations and detector acceptance asymmetries.

This is achieved by combining the number of both unweighted and weighted events from two oppositely polarized target cells, c ($c = U, D$), over two subperiods, p ($p = 1, 2$), during which the target polarization is reversed (↑↓,↓↑). The modified double ratio is defined as

$$R^{\mathrm{Y}W_{\mathrm{Y}}} = \begin{cases} \dfrac{\Delta^{W_{\mathrm{Y}}(q_{\mathrm{T}})}}{\sqrt{\Sigma^{W_{\mathrm{Y}}(q_{\mathrm{T}})}\,\Sigma}} & \text{if } M_{\mu\mu} \in (4.3, 8.5)\ \mathrm{GeV}/c^2, \\ \dfrac{\Delta^{W_{\mathrm{Y}}(f_{cp}Dq_{\mathrm{T}})}}{\sqrt{\Sigma^{W_{\mathrm{Y}}(f_{cp}Dq_{\mathrm{T}})}\,\Sigma^{W_{\mathrm{Y}}(f_{cp}D)}}} & \text{if } M_{\mu\mu} \in (4.0, 9.0)\ \mathrm{GeV}/c^2. \end{cases} \tag{6.21}$$

Here, the quantities $\Delta^{W_{\mathrm{Y}}(w)}$ and $\Sigma^{W_{\mathrm{Y}}(w)}$ are defined as the difference and sum of weighted event products in the respective target cells and subperiods:

$$\begin{aligned} \Delta^{W_{\mathrm{Y}}(w)} &= N_{U1}^{W_{\mathrm{Y}}(w)} N_{D2}^{W_{\mathrm{Y}}(w)} - N_{U2}^{W_{\mathrm{Y}}(w)} N_{D1}^{W_{\mathrm{Y}}(w)}, \\ \Sigma^{W_{\mathrm{Y}}(w)} &= N_{U1}^{W_{\mathrm{Y}}(w)} N_{D2}^{W_{\mathrm{Y}}(w)} + N_{U2}^{W_{\mathrm{Y}}(w)} N_{D1}^{W_{\mathrm{Y}}(w)}, \quad \Sigma = N_{U1}N_{D2} + N_{U2}N_{D1}, \end{aligned} \tag{6.22}$$

where $w \in \{q_{\mathrm{T}}, f_{cp}D, f_{cp}Dq_{\mathrm{T}}\}$. $N_{U1}, N_{D2}, N_{U2}, N_{D1}$ denote the number of events in the respective target cells and subperiods, while the corresponding weighted sums $N_{U1}^{W_{\mathrm{Y}}(w)}, N_{D2}^{W_{\mathrm{Y}}(w)}, N_{U2}^{W_{\mathrm{Y}}(w)}, N_{D1}^{W_{\mathrm{Y}}(w)}$ are defined as integrals over the event distributions:

$$N_{cp} = \int \frac{\mathrm{d}N_{cp}}{\mathrm{d}\Phi}\,\mathrm{d}\Phi, \quad N_{cp}^{W_{\mathrm{Y}}(w)} = \int \frac{\mathrm{d}N_{cp}^{W_{\mathrm{Y}}(x)}}{\mathrm{d}\Phi}\,\mathrm{d}\Phi, \tag{6.23}$$

where the integral runs over the relevant phase space Φ for each target cell and subperiod.

To determine the statistical uncertainty, a covariance matrix is employed. The statistical uncertainty of the modified double ratio is given by:

$$\sigma^2_{R^{\mathrm{Y}W_{\mathrm{Y}}}} = \boldsymbol{\partial} R^{\mathrm{Y}W_{\mathrm{Y}}} \times \boldsymbol{\Sigma} \times \left(\boldsymbol{\partial} R^{\mathrm{Y}W_{\mathrm{Y}}}\right)^{\mathrm{T}}, \tag{6.24}$$

where $\boldsymbol{\partial} R^{\mathrm{Y}W_{\mathrm{Y}}}$ denotes the vector of partial derivatives of the modified double ratio with respect to the underlying event counts. In this case, it is an 8-component vector composed of the partial derivatives with respect to the four unweighted and four weighted event yields used in Eq. (6.21). The matrix $\boldsymbol{\Sigma}$ is the corresponding 8×8 covariance matrix, which accounts for statistical correlations between these event counts.

The covariance matrix $\boldsymbol{\Sigma}$ is defined as:

$$\boldsymbol{\Sigma} = \begin{bmatrix} \boldsymbol{\Sigma}_{U1}^{2\times2} & 0 & 0 & 0 \\ 0 & \boldsymbol{\Sigma}_{U2}^{2\times2} & 0 & 0 \\ 0 & 0 & \boldsymbol{\Sigma}_{D1}^{2\times2} & 0 \\ 0 & 0 & 0 & \boldsymbol{\Sigma}_{D2}^{2\times2} \end{bmatrix}. \tag{6.25}$$

This structure assumes that correlations exist only between weighted and unweighted events within the same target cell and subperiod, while event counts corresponding to different values of c and p are entirely independent. The calculation procedure is identical for both subperiods and target cells, making it convenient to introduce the cp index. The sub-matrices $\boldsymbol{\Sigma}_{cp}^{2\times2}$, corresponding to each target cell and subperiod

($cp = U1, U2, D1, D2$), are given by:

$$\boldsymbol{\Sigma}_{cp}^{2\times 2} = \begin{cases} \begin{bmatrix} \left(\sigma_{N_{cp}^{W_\Upsilon(w)}}\right)^2 & \mathrm{cov}(N_{cp}^{W_\Upsilon(w)}, N_{cp}) \\ \mathrm{cov}(N_{cp}, N_{cp}^{W_\Upsilon(w)}) & \left(\sigma_{N_{cp}}\right)^2 \end{bmatrix}, & \text{if } M_{\mu\mu} \in (4.3, 8.5)\ \mathrm{GeV}/c^2, \\ \\ \begin{bmatrix} \left(\sigma_{N_{cp}^{W_\Upsilon(w')}}\right)^2 & \mathrm{cov}(N_{cp}^{W_\Upsilon(w')}, N_{cp}^{W_\Upsilon(w)}) \\ \mathrm{cov}(N_{cp}^{W_\Upsilon(w)}, N_{cp}^{W_\Upsilon(w')}) & \left(\sigma_{N_{cp}^{W_\Upsilon(w)}}\right)^2 \end{bmatrix}, & \text{if } M_{\mu\mu} \in (4.0, 9.0)\ \mathrm{GeV}/c^2, \end{cases} \tag{6.26}$$

where $W_\Upsilon(w) = W_\Upsilon(f_{cp}D)$ and $W_\Upsilon(w') = W_\Upsilon(f_{cp}Dq_\mathrm{T})$.

The following relations define the variances and covariance used in the covariance matrix:

$$\begin{gathered} \left(\sigma_{N_{cp}^{W_\Upsilon(w)}}\right)^2 = \sum_i w_i^2, \quad \left(\sigma_{N_{cp}}\right)^2 = \sum_i 1_i = N_{cp} \\ \mathrm{cov}(N_{cp}, N_{cp}^{W_\Upsilon(w)}) = \sum_i 1_i \times w_i = N_{cp}^{W_\Upsilon(w)} \end{gathered} \tag{6.27}$$

Here, the index i runs over all events within a given angular bin Φ, and collected from a specific target cell c and subperiod p. A detailed derivation of these equations is provided in Appendix A.

6.3 Dependence of the Modified Double Ratio on Asymmetry

This section presents an examination of the relationship between the modified double ratio (Sec. 6.1) and the observable defined in Sec. 6.2. Since the connection between the measured modified double ratio and the underlying physical asymmetries depends on the dimuon mass range, the two cases are discussed separately in the following subsections.

The following assumptions underpin the analysis:

1. **Dilution factor ratio:**The ratio of the dilution factors between the two target cells does not vary across the subperiods:

$$\frac{f_{U1}}{f_{D1}} = \frac{f_{U2}}{f_{D2}} \quad \Rightarrow \quad f_{U1}f_{D2} = f_{U2}f_{D1} \tag{6.28}$$

2. **Luminosity ratio:** The combination of beam flux, b, and target effective length, l, does not change between subperiods:

$$L_{cp} = b_p l_c \Rightarrow L_{U1}L_{D2} = L_{U2}L_{D1} \tag{6.29}$$

3. **"Reasonable" assumption:** The ratio of acceptances between the upstream and downstream target cells remains constant across the two subperiods, expressed mathematically as

$$\frac{a_{U1}(\Phi)}{a_{D1}(\Phi)} = \frac{a_{U2}(\Phi)}{a_{D2}(\Phi)} \quad \Rightarrow \quad a_{U1}(\Phi)a_{D2}(\Phi) = a_{U2}(\Phi)a_{D1}(\Phi) \tag{6.30}$$

4. **Negligible Quadratic Contributions:** The squared term $F_{\mathrm{T}}^{\sin(\Phi)W}$ is assumed to be negligible compared to the linear ones

$$|\boldsymbol{S}_{\mathrm{T},cp}|^2 \left(F_{\mathrm{T}}^{\sin(\Phi)W_{\mathrm{Y}}}\right)^2 \ll 2|\boldsymbol{S}_{\mathrm{T},cp}|F_{\mathrm{U}}^{1W_{\mathrm{Y}}}F_{\mathrm{T}}^{\sin(\Phi)W_{\mathrm{Y}}} \tag{6.31}$$

6.3.1 Standard Mass Range

In the standard mass interval, events are either unweighted or weighted solely by powers of the transverse dimuon momentum q_{T}. It is reflected in the superscript of the modified structure function, denoted as $F_{\mathrm{X}}^{\mathrm{Y}W_{\mathrm{Y}}(q_{\mathrm{T}})}$.

Calculation for $\Phi = \varphi_{\mathrm{S}}$

Let us start with the expression for the product of event counts in the $U1$ and $D2$ cells:

$$\begin{aligned} N_{U1}N_{D2} =& 4\pi^2 C_0^2 L_{U1}L_{D2}a_{U1}a_{D2}\langle 1+\cos^2\theta_{\mathrm{CS}}\rangle^2 \\ & \left(F_{\mathrm{U}}^{1} + |\boldsymbol{S}_{\mathrm{T},U1}|F_{\mathrm{T}}^{\sin(\Phi)}\sin\Phi\right)\left(F_{\mathrm{U}}^{1} + |\boldsymbol{S}_{\mathrm{T},D2}|F_{\mathrm{T}}^{\sin(\Phi)}\sin\Phi\right). \end{aligned} \tag{6.32}$$

When considering the configuration with target polarizations pointing "up" ($\uparrow$, $cp = U1, D2$), and neglecting the quadratic term as justified in Eq. (6.31), the resulting expression for the product of event counts simplifies to:

$$\begin{aligned} N_{U1}N_{D2} =& 4\pi^2 C_0^2 L_{U1}L_{D2}a_{U1}a_{D2}\langle 1+\cos^2\theta_{\mathrm{CS}}\rangle^2 \Bigg[\left(F_{\mathrm{U}}^{1}\right)^2 \\ & + \left(|\boldsymbol{S}_{\mathrm{T},U1}| + |\boldsymbol{S}_{\mathrm{T},D2}|\right) F_{\mathrm{U}}^{1}F_{\mathrm{T}}^{\sin(\Phi)}\sin\Phi\Bigg]. \end{aligned} \tag{6.33}$$

In the reversed configuration, corresponding to $U2$ and $D1$, the polarizations are flipped (oriented "down", $\downarrow$). As a consequence, the azimuthal angle of the transverse spin vector, φ_{S}, is effectively shifted by π, which reverses the sign of the $\sin\Phi$ modulation:

$$\begin{aligned} N_{U2}N_{D1} =& 4\pi^2 C_0^2 L_{U1}L_{D2}a_{U1}a_{D2}\langle 1+\cos^2\theta_{\mathrm{CS}}\rangle^2 \Bigg[\left(F_{\mathrm{U}}^{1}\right)^2 \\ & - \left(|\boldsymbol{S}_{\mathrm{T},D1}| + |\boldsymbol{S}_{\mathrm{T},U2}|\right) F_{\mathrm{U}}^{1}F_{\mathrm{T}}^{\sin(\Phi)}\sin\Phi\Bigg]. \end{aligned} \tag{6.34}$$

The expressions for the weighted event count will resemble Eqs (6.33) and (6.34), nonetheless, there will be an additional term accounting for the weighting, denoted as

$F_{\mathrm{X}}^{\mathrm{Y}W_{\mathrm{Y}}(q_{\mathrm{T}})}$. The $\Delta^{W_{\mathrm{Y}}(q_{\mathrm{T}})}$ takes the form:

$$
\begin{aligned}
N_{U2}^{W_{\mathrm{Y}}(q_{\mathrm{T}})}N_{D1}^{W_{\mathrm{Y}}(q_{\mathrm{T}})} - N_{U1}^{W_{\mathrm{Y}}(q_{\mathrm{T}})}N_{D2}^{W_{\mathrm{Y}}(q_{\mathrm{T}})} = {} & 4\pi^2 C_0^2 \langle (1+\cos^2\theta_{\mathrm{CS}})^2\rangle \\
& \Bigg\{ \Big(L_{U1}L_{D2}a_{U1}a_{D2} - L_{U2}L_{D1}a_{U2}a_{D1}\Big)\Big(F_{\mathrm{U}}^{1W_{\mathrm{Y}}(q_{\mathrm{T}})}\Big)^2 \\
& + \Big(L_{U1}L_{D2}a_{U1}a_{D2} + L_{U2}L_{D1}a_{U2}a_{D1}\Big) \\
& \quad \times \Bigg[\Big(|\boldsymbol{S}_{\mathrm{T},U2}| + |\boldsymbol{S}_{\mathrm{T},D1}| + |\boldsymbol{S}_{\mathrm{T},U1}| + |\boldsymbol{S}_{\mathrm{T},D2}|\Big) \\
& \quad \times F_{\mathrm{U}}^{1W_{\mathrm{Y}}(q_{\mathrm{T}})} F_{\mathrm{T}}^{\sin(\Phi)W_{\mathrm{Y}}(q_{\mathrm{T}})} \sin\Phi \Bigg]\Bigg\}.
\end{aligned}
\tag{6.35}
$$

At this point, all assumptions introduced at the beginning of Sec.6.3, namely Eq.(6.29) and Eq. (6.30), are applied. This leads to the following simplified form of the equations:

$$
\begin{aligned}
N_{U2}^{W_{\mathrm{Y}}(q_{\mathrm{T}})}N_{D1}^{W_{\mathrm{Y}}(q_{\mathrm{T}})} - N_{U1}^{W_{\mathrm{Y}}(q_{\mathrm{T}})}N_{D2}^{W_{\mathrm{Y}}(q_{\mathrm{T}})} = {} & 4\pi^2 C_0^2 b_1 b_2 l_U l_D a_{D1} a_{D2} \\
& \times \Bigg[(|\boldsymbol{S}_{\mathrm{T},U2}| + |\boldsymbol{S}_{\mathrm{T},D1}| + |\boldsymbol{S}_{\mathrm{T},U1}| + |\boldsymbol{S}_{\mathrm{T},D2}|) \\
& \times \langle 1+\cos^2\theta_{\mathrm{CS}}\rangle^2 F_{\mathrm{U}}^{1W_{\mathrm{Y}}(q_{\mathrm{T}})} F_{\mathrm{T}}^{\sin(\Phi)W_{\mathrm{Y}}(q_{\mathrm{T}})} \sin\Phi \Bigg].
\end{aligned}
\tag{6.36}
$$

For the weighted case, the sum of event counts is given by:

$$
N_{U2}^{W_{\mathrm{Y}}(q_{\mathrm{T}})}N_{D1}^{W_{\mathrm{Y}}(q_{\mathrm{T}})} + N_{U1}^{W_{\mathrm{Y}}(q_{\mathrm{T}})}N_{D2}^{W_{\mathrm{Y}}(q_{\mathrm{T}})} = 8\pi^2 C_0^2 b_1 b_2 l_U l_D a_{D1} a_{D2} \Big(\langle 1+\cos^2\theta_{\mathrm{CS}}\rangle F_{\mathrm{U}}^{1W_{\mathrm{Y}}(q_{\mathrm{T}})}\Big)^2. \tag{6.37}
$$

For the unweighted case, the corresponding sum is:

$$
N_{U2}N_{D1} + N_{U1}N_{D2} = 8\pi^2 C_0^2 b_1 b_2 l_U l_D a_{D1} a_{D2} \Big(\langle 1+\cos^2\theta_{\mathrm{CS}}\rangle F_{\mathrm{U}}^{1}\Big)^2. \tag{6.38}
$$

If the polarization differences between the cells and subperiods are negligible with respect to the polarization-independent term, the modified response function can be expressed as:

$$
R^{\mathrm{Y}W_{\mathrm{Y}}(q_{\mathrm{T}})}(\Phi) = (|\boldsymbol{S}_{\mathrm{T},U2}| + |\boldsymbol{S}_{\mathrm{T},D1}| + |\boldsymbol{S}_{\mathrm{T},U1}| + |\boldsymbol{S}_{\mathrm{T},D2}|) \frac{F_{\mathrm{T}}^{\sin(\Phi)W_{\mathrm{Y}}(q_{\mathrm{T}})}}{F_{\mathrm{U}}^{1}} \sin\Phi. \tag{6.39}
$$

Calculation for $\Phi = 2\varphi_{\mathrm{CS}} \pm \varphi_{\mathrm{S}}$

The product of event counts in the $U1$ and $D2$ cells is given by:

$$
\begin{aligned}
N_{U1}N_{D2} = 4\pi^2 C_0^2 L_{U1}L_{D2}a_{U1}a_{D2} \Bigg[& \Big(\langle 1+\cos^2\theta_{\mathrm{CS}}\rangle F_{\mathrm{U}}^{1}\Big)^2 \\
& + (|\boldsymbol{S}_{\mathrm{T},U1}| + |\boldsymbol{S}_{\mathrm{T},D2}|)\, F_{\mathrm{U}}^{1} F_{\mathrm{T}}^{\sin(\Phi)} \langle 1+\cos^2\theta_{\mathrm{CS}}\rangle \langle 1-\cos^2\theta_{\mathrm{CS}}\rangle \sin\Phi \Bigg].
\end{aligned}
\tag{6.40}
$$

$$\begin{aligned} N_{U2}N_{D1} = 4\pi^2 C_0^2 L_{U1} L_{D2} a_{U1} a_{D2} \Bigg[& \left(\langle 1+\cos^2\theta_{\rm CS}\rangle F_{\rm U}^{1} \right)^2 \\ & - \left(|\boldsymbol{S}_{{\rm T},D1}| + |\boldsymbol{S}_{{\rm T},U2}| \right) F_{\rm U}^{1} F_{\rm T}^{\sin(\Phi)} \langle 1+\cos^2\theta_{\rm CS}\rangle \langle 1-\cos^2\theta_{\rm CS}\rangle \sin\Phi \Bigg]. \end{aligned} \tag{6.41}$$

As previously stated, the expressions for the weighted event count will resemble Eq. (6.40) and Eq. (6.41) with an additional term accounting for the weighting, denoted as $F_{\rm X}^{{\rm Y}W_{\rm Y}(q_{\rm T})}$. Using assumptions stated in Eqs(6.29– (6.31)), individual factors appearing in Eq. (6.21) for this modulation are as follows:

$$\begin{aligned} N_{U2}^{W_{\rm Y}(q_{\rm T})} N_{D1}^{W_{\rm Y}(q_{\rm T})} - N_{U1}^{W_{\rm Y}(q_{\rm T})} N_{D2}^{W_{\rm Y}(q_{\rm T})} = & \; 4\pi^2 C_0^2 b_1 b_2 l_U l_D a_{D1} a_{D2} \\ & \times \Bigg[\left(|\boldsymbol{S}_{{\rm T},U2}| + |\boldsymbol{S}_{{\rm T},D1}| + |\boldsymbol{S}_{{\rm T},U1}| + |\boldsymbol{S}_{{\rm T},D2}| \right) \\ & \times \langle 1+\cos^2\theta_{\rm CS}\rangle \langle 1-\cos^2\theta_{\rm CS}\rangle \\ & \times F_{\rm U}^{1W_{\rm Y}(q_{\rm T})} F_{\rm T}^{\sin(\Phi)W_{\rm Y}(q_{\rm T})} \sin\Phi \Bigg]. \end{aligned} \tag{6.42}$$

The formulas for both weighted and unweighted sums of products remain unchanged and are represented as indicated in Eq. (6.38) and Eq. (6.37). The final formula could be expressed as:

$$R^{{\rm Y}W_{\rm Y}(q_{\rm T})}(\Phi) = \left(|\boldsymbol{S}_{{\rm T},U2}| + |\boldsymbol{S}_{{\rm T},D1}| + |\boldsymbol{S}_{{\rm T},U1}| + |\boldsymbol{S}_{{\rm T},D2}| \right) \frac{\langle 1-\cos^2\theta_{\rm CS}\rangle}{\langle 1+\cos^2\theta_{\rm CS}\rangle} \frac{F_{\rm T}^{\sin(\Phi)W_{\rm Y}(q_{\rm T})}}{F_{\rm U}^{1}} \sin\Phi. \tag{6.43}$$

6.3.2 Extended Mass Range

The procedures used to determine the modified double ratio in the extended mass interval are analogous to those applied in the standard mass range. However, in this case, events are not only weighted by $q_{\rm T}$ but also diluton factor f_{cp} and kinematic factor $D = 1 \pm \cos^2\theta_{\rm CS}$ which leads to more complicated formulas for the final modified double ratio.

Calculation for $\Phi = \varphi_{\rm S}$

The analysis proceeds under the assumption of no variation in the dilution factor between subperiods, as defined in Eq. (6.28):

$$\begin{aligned} N_{U1}^{W_{\rm Y}(f_{cp}D)} N_{D2}^{W_{\rm Y}(f_{cp}D)} = 4\pi^2 C_0^2 f_{U1} f_{D2} L_{U1} L_{D2} a_{U1} a_{D2} \langle (1+\cos^2\theta_{\rm CS})^2 \rangle^2 \Bigg\{ & \left(F_{\rm U}^{1W_{\rm Y}(f_{cp}D)} \right)^2 + \\ & \left(|\boldsymbol{S}_{{\rm T},D1}| + |\boldsymbol{S}_{{\rm T},D2}| \right) F_{\rm U}^{1W_{\rm Y}(f_{cp}D)} F_{\rm T}^{\sin(\Phi)W_{\rm Y}(f_{cp}D)} \sin\Phi \Bigg\}. \end{aligned} \tag{6.44}$$

As before, in the scenario where it is polarised downward, such as with $cp = U2, D1$, the angle $\varphi_{\rm S}$ undergoes a shift by π. This results in a negative sign preceding the $\sin\Phi$

modulation:

$$N_{U2}^{W_{\mathrm{Y}}(f_{cp}D)} N_{D1}^{W_{\mathrm{Y}}(f_{cp}D)} = 4\pi^2 C_0^2 f_{U1} f_{D2} L_{U1} L_{D2} a_{U1} a_{D2} \langle (1+\cos^2\theta_{\mathrm{CS}})^2 \rangle^2 \Big\{ \left(F_{\mathrm{U}}^{1W_{\mathrm{Y}}(f_{cp}D)} \right)^2 - (|\boldsymbol{S}_{\mathrm{T},D1}| + |\boldsymbol{S}_{\mathrm{T},D2}|)\, F_{\mathrm{U}}^{1W_{\mathrm{Y}}(f_{cp}D)} F_{\mathrm{T}}^{\sin(\Phi) W_{\mathrm{Y}}(f_{cp}D)} \sin\Phi \Big\}. \tag{6.45}$$

The equations for additional weighting by q_{T} retain the form of Eq. (6.44) and Eq. (6.45), with weights replaced by $W_{\mathrm{Y}}(f_{cp}Dq_{\mathrm{T}})$. Under the same assumptions, the difference in event counts can be expressed as:

$$\begin{aligned} N_{U1}^{W_{\mathrm{Y}}(f_{cp}Dq_{\mathrm{T}})} N_{D2}^{W_{\mathrm{Y}}(f_{cp}Dq_{\mathrm{T}})} - N_{U2}^{W_{\mathrm{Y}}(f_{cp}Dq_{\mathrm{T}})} N_{D1}^{W_{\mathrm{Y}}(f_{cp}Dq_{\mathrm{T}})} &= 4\pi^2 C_0^2 \langle (1+\cos^2\theta_{\mathrm{CS}})^2 \rangle^2 \\ &\times b_1 b_2 l_U l_D a_{D1} a_{D2} f_{U1} f_{D2} \Bigg[\left(F_{\mathrm{U}}^{1W_{\mathrm{Y}}(f_{cp}Dq_{\mathrm{T}})} \right)^2 \\ + \Big(|\boldsymbol{S}_{\mathrm{T},U2}| + |\boldsymbol{S}_{\mathrm{T},D1}| + |\boldsymbol{S}_{\mathrm{T},U1}| + |\boldsymbol{S}_{\mathrm{T},D2}| \Big) & F_{\mathrm{U}}^{1W_{\mathrm{Y}}(f_{cp}Dq_{\mathrm{T}})} F_{\mathrm{T}}^{\sin(\Phi) W_{\mathrm{Y}}(f_{cp}Dq_{\mathrm{T}})} \sin\Phi \Bigg]. \end{aligned} \tag{6.46}$$

Analogically:

$$\begin{aligned} N_{U1}^{W_{\mathrm{Y}}(f_{cp}Dq_{\mathrm{T}})} N_{D2}^{W_{\mathrm{Y}}(f_{cp}Dq_{\mathrm{T}})} + N_{U2}^{W_{\mathrm{Y}}(f_{cp}Dq_{\mathrm{T}})} N_{D1}^{W_{\mathrm{Y}}(f_{cp}Dq_{\mathrm{T}})} &= 8\pi^2 C_0^2 b_1 b_2 l_U l_D a_{D1} a_{D2} f_{U1} f_{D2} \\ &\times \left(\langle (1+\cos^2\theta_{\mathrm{CS}})^2 \rangle F_{\mathrm{U}}^{1W_{\mathrm{Y}}(f_{cp}Dq_{\mathrm{T}})} \right)^2, \end{aligned} \tag{6.47}$$

$$\begin{aligned} N_{U1}^{W_{\mathrm{Y}}(f_{cp}D)} N_{D2}^{W_{\mathrm{Y}}(f_{cp}D)} - N_{U2}^{W_{\mathrm{Y}}(f_{cp}D)} N_{D1}^{W_{\mathrm{Y}}(f_{cp}D)} &= 8\pi^2 C_0^2 b_1 b_2 l_U l_D a_{D1} a_{D2} f_{U1} f_{D2} \\ &\times \left(\langle (1+\cos^2\theta_{\mathrm{CS}})^2 \rangle F_{\mathrm{U}}^{1W_{\mathrm{Y}}(f_{cp}D)} \right)^2. \end{aligned} \tag{6.48}$$

As in the case of the standard mass range and the φ_{S} modulation, the dependence on the angle θ_{CS} is removed, resulting in the following final expression for the modified double ratio:

$$R^{\mathrm{Y}W_{\mathrm{Y}}(f_{cp}Dq_{\mathrm{T}})}(\Phi) = (|\boldsymbol{S}_{\mathrm{T},U2}| + |\boldsymbol{S}_{\mathrm{T},D1}| + |\boldsymbol{S}_{\mathrm{T},U1}| + |\boldsymbol{S}_{\mathrm{T},D2}|)\, \frac{F_{\mathrm{T}}^{\sin(\Phi) W_{\mathrm{Y}}(f_{cp}Dq_{\mathrm{T}})}}{F_{\mathrm{U}}^{1W_{\mathrm{Y}}(f_{cp}D)}} \sin\Phi. \tag{6.49}$$

Calculation for $\Phi = 2\varphi_{\mathrm{CS}} \pm \varphi_{\mathrm{S}}$

For angular modulations involving the azimuthal combinations $\Phi = 2\phi_{\mathrm{CS}} \pm \phi_S$, incorporating the weighting factor $D = 1 - \cos^2\theta_{\mathrm{CS}}$ significantly modifies the dependence of the modified double ratio. Assuming the same conditions as in the preceding cases (Eqs 6.28–6.31), the product of event counts for the "up" polarization configuration can be expressed as:

$$N_{U1}^{W_{\mathrm{Y}}(f_{cp}D)} N_{D2}^{W_{\mathrm{Y}}(f_{cp}D)} = 4\pi^2 C_0^2 f_{U1} f_{D2} L_{U1} L_{D2} a_{U1} a_{D2} \Big\{ \left(\langle 1-\cos^4\theta_{\mathrm{CS}} \rangle F_{\mathrm{U}}^{1WW_{\mathrm{Y}}(f_{cp}D)} \right)^2 + (|\boldsymbol{S}_{\mathrm{T},D1}| + |\boldsymbol{S}_{\mathrm{T},D2}|)\, \langle 1-\cos^4\theta_{\mathrm{CS}} \rangle \langle (1-\cos^2\theta_{\mathrm{CS}})^2 \rangle F_{\mathrm{U}}^{1W_{\mathrm{Y}}(f_{cp}D)} F_{\mathrm{T}}^{\sin(\Phi) W_{\mathrm{Y}}(f_{cp}D)} \sin\Phi \Big\}. \tag{6.50}$$

For "down" polarisation:

$$N_{U2}^{W_{\mathrm{Y}}(f_{cp}D)}N_{D1}^{W_{\mathrm{Y}}(f_{cp}D)} = 4\pi^2 C_0^2 f_{U2}f_{D1}L_{U2}L_{D1}a_{U2}a_{D1}\Bigg\{ \left(\langle 1-\cos^4\theta_{\mathrm{CS}}\rangle F_{\mathrm{U}}^{1W_{\mathrm{Y}}(f_{cp}D)}\right)^2 - \\ \left(|\boldsymbol{S}_{\mathrm{T},U2}| + |\boldsymbol{S}_{\mathrm{T},D1}|\right)\langle 1-\cos^4\theta_{\mathrm{CS}}\rangle\langle(1-\cos^2\theta_{\mathrm{CS}})^2\rangle F_{\mathrm{U}}^{1W_{\mathrm{Y}}(f_{cp}D)}F_{\mathrm{T}}^{\sin(\Phi)W_{\mathrm{Y}}(f_{cp}D)}\sin\Phi\Bigg\}. \tag{6.51}$$

Then:

$$N_{U1}^{W_{\mathrm{Y}}(f_{cp}Dq_{\mathrm{T}})}N_{D2}^{W_{\mathrm{Y}}(f_{cp}Dq_{\mathrm{T}})} - N_{U2}^{W_{\mathrm{Y}}(f_{cp}Dq_{\mathrm{T}})}N_{D1}^{W_{\mathrm{Y}}(f_{cp}Dq_{\mathrm{T}})} = 4\pi^2 C_0^2\langle 1-\cos^4\theta_{\mathrm{CS}}\rangle\langle(1-\cos^2\theta_{\mathrm{CS}})^2\rangle \\ \times b_1b_2l_Ul_Da_{D1}a_{D2}f_{U1}f_{D2}\Bigg[\left(F_{\mathrm{U}}^{1W_{\mathrm{Y}}(f_{cp}Dq_{\mathrm{T}})}\right)^2 \\ +\Bigg(|\boldsymbol{S}_{\mathrm{T},U2}| + |\boldsymbol{S}_{\mathrm{T},D1}| + |\boldsymbol{S}_{\mathrm{T},U1}| + |\boldsymbol{S}_{\mathrm{T},D2}|\Bigg)F_{\mathrm{U}}^{1W_{\mathrm{Y}}(f_{cp}Dq_{\mathrm{T}})}F_{\mathrm{T}}^{\sin(\Phi)W_{\mathrm{Y}}(f_{cp}Dq_{\mathrm{T}})}\sin\Phi\Bigg]. \tag{6.52}$$

Analogically:

$$N_{U1}^{W_{\mathrm{Y}}(f_{cp}Dq_{\mathrm{T}})}N_{D2}^{W_{\mathrm{Y}}(f_{cp}Dq_{\mathrm{T}})} + N_{U2}^{W_{\mathrm{Y}}(f_{cp}Dq_{\mathrm{T}})}N_{D1}^{W_{\mathrm{Y}}(f_{cp}Dq_{\mathrm{T}})} = 8\pi^2 C_0^2 b_1b_2l_Ul_Da_{D1}a_{D2}f_{U1}f_{D2} \\ \times\left(\langle 1-\cos^4\theta_{\mathrm{CS}}\rangle F_{\mathrm{U}}^{1W_{\mathrm{Y}}(f_{cp}Dq_{\mathrm{T}})}\right)^2, \tag{6.53}$$

$$N_{U1}^{W_{\mathrm{Y}}(f_{cp}D)}N_{D2}^{W_{\mathrm{Y}}(f_{cp}D)} - N_{U2}^{W_{\mathrm{Y}}(f_{cp}D)}N_{D1}^{W_{\mathrm{Y}}(f_{cp}D)} = 8\pi^2 C_0^2 b_1b_2l_Ul_Da_{D1}a_{D2}f_{U1}f_{D2} \\ \times\left(\langle 1-\cos^4\theta_{\mathrm{CS}}\rangle F_{\mathrm{U}}^{1W_{\mathrm{Y}}(f_{cp}D)}\right)^2. \tag{6.54}$$

Finally, the dependence of the modified double ratio on the structure function in the extended range of the mass for the modulation $\varphi_{\mathrm{S}} \pm 2\varphi_{\mathrm{CS}}$ takes the form:

$$R^{\mathrm{Y}W_{\mathrm{Y}}(f_{cp}Dq_{\mathrm{T}})}(\Phi) = \left(|\boldsymbol{S}_{\mathrm{T},U2}| + |\boldsymbol{S}_{\mathrm{T},D1}| + |\boldsymbol{S}_{\mathrm{T},U1}| + |\boldsymbol{S}_{\mathrm{T},D2}|\right) \\ \times\frac{\langle 1-\cos^2\theta_{\mathrm{CS}}\rangle}{\langle 1-\cos^4\theta_{\mathrm{CS}}\rangle}\frac{F_{\mathrm{T}}^{\sin(\Phi)W_{\mathrm{Y}}(f_{cp}Dq_{\mathrm{T}})}}{F_{\mathrm{U}}^{1W_{\mathrm{Y}}(f_{cp}D)}}\sin\Phi. \tag{6.55}$$

6.4 Differences Between Standard and Extended Mass Ranges

6.4.1 Kinematic Factor

This section compares the modified double ratio between the standard and extended mass ranges, emphasizing differences in the weighting methods applied to the data. The functional forms of the modified double ratio for individual modulations and mass ranges are summarized in Table 6.1. For the Sivers modulation, the kinematic factor $\tilde{D}$ is independent of the angle θ_{CS} in both the standard and extended mass ranges.

Table 6.1: Modified double ratio $R^{W(q_\mathrm{T})}_{\mathrm{mod}}/\sin\Phi$, divided by $\sin\Phi$ to obtain the modulation amplitude A_{raw}, for different $M_{\mu\mu}$ ranges.

A_{raw} \ Φ	φ_S	$2\varphi_{\mathrm{CS}} \pm \varphi_\mathrm{S}$
Standard Range: $M_{\mu\mu} \in (4.3,\ 8.5)$ GeV$/c^2$		
$\frac{R^{\mathrm{Y}W_\mathrm{Y}(q_\mathrm{T})}}{\sin\Phi}$	$\langle f\rangle\langle P\rangle \frac{F_\mathrm{T}^{\sin(\Phi)W_\mathrm{Y}(q_\mathrm{T})}}{F_\mathrm{U}^1}$	$\langle f\rangle\langle P\rangle \frac{\langle 1-\cos^2\theta_{\mathrm{CS}}\rangle}{\langle 1+\cos^2\theta_{\mathrm{CS}}\rangle} \frac{F_\mathrm{T}^{\sin(\Phi)W_\mathrm{Y}(q_\mathrm{T})}}{F_\mathrm{U}^1}$
Extended Range: $M_{\mu\mu} \in (4.0,\ 9.0)$ GeV$/c^2$		
$\frac{R^{\mathrm{Y}W_\mathrm{Y}(f_{cp}Dq_\mathrm{T})}}{\sin\Phi}$	$\langle f\rangle\langle P\rangle \frac{F_\mathrm{T}^{\sin(\Phi)W_\mathrm{Y}(f_{cp}Dq_\mathrm{T})}}{F_\mathrm{U}^{1W_\mathrm{Y}(f_{cp}D)}}$	$\langle f\rangle\langle P\rangle \frac{\langle (1-\cos^2\theta_{\mathrm{CS}})^2\rangle}{\langle 1-\cos^4\theta_{\mathrm{CS}}\rangle} \frac{F_\mathrm{T}^{\sin(\Phi)W_\mathrm{Y}(f_{cp}Dq_\mathrm{T})}}{F_\mathrm{U}^{1W_\mathrm{Y}(f_{cp}D)}}$

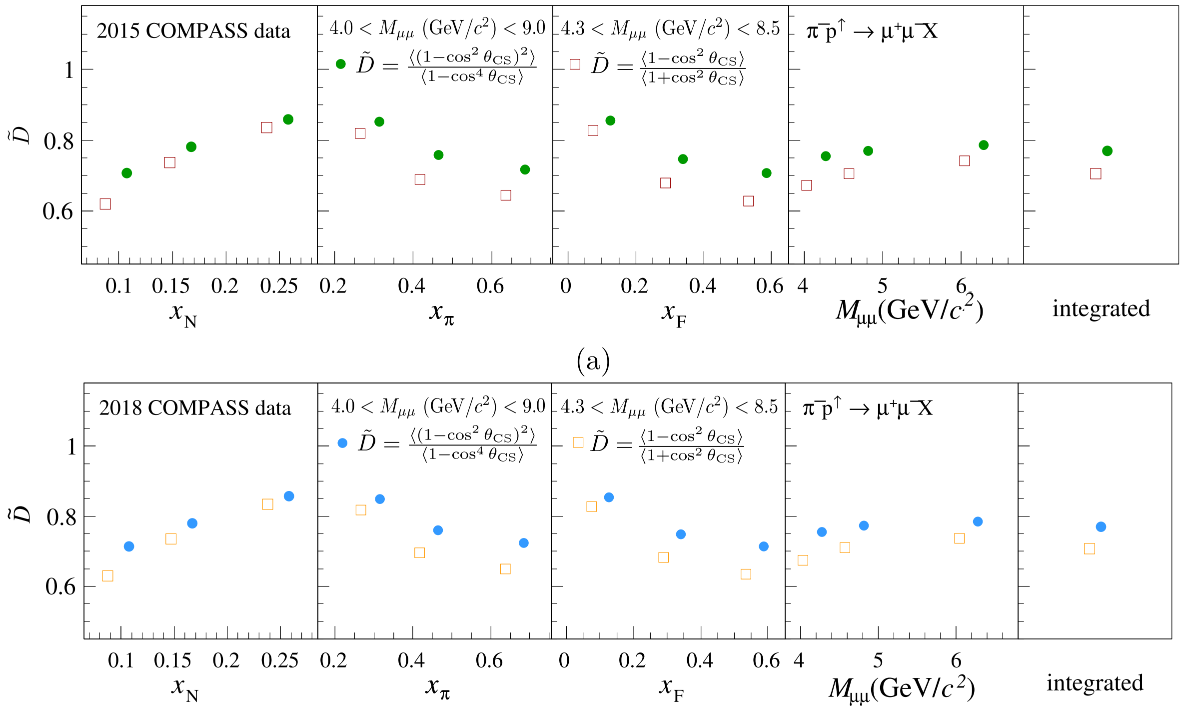

(a)

(b)

Figure 6.1: Comparison of the kinematic factors based on formulas in Eq. (6.56): (a) 2015 (b) 2018.

However, for the modulation $\varphi_\mathrm{S} \pm \varphi_{\mathrm{CS}}$, $\tilde{D}$ exhibits a dependence on θ_{CS} that takes different forms for each mass range:

$$\tilde{D} = \begin{cases} \frac{\langle 1-\cos^2\theta_{\mathrm{CS}}\rangle}{\langle 1+\cos^2\theta_{\mathrm{CS}}\rangle} & \text{for } M_{\mu\mu} \in (4.3,\ 8.5)\,\mathrm{GeV}/c^2, \\ \frac{\langle (1-\cos^2\theta_{\mathrm{CS}})^2\rangle}{\langle 1-\cos^4\theta_{\mathrm{CS}}\rangle} & \text{for } M_{\mu\mu} \in (4.0,\ 9.0)\,\mathrm{GeV}/c^2. \end{cases} \tag{6.56}$$

The average values of the kinematic factor $\tilde{D}$ are presented in Figs 6.1a and 6.1b. For the extended mass range, $\tilde{D}$ increases by roughly 11% compared to the standard range.

6.4.2 Impact of Mass Range on the Dilution Factor

As shown in Table 6.1, the functional forms differ between the standard and extended mass ranges to account for the significant background in the latter. This section focuses on the dilution factor and its application in both ranges.

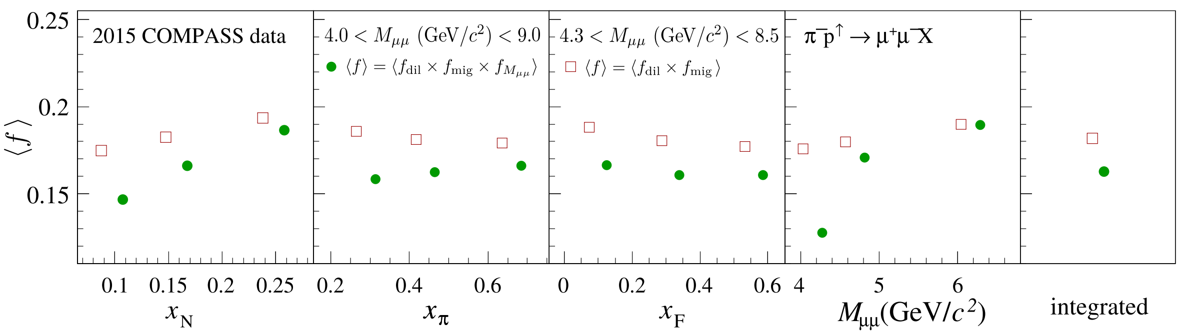

(a)

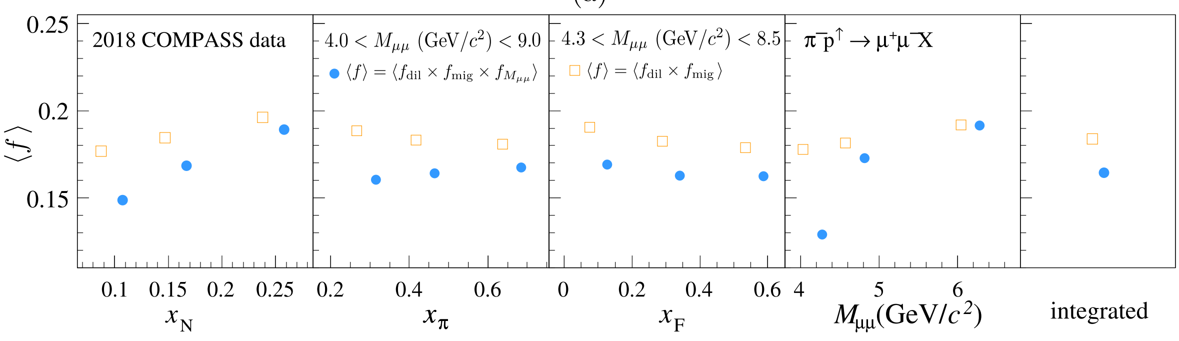

(b)

Figure 6.2: Comparison of the dilution factors obtained for the standard and extended $M_{\mu\mu}$ ranges in: (a) 2015 and (b) 2018.

In the standard mass interval, $M_{\mu\mu} \in (4.3,\ 8.5)\,\mathrm{GeV}/c^2$, the background is relatively small and stable, allowing the dilution factor to be applied as a constant, averaged over all events. The average incorporates the primary dilution factor $f_{\rm dil}$, extracted directly from the PHAST[2], together with a migration correction $f_{\rm mig}$ that accounts for bin smearing caused by limited resolution.

Considering the extended mass domain, $M_{\mu\mu} \in (4.0,\ 9.0)\,\mathrm{GeV}/c^2$, the background contribution becomes significant, especially at lower masses, where signal purity drops rapidly. In this case, applying a single average value for the dilution factor would fail to reflect the true background structure across the spectrum. To correct for this effect, the correction term $f_{M_{\mu\mu}}$ is applied individually to each event:

$$f_{M_{\mu\mu}} = 1 - e^{p_0 + p_1 M_{\mu\mu}}, \tag{6.57}$$

where the fitted values are $p_0 = 13.6$, $p_1 = -3.6$[3]. This approach ensures that both the mass dependence of the contamination and the associated angular correlations are correctly accounted for, thereby improving the reliability of the extracted asymmetries.

[2]The dilution factor $f_{\rm dil}$ is accessed via `PaAlgo::GetDYdilutionFactor`

[3]The function decreases rapidly with invariant mass: $f_{M_{\mu\mu}} \approx 0.5$ near the lower bound and approaches 1 above 5 GeV/c^2, suppressing background effects.

As a result, in the extended mass range, the total dilution factor applied to each event takes the form:

$$f = f_{\mathrm{dil}} \times f_{\mathrm{mig}} \times f_{M_{\mu\mu}}. \tag{6.58}$$

Figs 6.2a and 6.2b show the averaged dilution factor values in each kinematic bin, while Tabs 6.2a and 6.2b summarise the corresponding percentage reductions observed in the extended mass range relative to the standard range.

Table 6.2: Percentage decrease of dilution factors in the extended mass range compared to the standard one, for each kinematic bin for both data samples.

(a)

Variable	1st bin	2nd bin	3rd bin
x_{N}	17.16	10.09	5.00
x_{π}	14.09	10.21	7.07
x_{F}	10.57	10.52	8.83
$M_{\mu\mu}$	28.05	5.73	1.03
Integrated		10.51	

(b)

Variable	1st bin	2nd bin	3rd bin
x_{N}	16.96	9.86	4.87
x_{π}	13.99	10.16	7.18
x_{F}	10.37	10.48	8.87
$M_{\mu\mu}$	28.03	5.73	1.03
Integrated		10.43	

In summary, due to significant differences in the asymmetry extraction for the two mass ranges, the following chapters present the results separately for $M_{\mu\mu} \in (4.3, 8.5)$ GeV/c^2 (Chapter 7) and $M_{\mu\mu} \in (4.0, 9.0)$ GeV/c^2 (Chapter 8). For clarity, the asymmetries from the standard mass range are hereafter denoted as WTSA, while those from the extended range are referred to as fD-WTSA to emphasize the event-by-event weighting by the dilution and kinematic factors.

Chapter 7

Standard Mass Range Analysis

A process cannot be understood by stopping it.
Understanding must move with the flow of the process,
must join it and flow with it.

— Frank Herbert, Dune

This chapter presents the extraction of the WTSA in the standard dimuon mass range, $M_{\mu\mu} \in (4.3, 8.5)$ GeV/c^2, following the procedure described in Sec. 6.3.1. The methodology is illustrated in Sec. 7.1, which includes an example of the modified double ratio, its fit, and the corresponding theoretical expectation. A discussion of the systematic studies and the evaluation of associated uncertainties is provided in Sec. 7.2. Finally, Sec. 7.3 presents the results for the standard mass range, including both statistical and systematic uncertainties.

7.1 Modified Double Ratio and Fit Quality

As shown in Tab. 6.1, the modulation amplitude, A_{raw}, can be expressed as:

$$A_{\text{raw}} = \frac{R^{\text{Y}W_{\text{Y}}(q_{\text{T}})}}{\sin\Phi} = \langle f\rangle\langle P\rangle\tilde{D}\frac{F_{\text{T}}^{\sin(\Phi)W_{\text{Y}}(q_{\text{T}})}}{F_{\text{U}}^{1}} = \langle f\rangle\langle P\rangle\tilde{D}A_{\text{T}}^{\sin(\Phi)W_{\text{Y}}(q_{\text{T}})}. \tag{7.1}$$

where $\langle f\rangle$, $\langle P\rangle$, and $\tilde{D}$ refer, respectively, to the average dilution factor, the average target polarization, and the average kinematic factor. For the Sivers asymmetry, $\tilde{D} = 1$, while for the pretzelosity and transversity asymmetries it takes the form $\langle 1 - \cos^2\theta_{\text{CS}}\rangle / \langle 1 + \cos^2\theta_{\text{CS}}\rangle$, as derived in Chapter 6.

The main goal of this analysis is to extract the $A_{\text{T}}^{\sin(\Phi)W(q_{\text{T}})}$. For this purpose, the data from each period are divided into eight equal-width bins in the azimuthal angle. In each bin, the ratio defined in Eq. (6.21) is evaluated, and the corresponding modulation amplitude A_{raw} is determined. To illustrate the extraction procedure and the interpretation of the measured asymmetries, Figs 7.1a, 7.1b, and 7.1c show examples of the modified double ratio method, including representative results and their fits.

An example of a χ^2/n_{df} value from a fit to the modified double ratio for the Sivers asymmetry, shown in Fig. 7.1a, indicates an underestimation of the uncertainties. This recurring issue, observed across various periods, arises because the modulation amplitude is lower than the statistical noise in the experimental data. Consequently, the

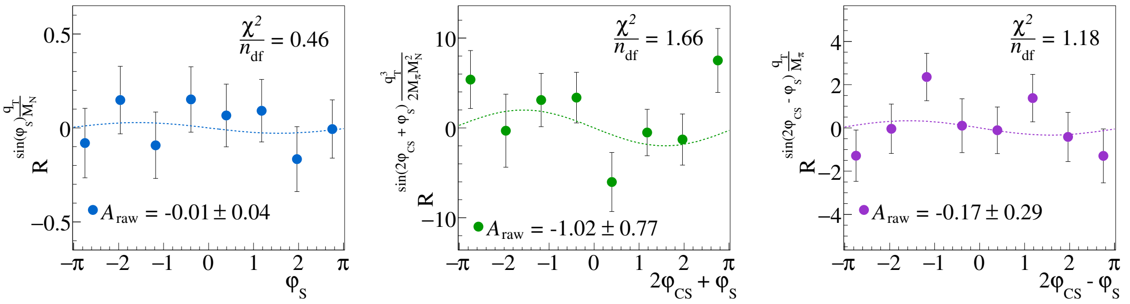

(a) (b) (c)

Figure 7.1: Example of the modified double ratio weighted by q_{T} for the integrated bin from the final period (Week 15) of the 2015 data-taking, for (a) Sivers, (b) pretzelosity, and (c) transversity. Each panel shows the modulation amplitude A_{raw} together with the χ^2/n_{df} value of the fitted function. Results from other weeks exhibit similar behavior and are therefore not shown.

fitting procedure produces an artificially reduced χ^2/n_{df} value. The remaining modulations, shown in Figs 7.1b and 7.1c, do not exhibit underestimated χ^2/n_{df} values. Owing to their larger modulation amplitudes, the uncertainties appear to be properly estimated, resulting in a consistent and reliable fit quality.

The asymmetries for each period are presented separately: the results for 2015 are shown in Fig. 7.2a, while those for 2018 are displayed in Fig. 7.2b. Asymmetries observed during the W14 and W15 periods in 2015, as well as during P08 in 2018, deviate from those measured in the remaining data-taking periods. These discrepancies may stem from differences in experimental conditions, such as variations in beam polarization, detector performance, or background levels. Alternatively, they could be the result of statistical fluctuations or systematic uncertainties specific to those periods.

The annual asymmetries, A[1], are obtained as statistically weighted averages of the asymmetries A_i measured in each data-taking period i ($i = \mathrm{W07}\ldots\mathrm{W15}$ for 2015 and $i = \mathrm{P01}\ldots\mathrm{P08}$ for 2018)[2]. The formulas for A and its statistical uncertainty σ_{stat} are given by:

$$A = \frac{\sum\limits_{i=1} \sigma_{\mathrm{stat},i}^{-2} A_i}{\sum\limits_{i=1} \sigma_{\mathrm{stat},i}^{-2}}, \qquad \sigma_{\mathrm{stat}}^2 = \frac{1}{\sum\limits_{i=1} \sigma_{\mathrm{stat},i}^{-2}}, \tag{7.2}$$

where $\sigma_{\mathrm{stat},i}$ denotes the statistical error of the asymmetry A_i.

[1]Hereafter, the full expression $A_{\mathrm{T}}^{\sin(\Phi)W_{\mathrm{Y}}(q_{\mathrm{T}})}$ is denoted simply as A for brevity.

[2]In 2015, the data-taking periods (W07–W15), referred to as "weeks," typically lasted about two weeks, with the target polarization reversed approximately once per week. In 2018, the periods (P01–P08) were longer, each covering roughly three to four weeks.

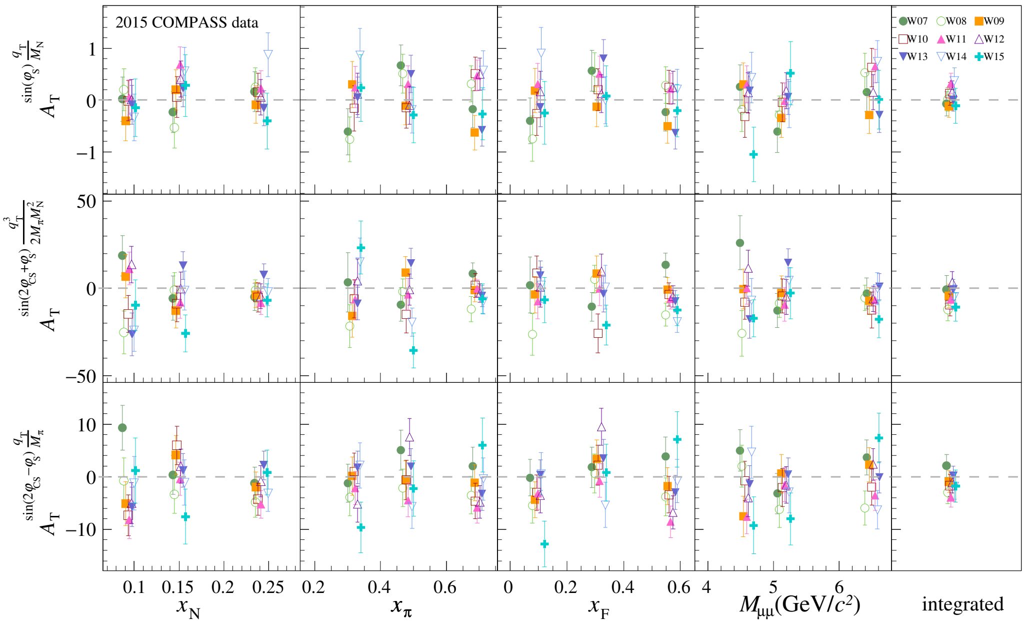

(a)

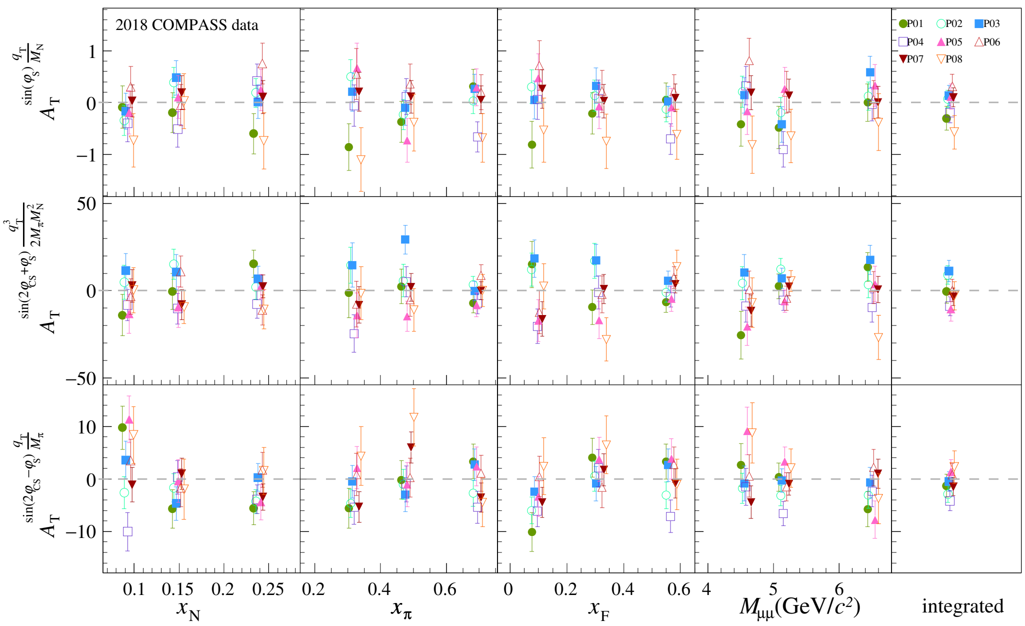

(b)

Figure 7.2: The q_{T} weighted TSAs from: (a) 9 periods of 2015, and (b) 8 periods of 2018 DY data-taking.

7.2 Systematic Studies

To evaluate the systematic uncertainty, two types of tests were performed. The first examined the compatibility of individual data-taking periods, as described in Sec.7.2.1. The second test focused on analyzing false asymmetries, which provided the final estimate of the systematic uncertainty, as detailed in Sec. 7.2.2.

7.2.1 Compatibility of Periods

To assess the compatibility of the individual data-taking periods, the distributions of so-called pulls denoted as ΔA_i, are constructed for each bin and kinematic variable. Each pull measures the deviation of the asymmetry A_i in period i from the overall weighted average A, normalized by the uncertainty of this difference:

$$\Delta A_i = \frac{A_i - A}{\sqrt{\sigma_i^2 - \sigma^2}}. \tag{7.3}$$

The pull distributions, evaluated independently for each kinematic bin, are presented for each kinematic variable in Figs 7.3a (2015 data) and 7.3b (2018 data), respectively. Assuming that the underlying asymmetry measurements A_i are normally distributed, the corresponding pull values ΔA_i are expected, in the ideal case, to follow a normal distribution with mean $\mu \approx 0$ and standard deviation $\sigma \approx 1$. The pull distributions for both the 2015 and 2018 data sets exhibit noticeable deviations from the expected normal distribution. This behavior can be attributed primarily to the insufficient number of entries in the histograms fitted within individual kinematic bins. As an alternative approach, a single pull distribution can be constructed by combining the events from all three kinematic bins corresponding to a given asymmetry and kinematic variable. Since the asymmetry is expected to remain constant within each bin of the kinematic variable, this procedure preserves the physical interpretation while significantly increasing the statistical precision as shown in Figs 7.4a and 7.4b. A 15% increase in the width of the pulls is observed, which may result from an insufficient number of entries in the pulls histogram or an underestimation of the systematic uncertainties of the mean asymmetries. This issue will be discussed in more detail in Chapter 8.

In addition, the χ^2 values per degree-of-freedom n_{df}, associated with the weighted averages are evaluated:

$$\frac{\chi^2}{n_{\mathrm{df}}} = \frac{1}{n_{\mathrm{per}} - 1} \sum_i \frac{(A_i - A)^2}{\sigma_i^2}, \tag{7.4}$$

where n_{per} is the number of periods[3]. The results presented in Fig. 7.5 indicate a significant underestimation of the asymmetry uncertainties in certain bins. This effect is especially pronounced in the first x_{N} bin for the 2018 data for the transversity asymmetry, as well as in the first and second bins for x_{N} and x_π, respectively, for the pretzelosity asymmetry in the 2015 data. Despite these observed deviations, evident both in the pull distributions and the reduced χ^2/n_{df} values, the discrepancies remain relatively small when compared to the dominant systematic effects related to false asymmetries, which are discussed in detail in the following chapter. Consequently,

[3] In the case of the 2015 data-taking, this corresponds to a number of weeks.

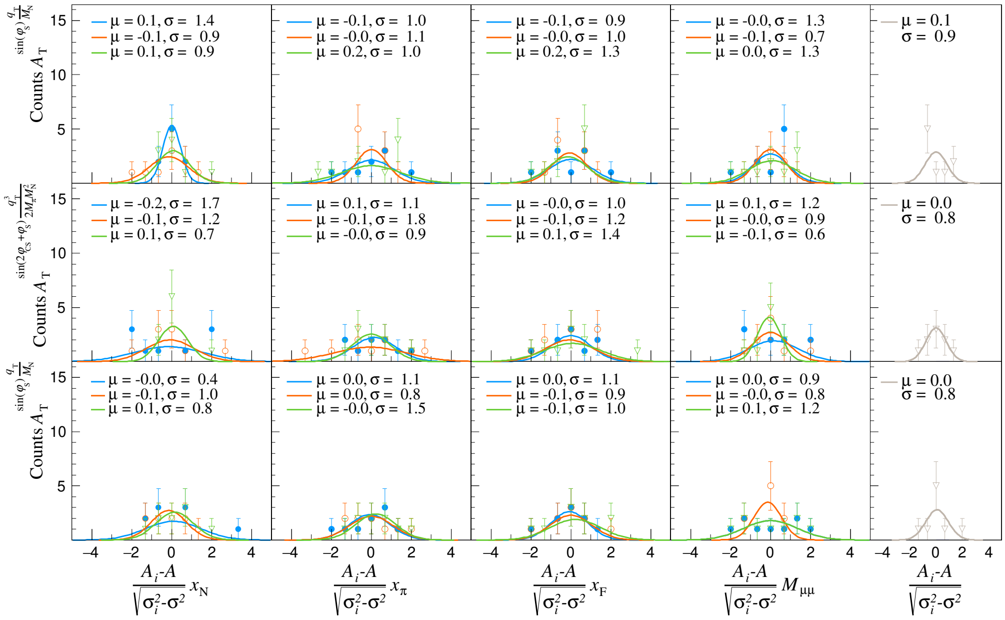

(a)

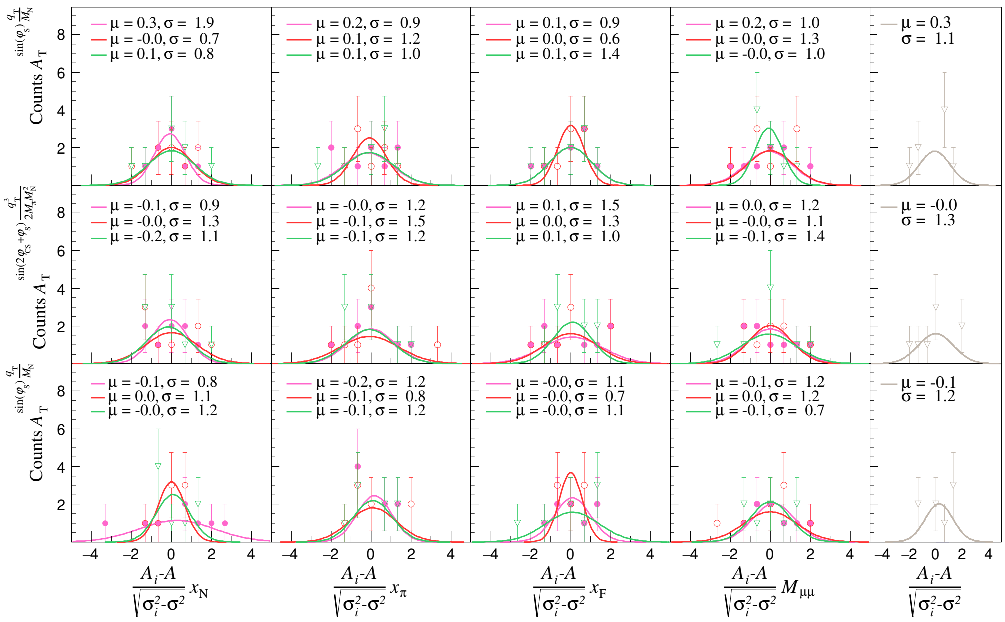

(b)

Figure 7.3: Distributions of pulls ΔA_i, evaluated independently for each kinematic bin and variable, for (a) the 2015 data sample and (b) the 2018 data sample. The vertical axis in each subplot shows the number of entries ("counts") corresponding to the pull values on the horizontal axis. The mean μ and standard deviation σ of each distribution are indicated in the legend of each subplot.

these minor incompatibilities between data-taking periods are considered sufficiently marginal and are not incorporated into the estimation of systematic uncertainties, allowing for a clearer focus on the more significant sources of uncertainty.

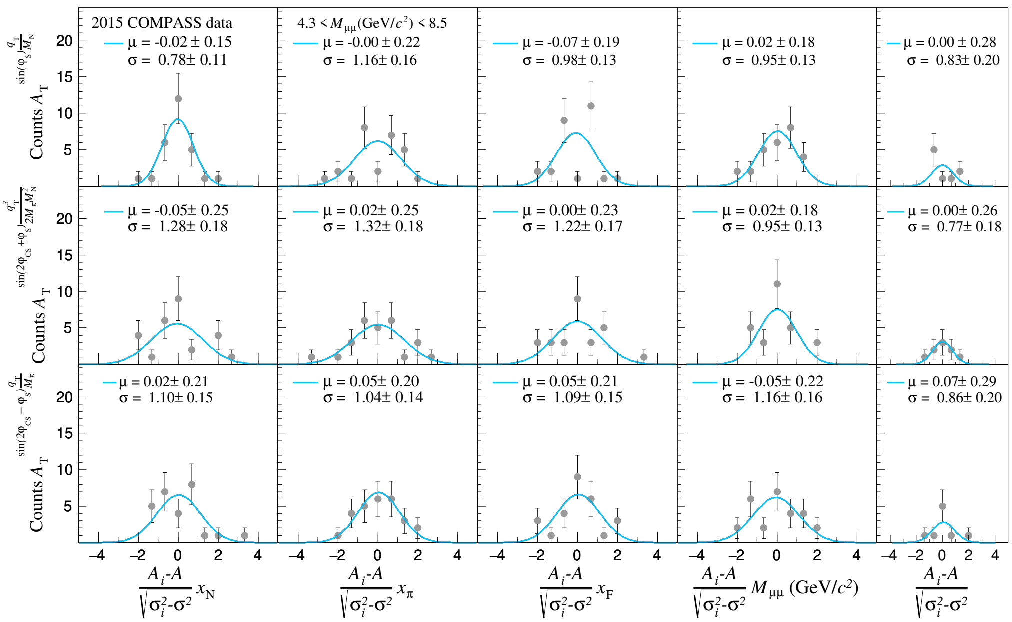

(a)

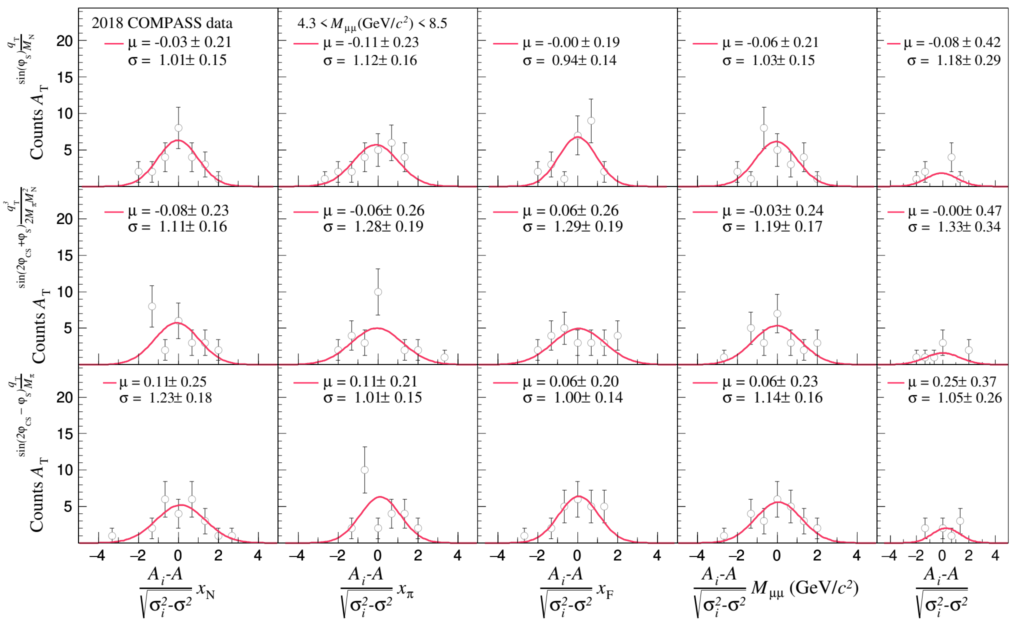

(b)

Figure 7.4: Distribution of pulls ΔA_i, evaluated independently for each kinematic variable (x_{N}, x_π, x_{F}, $M_{\mu\mu}$) across three kinematic bins, for (a) the 2015 data sample and (b) the 2018 data sample.

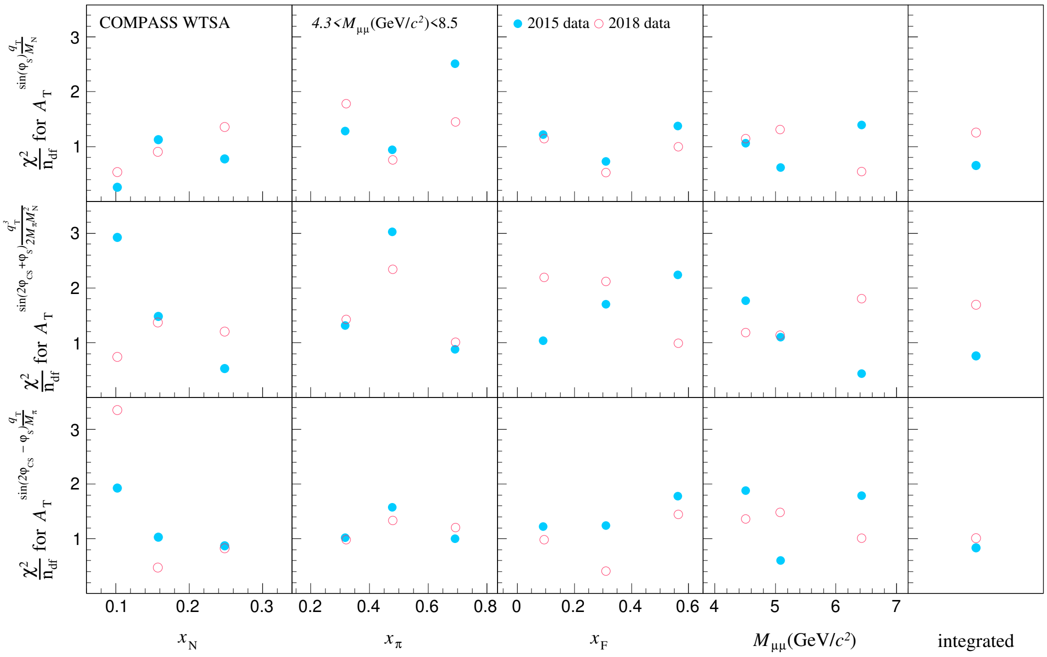

Figure 7.5: The reduced χ^2/n_{df} of the error-weighted averages of the asymmetries over the 9 periods in 2015 and 8 periods in 2018. The values on the horizontal axis correspond to the mean kinematic values of the respective variables (x_{N}, x_π, x_{F}, $M_{\mu\mu}$) within each bin.

7.2.2 False Asymmetries

In order to investigate the cancellation of acceptance effects in the modified double ratio, as defined in Eq. (6.21), the data are deliberately mixed to eliminate any physics asymmetries. This procedure ensures that any observed azimuthal modulation can be attributed exclusively to the characteristics of the experimental apparatus. To quantify potential distortions, false asymmetries are calculated using four distinct methods. This chapter outlines the methodology employed for the generation and evaluation of these false asymmetries, which serve as a baseline for understanding and mitigating experimental biases in the analysis. The false asymmetries are calculated using four distinct methods, each designed to minimize or cancel out physics effects and isolate the contribution of acceptance-related modulations.
These methods are outlined below:

1. **Event Mixing:** Events are randomly mixed between the two subperiods within each period. The mixing procedure is demostrated in Fig. 7.6. This randomization is designed to ensure that the average polarization within each subperiod and target cell remained negligible, provided that the distribution of statistics between subperiods is sufficiently balanced. As a result, potential polarization-related biases could be effectively eliminated.

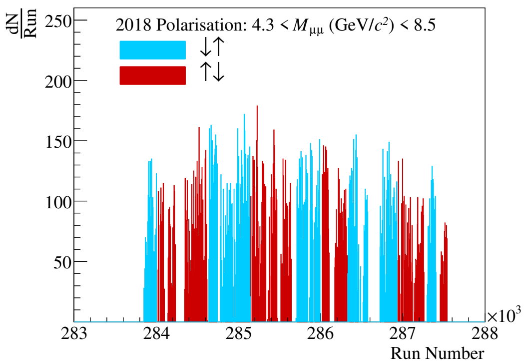

(a) True Subperiods: Each period consists of two subperiods. The polarization reverses approximately in the middle of each period.

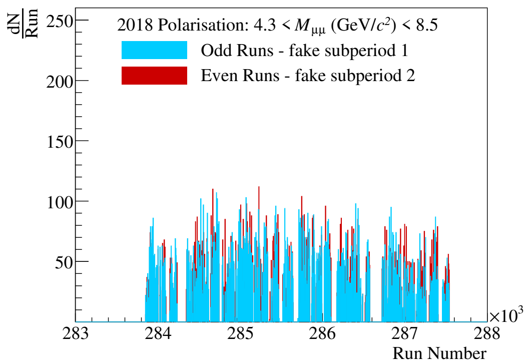

(b) Fake subperiods: Data randomized by assigning odd runs to one subperiod and even runs to the other within each period.

Figure 7.6: Distribution of events in 2018 data-taking within: (a) true subperiods, (b) fake subperiods.

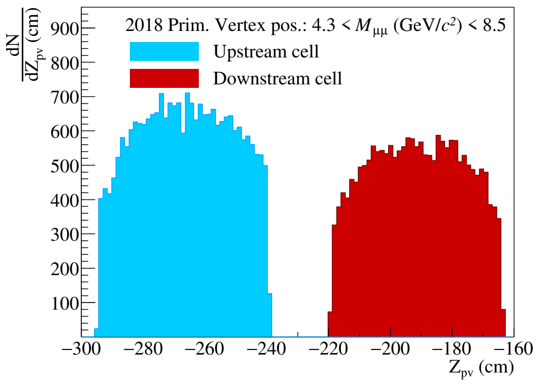

(a)

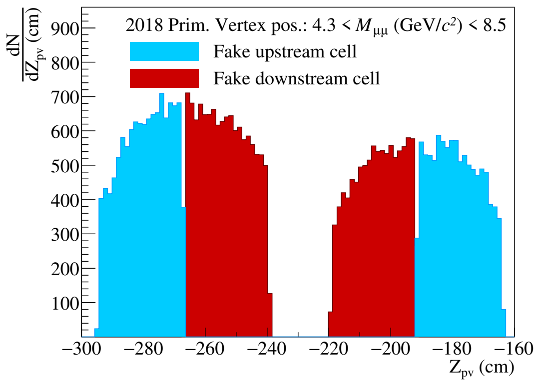

(b)

Figure 7.7: Distribution of primary vertex position Z_{vert} in 2018 data-taking within: (a) true and (b) fake target cells.

2. **Cell Mixing:** Each target cell is divided into two halves as presented in Fig. 7.7, which are then combined to form "inner" and "outer" cells. Although the average polarization within each cell remained non-zero, it is expected that the mixing process would effectively cancel out any polarization differences in the modified double ratio.

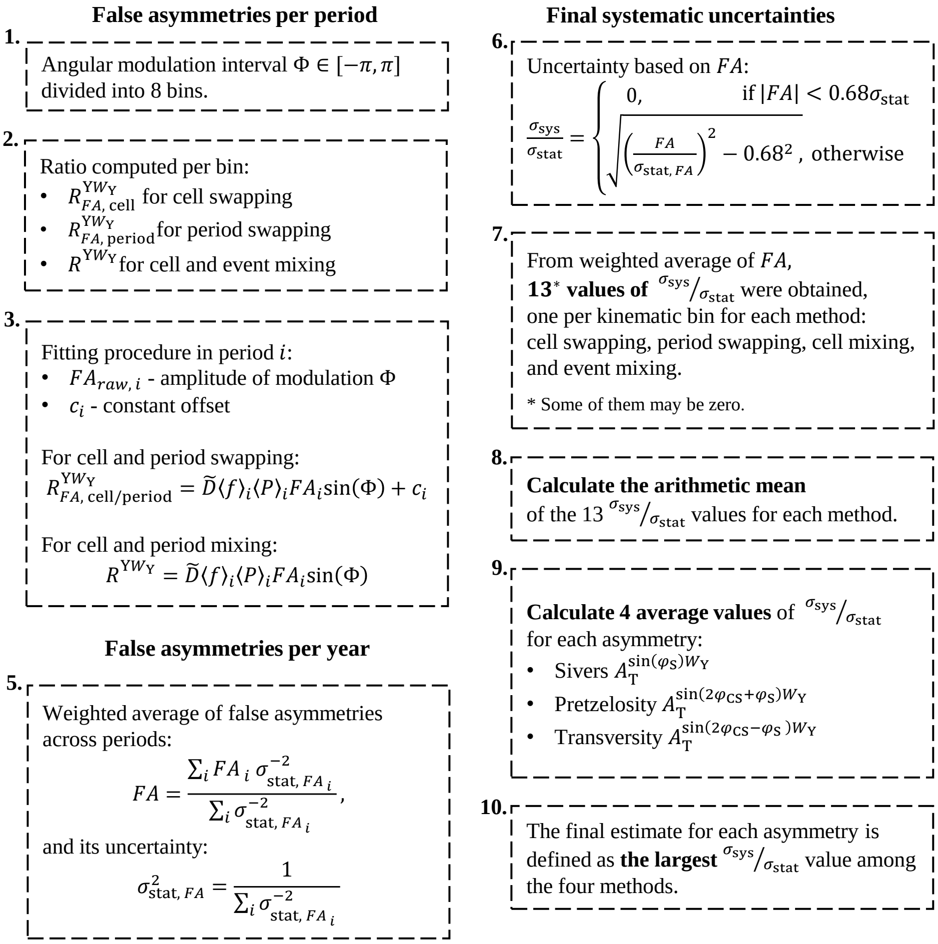

Figure 7.8: Scheme for estimating systematic uncertainty based on false asymmetry calculations.

3. **Cell Swapping:** To evaluate how variations in acceptance between the upstream and downstream target cells influence the measured asymmetry, the following ratio is introduced:

$$R^{\mathrm{YW_Y}}_{FA,\mathrm{cell}} = \frac{N_{U1}^{W_{\mathrm{Y}}(w)} N_{U2}^{W_{\mathrm{Y}}(w)} - N_{D2}^{W_{\mathrm{Y}}(w)} N_{D1}^{W_{\mathrm{Y}}(w)}}{\sqrt{(N_{U1}^{W_{\mathrm{Y}}(w)} N_{U2}^{W_{\mathrm{Y}}(w)} + N_{D2}^{W_{\mathrm{Y}}(w)} N_{D1}^{W_{\mathrm{Y}}(w)})(N_{U1}N_{U2} + N_{D2}N_{D1})}} \propto \frac{a_{U1}a_{U2} - a_{D1}a_{D2}}{a_{U1}a_{U2} + a_{D1}a_{D2}}. \tag{7.5}$$

where $w \propto q_{\mathrm{T}}$[4]. In this expression, $R^{\mathrm{YW_Y}}_{FA,\mathrm{cell}}$ becomes zero when the acceptance of the upstream and downstream cells is identical, which represents a stricter requirement than that of the standard ratio in Eq. (6.21).

[4]Following the convention introduced in Chapter 6, w is used instead of q_{T} to simplify the notation, allowing its consistent application to the extended mass range, where different weight functions are used.

4. **Period Swapping:** This ratio is designed to test for acceptance variations between different data-taking subperiods while cancelling physics asymmetries. It is defined as:

$$R^{\mathrm{Y}W_{\mathrm{Y}}}_{FA,\mathrm{period}} = \frac{N_{U1}^{W_{\mathrm{Y}}(w)} N_{D1}^{W_{\mathrm{Y}}(w)} - N_{U2}^{W_{\mathrm{Y}}(w)} N_{D2}^{W_{\mathrm{Y}}(w)}}{\sqrt{(N_{U1}^{W_{\mathrm{Y}}(w)} N_{D1}^{W_{\mathrm{Y}}(w)} + N_{U2}^{W_{\mathrm{Y}}(w)} N_{D2}^{W_{\mathrm{Y}}(w)})(N_{U1}N_{D1} + N_{U2}N_{D2})}} \propto \frac{a_{U1}a_{D1} - a_{U2}a_{D2}}{a_{U1}a_{D1} + a_{U2}a_{D2}}. \tag{7.6}$$

   In this formula, $R^{\mathrm{Y}W_{\mathrm{Y}}}_{FA,\mathrm{period}}$ becomes zero when the acceptance remains constant between the two subperiods.

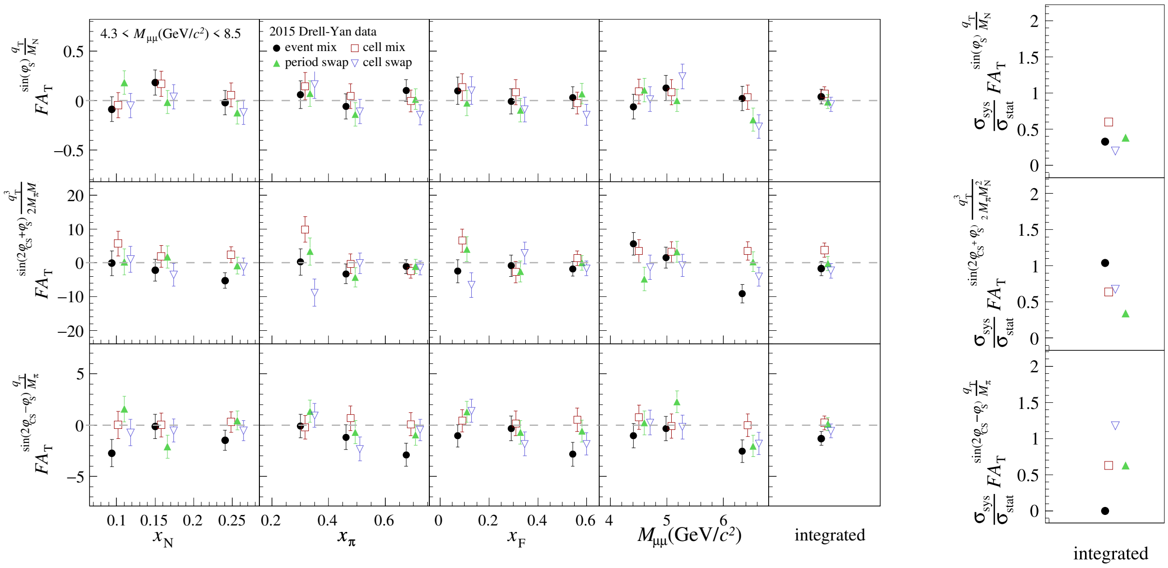

(a) (b)

Figure 7.9: Systematic analysis for the 2015 dataset: (a) annual false asymmetries obtained using four different methods: cell/period mixing and cell/event swapping, (b) ratio of systematic to statistical uncertainties derived from them, already averaged over the kinematic bins and binning variables.

These methods are employed to isolate the effects of the experimental apparatus, ensuring that the observed azimuthal modulations reflect the true experimental conditions rather than being influenced by underlying physics asymmetries. The following steps of the procedure used to evaluate the systematic uncertainties are illustrated in Fig 7.8, whereas the fitting of the modified double ratio, with an additional free parameter to account for effects related to cell and period swapping, is described in detail in the Appendix B.

The false asymmetries, along with the corresponding systematic uncertainties derived from them, are presented in Fig. 7.9 for the 2015 data and Fig. 7.10 for the 2018 data. Deviations from zero indicate the presence of non-negligible systematic effects, which must be accounted for in the analysis.

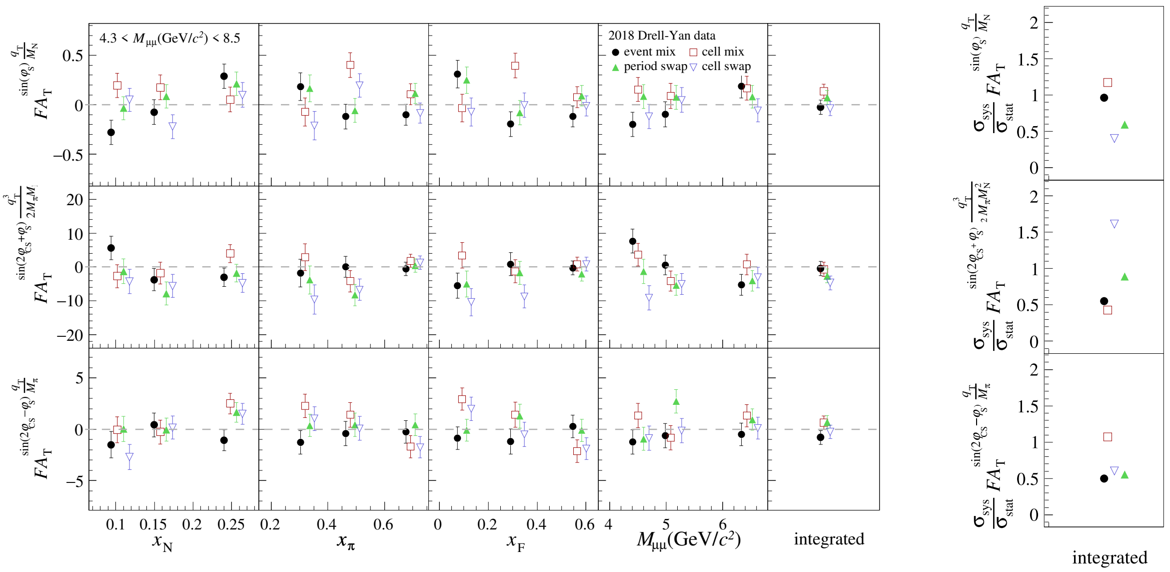

(a) (b)

Figure 7.10: Systematic analysis for the 2018 dataset: (a) annual false asymmetries obtained using four different methods: cell/period mixing and cell/event swapping, (b) ratio of systematic to statistical uncertainties derived from them, already averaged over the kinematic bins and binning variables.

The total systematic uncertainty for a given kinematic bin in the 2015 or 2018 dataset is calculated as:

$$\sigma_{\text{sys}} = x_{\text{FA}} \times \sigma_{\text{stat}}, \tag{7.7}$$

where x_{FA} denotes the ratio of systematic to statistical uncertainties for the corresponding asymmetry, as listed in Table 7.1.

Table 7.1: Relative magnitude of systematic uncertainties with respect to statistical uncertainties, given by $x_{\text{FA}} = \sigma_{\text{sys}}/\sigma_{\text{stat}}$.

Year	Sivers	Pretzelosity	Transversity
2015	0.6	1.04	1.19
2018	1.18	1.62	1.08

7.3 Final WTSA Results

7.3.1 Annual Asymmetries

In Fig. 7.11, the WTSAs are evaluated independently for each of the nine data-taking periods in 2015 and the eight periods in 2018 using Eq. (7.2).

Discrepancies between the 2015 and 2018 results are observed in certain kinematic bins, particularly x_π, x_F, and $M_{\mu\mu}$. These differences are attributed to contributions

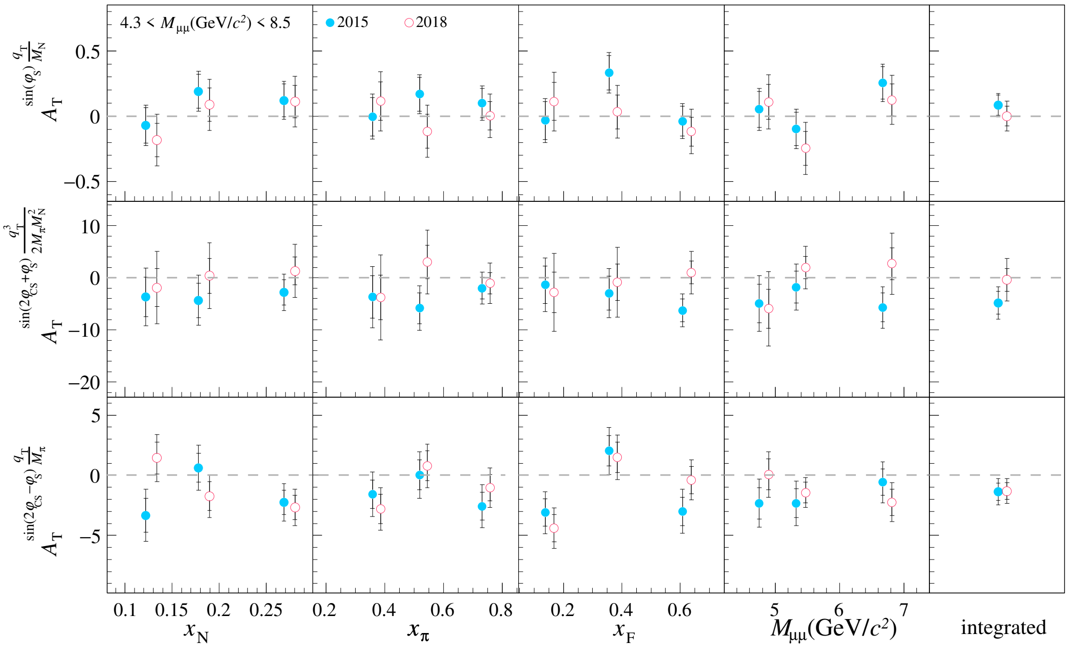

Figure 7.11: The annual WTSAs from the 2015 and 2018 COMPASS data.

from high q_T events occurring in specific data-taking periods, as illustrated in Figs 7.2a and 7.2b.

7.3.2 Combined Asymmetries

Let us consider the asymmetries measured in a given kinematic bin from two Drell–Yan data-taking years, 2015 and 2018, denoted A_{2015} and A_{2018}:

$$A_{2015} \pm \sigma_{2015,\text{stat}} \pm \sigma_{2015,\text{sys}}, \quad A_{2018} \pm \sigma_{2018,\text{stat}} \pm \sigma_{2018,\text{sys}}. \tag{7.8}$$

The corresponding total uncertainties for each year are calculated as:

$$\sigma_{2015,\text{tot}} = \sqrt{\sigma^2_{2015,\text{stat}} + \sigma^2_{2015,\text{sys}}}, \quad \sigma_{2018,\text{tot}} = \sqrt{\sigma^2_{2018,\text{stat}} + \sigma^2_{2018,\text{sys}}}. \tag{7.9}$$

The combined asymmetry, A_c, is then obtained as the weighted mean of the individual measurements:

$$A_c = \frac{A_{2015}\,\sigma^{-2}_{2015,\text{tot}} + A_{2018}\,\sigma^{-2}_{2018,\text{tot}}}{\sigma^{-2}_{2015,\text{tot}} + \sigma^{-2}_{2018,\text{tot}}}, \tag{7.10}$$

with the corresponding total uncertainty:

$$\sigma_{c,\text{tot}} = \frac{1}{\sqrt{\sigma^{-2}_{2015,\text{tot}} + \sigma^{-2}_{2018,\text{tot}}}}. \tag{7.11}$$

The final statistical and systematic components of the uncertainty are estimated separately using the following expressions:

$$\sigma_{c,\text{stat}} = \frac{1}{\sqrt{\sigma^{-2}_{2015,\text{stat}} + \sigma^{-2}_{2018,\text{stat}}}}, \quad \sigma_{c,\text{sys}} = \sqrt{\sigma^2_{c,\text{tot}} - \sigma^2_{c,\text{stat}}}. \tag{7.12}$$

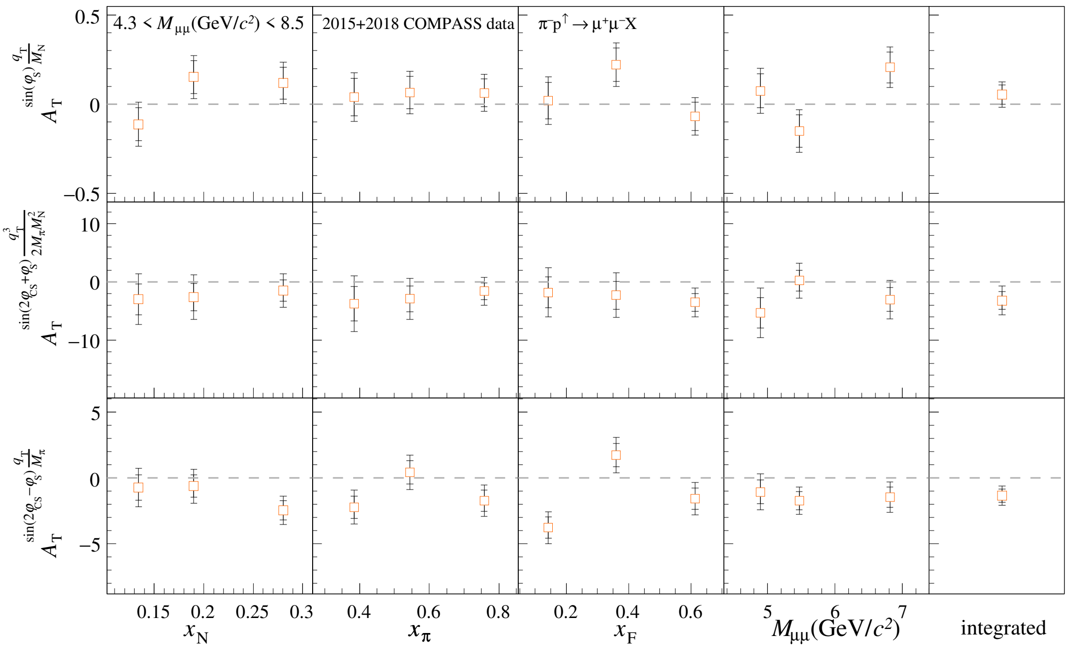

Figure 7.12: The combined WTSAs from the 2015 and 2018 COMPASS data.

The combined results derived from the formulas are presented in Fig. 7.12.

The Sivers WTSA, $A_T^{\sin(\varphi_S)q_T/M_N}$, is predicted to be positive across the entire kinematic range, in agreement with the COMPASS TSAs measurement [94]. The observed average Sivers WTSA is approximately one standard deviation above zero.

Transversity WTSA, $A_T^{\sin(2\varphi_{CS}-\varphi_S)q_T/M_\pi}$, is theoretically expected to be negative and larger in absolute magnitude than the Sivers asymmetry. This prediction is supported by the experimental results, where the average transversity WTSA is negative and deviates from zero with a statistical significance of approximately one standard deviation.

Pretzelosity WTSA, $A_T^{\sin(2\varphi_{CS}+\varphi_S)q_T^3/(2M_\pi M_N^2)}$, is predicted to be very small, due to both the limited size of the corresponding TMD PDFs and kinematic suppression effects [94]. The measured average value for the pretzelosity WTSA is about one standard deviation below zero. This negative shift is attributed to the cubic dependence on q_T introduced by the weighting procedure, which amplifies contributions at higher transverse momenta. This effect is specific to the pretzelosity WTSA and does not influence the Sivers or transversity asymmetries, whose weightings depend linearly on q_T.

Chapter 8

Extended Mass Range Analysis

We can judge our progress by the courage of our questions
and the depth of our answers,
our willingness to embrace what is true
rather than what feels good.

— Carl Sagan

This chapter extends the extraction of Drell–Yan asymmetries from the standard $M_{\mu\mu}$ range 4.3–8.5 GeV/c^2 to the broader 4.0–9.0 GeV/c^2 interval[1]. As discussed in Chapter 5, the extended range requires explicit treatment of background contributions, which are negligible in the standard dimuon mass range. The methodology builds on the procedures of Chapter 7, incorporating dilution and kinematic factor weightings (Sec. 6.3.2). The initial stage of the analysis, based on the modified double ratio method, is described in Sec. 8.1, followed by an analysis of the effects of weighting by dilution and kinematic factors in Sec. 8.2. Sec. 8.3 presents the Toy Monte Carlo study, Sec. 8.4 discusses the impact of outliers and the associated selection procedure, and Sec. 8.5 addresses systematic corrections. The final asymmetries, together with their interpretation and comparison to the COMPASS TSAs [94], are presented in Secs 8.6, 8.7, and 8.8.

8.1 Modified Double Ratio and Fit Quality

Following the approach of Chapter 7, the modulation amplitude $A_{\rm raw}$ is here defined with event-by-event weighting by the dilution factor and the kinematic factor (Tab. 6.1):

$$A_{\rm raw} = \frac{R^{\rm Y W_Y(fDq_T)}}{\sin\Phi} = \langle f\rangle\langle P\rangle\tilde{D}\frac{F_{\rm T}^{\sin(\Phi)W_{\rm Y}(fDq_{\rm T})}}{F_{\rm U}^{1}} = \langle f\rangle\langle P\rangle\tilde{D}A_{\rm T}^{\sin(\Phi)W_{\rm Y}(fDq_{\rm T})}, \qquad (8.1)$$

where $\langle P\rangle$ is the average target polarization, $\langle f\rangle$ the average dilution factor, and $\tilde{D}$ the average kinematic factor.

In contrast to the standard mass range, the extended analysis employs modified definitions of $\langle f\rangle$ and $\tilde{D}$. The dilution factor now incorporates a mass-dependent cor-

[1]As noted in Chapter 6, these asymmetries are collectively referred to as fD-WTSAs.

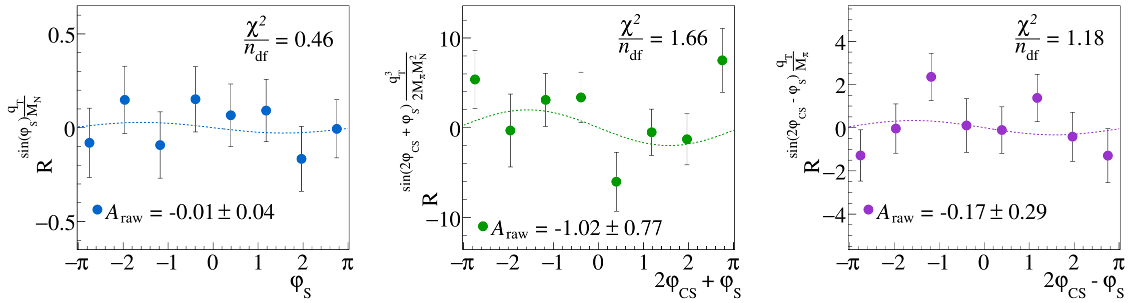

(a) (b) (c)

Figure 8.1: Example of the modified double ratio weighted by dilution factor f, kinematic factor D, and certain powers of q_{T}, for the integrated bin from the final period (Week 15) of the 2015 data-taking, for (a) Sivers, (b) pretzelosity, and (c) transversity. Each panel shows the modulation amplitude A_{raw} together with the χ^2 value of the fitted function. Results from other weeks exhibit similar behavior and are therefore not shown.

rection, as described in Sec. 6.4.2. The average kinematic factor, $\tilde{D}$, is set to 1 for the Sivers asymmetry. For the pretzelosity and transversity asymmetries, however, it is defined as $\tilde{D} = \langle(1-\cos^2\theta_{\mathrm{CS}})^2\rangle/\langle 1-\cos^4\theta_{\mathrm{CS}}\rangle$. Since the additional weighting factors affect both numerator and denominator, the resulting $R^{\mathrm{Y}W_{\mathrm{Y}}}$ remains comparable in magnitude to the values for $M_{\mu\mu} \in (4.3, 8.5)$ GeV/c^2 presented in Chapter 7. As shown in Figs 8.1a–8.1c, the modulation amplitudes follow trends similar to those in the standard mass range (Figs 7.1a–7.1c), with no significant deviations in the corresponding χ^2 values.

Asymmetries measured during each data-taking period in 2015 are presented in Fig. 8.2, while those corresponding to 2018 are shown in Fig. 8.3. As in the case of the standard mass range (Figs 7.2a and 7.2b), the asymmetries determined for individual periods show significant differences, both between specific subperiods within a single data-taking year and between the years 2015 and 2018. In particular, certain periods, such as W10 in 2015 and P08 in 2018, show pronounced deviations from the overall pattern. These effects, together with those related to the mass range extension and the additional event-by-event weighting procedure, are discussed in detail in Sec. 8.2.

8.2 Impact of Weighting

The fD-WTSAs, including both dilution (f) and kinematic (D) factors[2], are compared with WTSAs weighted only by transverse momentum. The average asymmetries and their uncertainties are recalculated using the weighted mean, as defined by Eq. (7.2). The statistical uncertainties of the fD-WTSAs and WTSAs[3] for both the 2015 and 2018 data sets are shown in Fig. 8.4. The results for the transversity asymmetries

[2]As shown in Chapter 6, the kinematic factor D used in the weighting corresponds to $1+\cos^2\theta_{\mathrm{CS}}$ for the Sivers asymmetry, and $1-\cos^2\theta_{\mathrm{CS}}$ for the pretzelosity and transversity asymmetries.

[3]The WTSA results are shown for comparison and serve as a baseline for the fD-WTSA results discussed in this chapter.

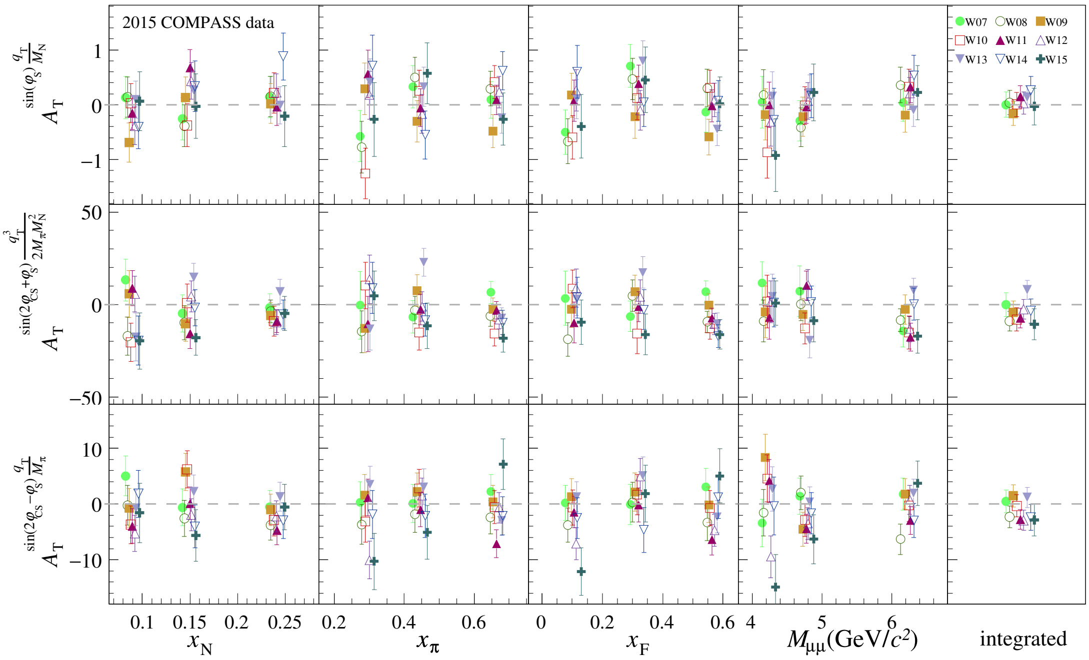

Figure 8.2: The TSAs weighted by f, D and q_T from 9 periods of 2015 Drell-Yann data-taking.

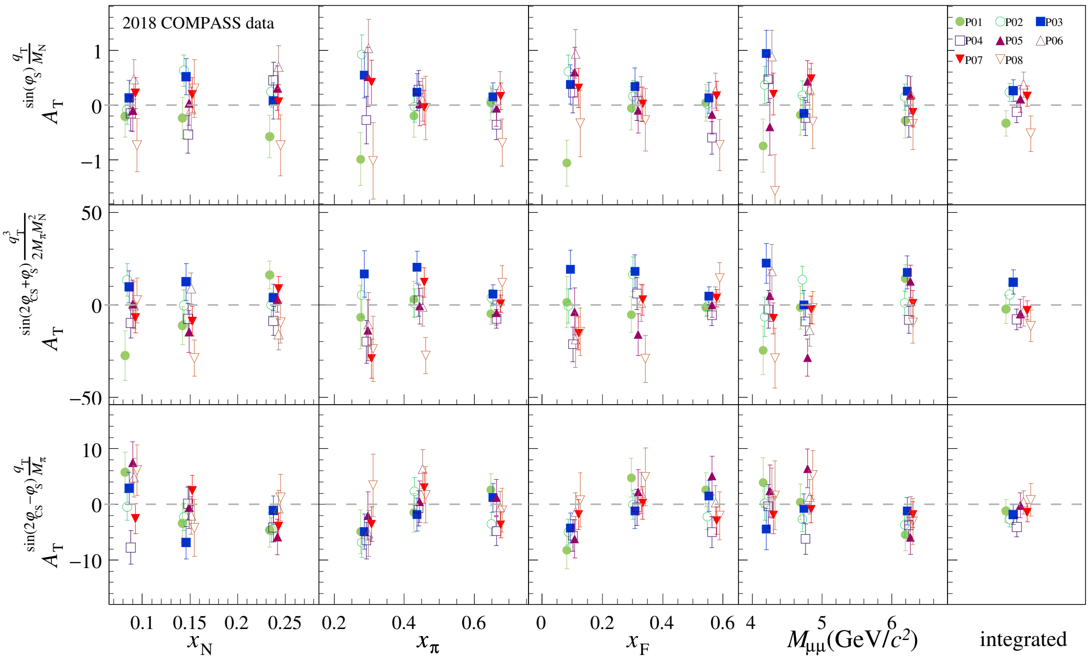

Figure 8.3: The TSAs weighted by f, D and q_T from 8 periods of 2018 Drell-Yann data-taking.

remain unchanged with the application of f and D weighting. For the pretzelosity asymmetries in the 2015 data, a slight reduction in statistical uncertainty is observed,

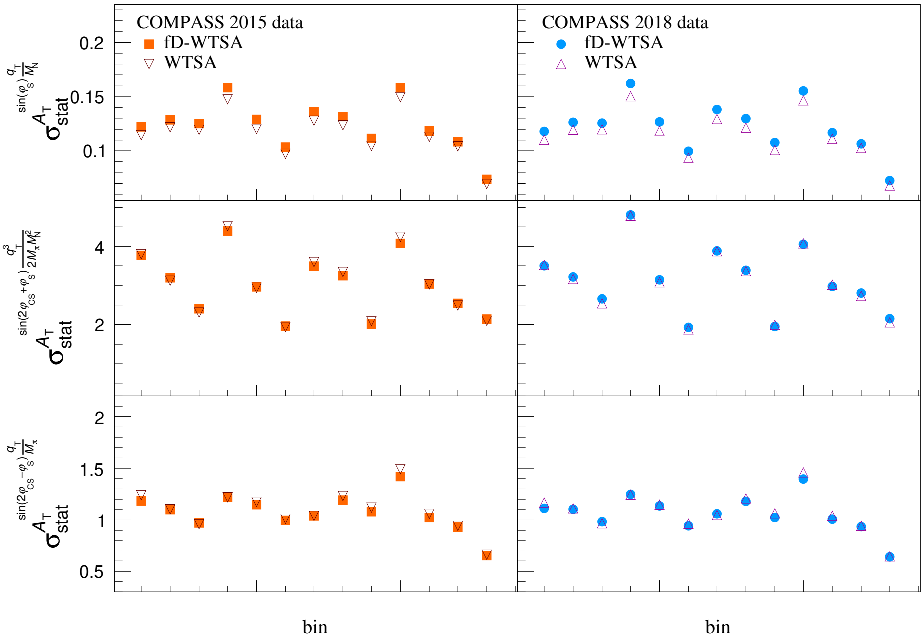

Figure 8.4: Statistical uncertainty values obtained for fD-WTSAs and WTSAs for 2015 (left) and 2018 (right). Points in each panel are grouped in sets of three: the first set corresponds to x_{N}, the second to x_{π}, the third to x_{F}, and the fourth to $M_{\mu\mu}$ bins. The last point represents the result integrated over the full kinematic range.

indicating a potential gain in precision. An unexpected increase in the uncertainty of the Sivers asymmetries led to a detailed review of the weighting procedure, input data, and MC simulations, as discussed in Sec. 8.3.

An additional indication of a potential issue emerged from a systematic test in which the fD-WTSAs are calculated for each year by treating the entire dataset as a large single period. These results are then compared with the average values obtained from individual "real" periods[4] to assess the consistency of the measurements. The analysis revealed discrepancies between the two approaches, as shown in Figs 8.5 and 8.6. While the Sivers and transversity fD-WTSAs and their statistical uncertainties remain consistent across both methods, significant differences are observed for the pretzelosity fD-WTSAs, particularly in the $M_{\mu\mu}$ bin. Asymmetries derived from the full-year method deviated notably from those obtained by averaging over individual periods, with substantially larger uncertainties when the dataset is treated as a single period. This effect is primarily attributed to outlier events, which result from variations in experimental conditions, detector performance, or background contributions across data-taking intervals. A detailed description and analysis of these outliers is provided in Sec. 8.4.

[4] "Real" periods are defined by the COMPASS Collaboration as intervals of relative spectrometer stability; the polarization is reversed approximately in the middle of each period.

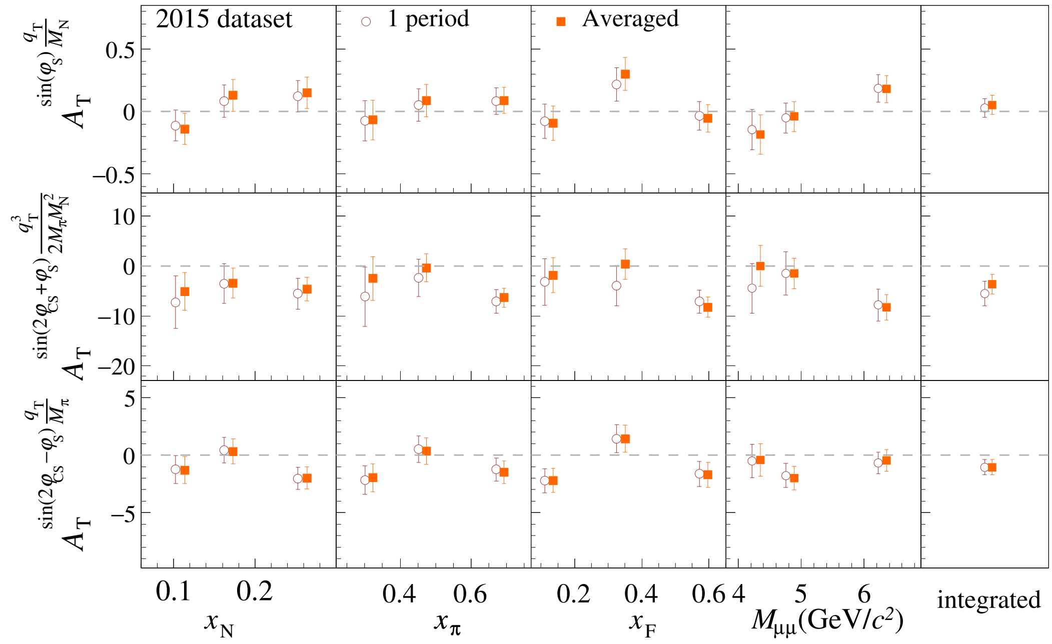

Figure 8.5: Asymmetries averaged over periods (orange filled points) compared to treating the entire year as a single period (burgundy open points) in 2015.

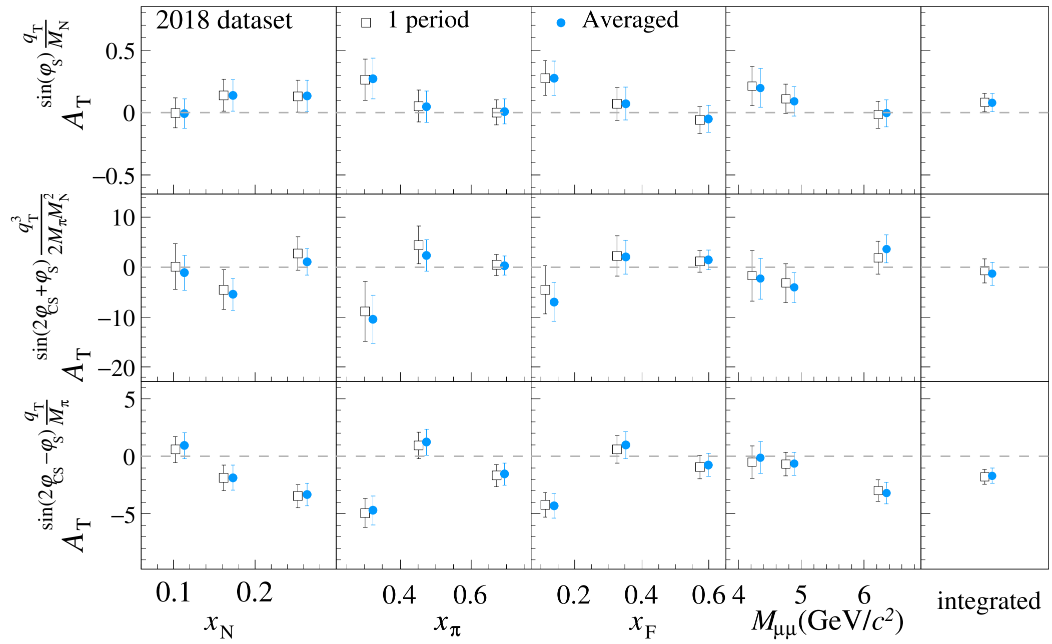

Figure 8.6: Asymmetries averaged over periods (light blue filled points) compared to treating the entire year as a single period (dark blue open points) in 2018.

8.3 Toy Monte Carlo Study

To investigate the observed increase in uncertainty for the Sivers asymmetry when applying the fD-WTSA method, a dedicated toy MC study is conducted. In this approach, simplified simulated datasets are generated without introducing physical asymmetries, following statistical distributions of the DY data that replicate the measured observables. The study aimed to evaluate whether correlations among the dilution factor f, the kinematic factor D, and q_{T} could account for the increased uncertainty. Simulations are performed under both uncorrelated and correlated input scenarios to isolate the effect of these dependencies.

8.3.1 Monte Carlo Samples

To evaluate how each of these factors influences the statistical uncertainty of the extracted asymmetries, two types of Monte Carlo simulations are performed: the uncorrelated MC (uncorr. MC) and the fD-q_{T} correlated MC (fD-q_{T} corr. MC). A schematic representation of the generation procedures for both approaches is shown in Fig. 8.7. Four datasets with increasing event statistics were generated to allow a more robust

Figure 8.7: Schematic comparison of the uncorrelated and fD–q_{T} correlated MC approaches.

comparison between the two scenarios.

1. **Baseline:** Simulated with the same statistics as the 2018 dataset (8 replicas).

2. **10-fold increase in periods:** Total statistics increased tenfold (80 replicas).

3. **100-fold increase in periods:** Statistics scaled 100 times (800 replicas).

4. **100-fold periods with 5-fold more events:** 800 replicas with 5 times more events per replica.

For each generated sample, both the fD-WTSAs and WTSAs are extracted[5]. The MC asymmetry evaluation serves as a validation step, confirming that the MC samples are correctly generated, and is presented in App. C. The key results for the subsequent analysis, namely the uncertainties of the fD-WTSAs and WTSAs, are presented in Sec. 8.3.2, while the analysis of the pulls obtained for the method with increased statistics is discussed in Sec. 8.3.3.

8.3.2 Statistical Error Comparison

Fig. 8.8 shows the statistical uncertainties from both uncorrelated and fD-q_T correlated Monte Carlo simulations at baseline statistics, alongside those from the 2018 Drell–Yan data.

For the uncorrelated MC cases, the uncertainties of the Sivers WTSAs and fD-WTSAs are nearly identical. In the correlated case, however, the uncertainties of the WTSAs are smaller than those of the corresponding fD-WTSAs. The increase in uncertainty due to the fD-q_T correlation closely follows the trend observed in the experimental data.

For the transversity and pretzelosity asymmetries, the uncorrelated simulation gives smaller uncertainties when using the fD-weighted method. This effect arises from using different formulas for the average kinematic factor $\tilde{D}$ (defined in Eq. (6.56)). The $\tilde{D}$ values in the fD-weighted method are systematically larger than in the standard WTSAs, as illustrated in Figs 6.1a and 6.1b. In the fD-q_T correlated scenario, uncertainties for the transversity and pretzelosity asymmetries are generally larger when using the standard WTSA method. In a few bins, notably the first in x_N and the third in x_π, both weighting methods yield nearly identical uncertainties. These MC studies show that correlations among f, D, and q_T affect the statistical uncertainties of the extracted asymmetries, with the largest impact on the Sivers asymmetry. Since the observed increase in uncertainty remains below $\sim 3\%$, it is not included in the systematic uncertainty.

8.3.3 Impact of Period Statistics on Uncertainty Estimation

An example of fD-WTSA pull distributions for 800 MC replicas is shown in Fig. 8.9a[6]. The pull widths exceed the expected value of 1 by approximately 6% for the Sivers asymmetry, 12% for pretzelosity, and 7% for transversity. In the integrated bin, the deviations are smaller, at 2%, 6%, and 3%, respectively[7].

[5]The WTSAs are calculated as a baseline to provide a reference for assessing the impact of incorporating the dilution factor f and kinematic factor D in the fD-WTSAs.

[6]The shown pulls correspond to the fD-q_T correlated case for the fD-WTSA, since the fD-q_T WTSAs and both uncorrelated cases exhibit a similar trend.

[7]Assuming correctly estimated uncertainties, the distribution of pulls is expected to follow a Gaussian distribution with mean $\mu \approx 0$ and standard deviation $\sigma \approx 1$.

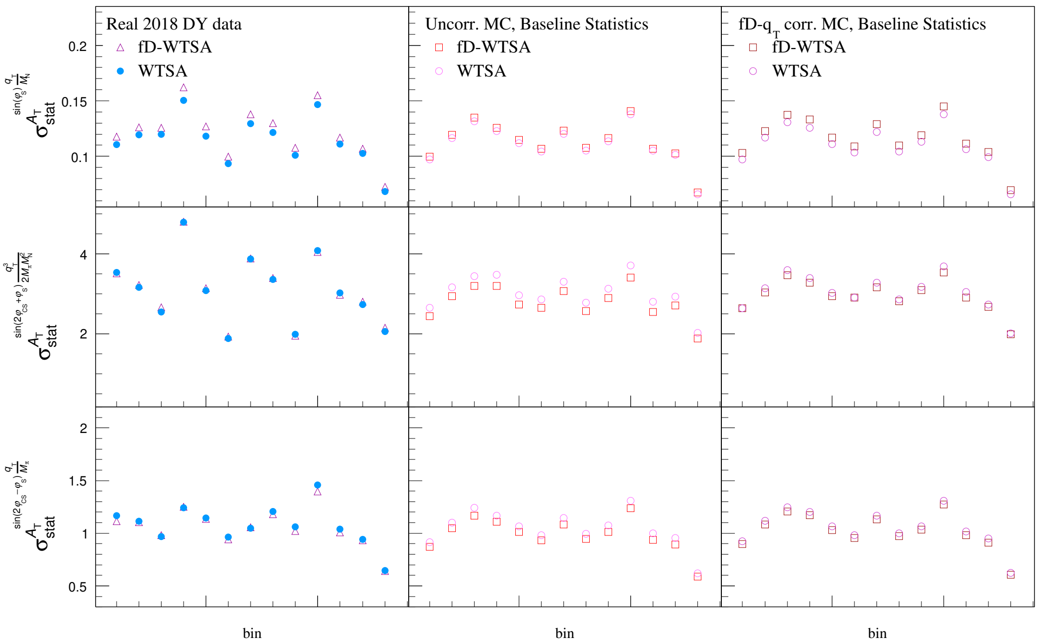

Figure 8.8: Statistical uncertainty values obtained from uncorrelated and fD-q_{T} correlated Monte Carlo samples for baseline statistics, presented alongside a comparison with real 2018 data.

Increasing the number of events per period by a factor of five reduces the pull widths to $\sigma \approx 1$, as shown in Fig. 8.9b. This indicates that the observed underestimation arises from the non-Gaussian distribution of the weighted sums in the modified double ratio, which violates the assumptions underlying the error propagation formula used to derive Eq. (6.24). The magnitude of this effect depends on the specific asymmetry, likely because the validity of the Gaussian approximation is influenced not only by the number of events but also by the order of the powers of q_{T} entering the sums (first power for Sivers and transversity, third power for pretzelosity). To address this issue, the uncertainty is adjusted by rescaling the statistical uncertainties derived from Eq. (6.24), using the factors presented in Tab. 8.1.

Table 8.1: Correction factors applied to the statistical uncertainties of the modified double ratio to address their underestimation.

	$R^{\sin(\varphi_{\mathrm{S}})\frac{q_{\mathrm{T}}}{M_{\mathrm{N}}}}$	$R^{\sin(2\varphi_{\mathrm{CS}}+\varphi_{\mathrm{S}})\frac{q_{\mathrm{T}}^3}{2M_\pi M_{\mathrm{N}}^2}}$	$R^{\sin(2\varphi_{\mathrm{CS}}-\varphi_{\mathrm{S}})\frac{q_{\mathrm{T}}}{M_\pi}}$
Bins of x_{N}, x_π, x_{F}, $M_{\mu\mu}$:	1.06	1.12	1.07
Integrated bin:	1.02	1.06	1.03

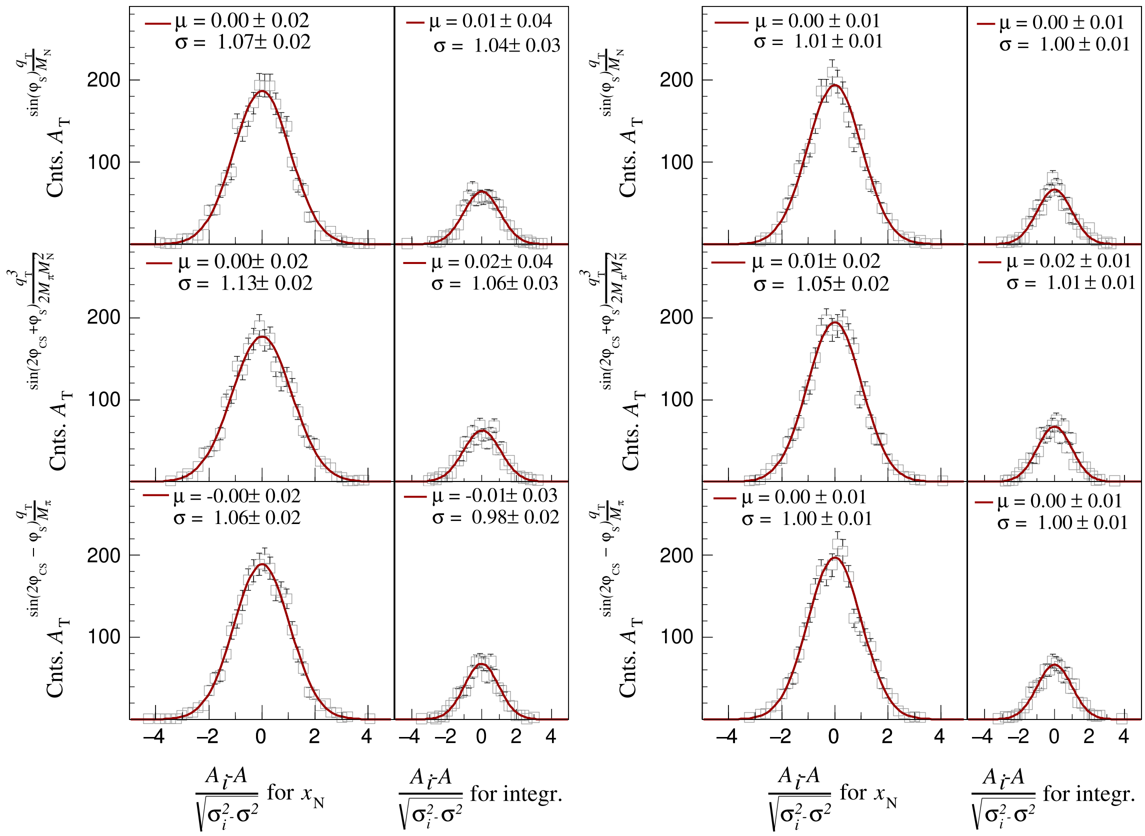

(a) (b)

Figure 8.9: Pulls from fD-q_T correlated Monte Carlo samples for x_N bins and integrated bin: (a) 800 MC replicas, (b) 800 replicas with 5 times more events per replica. Each histogram contains a total number of entries equal to 800 times the number of bins.

8.4 Outlier Weights

Events with very large weights can increase the statistical uncertainty and affect the stability of the results. Since the q_T-weighting methods are particularly sensitive to this effect, a cutoff is introduced to remove events with unphysically large weights that could bias the analysis.

To determine an appropriate cutoff, Monte Carlo simulations were performed using a realistic q_T distribution [128]. The intrinsic transverse momentum of partons, k_T, was modeled with a Gaussian distribution of width 0.9 GeV/c. In these simulations, the observables used in the weighting procedure were available both at the “true” level, before detector effects, and at the “reco” level, after applying detector response and reconstruction algorithms. Comparing the true and reco distributions allowed a systematic evaluation of the reconstruction resolution and its impact on the resulting weights.

Since the pretzelosity weight depends on q_T^3, the resolution study was extended beyond q_T to include the detector-dependent component of the full weighting factor, $Dq_T^3/(2M_\pi M_N^2)$. As shown in Figs 8.10a and 8.10b, reconstruction effects are pronounced when this factor exceeds 300, referred to as the Dq_T threshold. While the true distributions from the MC simulations follow the expected physical behavior, the

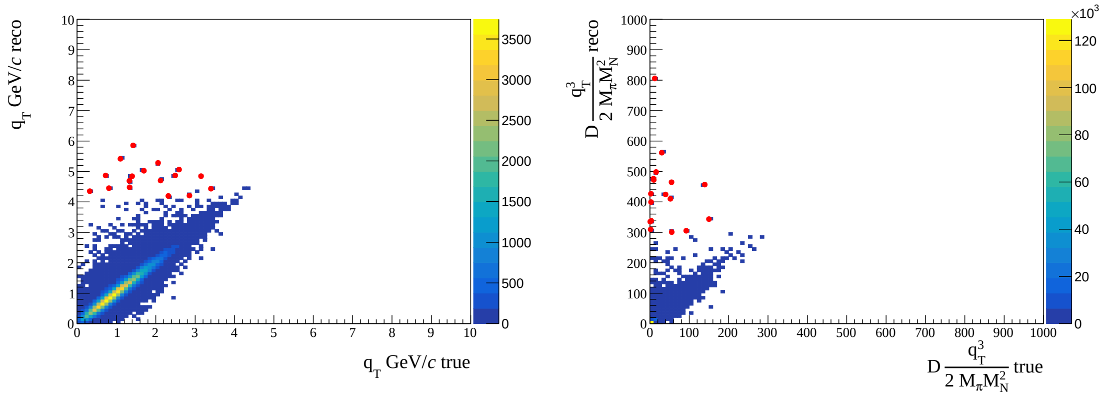

(a) (b)

Figure 8.10: Monte Carlo resolutions, red points indicate excluded events: (a) transverse dimuon momenta, (b) Dq_{T}-weight.

corresponding reconstructed ones exhibit unphysical distortions in this high-weight region..

Building on the resolution study, the next step is to assess whether applying the Dq_{T} threshold has a significant impact on the analysis. To this end, the cut is tested in both the standard and extended mass ranges, although it is not applied in the main analysis for the standard range. As shown in Fig. 8.11, its effect is minimal, removing only the extreme tail of the distribution and affecting about 0.1% of all events. This indicates that events with the largest weights are not concentrated in regions where the DY signal is strongly suppressed. The fraction of removed events and the corresponding event counts are presented in Tab. 8.2[8].

Table 8.2: Number and fraction of events excluded by the Dq_{T} cut for the standard and extended $M_{\mu\mu}$ ranges.

Standard range: (4.3, 8.5) GeV/c^2		
Year	**Events**	%
2015	50	0.12
2018	47	0.11
Extended range: (4.0, 9.0) GeV/c^2		
Year	**Events**	%
2015	66	0.11
2018	67	0.11

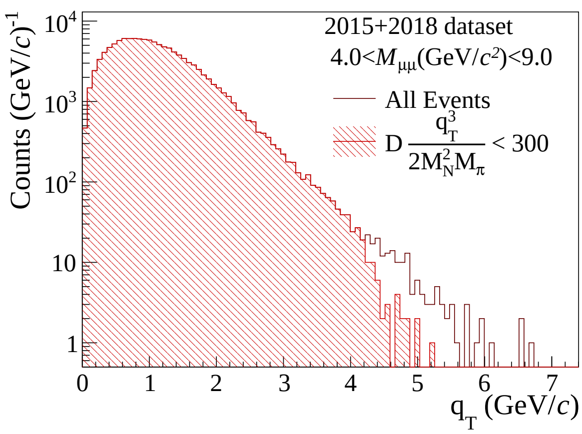

Figure 8.11: Transverse dimuon momentum distribution for $M_{\mu\mu} \in (4.0, 9.0)\,\mathrm{GeV}/c^2$.

The annual asymmetries, after applying the weight cutoff, are shown in Figs 8.12a and 8.12b. They are presented from two perspectives: averaged directly over the full

[8]Although the Dq_{T} cut was not applied when extracting the asymmetry in the standard mass range, the number of excluded events and their corresponding fraction are reported here for reference.

data-taking year, and obtained by first calculating them for each period separately and then averaging the results. Despite averaging over the full year, residual discrepancies remain, most notably in the pretzelosity. To account for this, an additional correction is applied and treated as a source of systematic uncertainty, as discussed in Sec. 8.5.2.

As an alternative to the $D\,q_{\mathrm{T}}^3/(2\,M_\pi\,M_{\mathrm{N}}^2) < 300$ selection, a stricter requirement of $q_{\mathrm{T}} < 2.5$ GeV/c is introduced, referred to as the q_{T} threshold. This choice is motivated by the validity condition of TMD factorization, which requires $q_{\mathrm{T}} \ll \sqrt{Q^2}$. The corresponding asymmetries are shown in Figs 8.13a and 8.13b. While the asymmetry values and uncertainties remain stable, the stricter cut significantly reduces the accessible phase space, violating the assumption of full q_{T} integration in the weighted asymmetry approach. Therefore, the q_{T} cut is not used as the primary selection; the results are provided as supplementary material, offering a complementary view on the stability of the extracted asymmetries.

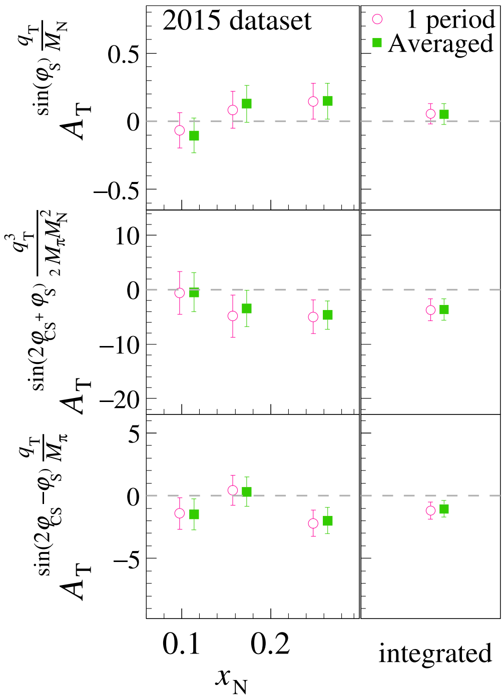

(a)

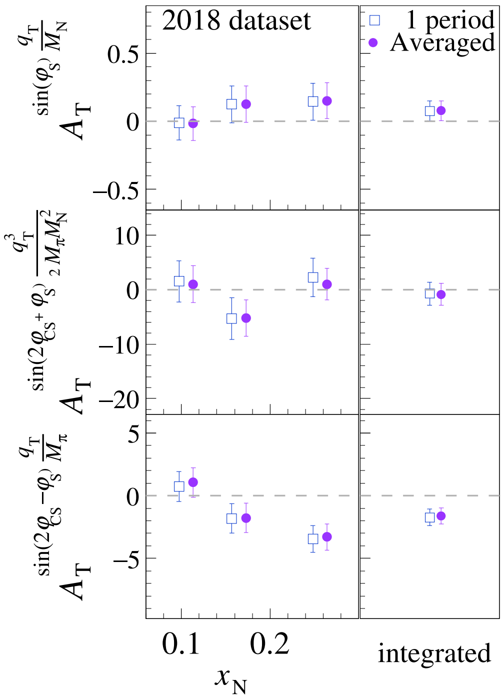

(b)

Figure 8.12: Asymmetries in x_{N} bins and in the integrated bin, comparing averages over individual periods with a single-year treatment, for $D\,q_{\mathrm{T}}^3/(2\,M_\pi\,M_{\mathrm{N}}^2) < 300$: (a) 2015, (b) 2018.

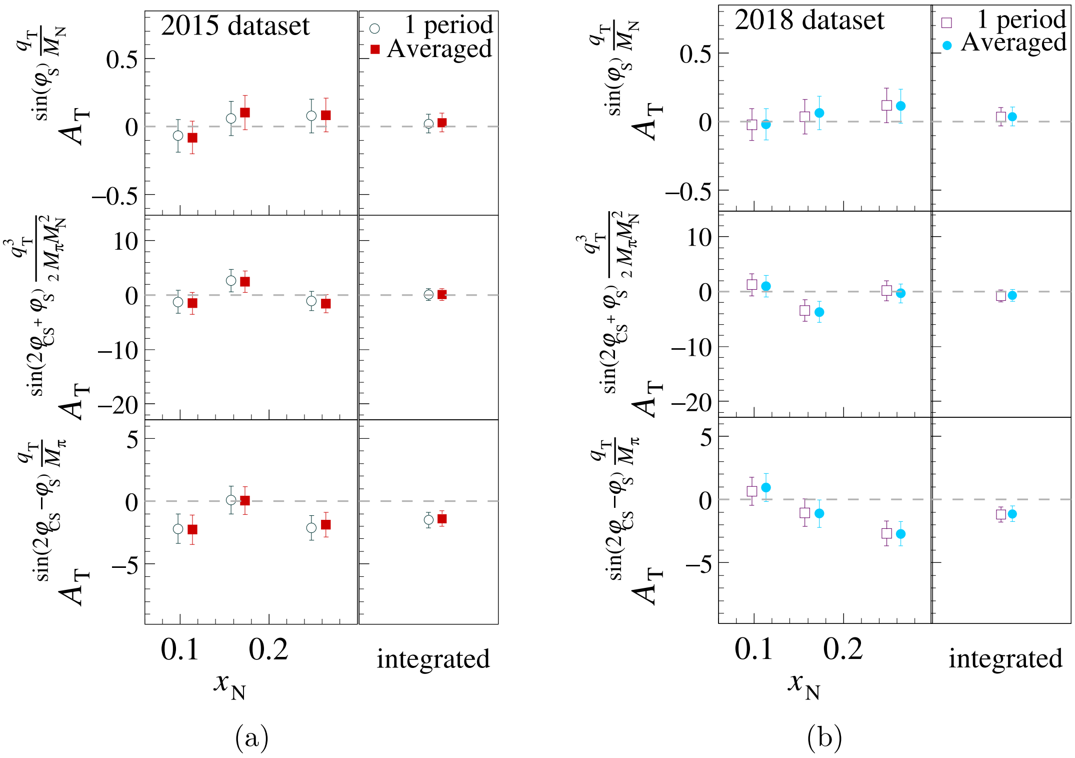

Figure 8.13: Asymmetries in x_N bins and in the integrated bin, comparing averages over individual periods with a single-year treatment, for $q_T < 2.5$ GeV/c: (a) 2015, (b) 2018.

As shown in Tab. 8.3, the q_T cut removes approximately 3.4% of the events from the dataset, while the Dq_T cut affects only about 0.1%. The number and fraction of excluded events for both data-taking periods are summarized in the table on the right. The distributions of cut-off events are illustrated in Appendix E, where the weights associated with each dependency are plotted as functions of q_T.

Table 8.3: Number and percentage of excluded events due to q_T cut for the extended dimuon mass range.

$q_T > 2.5$ GeV/c		
Year	**Events**	**%**
2015	1956	3.38
2018	2123	3.43

8.5 Systematic Studies

The systematic study follows the procedure outlined in Sec. 7.2. Data-taking period compatibility is discussed in Sec. 8.5.1, while Sec. 8.5.2 addresses an additional correction for data inhomogeneity. Sec. 8.5.3 presents the false asymmetry results, including a revised treatment for the integrated bin.

The systematic uncertainty analysis is divided into several independent contributions, which are added in quadrature:

$$\sigma_{\text{sys}}^2 = \sum_{\text{s}} \left(\sigma_{\text{sys}}^{\text{s}}\right)^2 , \tag{8.2}$$

where s denotes the type of source considered in the analysis.

8.5.1 Compatibility of Periods

As in the case of the standard mass range discussed in Sec. 7.2.1, the compatibility of data from different periods is assessed using the pull distributions. Examples for the x_N bins and for the integrated bin are shown in Fig. 8.14a (with the D, q_T cut applied) and in Fig. 8.14b (with the q_T cut applied). Owing to the limited number of bins, the parameters of the Gaussian fits, the mean μ and width σ, are determined with sizable uncertainties. The extracted σ values for both the Dq_T and q_T selections in 2015 and 2018 are consistent with unity within errors, indicating good compatibility between data-taking periods. Compared to the standard mass range (Figs 7.4a and 7.4b), the pull widths are smaller by about 10%, mainly due to the rescaling of statistical uncertainties discussed in Sec. 8.3.3. Consistent results from the χ^2/n_df analysis are presented in Appendix D.1. Consequently, the correction for the pull width was not incorporated into the evaluation of the systematic uncertainties.

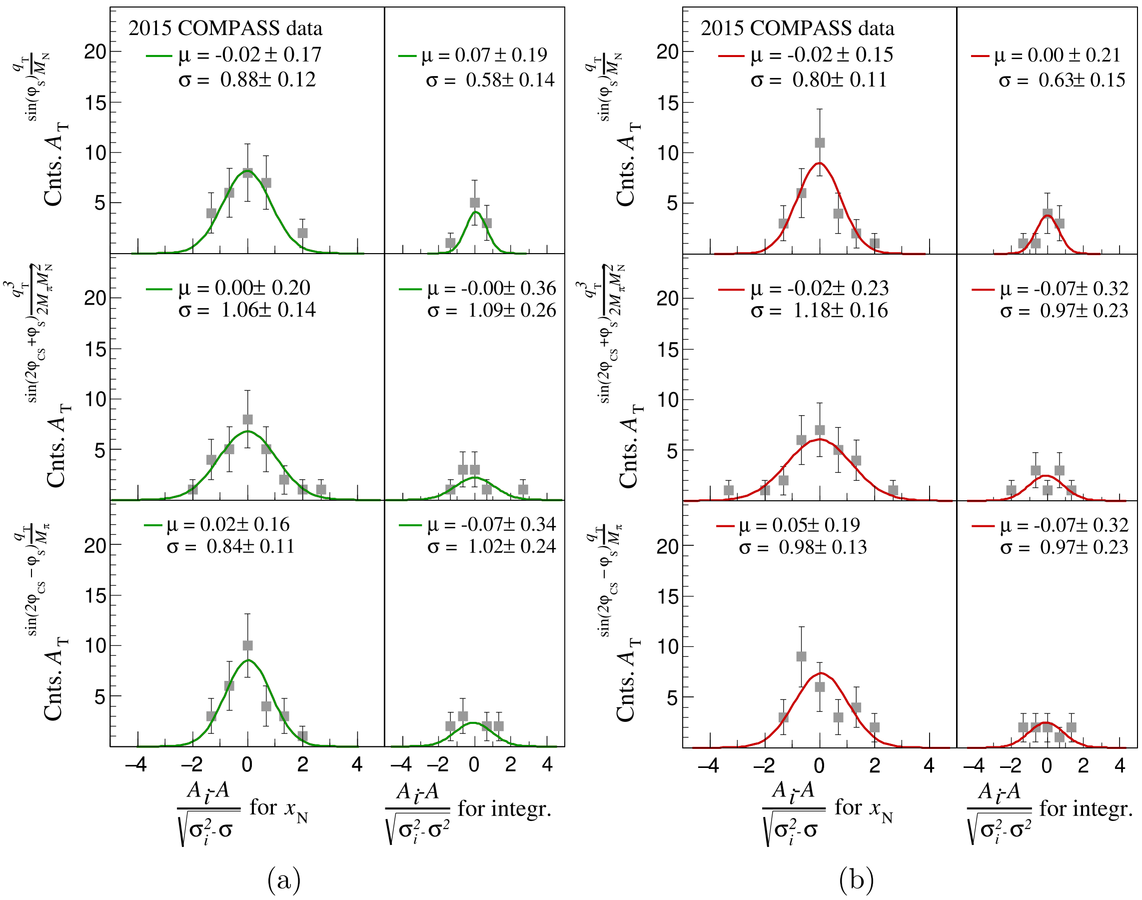

Figure 8.14: Pulls for the fD-WTSAs in the nine periods of 2015, fitted with normal distributions: (a) $D\, q_\mathrm{T}^3/(2\, M_\pi\, M_\mathrm{N}^2) < 300$, (b) $q_\mathrm{T} < 2.5$ GeV$/c$. Each histogram has nine times the number of bin entries.

8.5.2 Systematic Differences Between Period-Averaged and Full-Year Approaches

As noted in Sec. 8.2, asymmetries averaged over individual periods can differ from those computed for the full year, mainly due to data inhomogeneity. Even with the Dq_{T} cut (Figs 8.12a and 8.12b), the differences persist. In contrast, applying q_{T} cut largely reduces the effect. For the Dq_{T} selection, an additional correction is applied to account for residual differences, with the procedure described below.

1. **Calculation of Differences:** The deviation of the asymmetry in each period, $a_{1\ \mathrm{period}}$, from the average asymmetry, a_{avg}, is computed as:

$$\Delta a = |a_{1\ \mathrm{period}} - a_{\mathrm{avg}}| \tag{8.3}$$

2. **Uncertainty Estimation:** The total uncertainty of the asymmetry, σ, is evaluated by combining the uncertainties associated with the single-period measurement, $\sigma_{1\ \mathrm{period}}$, and the asymmetry averaged over all periods, σ_{avg}, taking into account their correlation:

$$\sigma^2 = \sigma^2_{1\ \mathrm{period}} + \sigma^2_{\mathrm{avg}} - 2\,\sigma_{1\ \mathrm{period}}\,\sigma_{\mathrm{avg}}. \tag{8.4}$$

   The last term represents the correlation between the two estimates and is included under the assumption of full correlation.

3. **Systematic Uncertainty Determination:** The systematic uncertainty arising from data inhomogeneity is denoted as $\sigma^{\mathrm{DH}}_{\mathrm{sys}}$. It is assigned only when the observed deviation exceeds the statistical uncertainty:

$$\sigma^{\mathrm{DH}}_{\mathrm{sys}} = \begin{cases} 0 & \text{if } \Delta a < \sigma, \\ \sqrt{\Delta a^2 - \sigma^2} & \text{otherwise.} \end{cases} \tag{8.5}$$

8.5.3 False Asymmetries

In this section, the systematic uncertainties are evaluated using the false asymmetries. The scaling factors introduced in standard mass range analysis, x_{FA}[9], are calculated using the Dq_{T} selection and subsequently applied to the analysis for both discussed datasets: with $Dq^3_{\mathrm{T}}/(2M_\pi M^2_{\mathrm{N}}) < 300$ and $q_{\mathrm{T}} < 2.5$,GeV/c cuts[10]. All related plots of false asymmetries and minor formula modifications are provided in Appendix D.2. The only difference compared to the analysis in the standard mass range is the evaluation of the uncertainty for the integrated bin, which is outlined below.

1. **Calculation of Weighted Average of Asymmetries and their Uncertainty in 3 Bins:** For each kinematic variable (x_{N}, x_π, x_{F}, and $M_{\mu\mu}$), the data

[9] As described in Sec. 7.2.2, scaling factors, x_{FA}, are multiplied by the annual statistical uncertainty in each kinematic bin to obtain the systematic uncertainties from false asymmetries.

[10] False asymmetries were not directly calculated for the dataset with q_{T} cut, as this selection reduces the accessible phase space and could lead to an underestimation of systematic effects.

are provided in three bins. In each bin, the asymmetry A_i and its statistical uncertainty $\sigma_{\mathrm{stat},i}$ are given. The statistical weight for each bin is defined as

$$v_i = \frac{1}{\sigma^2_{\mathrm{stat},i}}. \tag{8.6}$$

The weighted asymmetry A and its statistical uncertainty σ_{stat} for a given kinematic variable are computed as

$$A = \frac{\sum_{i=1}^{3} v_i A_i}{\sum_{i=1}^{3} v_i}, \quad \sigma_{\mathrm{stat}} = \frac{1}{\sqrt{\sum_{i=1}^{3} v_i}}, \tag{8.7}$$

Here, the summation explicitly runs over the three bins in each kinematic variable. This procedure is repeated independently for x_{N}, x_π, x_{F}, and $M_{\mu\mu}$ to obtain the weighted asymmetries and their uncertainties for each quantity.

2. **Systematic Uncertainty with Correlation Between Bins:** The systematic uncertainty from false asymmetries is calculated assuming a complete correlation between the three bins in each kinematic variable (x_N, x_π, x_{F}, and $M_{\mu\mu}$). The total systematic uncertainty $\sigma^{\mathrm{FA}}_{\mathrm{sys}}$ is given by:

$$\left(\sigma^{\mathrm{FA}}_{\mathrm{sys}}\right)^2 = \sum_{i=1}^{3}\sum_{j=1}^{3} \left(\frac{\partial A}{\partial A_i}\right)\left(\frac{\partial A}{\partial A_j}\right) \sigma^{\mathrm{FA}}_{\mathrm{sys},i}\, \sigma^{\mathrm{FA}}_{\mathrm{sys},j}, \tag{8.8}$$

where $\sigma^{\mathrm{FA}}_{\mathrm{sys},i}$ is the systematic uncertainty for bin i, and the partial derivatives of the asymmetry A with respect to each bin are:

$$\frac{\partial A}{\partial A_i} = \frac{v_i}{\sum_{i=1}^{3} v_i}. \tag{8.9}$$

Eq. (8.8) then becomes:

$$\left(\sigma^{\mathrm{FA}}_{\mathrm{sys}}\right)^2 = \frac{1}{\left(\sum_{i=1}^{3} v_i\right)^2} \sum_{i=1}^{3}\sum_{j=1}^{3} v_i v_j\, \sigma^{\mathrm{FA}}_{\mathrm{sys},i}\, \sigma^{\mathrm{FA}}_{\mathrm{sys},j}. \tag{8.10}$$

Since the sums over i and j are identical, the equation simplifies to:

$$\sigma^{\mathrm{FA}}_{\mathrm{sys}} = \sqrt{\frac{\left(\sum_{i=1}^{3} v_i\, \sigma^{\mathrm{FA}}_{\mathrm{sys},i}\right)^2}{\left(\sum_{i=1}^{3} v_i\right)^2}}. \tag{8.11}$$

3. **Systematic Uncertainty Determination for Integrated Bin:** To estimate the absolute systematic uncertainty for the integrated bin, we computed the average of the systematic uncertainties across the four kinematic variables.

Table 8.4: Ratio of systematic to statistical uncertainties, x_{FA}, derived from binned variables under the selection $Dq_{\mathrm{T}}^3/(2, M_\pi, M_{\mathrm{N}}^2) < 300$, representing the relative contribution of false asymmetries to the total systematic uncertainty.

Year	Sivers	Pretzelosity	Transversity
2015	0.65	0.61	0.87
2018	1.01	0.67	0.97

8.6 Final Asymmetry Results

8.6.1 Annual Asymmetries

The fD-WTSA determined separately for each of the nine data-taking periods in 2015 and the eight periods in 2018, are used to extract the annual asymmetries according to Eq. (7.2). The results with the Dq_{T} cut are presented in Fig. 8.15, and those with the q_{T} cut in Fig. 8.16.

The sources of systematic uncertainty differ between the two asymmetry extractions. For the Dq_{T} selection, the uncertainty arises from two main contributions: false asymmetries ($\sigma_{\mathrm{sys}}^{\mathrm{FA}}$) and data inhomogeneity ($\sigma_{\mathrm{sys}}^{\mathrm{DH}}$). In terms of q_{T} selection, false asymmetries constitute the only source of systematic uncertainty. The Sivers and transversity asymmetries are consistent and exhibit comparable uncertainties for both selection conditions. In contrast, the pretzelosity asymmetry exhibits a clear reduction in both statistical and systematic uncertainties under the q_{T} cut, primarily due to the removal of events with exceptionally large weights that remain included under the Dq_{T} selection.

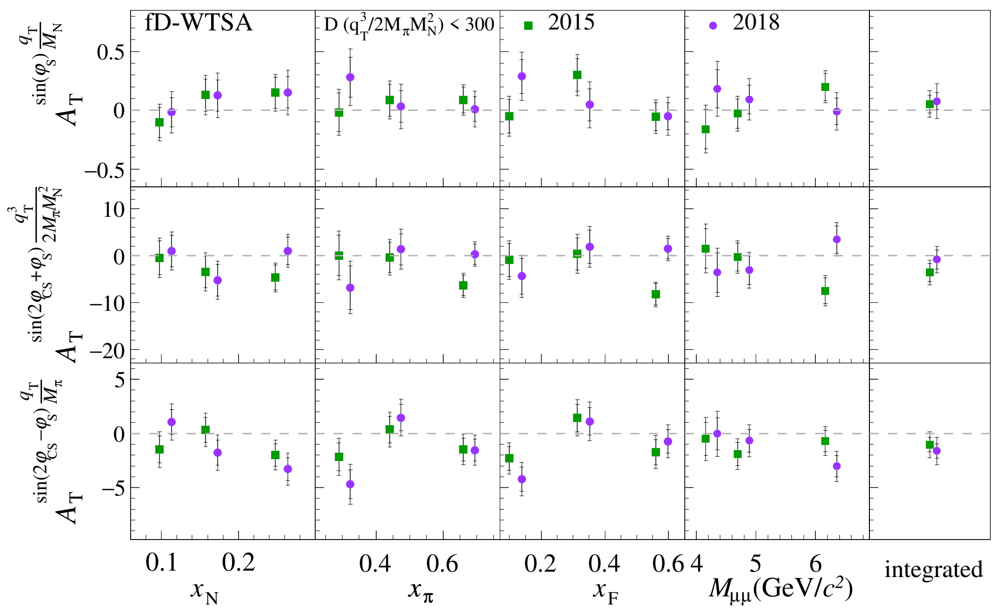

Figure 8.15: The annual fD-WTSAs from the 2015 and 2018 COMPASS data for $D\,q_{\mathrm{T}}^3/(2\,M_\pi\,M_{\mathrm{N}}^2) < 300$.

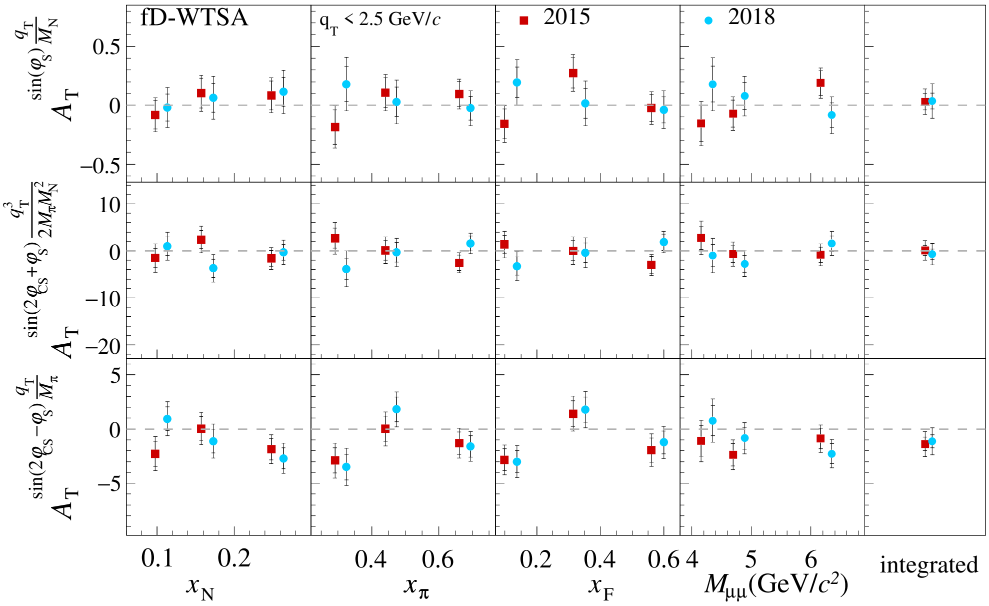

Figure 8.16: The annual fD-WTSAs from the 2015 and 2018 COMPASS data for $q_T < 2.5$ GeV/c.

8.6.2 Correction for Year-to-Year Discrepancies

In certain kinematic bins, particularly those corresponding to x_π, x_F, and $M_{\mu\mu}$, differences are observed between the 2015 and 2018 results for both the Dq_T and q_T selections. Since no clear explanation for these discrepancies is identified—aside from their correlation with events at large q_T—they are treated as an additional source of systematic uncertainty. The corresponding procedure for estimating this uncertainty is described below.

1. **Calculation of the Asymmetry Difference** The absolute difference in asymmetry values between 2015 and 2018 is computed as:

$$\Delta a = |a_{2015} - a_{2018}|. \tag{8.12}$$

2. **Estimation of the Combined Statistical Uncertainty** The total statistical uncertainty on the difference is calculated by adding the individual uncertainties in quadrature:

$$\sigma = \sqrt{\sigma_{2015}^2 + \sigma_{2018}^2}. \tag{8.13}$$

3. **Evaluation of the Systematic Uncertainty** The systematic uncertainty due to annual differences between data-taking years is estimated as follows. If the observed difference exceeded the combined statistical uncertainty, the excess is attributed to a systematic effect. The corresponding systematic uncertainty, denoted $\sigma_{\text{sys}}^{\text{AD}}$, is then defined as:

$$\sigma_{\text{sys}}^{\text{AD}} = \begin{cases} 0 & \text{if } \Delta a < \sigma, \\ \sqrt{\Delta a^2 - \sigma^2} & \text{otherwise.} \end{cases} \tag{8.14}$$

8.6.3 Combined Asymmetries

To obtain the final statistical and systematic uncertainties for the combined 2015 and 2018 results, the procedure described in Sec. 7.3.2 is applied. The combined asymmetries, including the uncertainties arising from each applied correction, are provided in Appendix F. Fig. 8.17 shows the combined fD-WTSAs for both selection criteria. A detailed analysis of these results is presented in the subsequent two sections.

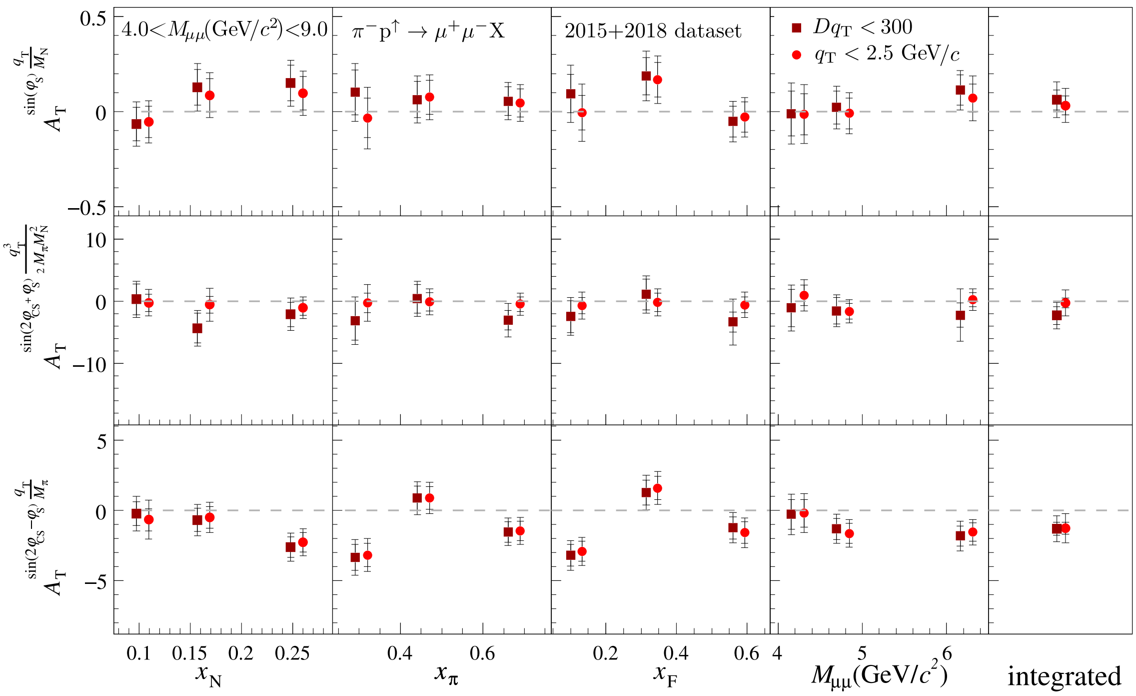

Figure 8.17: The combined fD-WTSAs from the 2015 and 2018 COMPASS data for the two sections described.

8.7 Impact of Mass Range Expansion on Asymmetry Results

To directly evaluate the effect of the mass-range extension, the fD-WTSAs were recalculated for the standard mass range and compared with those obtained using the extended range. This comparison isolates the influence of the mass range itself, independent of any changes in the calculation procedure. An example of the measured asymmetries for the x_{N} bins and the integrated bin is presented in Figs 8.18a and 8.18b. A reduction in total uncertainties of approximately 11-30% for $q_{\mathrm{T}} < 2.5$ GeV$/c$ and 20-40% for $Dq_{\mathrm{T}}^3/(2M_\pi M_{\mathrm{N}}^2) < 300$ is observed[11], demonstrating the improved precision achieved with the extended mass range.

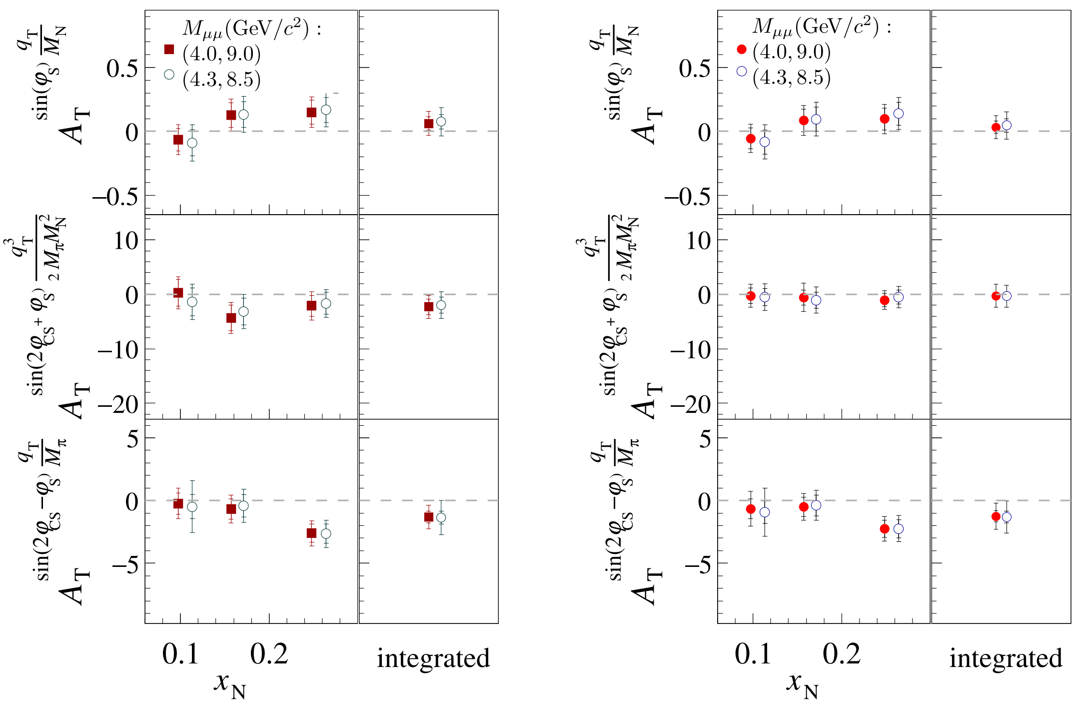

(a) (b)

Figure 8.18: The fD-WTSAs from the combined 2015 and 2018 data, shown for both the extended and standard mass ranges: (a) $D\,q_{\mathrm{T}}^3/(2\,M_\pi\,M_{\mathrm{N}}^2) < 300$, (b) $q_{\mathrm{T}} < 2.5$ GeV$/c$.

[11] Uncertainties in the $M_{\mu\mu}$ bins decrease by approximately 2-5%, although direct comparison is limited by the redefined binning after the mass range extension.

8.8 Transverse Momentum-Scaled Asymmetries

To assess compatibility and enable direct comparison with the unweighted TSA asymmetries, the annual results obtained with theDq_{T} and q_{T} cuts were rescaled by the corresponding average q_{T} weights. The combined asymmetries from the rescaled data are compared with the TSA results [94] in Fig. 8.19.

For both the Sivers and transversity asymmetries, the values obtained using the q_{T} scaling cut agree with those from the Dq_{T} selection, demonstrating the stability of the extracted asymmetries. Despite the phase-space restriction imposed to remain within the validity of TMD factorization, the results remain consistent. Even for the pretzelosity asymmetry, which involves a q_{T}^3 scaling factor and is more sensitive to statistical fluctuations, agreement is observed within the systematic uncertainties. Overall, the results are compatible with the corresponding TSA analysis.

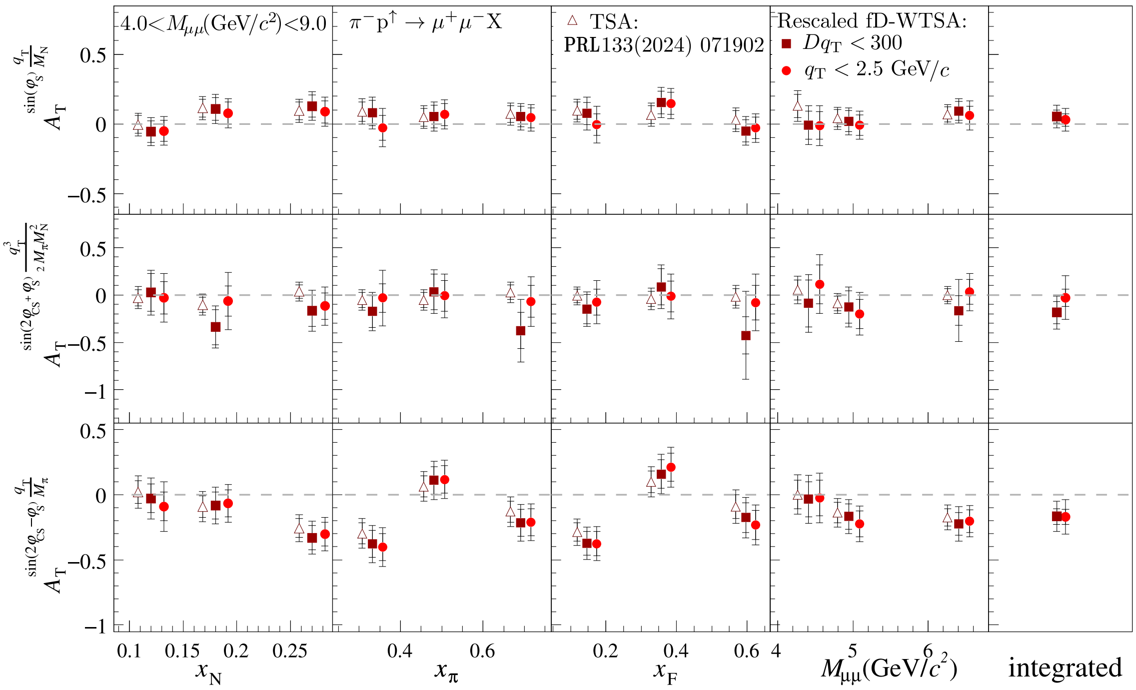

Figure 8.19: The combined rescaled fD-WTSAs from the 2015 and 2018 COMPASS data for the two selection criteria, together with the corresponding TSAs [94].

Chapter 9

Accessing TMD PDFs via Weighted Asymmetries

All of physics is either impossible or trivial.
It is impossible until you understand it,
and then it becomes trivial.

— Ernest Rutherford

The asymmetries obtained in Chapter 8 are used to extract the k_{T}^2 moments of the Sivers and Boer–Mulders TMD PDFs. This study provides a foundation for a more detailed investigation of TMD PDFs, which will be pursued in future work. The analysis begins with the extraction of the first k_{T}^2 moment of the Sivers TMD PDF in Sec. 9.1, and then proceeds to the extraction of the first k_{T}^2 moment of the Boer–Mulders function in Sec. 9.2.

9.1 Extraction of the Nucleon Sivers Effect

Among the measured fD-WTSAs, the Sivers asymmetry is particularly interesting, as it directly probes the nucleon TMD Sivers function. The corresponding asymmetry expression in the TMD-factorised framework, given in Eq. (2.52), involves a sum over all quark flavours. In the COMPASS experiment, the valence quark region of both the pion and the nucleon was probed. Consequently, only valence quarks are relevant, and sea quarks can be safely neglected. Therefore, restricting the sum to valence quarks leads to the simplified expression[1]:

$$A_{\mathrm{T}}^{\sin\varphi_{\mathrm{S}}\,\frac{q_{\mathrm{T}}}{M_{\mathrm{N}}}} \approx 2\,\frac{f_{1\mathrm{T,\,N}}^{\perp(1)\mathrm{u}}(x_{\mathrm{N}})}{f_{1,\,\mathrm{N}}^{\mathrm{u}}(x_{\mathrm{N}})}. \tag{9.1}$$

where $f_{1\mathrm{T,N}}^{\perp(1)\mathrm{u}}(x_{\mathrm{N}})$ denotes the first k_{T}^2 moment of the Sivers TMD PDF for u-quark, while $f_{1,\mathrm{N}}^{\mathrm{u}}(x_{\mathrm{N}})$ represents the number density of the corresponding quark in the nucleon[2].

[1] In this case, for the π^- ($\mathrm{d\bar{u}}$), the d and $\mathrm{\bar{u}}$ quarks dominate, whereas for the proton (uud), the valence u and d quarks provide the main contributions to TMD PDFs.

[2] The dependence on Q^2 has been omitted for clarity of notation.

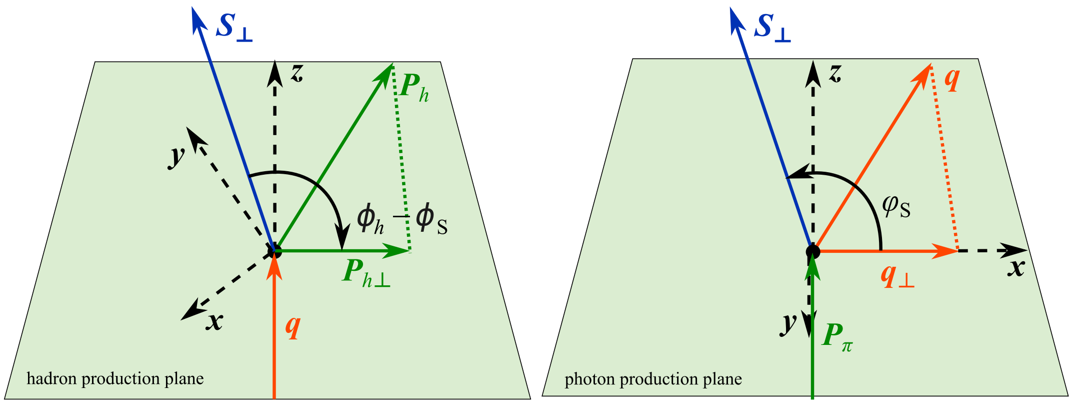

(a) (b)

Figure 9.1: The Sivers angles in the (a) Drell–Yan target frame and (b) SIDIS $\gamma^* N$ frame along the z-axis have opposite orientations. As a result, reversing the sign of the Sivers function between the processes does not affect the sign of the Sivers asymmetry [128].

Since a key aim of this section is the comparison of the extracted first k_{T}^2 moment of the Sivers TMD PDF with analogical recent SIDIS COMPASS results, it is crucial to first clarify the conventions for signs and angular definitions of the Sivers asymmetry in these two processes. In SIDIS, the Sivers angle is defined as $\phi_{\mathrm{h}} - \phi_{\mathrm{S}}$ in the $\gamma^* N$ frame, as illustrated in Fig. 9.1a. In the Drell–Yan process, the Sivers angle φ_{S} is specified in the target rest frame, as shown in Fig. 9.1b. At the same time, QCD predicts a fundamental process dependence of the Sivers function, expressed in Eq. (1.18). Taking into account the difference in angular conventions, the Sivers asymmetry is expected to have the same sign in both processes. This relies on the dominance of the same quark flavour in each reaction, which is indeed the case for SIDIS in $\mu^+\,\mathrm{p}^\uparrow$ and for $\pi^-\,\mathrm{p}^\uparrow$ Drell–Yan. Consequently, and in accordance with the predicted sign change of the Sivers function between Drell–Yan and SIDIS (Eq. (1.18)), a minus sign must be included when extracting the first k_{T}^2 moment from the measured asymmetry.

Accordingly, the first k_{T}^2 moment of the Sivers function is obtained from Eq. (9.1) as:

$$f_{1\mathrm{T,N}}^{\perp(1)\mathrm{u}}(x_{\mathrm{N}}) = -\frac{1}{2}\, A_{\mathrm{T}}^{\mathrm{Sivers}}\, f_{1,\mathrm{N}}^{\mathrm{u}}(x_{\mathrm{N}}). \tag{9.2}$$

Its uncertainty is evaluated by propagating only the total uncertainty of the measured asymmetry, while the unpolarised u-quark distribution is assumed to be precisely known:

$$\sigma_{f_{1\mathrm{T,N}}^{\perp(1)\mathrm{u}}} = \frac{1}{2}\, f_{1,\mathrm{N}}^{u}\, \sigma_{A_{\mathrm{T}}^{\mathrm{Sivers}}}, \tag{9.3}$$

where $A_{\mathrm{T}}^{\mathrm{Sivers}}$ denotes the Sivers fD-WTSA asymmetry, and $\sigma_{A_{\mathrm{T}}^{\mathrm{Sivers}}}$ its total uncertainty[3].

The first k_{T}^2 moment of the Sivers TMD PDFs was extracted in three x_{N} bins as well as for the integrated bin covering the full DY statistics, using two selection criteria: $Dq_{\mathrm{T}}^3/(2M_\pi M_{\mathrm{N}}^2) < 300$ and $q_{\mathrm{T}} < 2.5$ GeV/c. This so-called point-by-point extraction was originally developed for an analogous analysis in SIDIS [138]. The well-known proton number densities were taken from the CTEQ5D set in the LHAPDF

[3]For clarity, the asymmetry symbol is simplified from $A_{\mathrm{T}}^{\sin\varphi_{\mathrm{S}}\frac{q_{\mathrm{T}}}{M_{\mathrm{N}}}}$ to $A_{\mathrm{T}}^{\mathrm{Sivers}}$.

library [139] at the mean values of x_{N} and Q^2 (Fig. 9.2) for each of the three bins. For the integrated point, $f_{1\mathrm{T,N}}^{\perp(1)\mathrm{u}}$ was evaluated at $Q^2 = 26$ GeV^2 and $x = 0.157$, corresponding to the COMPASS DY data-taking conditions for the combined 2015 and 2018 runs. The number density distributions for all quark flavours at the COMPASS scale are shown in Fig. 9.3.

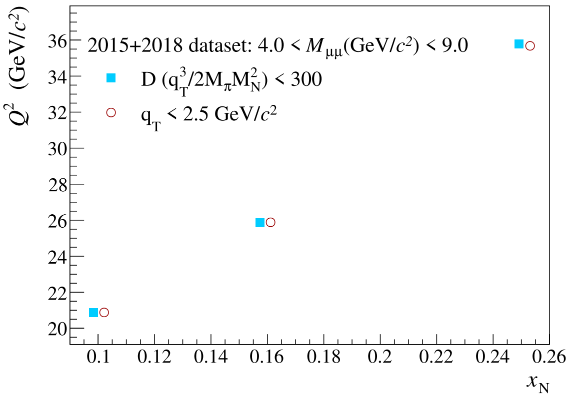

Figure 9.2: The Q^2 in the bins of x_{N} for the 2015 and 2018 DY data-taking campaigns. The points for q_{T} cut are staggered for clarity.

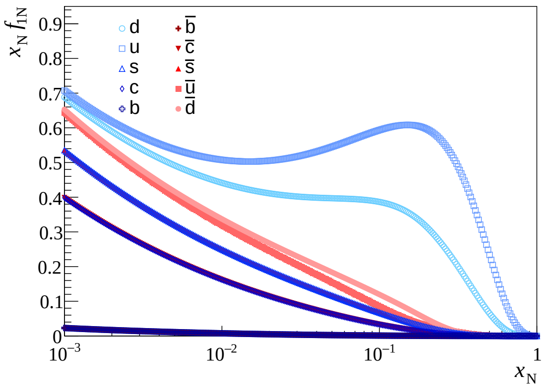

Figure 9.3: CTEQ5D proton PDFs [139] evaluated at $Q^2 = 26\,(\mathrm{GeV}/c)^2$, corresponding to the mean Q^2 value of the COMPASS Drell–Yan measurement.

A direct comparison of the first k_{T}^2 moment of the Sivers TMD PDF in SIDIS and DY is shown[4] in Figs 9.4a and 9.4b, with Fig. 9.4a corresponding to an extraction from fD-WTSA with a cut of $Dq_{\mathrm{T}}^3/(2M_\pi M_{\mathrm{N}}^2) < 300$, and Fig. 9.4b showing the result with $q_{\mathrm{T}} < 2.5$ GeV$/c$. In both cases, the significantly larger statistical uncertainties in the Drell–Yan measurement primarily reflect the fact that the COMPASS experimental setup was not fully optimalised to Drell–Yan, resulting in a smaller number of collected events compared to the SIDIS measurements. Despite these differences, the extracted values of $f_{1\mathrm{T,N}}^{\perp(1)\mathrm{u}}(x_{\mathrm{N}})$ show satisfactory agreement with recent extractions from COMPASS SIDIS data, as well as with phenomenological estimates [140]. The results are summarized in Tabs 9.1a and 9.1b.

A comparison of the first k_{T}^2 moments across the three x_{N} bins for the two selection cuts shows differences ranging from about 16% in the first bin to approximately 35% in the remaining bins. For the integrated bin, the $f_{1\mathrm{T,N}}^{\perp(1)\mathrm{u}}$ is roughly twice as large under the $Dq_{\mathrm{T}}^3/(2M_\pi M_{\mathrm{N}}^2) < 300$ cut compared to $q_{\mathrm{T}} < 2.5$ GeV$/c$. Imposing the q_{T} cut removes events with unusually large weights. In contrast, the Dq_{T} condition allows such events to remain, which leads to an increase in the uncertainty of the asymmetry (see Sec. 8.6.3), and consequently also affects the extracted TMD PDFs.

For two of the three x_{N} bins, as well as for the integrated one, the first k_{T}^2 moment of the Sivers function points toward negative values. This behavior is consistent with the predicted sign change associated with its T-odd nature (see Eq. (1.18)). The first point at low x_{N} exhibits an inconclusive trend, likely due to the approximations employed in the extraction procedure. In particular, Eq. (9.1) neglects the contributions

[4] In COMPASS, the SIDIS and DY measurements were performed at different Q^2, where the Sivers functions could in principle be modified by QCD evolution. These effects are neglected.

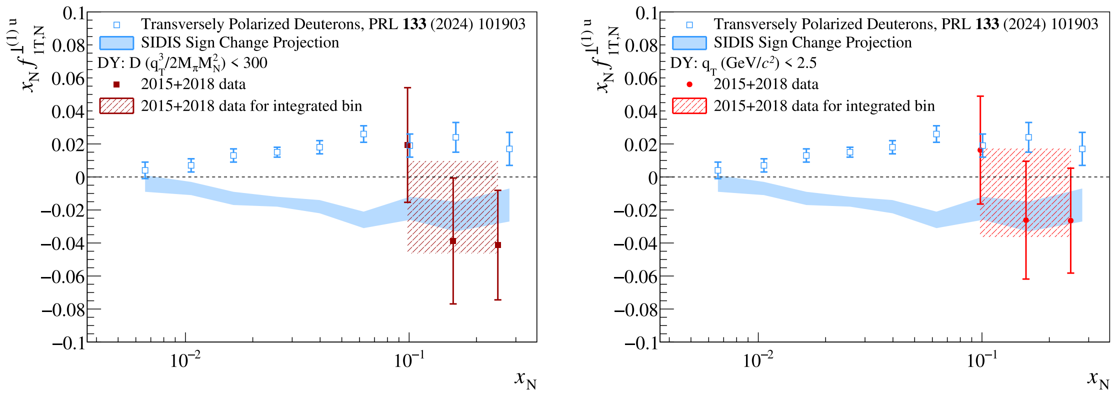

(a) (b)

Figure 9.4: Comparison with the point-by-point extraction from DY fD-WTSA and SIDIS asymmetries [141], using the same unpolarized proton PDFs (CTEQ5D [139]). Panel (a) represents extraction from fD-WTSA with $Dq_T^3/2M_\pi M_N^2 < 300$ cut, while panel (b) with $q_T < 2.5$ GeV/c cut. The blue shaded bands indicate the projected sign change based on the SIDIS results [141], while the red bands correspond to the measured $f_{1T,N}^{\perp(1)u}$ and its total uncertainty for the integrated bin.

Table 9.1: The first k_T^2 moment of Sivers TMD PDFs extracted from DY fD-WTSA measurements with: (a) $Dq_T^3/(2M_\pi M_N^2) < 300$ cut, (b) $q_T < 2.5$ GeV/c cut.

(a)

x_N	A_T^{Sivers}	$f_{1T}^{\perp(1)u}$
0.097	-0.067 ± 0.118	0.019 ± 0.035
0.157	0.128 ± 0.126	-0.039 ± 0.039
0.248	0.150 ± 0.121	-0.041 ± 0.034
Integrated point		
x_N	A_T^{Sivers}	$f_{1T}^{\perp(1)u}$
0.157	0.062 ± 0.094	-0.0183 ± 0.0280

(b)

x_N	A_T^{Sivers}	$f_{1T}^{\perp(1)u}$
0.097	-0.055 ± 0.111	0.016 ± 0.033
0.157	0.086 ± 0.118	-0.026 ± 0.036
0.248	0.096 ± 0.116	-0.026 ± 0.032
Integrated point		
x_N	A_T^{Sivers}	$f_{1T}^{\perp(1)u}$
0.157	0.032 ± 0.090	-0.0096 ± 0.0267

of sea quarks, an assumption that is well justified at intermediate and large x_{N}, where valence-quark contributions dominate. In the first bin, corresponding to the lowest x_{N} values, the deviation from the sign-change prediction may be partly related to this approximation, as the influence of sea quarks in this region becomes more significant.

9.2 Extraction of the Pion Boer–Mulders Effect

According to Eq.(2.53), the transversity asymmetry provides insight not only into the proton transversity TMD PDF but also into the first k_{T}^2 moment of the Boer-Mulders TMD PDF for the pion. Since the COMPASS Collaboration has already measured proton transversity via SIDIS [142, 143], the present analysis is focused on the extraction of the Boer-Mulders function.

Let us first assume that the Boer–Mulders and transversity TMD PDFs of sea quarks vanish. This is motivated by the fact that the sea-quark transversity extracted from current experimental data is consistent with zero [144], while the Boer–Mulders function of sea quarks remains unknown. This leads to the following simplified of Eq.(2.53):

$$A_{\mathrm{T}}^{\sin(2\varphi_{\mathrm{CS}}-\varphi_{\mathrm{S}})\frac{q_{\mathrm{T}}}{M_\pi}}(x_\pi, x_{\mathrm{N}}) \approx -2e_u^2 \frac{h_{1,\pi}^{\perp(1)\bar{\mathrm{u}}}(x_\pi)\, h_{1,\mathrm{N}}^{\mathrm{u}}(x_{\mathrm{N}})}{\sum_q e_{\mathrm{q}}^2 \left[f_{1,\pi}^{\bar{q}}(x_\pi)\, f_{1,\mathrm{N}}^{q}(x_{\mathrm{N}}) + (\mathrm{q} \leftrightarrow \bar{\mathrm{q}})\right]}. \tag{9.4}$$

where $h_{1,\mathrm{N}}^{\mathrm{u}}(x_{\mathrm{N}})$ represents the transversity distribution of the proton, and $h_{1,\pi}^{\perp(1)\bar{\mathrm{u}}}(x_\pi)$ is the first k_{T}^2 moment of the Boer–Mulders function of the pion.

Considering that only valence quarks contribute to the denominator, the following expression is used for the extraction[5]:

$$A_{\mathrm{T}}^{\sin(2\varphi_{\mathrm{CS}}-\varphi_{\mathrm{S}})\frac{q_{\mathrm{T}}}{M_\pi}}(x_\pi, x_{\mathrm{N}}) \approx -2\, \frac{h_{1,\pi}^{\bar{\mathrm{u}}\perp(1)}(x_\pi)\, h_{1,\mathrm{N}}^{\mathrm{u}}(x_{\mathrm{N}})}{f_{1,\pi}^{\bar{\mathrm{u}}}(x_\pi)\, f_{1,\mathrm{N}}^{\mathrm{u}}(x_{\mathrm{N}})} \tag{9.5}$$

The pion number density, a TMD PDF not as precisely determined as that of the proton, was taken from the GRV-PI LO set [145]. It was evaluated at the mean values of x_π and Q^2 for each of the three bins (Fig. 9.5), and at $Q^2 = 26$ (GeV/c)^2 with $x_\pi = 0.5$ for the integrated one. The pion number density distributions at the COMPASS scale are shown in Fig. 9.6.

While the number densities of the pion and nucleon appearing in the denominator of Eq. (9.5) can be readily obtained from global PDF sets such as those available in LHAPDF [146], the transversity distribution used in the numerator is poorly known. In this analysis, the transversity distribution used in the numerator is taken from the point-by-point extraction [143], which will be discussed in more detail in the following section.

[5] As discussed in Sec. 9.1, valence–sea and sea–sea terms are strongly suppressed in the COMPASS kinematic region due to the small magnitude of the sea-quark PDFs.

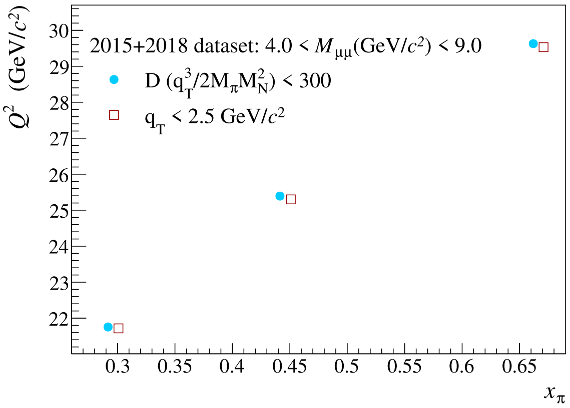

Figure 9.5: The Q^2 in the bins of x_π for the 2015 and 2018 DY data-taking campaigns. The points for q_T cut are staggered for clarity.

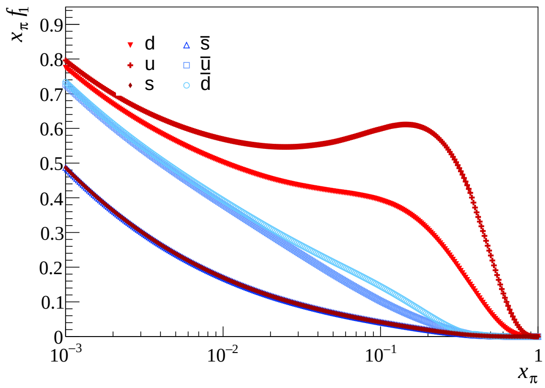

Figure 9.6: GRV-PI LO pion PDFs [145] evaluated at $Q^2 = 26\,(\mathrm{GeV}/c)^2$, corresponding to the mean Q^2 value of the COMPASS Drell–Yan measurement.

9.2.1 Transversity TMD PDF from SIDIS data

The transversity distributions were extracted from Collins asymmetries in SIDIS COMPASS data [142]. The corresponding Q^2 values rise with x_N, ranging roughly from 20 to 36 $(\mathrm{GeV}/c)^2$ for $x_\mathrm{N} \in [0.095, 0.3]$ (Fig. 9.2). The extracted points are then fitted using a simple functional form:

$$h_{1,\mathrm{N}}^{\mathrm{u}}(x_\mathrm{N}) = a\,\frac{x_\mathrm{N}^b(1-x_\mathrm{N})^c}{B(b+1,c+1)}, \tag{9.6}$$

where $B(b+1, c+1)$, defined by

$$B(b+1,c+1) = \int_0^1 t^b(1-t)^c\,dt, \tag{9.7}$$

is the Beta function, which ensures proper normalization of the distribution and reduces correlations between the overall normalization a and the shape parameters b and c.

Table 9.2: Fit parameters with uncertainties and corresponding correlation matrix for transversity distribution.

Parameter	Value
a	0.081 ± 0.061
b	1.302 ± 0.646
c	3.37 ± 4.27

Parameter pair	Correlation coefficient
corr(a,b)	-0.82
corr(a,c)	-0.95
corr(b,c)	0.94

The fit results are shown in Fig. 9.7, and the corresponding parameters are listed in Tab. 9.2. The uncertainty band of the fit function was obtained from the covariance matrix using standard error propagation. Comparison with the exact values for the analysed datasets, given in Tabs. 9.3a and 9.3b, shows differences in x_N of about 0.03%[6], which proportionally affect the extracted transversity TMD PDF values. These

[6]For simplicity, it is assumed that the values x_N have no associated uncertainty (i.e., their measurement uncertainty is negligible).

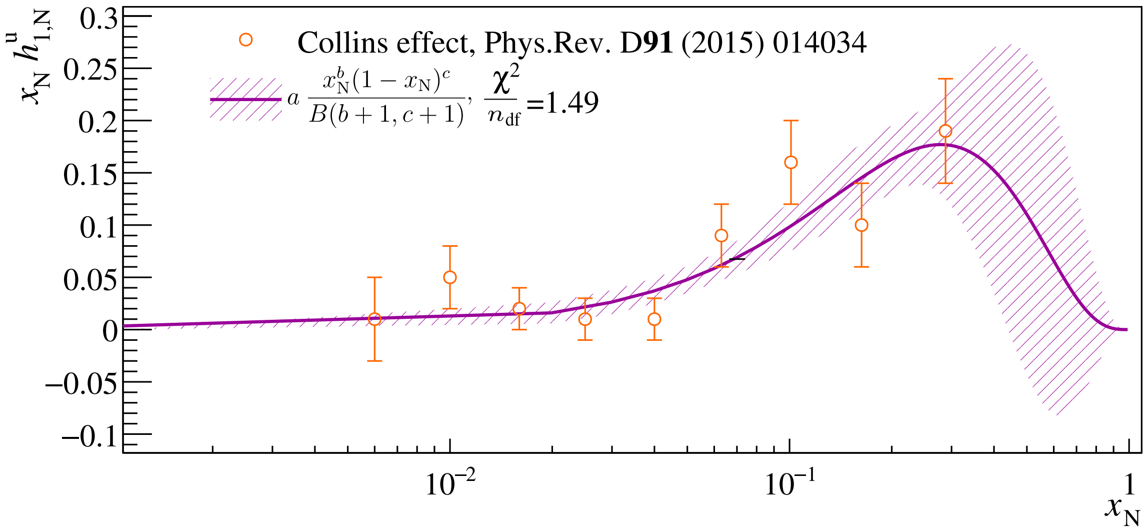

Figure 9.7: The fit of transversity extracted from Collins asymmetries from SIDIS COMPASS data [142].

differences are negligible compared to the variations in the transversity asymmetry and do not significantly impact the evaluated $h_{1,\mathrm{N}}^{\perp(1)\mathrm{u}}(x_\mathrm{N})$.

Table 9.3: The transversity TMD PDFs from the fit [142], shown for each kinematic bin, evaluated for datasets with: (a) $Dq_\mathrm{T}^3/(2M_\pi M_\mathrm{N}^2) < 300$ cut, and (b) $q_\mathrm{T} < 2.5$ GeV/c cut.

(a)

x_N	$\langle Q^2\rangle(\mathrm{GeV}/c)^2$	$h^\mathrm{u}_{1,\mathrm{N}}$	$\sigma_{h^\mathrm{u}_{1,\mathrm{N}}}$
0.200	21.75	0.188	0.017
0.158	25.39	0.167	0.017
0.128	29.63	0.141	0.015

(b)

x_N	$\langle Q^2\rangle(\mathrm{GeV}/c)^2$	$h^\mathrm{u}_{1,\mathrm{N}}$	$\sigma_{h^\mathrm{u}_{1,\mathrm{N}}}$
0.202	21.72	0.188	0.017
0.159	25.30	0.167	0.017
0.128	29.59	0.141	0.015

9.2.2 Final Extraction of Boer–Mulders Effect

The Boer–Mulders TMD PDF can be parametrized as [147]:

$$h_{1,\pi}^{\perp\,\bar{\mathrm{u}}}(x_\pi, k_{\pi\mathrm{T}}^2) = \frac{\alpha_\mathrm{T}}{\pi}\, c_\pi^{\bar{\mathrm{u}}}\, \frac{M_c M_\pi}{\boldsymbol{k}_{\pi\mathrm{T}}^2 + M_C^2}\, e^{-\alpha_\mathrm{T}\boldsymbol{k}_{\pi\mathrm{T}}^2}\, f_{1\pi}^{\bar{\mathrm{u}}}(x_\pi), \tag{9.8}$$

where the parameters are fixed by a fit to NA10 Drell-Yan data [43, 44]:

$$M_C = 2.3\,\mathrm{GeV}, \quad \alpha_\mathrm{T} = 1\,\mathrm{GeV}^{-2}, \quad c_\pi^{\bar{\mathrm{u}}} = 1.$$

The transverse momentum $\boldsymbol{k}_{\pi\mathrm{T}}$ is written in polar coordinates as $\boldsymbol{k}_{\pi\mathrm{T}} = k_{\pi\mathrm{T}}(\cos\varphi_k,\, \sin\varphi_k)$, where $k_{\pi\mathrm{T}}$ is the magnitude of the transverse momentum and φ_k its azimuthal angle. After integrating over φ_k, the dependence on the transverse direction vanishes, and Eq. (9.8) reduces to:

$$h_{1,\pi}^{\perp\,\bar{\mathrm{u}}}(x_\pi, k_{\pi\mathrm{T}}^2) = 2k_{\pi\mathrm{T}}\alpha_\mathrm{T}\, c_\pi^{\bar{\mathrm{u}}}\, \frac{M_c M_\pi}{k_{\pi\mathrm{T}}^2 + M_C^2}\, e^{-\alpha_\mathrm{T} k_{\pi\mathrm{T}}^2}\, f_{1\pi}^{\bar{\mathrm{u}}}(x_\pi). \tag{9.9}$$

The first k_{T}^2 moment of the Boer–Mulders TMD PDF, according to Eq. (2.28), can be expressed as:

$$h_{1,\pi}^{\perp(1)\bar{u}}(x_\pi) = \frac{\alpha_{\mathrm{T}} c_\pi^{\bar{u}} M_C}{M_\pi} f_{1,\pi}^{\bar{u}}(x_\pi) \int_0^\infty dk_{\pi\mathrm{T}} \frac{k_{\pi\mathrm{T}}^3}{k_{\pi\mathrm{T}}^2 + M_C^2} e^{-\alpha_{\mathrm{T}} k_{\pi\mathrm{T}}^2} \tag{9.10}$$

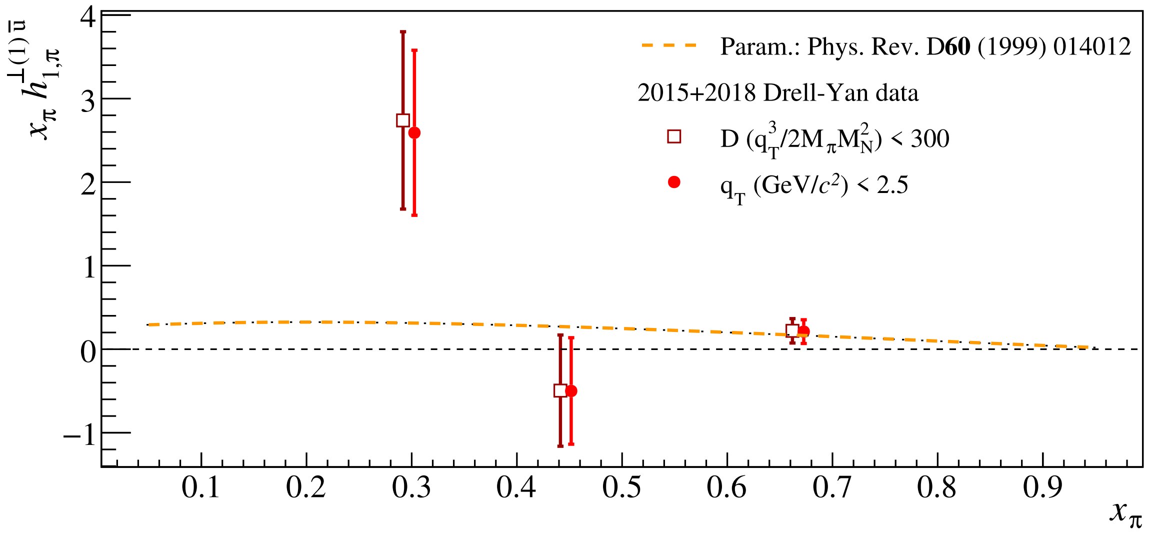

Figure 9.8: Extracted values of the first k_{T}^2 moment of the Boer–Mulders functions shown alongside a parametrization curve based on Ref. [147]. For clarity, the points corresponding to the $q_{\mathrm{T}} < 2.5\,\mathrm{GeV}/c$ are shifted horizontally.

Coming back to Eq. (9.6), the first k_{T}^2 moment of the Boer–Mulders TMD PDF is extracted. Parton densities are taken from the LHAPDF library [146], using the CTEQ5D set for the nucleon [139] and the GRVPI set for the pion [145]. The uncertainties were calculated from the total errors of the weighted asymmetries and from the uncertainties obtained by interpolation of the transversity TMD PDFs fit, using standard error propagation:

$$\sigma_{h_{1,\pi}^{\perp(1)\bar{u}}} = \sqrt{\left(\frac{f_{1,\mathrm{N}}^{\mathrm{u}} f_{1,\pi}^{\bar{u}}}{2h_{1,\mathrm{N}}^{\mathrm{u}}}\right)^2 \sigma_{A_{\mathrm{T}}^{\mathrm{Tranv}}}^2 + \left(\frac{A_{\mathrm{T}}^{\mathrm{Tranv}} f_{1,\mathrm{N}}^{\mathrm{u}} f_{1,\pi}^{\bar{u}}}{2\left(h_{1,\mathrm{N}}^{\mathrm{u}}\right)^2}\right)^2 \sigma_{h_{1,\mathrm{N}}^{\mathrm{u}}}^2}, \tag{9.11}$$

where $A_{\mathrm{T}}^{\mathrm{Tranv}}$ denotes transversity fD-WTSA, while $\sigma_{A_{\mathrm{T}}^{\mathrm{Tranv}}}$ its total uncertainty[7].

The first k_{T}^2 moment of valence Boer–Mulders function[8] of pion is shown in the Fig. 9.8, and the corresponding numerical values are listed in Tabs 9.4a and 9.4b.

Significant differences in the uncertainties in three bins are observed, primarily due to the first term in Eq. (9.11) associated with the asymmetry uncertainty. While the uncertainties of the fD-WTSA remain almost constant, the pion number density decreases by 86% from the first to the last bin, leading to a marked reduction in

[7]For clarity, the asymmetry symbol has been simplified from $A_{\mathrm{T}}^{\sin(2\varphi_{\mathrm{CS}}-\varphi_{\mathrm{S}})\frac{q_{\mathrm{T}}}{M_\pi}}$ to $A_{\mathrm{T}}^{\mathrm{Tranv}}$. For the same reason, the dependence of $h_{1,\mathrm{N}}^{\mathrm{u}}$ on x_{N} is omitted.

[8]In this case, one could write $k_{\pi\mathrm{T}}^2$, but the general form k_{T}^2 is retained for clarity.

Table 9.4: The first k_T^2 moment of the Boer–Mulders TMD PDFs of the pion extracted from SIDIS transversity TMD PDFs [142] and DY transversity fD-WTSA with: (a) $Dq_\mathrm{T}^3/(2M_\pi M_\mathrm{N}^2) < 300$ cut, (b) $q_\mathrm{T} < 2.5$ GeV/c cut.

(a)

x_π	x_N	$A_\mathrm{T}^\mathrm{Tranv}$	$f_{1,\pi}^{\bar{\mathrm{u}}}$	$f_{1,\mathrm{N}}^{\mathrm{u}}$	$h_{1,\pi}^{\perp(1)\bar{\mathrm{u}}}$
0.292	0.200	-3.343 ± 1.260	0.519	0.600	2.775 ± 1.076
0.441	0.158	0.876 ± 1.117	0.311	0.608	-0.496 ± 0.667
0.662	0.128	-1.520 ± 0.997	0.074	0.604	0.242 ± 0.161

(b)

x_π	x_N	$A_\mathrm{T}^\mathrm{Tranv}$	$f_{1,\pi}^{\bar{\mathrm{u}}}$	$f_{1,\mathrm{N}}^{\mathrm{u}}$	$h_{1,\pi}^{\perp(1)\bar{\mathrm{u}}}$
0.293	0.202	-3.179 ± 1.178	0.518	0.592	2.621 ± 1.000
0.442	0.159	0.885 ± 1.126	0.312	0.608	-0.500 ± 0.638
0.663	0.128	-1.460 ± 0.973	0.074	0.550	0.231 ± 0.156

the total uncertainty with increasing x_π. These factors account for over 94% of the total uncertainty. In contrast, the contribution from the transversity TMD PDFs is negligible, ranging from 0.5% to 6%, reflecting their smaller uncertainties relative to those of the asymmetries.

The first data point shown in Fig. 9.8 are not fully compatible with the parametrization, regardless of the selection applied. This may indicate deviations from the commonly assumed Gaussian Ansatz for the transverse momentum k_T, which models the intrinsic parton transverse momentum in the nucleon. Furthermore, the analysis relies on a single set of number density PDFs, which is particularly relevant for pions, whose distributions are less well constrained than those of nucleons. As a result, the choice of PDFs can significantly affect the extracted first k_T^2 moment of the Boer–Mulders TMD PDFs [148].

Chapter 10

Conclusion and Outlook

Tiger got to hunt. Bird got to fly.
Man got to ask himself "why, why, why?".
Tiger got to rest. Bird got to land.
Man got to tell himself he understand.

— Kurt Vonnegut,
The Book of Bonkonon in Cat's Cradle

10.1 Summary

The three-dimensional structure of the nucleon is a rapidly growing area of research in hadronic physics. COMPASS experiment at CERN has played a significant role in probing the transverse spin structure of the nucleon. In 2015 and 2018, the experiment conducted Drell–Yan measurements using a 190 GeV negative pion beam directed at a transversely polarised ammonia target[1] in the reaction:

$$\pi^- + \mathrm{p}^\uparrow \to \gamma^* + X \to \mu^+ + \mu^- + \mathrm{X}.$$

This work summarizes the four years of research effort by addressing two key topics. First, it focuses on extracting transverse-momentum weighted transverse-spin dependent azimuthal asymmetries. Second, it is dedicated to determining the k_{T}^2-moments of transverse momentum dependent parton distribution functions.

The theoretical background and broader context for the study, briefly introducing the parton model through the DIS is provided in Chapter 1. In Chapter 2, the DY process, which forms the core of this thesis, is examined, with particular emphasis on developing a transverse momentum weighting technique. This method effectively avoids the challenging convolutions between transverse momentum dependent parton distribution functions which appear in the LO DY cross section within the TMD framework. The procedure enabled the derivation of exact relations between structure functions and azimuthal asymmetries in terms of products of TMD PDFs. Chapter 3 briefly reviewed the current understanding of both collinear PDF and the less explored TMD PDF, thus

[1] In addition to the transversely polarised ammonia target, unpolarised aluminium and tungsten targets were installed during the DY data-taking. Their results lie beyond the scope of this thesis.

identifying promising directions for future research. The overview of the COMPASS experiment, focusing on the experimental setup used in the 2015 and 2018 DY data-taking campaigns, is described in Chapter 4.

Chapter 5 summarizes the DY analysis in two dimuon mass intervals:

- a nearly 96% DY region, $M_{\mu\mu} \in (4.3,\, 8.5)\,\mathrm{GeV}/c^2$,
- an extended range, $M_{\mu\mu} \in (4.0,\, 9.0)\,\mathrm{GeV}/c^2$, following the COMPASS TSA analysis [94].

The comparison shows consistent kinematic distributions and dilution factors between the two ranges. Because of non-negligible background contributions outside the pure DY region, the extended mass range required a modified extraction method with event-by-event weighting by the dilution and kinematic factors. Chapter 6 details the asymmetry extraction method for both standard and extended mass ranges, emphasizing how event-by-event weighting affects experimental observables. The fD-WTSA approach, specifically developed for the extended mass region, resulted in an increase of about 11% in the average kinematic factor and a decrease of roughly 10% in the average dilution factor relative to the standard analysis.

In Chapter 7, the analysis of WTSAs in the so-called standard dimuon mass range, $M_{\mu\mu} \in (4.3,\, 8.5)\,\mathrm{GeV}/c^2$, is outlined. The average Sivers WTSA is found to be approximately 1 standard deviation above zero, in agreement with the theoretical prediction of positive asymmetries across the explored kinematic region. The measured transversity WTSAs show a negative average value with a significance of about 1 standard deviation, supporting the corresponding theoretical predictions. Due to the kinematic suppression of pretzelosity TMD PDFs in the COMPASS (Q^2, x) range, pretzelosity asymmetries are expected to be small [94]. The WTSA results show a negative average shift of about 1 standard deviation, reflecting the cubic dependence on transverse momentum, q_T^3, which enhances negative contributions in the high-q_T region.

The analysis in Chapter 8 explores the broader range of $M_{\mu\mu} \in (4.0,\, 9.0)\,\mathrm{GeV}/c^2$ using the fD-WTSA approach, which accounts for event-by-event dilution and kinematic weights. Two independent data sets, defined by different selection criteria, were analyzed to assess systematic effects:

- $Dq_\mathrm{T}^3/(2M_\pi M_\mathrm{N}^2) < 300$ to suppress reconstruction artifacts and improve the quality of the selected events,
- $q_\mathrm{T} < 2.5$ GeV/c to restrict the data to the TMD applicability region.

Despite notable differences in phase space cutoffs and systematic corrections, the Sivers and transversity fD-WTSAs results are consistent across the two data samples. They also agree with theoretical predictions [98] and with measurements from the standard mass range. In contrast, pretzelosity fD-WTSAs suffer from relatively large systematic uncertainties under the cut $Dq_\mathrm{T}^3/(2M_\pi M_\mathrm{N}^2) < 300$ caused by the very large fDq_T weights. These effects are eliminated when the $q_\mathrm{T} < 2.5$ GeV/c cut is applied. For comparison with TSA results, asymmetries from both selection methods were rescaled by the average q_T weights. The resulting combined measurements are stable and agree within uncertainties with the TSA analysis [94], even in the presence of the strong q_T^3 dependence of pretzelosity.

In Chapter 9, TMD PDFs are extracted from asymmetry measurements in the extended mass range. The first k_{T}^2 moment of the Sivers TMD PDFs exhibits moderate sensitivity to the selection criteria, with differences of 16–35% in three x_{N} bins between the Dq_{T} and q_{T} cuts. The integrated value from the Dq_{T} selection is approximately 1.5 times smaller due to the presence of events with large q_{T} weights, which are suppressed by the tighter q_{T} cut. The Boer–Mulders first moment deviates from the Gaussian Ansatz, highlighting limitations of the model and the incomplete knowledge of the pion PDFs.

The method of weighted asymmetries has proven to be a valuable tool in the study of TMD PDFs, offering direct and transparent interpretations within the TMD framework. While the results from COMPASS are expected to remain among the most significant in this field for the next five years or more, upcoming initiatives such as EIC and LHCspin will offer unique opportunities for further investigations of TMD QCD. They will be briefly described in the following section.

10.2 Future prospects

The EIC is a flagship project in nuclear and high-energy physics and a central component of the future U.S. research infrastructure. The EIC will be the first collider to provide polarised electron–proton and electron–nucleus collisions, operating at center-of-mass energies from $\sqrt{s} = 20$ to 140 GeV per nucleon for ep and up to $\sqrt{s} = 89$ GeV per nucleon for eA. The facility aims to deliver 10-100 fb^{-1} per year with both electron and proton beam up to 70% polarisation [149]. It will grant access to previously poorly known regions in both x and Q^2, especially low-x region dominated by gluons and sea quarks. In Fig. 10.1, the (Q^2, x) coverage for Sivers and Collins asymmetries is shown, while Fig. 10.2 illustrates the expected statistical precision for the u-quark Sivers TMD PDF. The low-x coverage is particularly important, as it will provide new insights into parton behavior in this regime.

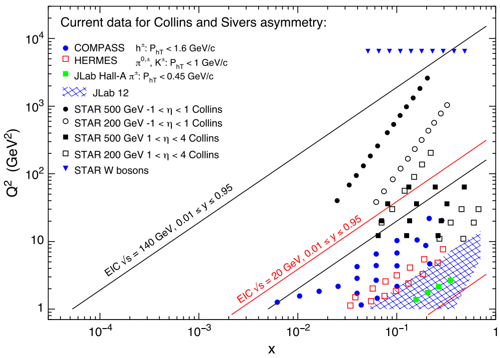

Figure 10.1: The kinematic coverage in parton momentum fraction x and resolution Q^2 accessible at the EIC [149] for the Sivers and Collins effects in SIDIS compared to other experiments for two exemplary energy configurations.

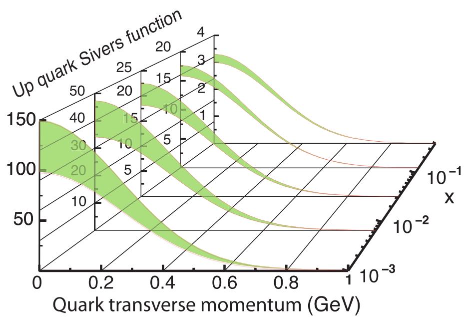

Figure 10.2: Projected statistical precision for the up-quark Sivers distribution in quark transverse momentum k_{T} across 5 representative x values within the EIC kinematic range [150].

As part of LHCb, the LHCspin Collaboration will explore the nucleon structure via high-energy polarised fixed-target measurements. With beam energies from 450 to 6800

GeV/nucleon, protons or lead ions can be collided with gas targets of different atomic numbers, achieving nucleon-nucleon CM energies $\sqrt{s} = 29 - 113$ GeV/nucleon [151]. The LHCb fixed-target programme uses a System for Measuring Overlap with Gas (SMOG), which injects a noble gas of a low pressure into the LHC beam pipe, creating an internal gas target. In future operations, the target is expected to be transversely polarised. To test LHCb capability to operate simultaneously in collision and fixed-target modes, Monte Carlo simulations were performed. The gas was modeled with a uniform transverse distribution and a triangular longitudinal profile. The resulting vertex distributions show two distinct peaks for beam-beam and beam-gas interactions, confirming that their collision points remain spatially separated (Fig. 10.3) [151]. The

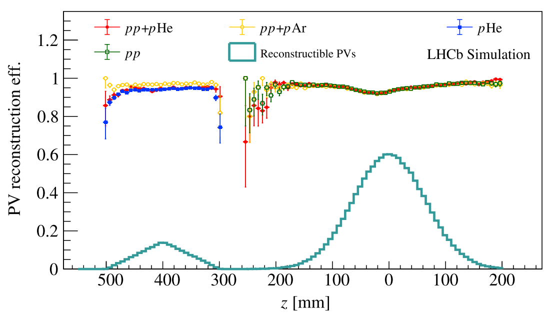

Figure 10.3: Distributions of the coordinate along the beam axis (z) for the reconstructed vertices (dark cyan) in LHCspin [151]. Results are shown for simulated samples of different collision systems: pp stand-alone (green), pHe stand-alone (blue), pp + pHe (red), and pp + pAr (yellow).

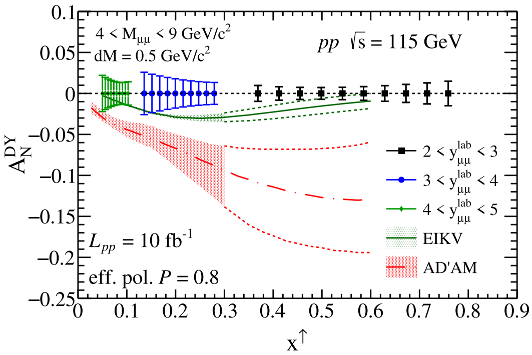

Figure 10.4: LHCspin statistical projections for the DY Sivers asymmetries as a function of polarised target nucleon $x^{\uparrow}$ [152] along with predictions (AD'AM [153] and EIKV [154]). The bands are filled where constrained by SIDIS data ($x^{\uparrow} \leqslant 0.3$) and hollow where extrapolated.

potential of LHCspin is illustrated using the Sivers asymmetry. Projected precision for the single-polarised DY[2].Sivers asymmetry $A_{\mathrm{N}}^{\mathrm{DY}}$ [152] is shown in Fig. 10.4, assuming 10 fb^{-1} per year, and compared to theoretical predictions from AD'AM [153] and EIKV [154]. Such measurements would allow constraints on the quark Sivers effect up to $x^{\uparrow} \simeq 0.75$[152] in a polarised target nucleon [152] and provide a direct test of the predicted sign reversal of the corresponding TMD PDF when compared to SIDIS.

While the full scientific potential of EIC and LHCspin goes beyond the scope of this work, it is clear that these experiments will provide important insights into nucleon spin structure. Together, they offer a complementary approach, opening new directions in QCD research.

[2]These predictions cover both $\mathrm{p\,p}^{\uparrow}$ and $\mathrm{p} + {}^{3}\mathrm{He}^{\uparrow}$ DY processes.

Appendix A

Determination of Covariance Matrix Coefficients

The following calculations aim to determine the elements of the covariance matrix used to evaluate the uncertainty of the modified double ratio, as presented in Sec. 6.2. Assume that events in a given subperiod p and originating from a specific cell c are entirely independent of events from other cp states. As such, the statistical treatment follows a general form, and we adopt the following notation:

- N is the total number of events in a given p and c.
- $(n_{cp})_i$ represents the probability that a specific event in subperiod p originates from cell c and satisfies the event selection criteria:

$$(n_{cp})_i = \begin{cases} 1, & \text{if the event belongs to the specific } cp \text{ state,} \\ 0, & \text{otherwise.} \end{cases}$$

- w_i are event-specific weights, which are proportional to the transverse momentum q_{T}, i.e., $w_i \sim q_{\mathrm{T}}$.

Event Counts and Expectation Values

The number of unweighted events in subperiod p, originating from cell c and satisfying the event selection, is given by:

$$N_{cp} = \sum_{i=1}^{N} (n_{cp})_i. \tag{A.1}$$

Similarly, the weighted event count is expressed as[1]:

$$N_{cp}^{W_{\mathrm{Y}}} = \sum_{i=1}^{N} (n_{cp})_i w_i. \tag{A.2}$$

The expectation value of N_{cp} follows from the linearity of expectation:

$$\langle N_{cp} \rangle = \left\langle \sum_{i=1}^{N} (n_{cp})_i \right\rangle = \langle N \rangle \langle n_{cp} \rangle. \tag{A.3}$$

[1]As introduced in Chapter 6, the symbol $N_{cp}^{W_{\mathrm{Y}}}$ contains an extra factor, which is explicitly written as $N_{cp}^{W_{\mathrm{Y}}}(w)$. In the following, this factor has been omitted for simplicity.

A.1 Expectation Value and Variance of N_{cp}

Assuming that individual events within the same category (c, p) are independent, the expectation value of N_{cp}^2 can be expressed as:

$$\langle N_{cp}^2 \rangle = \left\langle \sum_i^N (n_{cp})_i \sum_j^N (n_{cp})_j \right\rangle . \tag{A.4}$$

Expanding the summation:

$$\langle N_{cp}^2 \rangle = \left\langle \sum_{i=j}^N (n_{cp})_i (n_{cp})_i \right\rangle + \left\langle \sum_{i \neq j}^N (n_{cp})_i (n_{cp})_j \right\rangle . \tag{A.5}$$

Since events are independent:

$$\langle N_{cp}^2 \rangle = \langle N \rangle \langle n_{cp}^2 \rangle + \langle N(N-1) \rangle \langle n_{cp} \rangle^2 . \tag{A.6}$$

Using $\langle N(N-1) \rangle = \langle N^2 \rangle - \langle N \rangle$:

$$\langle N_{cp}^2 \rangle = \langle N \rangle \sigma_{n_{cp}}^2 + \langle N^2 \rangle \langle n_{cp} \rangle^2 . \tag{A.7}$$

The variance of N_{cp} is given by:

$$(\sigma_{N_{cp}})^2 = \langle N_{cp}^2 \rangle - \langle N_{cp} \rangle^2 . \tag{A.8}$$

Substituting the expression for $\langle N_{cp}^2 \rangle$:

$$(\sigma_{N_{cp}})^2 = \langle N \rangle \sigma_{n_{cp}}^2 + \langle n_{cp} \rangle^2 \sigma_N^2 . \tag{A.9}$$

Assuming a Poisson distribution for N where $\sigma_N^2 = \langle N \rangle$:

$$(\sigma_{N_{cp}})^2 = \langle N \rangle \sigma_{n_{cp}}^2 + \langle N \rangle \langle n_{cp} \rangle^2 = \langle N \rangle \langle (n_{cp})^2 \rangle = N_{cp} . \tag{A.10}$$

A.2 Expectation Value and Variance of $N_{cp}^{W_\mathrm{Y}}$

For weighted events, the expectation value of $N_{cp}^{W_\mathrm{Y}}$ is:

$$\langle N_{cp}^{W_\mathrm{Y}} \rangle = \left\langle \sum_i^N (n_{cp})_i w_i \right\rangle = \langle N \rangle \langle n_{cp} W_\mathrm{Y} \rangle . \tag{A.11}$$

The expectation value of $(N_{cp}^{W_\mathrm{Y}})^2$ follows similarly:

$$\langle (N_{cp}^{W_\mathrm{Y}})^2 \rangle = \left\langle \sum_{i=j}^N (n_{cp})_i w_i (n_{cp})_i w_i \right\rangle + \left\langle \sum_{i \neq j}^N (n_{cp})_i w_i (n_{cp})_j w_j \right\rangle . \tag{A.12}$$

Applying independence assumptions:

$$\langle (N_{cp}^{W_\mathrm{Y}})^2 \rangle = \langle N \rangle \langle n_{cp}^2 W_\mathrm{Y}^2 \rangle + \langle N^2 \rangle \langle n_{cp} W_\mathrm{Y} \rangle^2 - \langle N \rangle \langle n_{cp} W_\mathrm{Y} \rangle^2 . \tag{A.13}$$

Thus, the variance of $N_{cp}^{W_\mathrm{Y}}$ is:

$$(\sigma_{N_{cp}^{W_\mathrm{Y}}})^2 = \langle N\rangle \sigma^2_{n_{cp}W} + \langle n_{cp}W_\mathrm{Y}\rangle^2 \sigma_N^2. \tag{A.14}$$

Again, assuming Poisson statistics for N ($\sigma_N^2 = \langle N\rangle$):

$$(\sigma_{N_{cp}^{W_\mathrm{Y}}})^2 = \langle N\rangle \sigma^2_{n_{cp}W} + \langle N\rangle\langle n_{cp}W_\mathrm{Y}\rangle^2. \tag{A.15}$$

Since $(n_{cp})_i$ can only be 0 or 1, it follows that:

$$\langle (n_{cp})^2 W_\mathrm{Y}^2\rangle = \langle n_{cp} W_\mathrm{Y}^2\rangle. \tag{A.16}$$

Thus,

$$\left(\sigma_{N_{cp}^{W_\mathrm{Y}}}\right)^2 = \frac{\langle N\rangle\langle n_{cp}W_\mathrm{Y}^2\rangle}{\langle N\rangle} = \sum_i w_i^2. \tag{A.17}$$

A.3 Derivation of Covariance

The covariance between the total event count N_{cp} and the weighted event count $N_{cp}^{W_\mathrm{Y}}$ can be computed analogously to the uncertainty in N_{cp}. Specifically, we evaluate the expectation value:

$$\begin{aligned}
\langle N_{cp}N_{cp}^{W_\mathrm{Y}}\rangle &= \left\langle \sum_{i=1}^{N}(n_{cp})_i \sum_{j=1}^{N}(n_{cp})_j w_j \right\rangle \\
&= \left\langle \sum_{i=j}^{N}(n_{cp})_i w_i \right\rangle + \left\langle \sum_{i\neq j}^{N}(n_{cp})_i (n_{cp})_j w_j \right\rangle \\
&= \langle N\rangle\langle (n_{cp})^2 W_\mathrm{Y}\rangle + \langle N(N-1)\rangle\langle n_{cp}\rangle\langle n_{cp}W_\mathrm{Y}\rangle \\
&= \langle N\rangle\langle (n_{cp})^2 W_\mathrm{Y}\rangle + \langle N^2\rangle\langle n_{cp}\rangle\langle n_{cp}W_\mathrm{Y}\rangle - \langle N\rangle\langle n_{cp}\rangle\langle n_{cp}W_\mathrm{Y}\rangle.
\end{aligned} \tag{A.18}$$

Since $(n_{cp})_i$ takes only the values 0 or 1, it follows that:

$$\langle (n_{cp})^2 W_\mathrm{Y}\rangle = \langle n_{cp} W_\mathrm{Y}\rangle. \tag{A.19}$$

Inserting this into Eq. (A.18) gives:

$$\langle N_{cp}N_{cp}^{W_\mathrm{Y}}\rangle = \langle N\rangle\langle n_{cp}W_\mathrm{Y}\rangle + \langle N^2\rangle\langle n_{cp}\rangle\langle n_{cp}W_\mathrm{Y}\rangle - \langle N\rangle\langle n_{cp}\rangle\langle n_{cp}W_\mathrm{Y}\rangle. \tag{A.20}$$

The covariance is then given by:

$$\begin{aligned}
\mathrm{cov}(N_{cp}, N_{cp}^{W_\mathrm{Y}}) = {} & \langle N\rangle\langle n_{cp}W_\mathrm{Y}\rangle + \langle N^2\rangle\langle n_{cp}\rangle\langle n_{cp}W_\mathrm{Y}\rangle - \langle N\rangle\langle n_{cp}\rangle\langle n_{cp}W_\mathrm{Y}\rangle \\
& - \langle N\rangle^2\langle n_{cp}W_\mathrm{Y}\rangle\langle n_{cp}\rangle.
\end{aligned} \tag{A.21}$$

Assuming a Poisson distribution for N, where $\sigma_N^2 = \langle N\rangle$, we obtain:

$$
\begin{aligned}
\mathrm{cov}(N_{cp}, N_{cp}^{W_{\mathrm{Y}}}) &= \langle N\rangle\langle n_{cp}W_{\mathrm{Y}}\rangle - \langle N\rangle\langle n_{cp}\rangle\langle n_{cp}W_{\mathrm{Y}}\rangle + \langle N\rangle\langle n_{cp}\rangle\langle n_{cp}W_{\mathrm{Y}}\rangle \\
&= \langle N\rangle\langle n_{cp}W_{\mathrm{Y}}\rangle.
\end{aligned} \tag{A.22}
$$

Using the definition of weighted sum:

$$
N_{cp}^{W_{\mathrm{Y}}} = \sum_i w_i, \tag{A.23}
$$

we conclude:

$$
\mathrm{cov}(N_{cp}, N_{cp}^{W_{\mathrm{Y}}}) = N_{cp}^{W_{\mathrm{Y}}}. \tag{A.24}
$$

Appendix B

Fitting Procedure of False Asymmetries

The modified double ratio shown in the Eq. 6.21 is parametrized in terms of the unweighted number of events ($N_{U1}, N_{D2}, N_{U2}, N_{D1}$), and the weighted ones ($N_{U1}^{W_{\mathrm{Y}}}$, $N_{D2}^{W_{\mathrm{Y}}}$, $N_{U2}^{W_{\mathrm{Y}}}$, $N_{D1}^{W_{\mathrm{Y}}}$). The values of the weighted and unweighted number of events calculated in the Chapter 6 can be written in terms of its unpolarised $\sigma_{\mathrm{U}}^{W_{\mathrm{Y}}}$ and polarised $\sigma_{\mathrm{S}}^{W_{\mathrm{Y}}}$ parts of a cross-section:

$$\begin{aligned} N_{cp} &= b_p l_c a_{cp} \left[\sigma_{\mathrm{U}} + |\boldsymbol{S}_{\mathrm{T},cp}| \sigma_{\mathrm{S}} \sin\Phi\right], \\ N_{cp}^{W_{\mathrm{Y}}} &= b_p l_c a_{cp} \left[\sigma_{\mathrm{U}}^{W_{\mathrm{Y}}} + |\boldsymbol{S}_{\mathrm{T},cp}| \sigma_{\mathrm{S}}^{W_{\mathrm{Y}}} \sin\Phi\right]. \end{aligned} \tag{B.1}$$

The same formalism can be applied to the cases of cell swapping and period swapping, for which the modified double ratios are defined in an analogous manner. However, the corresponding expressions deviate significantly from the standard form given in Eq. 6.21, both in their analytical structure and in their dependence on the spin-dependent part of the cross-section. These differences must be properly taken into account when evaluating the extracted asymmetries and assessing potential systematic effects.

B.1 Cell Swapping

An alternative form of the modified double ratio, denoted $R_{FA,\mathrm{cell}}^{\mathrm{Y}W_{\mathrm{Y}}}$, is given in Eq. 7.5. Under the same assumptions outlined in Sec. 6.3—namely, the factorization of the dilution factor (Eq. 6.28), the luminosity ratio (Eq. 6.29), the set of reasonable approximations (Eq. 6.30), and the neglect of quadratic terms (Eq. 6.31)—the products of unweighted event yields from the same target cell can be expressed as:

$$\begin{aligned} N_{U1}N_{U2} &= a_{U1}\, a_{U2}\, b_1\, b_2\, l_{\mathrm{U}}^2 \left(\sigma_{\mathrm{U}} + \sigma_{\mathrm{S}} |\boldsymbol{S}_{\mathrm{T},U1}| \sin\Phi\right) \left(\sigma_{\mathrm{U}} - \sigma_{\mathrm{S}} |\boldsymbol{S}_{\mathrm{T},U2}| \sin\Phi\right) \\ &= a_{U1}\, a_{U2}\, b_1\, b_2\, l_{\mathrm{U}}^2 \left[\sigma_{\mathrm{U}}^2 + \sigma_{\mathrm{S}}\sigma_{\mathrm{U}} \sin\Phi \left(|\boldsymbol{S}_{\mathrm{T},U1}| - |\boldsymbol{S}_{\mathrm{T},U2}|\right) - \sigma_{\mathrm{S}}^2 |\boldsymbol{S}_{\mathrm{T},U1}||\boldsymbol{S}_{\mathrm{T},U2}| \sin^2\Phi\right] \\ &\approx a_{U1}\, a_{U2}\, b_1\, b_2\, l_{\mathrm{U}}^2 \left[\sigma_{\mathrm{U}}^2 + \sigma_{\mathrm{S}}\sigma_{\mathrm{U}} \sin\Phi \left(|\boldsymbol{S}_{\mathrm{T},U1}| - |\boldsymbol{S}_{\mathrm{T},U2}|\right)\right], \end{aligned} \tag{B.2}$$

$$
\begin{aligned}
N_{D1}N_{D2} &= a_{D1}\, a_{D2}\, b_1\, b_2\, l_D^2\, (\sigma_{\mathrm{U}} + \sigma_{\mathrm{S}}|\boldsymbol{S}_{\mathrm{T},D1}|\sin\Phi)\,(\sigma_{\mathrm{U}} - \sigma_{\mathrm{S}}|\boldsymbol{S}_{\mathrm{T},D2}|\sin\Phi) \\
&= a_{D1}\, a_{D2}\, b_1\, b_2\, l_D^2 \left[\sigma_{\mathrm{U}}^2 + \sigma_{\mathrm{S}}\sigma_{\mathrm{U}}\sin\Phi\,(|\boldsymbol{S}_{\mathrm{T},D2}| - |\boldsymbol{S}_{\mathrm{T},D1}|) - \sigma_{\mathrm{S}}^2|\boldsymbol{S}_{\mathrm{T},D1}||\boldsymbol{S}_{\mathrm{T},D2}|\sin^2\Phi\right] \\
&\approx a_{D1}\, a_{D2}\, b_1\, b_2\, l_D^2 \left[\sigma_{\mathrm{U}}^2 + \sigma_{\mathrm{S}}\sigma_{\mathrm{U}}\sin\Phi\,(|\boldsymbol{S}_{\mathrm{T},D2}| - |\boldsymbol{S}_{\mathrm{T},D1}|)\right].
\end{aligned}
\tag{B.3}
$$

In the case of the weighted number of events, the expressions take an analogous form, with the addition of a superscript "W_{Y}" on the cross-section components, $\sigma_{\mathrm{U}}^{W_{\mathrm{Y}}}$ and $\sigma_{\mathrm{S}}^{W_{\mathrm{Y}}}$. In the case of Eq. 7.5, the previously adopted simplifications cannot be applied. The full, unsimplified expression for the modified double ratio in the weighted case is given by:

$$
\begin{aligned}
R_{FA,\mathrm{cell}}^{\mathrm{Y}W_{\mathrm{Y}}} &= \left[\frac{\sigma_{\mathrm{S}}^{W_{\mathrm{Y}}}\,(a_{D1}a_{D2}l_D^2(|\boldsymbol{S}_{\mathrm{T},D1}| - |\boldsymbol{S}_{\mathrm{T},D2}|) + a_{U1}a_{U2}l_{\mathrm{U}}^2(|\boldsymbol{S}_{\mathrm{T},U1}| - |\boldsymbol{S}_{\mathrm{T},U2}|))}{\sigma_{\mathrm{U}}\,(a_{D1}a_{D2}l_D^2 + a_{U1}a_{U2}l_{\mathrm{U}}^2)}\right]\sin\Phi \\
&\quad + \frac{\sigma_{\mathrm{U}}^{W_{\mathrm{Y}}}\,(a_{U1}a_{U2}l_{\mathrm{U}}^2 - a_{D1}a_{D2}l_D^2)}{\sigma_{\mathrm{U}}\,(a_{D1}a_{D2}l_D^2 + a_{U1}a_{U2}l_{\mathrm{U}}^2)}.
\end{aligned}
\tag{B.4}
$$

Due to the non-standard formula, a key assumption is no longer valid. This leads to the emergence of a free term, which lacks a straightforward physical interpretation but cannot be neglected in the analysis of false asymmetries.

B.2 Period Swapping

Analogous calculations, as described in Sec. B.1, can be performed for the ratio in the case of period swapping $R_{FA,\mathrm{period}}^{\mathrm{Y}W_{\mathrm{Y}}}$. By again analyzing the products of weighted and unweighted event counts, this time originating from the same subperiod but from different target cells, one obtains:

$$
N_{U1}N_{D1} \approx a_{D1}a_{U1}b_1^2 l_D l_{\mathrm{U}}\sigma_{\mathrm{U}}\left[\sigma_{\mathrm{U}} + \sigma_{\mathrm{S}}\,(-|\boldsymbol{S}_{\mathrm{T},D1}| + |\boldsymbol{S}_{\mathrm{T},U1}|)\sin\Phi\right], \tag{B.5}
$$

$$
N_{D1}N_{D2} \approx a_{D2}a_{U2}b_2^2 l_D l_{\mathrm{U}}\sigma_{\mathrm{U}}\left[\sigma_{\mathrm{U}} + \sigma_{\mathrm{S}}\,(|\boldsymbol{S}_{\mathrm{T},D2}| - |\boldsymbol{S}_{\mathrm{T},U2}|)\sin\Phi\right]. \tag{B.6}
$$

Similar to the previous case, the expressions for the weighted number of events are derived by adding a superscript "W_{Y}" to the cross-section components. The full, unsimplified version of the Eq. 7.6 is as follows:

$$
\begin{aligned}
R_{FA,\mathrm{period}}^{\mathrm{Y}W_{\mathrm{Y}}} &= \left[-\frac{\sigma_{\mathrm{S}}^{W_{\mathrm{Y}}}\,(a_{D1}a_{U1}b_1^2(|\boldsymbol{S}_{\mathrm{T},D1}| - |\boldsymbol{S}_{\mathrm{T},U1}|) + a_{D2}a_{U2}b_2^2(|\boldsymbol{S}_{\mathrm{T},D2}| - |\boldsymbol{S}_{\mathrm{T},U2}|))}{(a_{D1}a_{U1}b_1^2 + a_{D2}a_{U2}b_2^2)\,\sigma_{\mathrm{U}}}\right]\sin\Phi \\
&\quad + \frac{(a_{D1}a_{U1}b_1^2 - a_{D2}a_{U2}b_2^2)\,\sigma_{\mathrm{U}}^{W_{\mathrm{Y}}}}{(a_{D1}a_{U1}b_1^2 + a_{D2}a_{U2}b_2^2)\,\sigma_{\mathrm{U}}}
\end{aligned}
\tag{B.7}
$$

Analogous to the cell swapping case, this ratio does not permit the application of reasonable assumptions, which leads to the emergence of an additional constant term, as observed in the Eq. B.4.

B.3 Cell and Period Mixing

In both event mixing and cell mixing, the ratio retains the same mathematical form as the cancelation of physical asymmetries is achieved either by altering the target cell assignments (cell mixing) or by randomly reassigning event polarizations (event mixing). As a result, Eq. 6.21 remains applicable, and the dependence of the ratio on the polarization pp mirrors the behavior described in Ses. 6.3.1.

Appendix C

MonteCarlo Asymmetries

Supplementary results from the Monte Carlo asymmetry studies discussed in Chapter 8 are presented here. To evaluate the effect of the extraction procedure on the measured values, two types of asymmetries were considered:

- WTSA, where events are weighted only by q_{T},
- fD-WTSA, where events are weighted not only by q_{T}, but also by the dilution factor f and the kinematic factor D.

The WTSA and fD-WTSA asymmetries obtained from the uncorrelated MC scenario, using a statistical sample 100 times larger than that of the real data (corresponding to 800 periods instead of 8), are shown in Fig. C.1a. The corresponding asymmetries for the fD-q_{T} correlated scenario are presented in Fig. C.1b. Although the analysis was performed for four different statistical samples[1], only one representative case is shown here. As no physical asymmetries were introduced in the samples, the results are consistent across all four scenarios and differ only in the magnitude of their statistical uncertainties. For both scenarios, the weighted transverse spin asymmetries lie within one-tenth of the statistical uncertainty of the real data, demonstrating agreement with zero and confirming that the extraction procedure does not generate spurious asymmetries.

The evolution of WTSAs and WTSAs uncertainties from both the uncorrelated and correlated MC simulations for all four statistical samples (including comparison with the 2018 real data) is shown in Fig. C.2a (uncorrelated fD-WTSA) and Fig. C.2b (fD-q_{T} correlated fD-WTSA). As the statistics increase, the uncertainty estimates for the WTSA (weighted only by q_{T}) and the fD-WTSA gradually converge, consistent with the law of large numbers, for both the fully uncorrelated MC and the scenario including fD-q_{T} correlations.

[1]Four statistical scenarios are considered: the baseline (8 period replicas, nominal statistics), 80 period replicas, 800 period replicas, and 800 replicas with five times more events per replica.

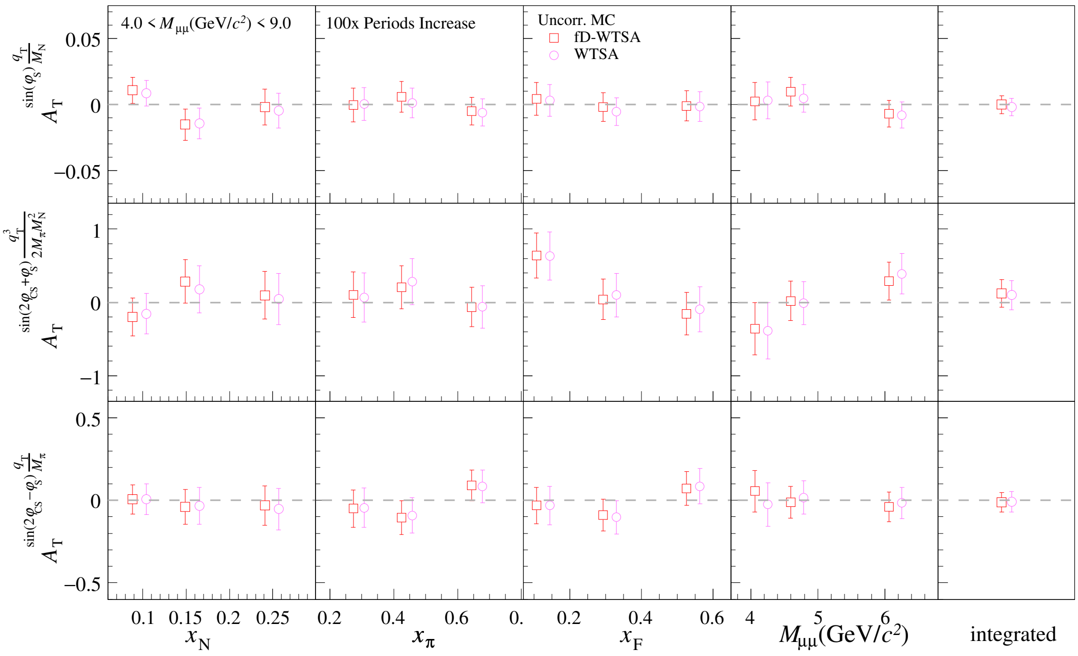

(a)

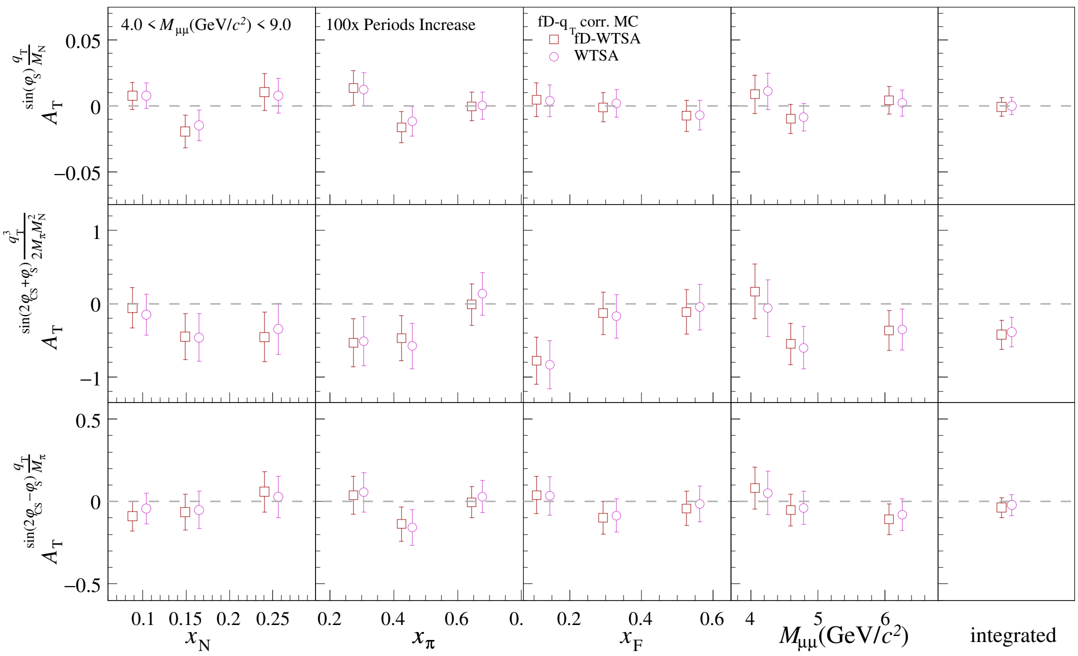

(b)

Figure C.1: Toy Monte Carlo asymmetries, WTSAs and fD-WTSAs, with a 100× increased statistics with respect to the 2018 data: (a) uncorrelated MC scenario, (b) fD-q_T correlated case.

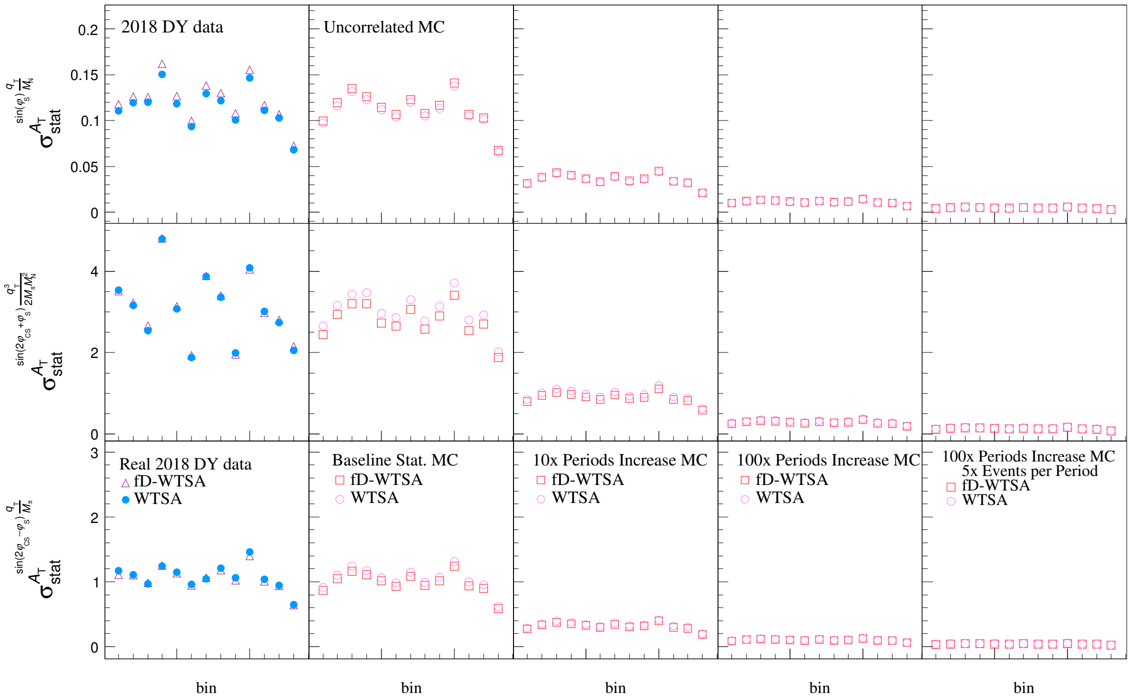

(a)

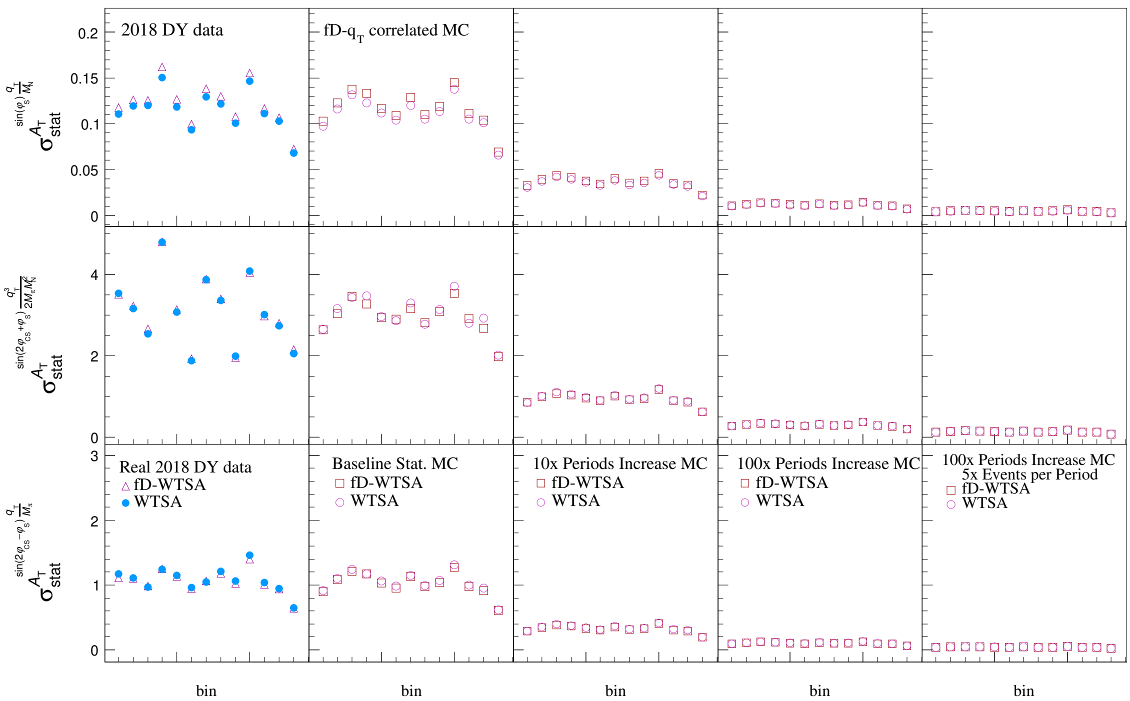

(b)

Figure C.2: Statistical uncertainties for WTSAs and fD-WTSAs obtained from four different MC scenarios (baseline, 80 replicas, 800 replicas, and 800 replicas with five times more events per replica), shown alongside a comparison with the 2018 real data: (a) uncorrelated scenario, (b) fD-q_{T} correlated scenario. As the Monte Carlo statistics increase, the uncertainties decrease accordingly, demonstrating the expected statistical scaling.

Appendix D

Supplementary Systematic Tests in the Extended Mass Range

D.1 Period Compatibility

The reduced χ^2/n_{df} of the error-weighted averages of the asymmetries over data-taking periods, calculated according to Eq. (7.4), provides a consistency check equivalent to that obtained from pull distributions (Chapter 8), with the advantage that it can be applied independently in each kinematic bin. As shown in Figs. D.1 and D.2, some χ^2/n_{df} values slightly exceed unity in a few kinematic bins across all asymmetries. However, in most cases the values fluctuate around one, indicating good compatibility between the periods.

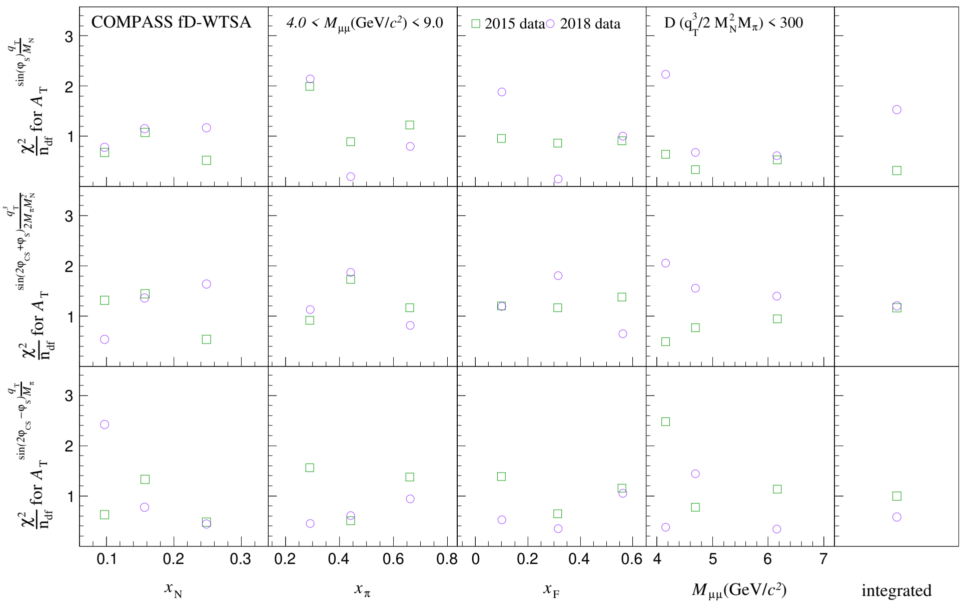

Figure D.1: Reduced χ^2/n_{df} values of the error-weighted averages of the asymmetries over the nine periods in 2015 and eight periods in 2018 for $D\, q_{\mathrm{T}}^3/(2\, M_\pi\, M_{\mathrm{N}}^2) < 300$.

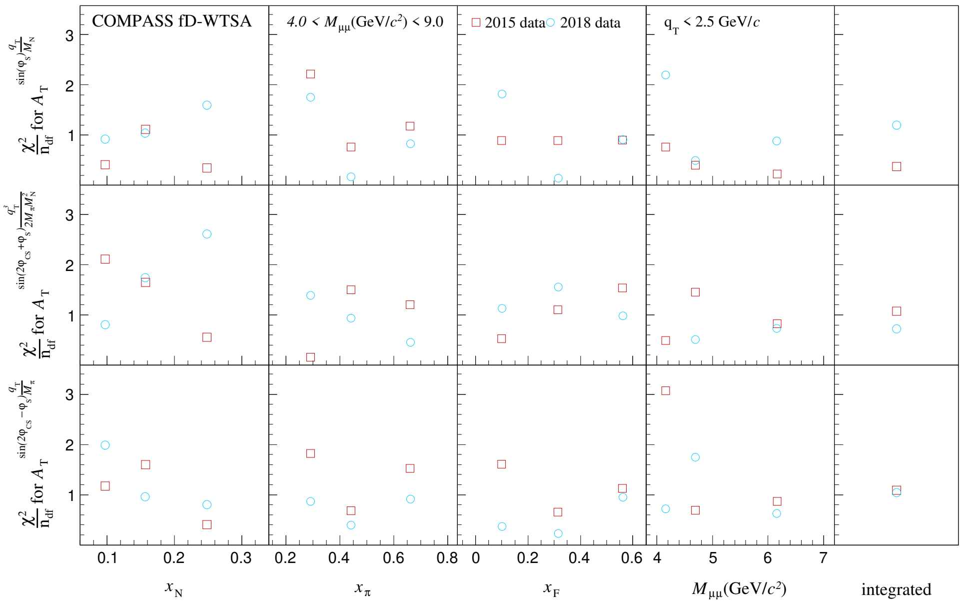

Figure D.2: Reduced χ^2/n_{df} values of the error-weighted averages of the asymmetries over the nine periods in 2015 and eight periods in 2018 for $D\,q_{\mathrm{T}} < 2.5$ GeV$/c$.

D.2 False Asymmetries

As detailed in Sec. 7.2.2, the false asymmetries were calculated using four distinct methods, each designed to suppress or cancel physics effects and isolate contributions from acceptance-related modulations.

For the extended mass range, the asymmetries are additionally weighted by f and D, which requires a modification of the ratios used in the period swapping and cell swapping procedures. In the case of period swapping, the modified ratio is defined as:

$$R^{\mathrm{Y}W_{\mathrm{Y}}}_{FA,\mathrm{period}} = \frac{N_{U1}^{W_{\mathrm{Y}}(w)} N_{D1}^{W_{\mathrm{Y}}(w)} - N_{U2}^{W_{\mathrm{Y}}(w)} N_{D2}^{W_{\mathrm{Y}}(w)}}{\sqrt{(N_{U1}^{W_{\mathrm{Y}}(w)} N_{D1}^{W_{\mathrm{Y}}(w)} + N_{U2}^{W_{\mathrm{Y}}(w)} N_{D2}^{W_{\mathrm{Y}}(w)})(N_{U1}^{W_{\mathrm{Y}}(w')} N_{D1}^{W_{\mathrm{Y}}(w')} + N_{U2}^{W_{\mathrm{Y}}(w')} N_{D2}^{W_{\mathrm{Y}}(w')})}}\,. \tag{D.1}$$

For cell swapping, the corresponding ratio is given by:

$$R^{\mathrm{Y}W_{\mathrm{Y}}}_{FA,\mathrm{cell}} = \frac{N_{U1}^{W_{\mathrm{Y}}(w)} N_{U2}^{W_{\mathrm{Y}}(w)} - N_{D2}^{W_{\mathrm{Y}}(w)} N_{D1}^{W_{\mathrm{Y}}(w)}}{\sqrt{(N_{U1}^{W_{\mathrm{Y}}(w)} N_{U2}^{W_{\mathrm{Y}}(w)} + N_{D2}^{W_{\mathrm{Y}}(w)} N_{D1}^{W_{\mathrm{Y}}(w)})(N_{U1}^{W_{\mathrm{Y}}(w')} N_{U2}^{W_{\mathrm{Y}}(w')} + N_{D2}^{W_{\mathrm{Y}}(w')} N_{D1}^{W_{\mathrm{Y}}(w')})}}\,. \tag{D.2}$$

In this context, w' represents the fD weight, and w represents the fDq_{T} weight.

The false asymmetries and the associated systematic uncertainties for the 2015 and 2018 data, obtained using the selection criterion $D\,q_{\mathrm{T}}^3/(2\,M_\pi\,M_{\mathrm{N}}^2) < 300$, are presented in Fig. D.3.

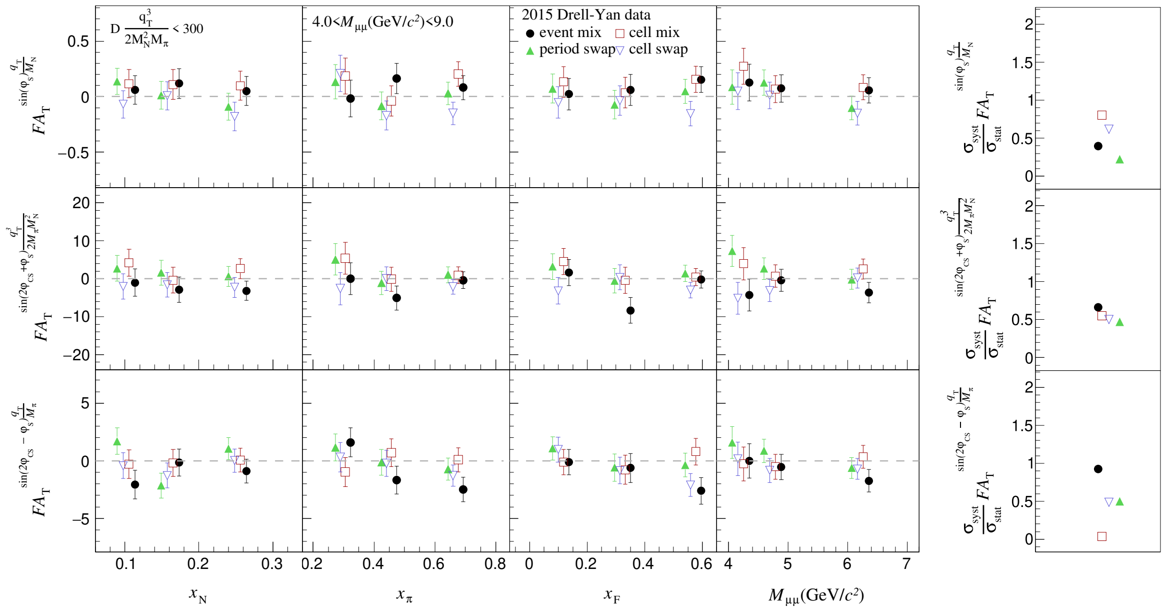

(a) (b)

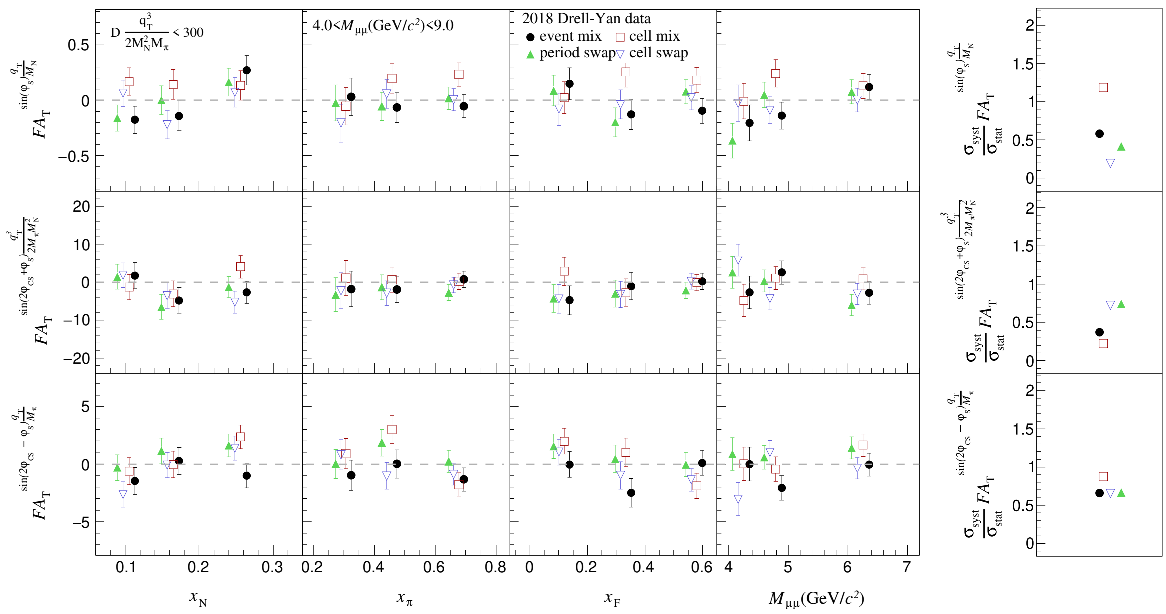

(c) (d)

Figure D.3: Systematic analysis for the 2015 and 2018 datasets with $D\, q_T^3/(2\, M_\pi\, M_N^2) < 300$: (a,c) annual false asymmetries obtained using four different methods: cell/period mixing and cell/event swapping, (b,d) ratio of systematic to statistical uncertainties derived from them, already averaged over the kinematic bins and binning variables.

Appendix E

Impact of Event Selection Criteria on Weight Distributions

Figs E.1a and E.1b illustrate the impact of different event selection criteria on the distributions of event weights for each asymmetry. The two-dimensional histograms show asymmetries weights as a function of q_{T}, comparing selections based on Dq_{T} with those employing the q_{T} criterion.

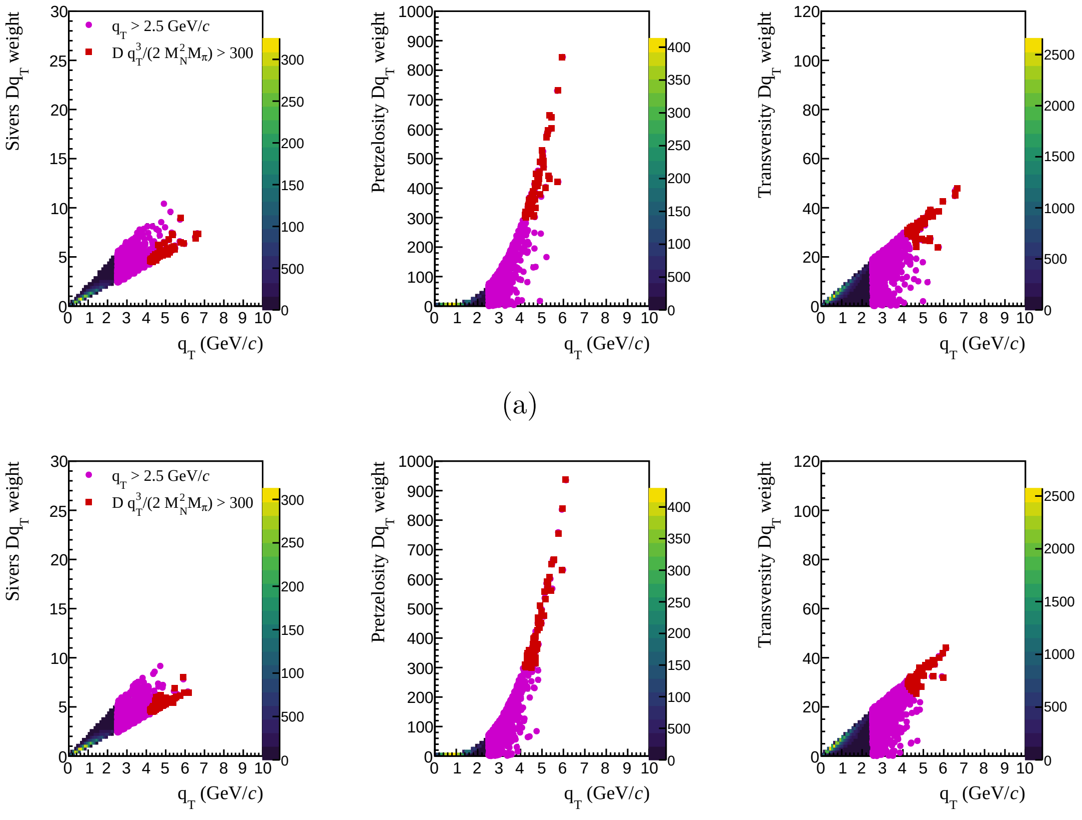

(a)

(b)

Figure E.1: Two-dimensional distributions of asymmetry weights versus q_{T} for Sivers, Pretzelosity, and Transversity, showing both q_{T} and Dq_{T} cuts: (a) 2015 dataset, (b) 2018 dataset.

Appendix F

Asymmetries Tables for Extended Mass Range

The weighted asymmetries, incorporating contributions from various uncertainties across different kinematic bins. The tables below present the precise values of the asymmetries together with their statistical and systematic uncertainties, as well as a decomposition into each contribution described in Chapter 8. The Sivers fD-WTSAs are shown in Tab. F.1 for the dataset with the $Dq_T^3/(2M_\pi M_N^2) < 300$ selection criteria, while those for $q_T < 2.5$ GeV/c^2 are presented in Tab. F.2. Similarly, the results for the Pretzelosity asymmetries are reported in Tab. F.3 and F.4, and those for the Transversity asymmetries in Tab. F.5 and F.6.

Table F.1: Sivers fD-WTSAs with Dq_T cut.

Bin	A_T^{Sivers}	σ_{stat}	σ_{sys}	$\sigma_{\text{sys}}^{\text{FA}}$	$\sigma_{\text{sys}}^{\text{DH}}$	$\sigma_{\text{sys}}^{\text{AD}}$
$\boldsymbol{x_N}$ **Bin**						
0.097	-0.230	0.855	0.876	0.781	0.172	0.355
0.157	-0.671	0.827	0.756	0.755	0.046	0.000
0.248	-2.602	0.736	0.684	0.671	0.134	0.000
$\boldsymbol{x_\pi}$ **Bin**						
0.290	-3.343	0.918	0.863	0.837	0.177	0.119
0.441	0.876	0.859	0.799	0.783	0.152	0.000
0.660	-1.520	0.731	0.676	0.670	0.097	0.000
$\boldsymbol{x_F}$ **Bin**						
0.100	-3.198	0.782	0.715	0.713	0.049	0.000
0.314	1.286	0.893	0.839	0.814	0.198	0.000
0.560	-1.231	0.793	0.732	0.725	0.092	0.000
$\boldsymbol{M_{\mu\mu}}$ **Bin**						
4.156	-0.276	1.054	0.978	0.961	0.174	0.000
4.693	-1.312	0.759	0.697	0.693	0.073	0.000
6.161	-1.820	0.702	0.806	0.641	0.130	0.473
Integrated	-1.311	0.468	0.741	0.736	0.091	0.000

Table F.2: Sivers fD-WTSAs with q_T cut.

Bin	A_T^{Sivers}	σ_{stat}	σ_{sys}	$\sigma_{\text{sys}}^{\text{FA}}$	$\sigma_{\text{sys}}^{\text{AD}}$
$\boldsymbol{x_N}$ **bin**					
0.097	-0.660	0.798	1.132	0.781	0.821
0.157	-0.510	0.770	0.755	0.755	0.000
0.248	-2.254	0.689	0.671	0.671	0.000
$\boldsymbol{x_\pi}$ **bin**					
0.291	-3.179	0.828	0.837	0.837	0.000
0.441	0.885	0.806	0.785	0.785	0.000
0.661	-1.460	0.706	0.669	0.669	0.000
$\boldsymbol{x_F}$ **bin**					
0.100	-2.917	0.713	0.713	0.713	0.000
0.315	1.602	0.834	0.816	0.816	0.000
0.561	-1.589	0.770	0.726	0.726	0.000
$\boldsymbol{M_{\mu\mu}}$ **bin**					
4.156	-0.191	0.981	0.962	0.962	0.000
4.693	-1.639	0.712	0.693	0.693	0.000
6.160	-1.545	0.654	0.641	0.641	0.000
Integrated bin					
0.000	-1.263	0.436	0.736	0.736	0.000

Table F.3: Pretzelosity fD-WTSAs with Dq_{T} cut.

Bin	$A_{\mathrm{T}}^{\mathrm{Pretz}}$	σ_{stat}	σ_{sys}	$\sigma_{\mathrm{sys}}^{\mathrm{FA}}$	$\sigma_{\mathrm{sys}}^{\mathrm{DH}}$	$\sigma_{\mathrm{sys}}^{\mathrm{AD}}$
x_{N} Bin						
0.097	0.310	2.453	1.574	1.574	0.000	0.000
0.157	-4.336	2.375	1.588	1.524	0.459	0.000
0.248	-2.107	1.959	1.695	1.250	0.105	1.144
x_{π} Bin						
0.290	-3.133	3.156	2.115	2.018	0.651	0.000
0.441	0.405	2.304	1.640	1.467	0.726	0.000
0.660	-3.037	1.535	2.203	0.983	0.028	1.972
x_{F} Bin						
0.100	-2.475	2.569	1.638	1.638	0.000	0.000
0.314	1.100	2.477	1.701	1.589	0.629	0.000
0.560	-3.354	1.566	3.334	1.002	0.000	3.180
$M_{\mu\mu}$ Bin						
4.156	-1.079	2.980	2.145	1.914	0.980	0.000
4.693	-1.547	2.118	1.452	1.350	0.525	0.000
6.161	-2.225	1.993	3.717	1.279	0.324	3.481
Integrated	-2.303	1.404	1.333	1.333	0.000	0.000

Table F.4: Pretzelosity fD-WTSAs with q_{T} cut.

Bin	$A_{\mathrm{T}}^{\mathrm{Pretz}}$	σ_{stat}	σ_{sys}	$\sigma_{\mathrm{sys}}^{\mathrm{FA}}$	$\sigma_{\mathrm{sys}}^{\mathrm{AD}}$
x_{N} bin					
0.097	-0.248	1.411	1.572	1.572	0.000
0.157	-0.572	1.380	2.216	1.520	1.612
0.248	-1.025	1.202	1.252	1.252	0.000
x_{π} bin					
0.291	-0.280	1.541	2.487	2.017	1.461
0.441	-0.075	1.458	1.473	1.473	0.000
0.661	-0.484	1.153	1.402	0.984	0.999
x_{F} bin					
0.100	-0.695	1.325	1.755	1.641	0.625
0.315	-0.148	1.482	1.584	1.584	0.000
0.561	-0.578	1.251	1.636	1.002	1.292
$M_{\mu\mu}$ bin					
4.156	0.943	1.689	1.908	1.908	0.000
4.693	-1.648	1.271	1.353	1.353	0.000
6.160	0.253	1.165	1.275	1.275	0.000
Integrated bin					
0.000	-0.246	0.774	1.332	1.332	0.000

Table F.5: Transversity fD-WTSAs with Dq_{T} cut.

Bin	$A_{\mathrm{T}}^{\mathrm{Transv}}$	σ_{stat}	σ_{sys}	$\sigma_{\mathrm{sys}}^{\mathrm{FA}}$	$\sigma_{\mathrm{sys}}^{\mathrm{DH}}$	$\sigma_{\mathrm{sys}}^{\mathrm{AD}}$
x_{N} Bin						
0.097	-0.065	0.089	0.076	0.074	0.021	0.000
0.157	0.128	0.095	0.082	0.079	0.025	0.000
0.248	0.150	0.094	0.076	0.076	0.003	0.000
x_{π} Bin						
0.290	0.102	0.118	0.096	0.096	0.007	0.000
0.441	0.064	0.095	0.079	0.078	0.010	0.000
0.660	0.055	0.076	0.063	0.063	0.003	0.000
x_{F} Bin						
0.100	0.094	0.101	0.112	0.084	0.012	0.075
0.314	0.187	0.098	0.087	0.082	0.034	0.000
0.560	-0.052	0.082	0.069	0.068	0.013	0.000
$M_{\mu\mu}$ Bin						
4.156	-0.010	0.117	0.112	0.097	0.028	0.052
4.693	0.022	0.087	0.072	0.071	0.008	0.000
6.161	0.113	0.080	0.066	0.065	0.008	0.000
Integrated	0.062	0.052	0.073	0.073	0.000	0.000

Table F.6: Transversity fD-WTSAs with q_{T} cut.

Bin	$A_{\mathrm{T}}^{\mathrm{Transv}}$	σ_{stat}	σ_{sys}	$\sigma_{\mathrm{sys}}^{\mathrm{FA}}$	$\sigma_{\mathrm{sys}}^{\mathrm{AD}}$
x_{N} bin					
0.097	-0.055	0.083	0.073	0.073	0.000
0.157	0.086	0.088	0.078	0.078	0.000
0.248	0.096	0.087	0.076	0.076	0.000
x_{π} bin					
0.291	-0.033	0.104	0.124	0.097	0.079
0.441	0.076	0.089	0.078	0.078	0.000
0.661	0.045	0.073	0.063	0.063	0.000
x_{F} bin					
0.100	-0.006	0.091	0.121	0.084	0.089
0.315	0.168	0.091	0.085	0.080	0.029
0.561	-0.029	0.079	0.067	0.067	0.000
$M_{\mu\mu}$ bin					
4.156	-0.013	0.108	0.111	0.096	0.057
4.693	-0.009	0.081	0.071	0.071	0.000
6.160	0.070	0.074	0.093	0.066	0.066
Integrated bin					
0.000	0.032	0.048	0.073	0.073	0.000

References

1. Rutherford, E. “The scattering of α and β particles by matter and the structure of the atom”. *Phil. Mag.* **21.** 669. (1911).
2. Chadwick, J. “Possible Existence of a Neutron”. *Nature.* **129.** 312. (1932).
3. Gell-Mann, M. “A Schematic Model of Baryons and Mesons”. *Phys. Lett.* **8.** 214. (1964).
4. Zweig, G. “An SU_3 model for strong interaction symmetry and its breaking”. Tech. rep. (CERN, Geneva, 1964).
5. Breidenbach, M. *et al.* “Observed Behavior of Highly Inelastic Electron-Proton Scattering”. *Phys. Rev. Lett.* **23.** 935. (1969).
6. Feynman, R. P. “Very High-Energy Collisions of Hadrons”. *Phys. Rev. Lett.* **23.** 1415. (1969).
7. Bjorken, J. D. and Paschos, E. A. “Inelastic Electron-Proton and γ-Proton Scattering and the Structure of the Nucleon”. *Phys. Rev.* **185.** 1975. (1969).
8. Jaffe, R. and Manohar, A. “The g1 problem: Deep inelastic electron scattering and the spin of the proton”. *Nuclear Physics B.* **337.** 509. (1990).
9. Close, F. and Roberts, R. “Consistent analysis of the spin content of the nucleon”. *Physics Letters B.* **316.** 165. (1993).
10. Ashman, J. *et al.* “A measurement of the spin asymmetry and determination of the structure function g1 in deep inelastic muon-proton scattering”. *Physics Letters B.* **206.** 364. (1988).
11. Ashman, J. *et al.* “An investigation of the spin structure of the proton in deep inelastic scattering of polarised muons on polarised protons”. *Nuclear Physics B.* **328.** 1. (1989).
12. Baum, G. *et al.* “Measurement of Asymmetry in Spin-Dependent e^-p Resonance-Region Scattering”. *Phys. Rev. Lett.* **45.** 2000. (1980).
13. Baum, G. *et al.* “New Measurement of Deep-Inelastic e^-p Asymmetries”. *Phys. Rev. Lett.* **51.** 1135. (1983).
14. Spin Muon Collaboration. “Spin asymmetries A_1 and structure functions g_1 of the proton and the deuteron from polarized high energy muon scattering”. *Phys. Rev. D.* **58.** 112001. (1998).
15. Airapetian, A. *et al.* “Measurement of the proton spin structure function g_1^p with a pure hydrogen target”. *Physics Letters B.* **442.** 484. (1998).

16. Anthony, P. L. *et al.* “Deep inelastic scattering of polarized electrons by polarized ^{3}He and the study of the neutron spin structure”. *Phys. Rev. D.* **54.** 6620. (1996).

17. E143 Collaboration. “Precision Measurement of the Deuteron Spin Structure Function g_1^d”. *Phys. Rev. Lett.* **75.** 25. (1995).

18. E154 Collaboration. “Precision Determination of the Neutron Spin Structure Function g_1^n”. *Phys. Rev. Lett.* **79.** 26. (1997).

19. COMPASS Collaboration. “Final COMPASS results on the deuteron spin-dependent structure function g1d and the Bjorken sum rule”. *Physics Letters B.* **769.** 34. (2017).

20. COMPASS Collaboration. “Leading and next-to-leading order gluon polarization in the nucleon and longitudinal double spin asymmetries from open charm muoproduction”. *Phys. Rev. D.* **87.** 052018. (2013).

21. Badelek, B., Krawczyk, M., Charchula, K. and Kwiecinski, J. “Small x physics in deep inelastic lepton hadron scattering”. *Rev. Mod. Phys.* **64.** 927. (1992).

22. Manohar, A. V. “An Introduction to Spin Dependent Deep Inelastic Scattering”. (1992). UCSD/PTH 92-10, Lectures presented at the Lake Louise Winter Institute.

23. PDG Collaboration. “Review of Particle Physics”. *Phys. Rev. D.* **110.** 030001. (2024).

24. Bjorken, J. D. “Asymptotic Sum Rules at Infinite Momentum”. *Phys. Rev.* **179.** 1547. (1969).

25. Callan, C. G. and Gross, D. J. “High-Energy Electroproduction and the Constitution of the Electric Current”. *Phys. Rev. Lett.* **22.** 156. (1969).

26. Dokshitzer, Y. L. “Calculation of the Structure Functions for Deep Inelastic Scattering and e^+e^- Annihilation by Perturbation Theory in Quantum Chromodynamics.” *Sov. Phys. JETP.* **46.** 641. (1977).

27. Gribov, V. N. and Lipatov, L. N. “Deep inelastic ep scattering in perturbation theory”. *Sov. J. Nucl. Phys.* **15.** 438. (1972).

28. Altarelli, G. and Parisi, G. “Asymptotic freedom in parton language”. *Nuclear Physics B.* **126.** 298. (1977).

29. Mulders, P. J. and Rodrigues, J. “Transverse momentum dependence in gluon distribution and fragmentation functions”. *Phys. Rev. D.* **63.** 094021. (2001).

30. Meißner, S., Metz, A. and Goeke, K. “Relations between generalized and transverse momentum dependent parton distributions”. *Phys. Rev. D.* **76.** 034002. (2007).

31. Sivers, D. “Single-spin production asymmetries from the hard scattering of pointlike constituents”. *Phys. Rev. D.* **41.** 83. (1990).

32. Boer, D. and Mulders, P. J. “Time-reversal odd distribution functions in leptoproduction”. *Physical Review D.* **57.** 5780. (1998).

33. Kotzinian, A. M. and Mulders, P. J. “Longitudinal quark polarization in transversely polarized nucleons”. *Phys. Rev. D.* **54.** 1229. (1996).

34. Ralston, J. P. and Soper, D. E. "Production of dimuons from high-energy polarized proton-proton collisions". *Nuclear Physics B.* **152.** 109. (1979).

35. Maji, T. and Chakrabarti, D. "Transverse structure of a proton in a light-front quark-diquark model". *Phys. Rev. D.* **95.** 074009. (2017).

36. Avakian, H., Efremov, A. V., Schweitzer, P. and Yuan, F. "Transverse momentum dependent distribution function $h_{1T}^{\perp}$ and th single spin asymmetry $A_{\mathrm{UT}}^{\sin(3\phi-\phi_S)}$". *Physical Review D.* **78.** 114024. (2008).

37. Belle Collaboration. "Measurement of azimuthal asymmetries in inclusive production of hadron pairs in e^+e^- annihilation at $\sqrt{s} = 10.58$ GeV". *Phys. Rev. D.* **78.** 032011. (2008).

38. Belle Collaboration. "Azimuthal asymmetries of back-to-back $\pi^{\pm} - (\pi^0,\ \eta,\ \pi^{\pm})$ pairs in e^+e^- annihilation". *Phys. Rev. D.* **100.** 092008. (2019).

39. BABAR Collaboration. "Measurement of Collins asymmetries in inclusive production of charged pion pairs in e^+e^- annihilation at BABAR". *Phys. Rev. D.* **90.** 052003. (2014).

40. BaBar Collaboration. "Collins asymmetries in inclusive charged KK and $K\pi$ pairs produced in e^+e^- annihilation". *Phys. Rev. D.* **92.** 111101. (2015).

41. BESIII Collaboration. "Measurement of Azimuthal Asymmetries in Inclusive Charged Dipion Production in e^+e^- Annihilations at $\sqrt{s} = 3.65$ GeV". *Phys. Rev. Lett.* **116.** 042001. (2016).

42. Lam, C. S. and Tung, W.-K. "Systematic approach to inclusive lepton pair production in hadronic collisions". *Phys. Rev. D.* **18.** 2447. (1978).

43. Falciano, S. *et al.* "Angular distributions of muon pairs produced by 194 GeV/c negative pions". *Z. Phys. C.* **31.** 513. (1986).

44. Guanziroli, M. *et al.* "Angular distributions of muon pairs produced by negative pions on deuterium and tungsten". *Z. Phys. C.* **37.** 545. (1988).

45. Conway, J. S. *et al.* "Experimental study of muon pairs produced by 252-GeV pions on tungsten". *Phys. Rev. D.* **39.** 92. (1989).

46. Boer, D. "Investigating the origins of transverse spin asymmetries at BNL RHIC". *Phys. Rev. D.* **60.** 014012. (1999).

47. FNAL E866/NuSea Collaboration. "Measurement of Angular Distributions of Drell-Yan Dimuons in $p + d$ Interactions at 800 GeV/c". *Phys. Rev. Lett.* **99.** 082301. (2007).

48. FNAL E866/NuSea Collaboration. "Measurement of Angular Distributions of Drell-Yan Dimuons in $p + p$ Interactions at 800 GeV/c". *Phys. Rev. Lett.* **102.** 182001. (2009).

49. Aaltonen, T. *et al.* "First Measurement of the Angular Coefficients of Drell-Yan e^+e^- Pairs in the Z Mass Region from $p\overline{p}$ Collisions at $\sqrt{s} = 1.96$ TeV". *Phys. Rev. Lett.* **106.** 241801. (2011).

50. CMS Collaboration. "Angular coefficients of Z bosons produced in pp collisions at $\sqrt{s}$=8 TeV and decaying to $\mu^+\mu^-$ as a function of transverse momentum and rapidity". *Physics Letters B.* **750.** 154. (2015).

51. Peng, J.-C., Chang, W.-C., McClellan, R. E. and Teryaev, O. “Interpretation of angular distributions of Z-boson production at colliders”. *Physics Letters B.* **758.** 384. (2016).

52. Nakano, K. “Measurement of Boer-Mulders Function via Drell-Yan Process by SeaQuest Experiment at Fermilab”. *International Journal of Modern Physics: Conference Series.* **40.** 1660041. (2016).

53. Scimemi, I. and Vladimirov, A. “Non-perturbative structure of semi-inclusive deep-inelastic and Drell-Yan scattering at small transverse momentum”. *Journal of High Energy Physics.* **2020.** 137. (2020).

54. Bacchetta, A. *et al.* “Unpolarized transverse momentum distributions from a global fit of Drell-Yan and semi-inclusive deep-inelastic scattering data”. *Journal of High Energy Physics.* **2022.** (2022).

55. Efremov, A., Goeke, K., Menzel, S., Metz, A. and Schweitzer, P. “Sivers effect in semi-inclusive DIS and in the Drell-Yan process”. *Physics Letters B.* **612.** 233. (2005).

56. Sissakian, A. N., Shevchenko, O. Y., Nagaytsev, A. P. and Ivanov, O. N. “Direct extraction of transversity and its accompanying T-odd distribution from the unpolarized and single-polarized Drell-Yan processes”. *Phys. Rev. D.* **72.** 054027. (2005).

57. Sissakian, A., Shevchenko, O., Nagaytsev, A., Denisov, O. and Ivanov, O. “Transversity and its accompanying T-odd distribution from Drell-Yan processes with pion-proton collisions”. *The European Physical Journal C.* **46.** 147. (2006).

58. Ethier, J. J. and Nocera, E. R. “Parton Distributions in Nucleons and Nuclei”. *Ann. Rev. Nucl. Part. Sci.* **70.** 43. (2020).

59. PHENIX Collaboration. “Charged-pion cross sections and double-helicity asymmetries in polarized $p + p$ collisions at $\sqrt{s} = 200$ GeV”. *Phys. Rev. D.* **91.** 032001. (2015).

60. PHENIX Collaboration. “Identified charged hadron production in $p+p$ collisions at $\sqrt{s} = 200$ and 62.4 GeV”. *Phys. Rev. C.* **83.** 064903. (2011).

61. STAR Collaboration. “Identified Hadron Compositions in $p + p$ and Au + Au Collisions at High Transverse Momenta at $\sqrt{s_{NN}} = 200$ GeV”. *Phys. Rev. Lett.* **108.** 072302. (2012).

62. Bailey, S., Cridge, T., Harland-Lang, L., Martin, A. and Thorne, R. “Parton distributions from LHC, HERA, Tevatron and fixed target data: MSHT20 PDFs”. *The European Physical Journal C.* **81.** (2021).

63. Borsa, I., Stratmann, M., Vogelsang, W., de Florian, D. and Sassot, R. “Next-to-Next-to-Leading Order Global Analysis of Polarized Parton Distribution Functions”. *Phys. Rev. Lett.* **133.** 151901. (2024).

64. HERMES Collaboration. “Quark helicity distributions in the nucleon for up, down, and strange quarks from semi-inclusive DIS”. *Phys. Rev. D.* **71.** 012003. (2005).

65. COMPASS Collaboration. “The polarised valence quark distribution from semi-inclusive DIS”. *Physics Letters B.* **660.** 458. (2008).

66. COMPASS Collaboration. “Measurement of the longitudinal spin transfer to λ and $\bar{\Lambda}$hyperons in polarised muon DIS”. *Eur. Phys. J. C.* **64.** 171. (2009).

67. HERMES Collaboration. “Leading-order determination of the gluon polarization from high-p T hadron electroproduction”. *Journal of High Energy Physics.* **1008.** 130. (2010).

68. COMPASS Collaboration. “Leading and next-to-leading order gluon polarization in the nucleon and longitudinal double spin asymmetries from open charm muoproduction”. *Phys. Rev. D.* **87.** 052018. (2013).

69. COMPASS Collaboration. “Leading order determination of the gluon polarisation from DIS events with high-P_{T} hadron pairs”. *Physics Letters B.* **718.** 922. (2013).

70. PHENIX Collaboration. “Inclusive cross section and double helicity asymmetry for π^0 production in $p+p$ collisions at $\sqrt{s} = 62.4$ GeV”. *Phys. Rev. D.* **79.** 012003. (2009).

71. PHENIX Collaboration. “Gluon-Spin Contribution to the Proton Spin from the Double-Helicity Asymmetry in Inclusive π^0 Production in Polarized $p+p$ Collisions at $\sqrt{s} = 200$ GeV”. *Phys. Rev. Lett.* **103.** 012003. (2009).

72. STAR Collaboration. “Neutral pion cross section and spin asymmetries at intermediate pseudorapidity in polarized proton collisions at $\sqrt{s} = 200$ GeV”. *Phys. Rev. D.* **89.** 012001. (2014).

73. PHENIX Collaboration. “Event structure and double helicity asymmetry in jet production from polarized $p+p$ collisions at $\sqrt{s} = 200$ GeV”. *Phys. Rev. D.* **84.** 012006. (2011).

74. STAR Collaboration. “Longitudinal and transverse spin asymmetries for inclusive jet production at mid-rapidity in polarized p+p collisions at $\sqrt{s}$=200 GeV”. *Phys. Rev. D.* **86.** 032006. (2012).

75. STAR Collaboration. “Precision Measurement of the Longitudinal Double-Spin Asymmetry for Inclusive Jet Production in Polarized Proton Collisions at $\sqrt{s} = 200$ GeV”. *Phys. Rev. Lett.* **115.** 092002. (2015).

76. PHENIX Collaboration. “Cross Section and Parity-Violating Spin Asymmetries of $W^{\pm}$ Boson Production in Polarized $p+p$ Collisions at $\sqrt{s} = 500$ GeV”. *Phys. Rev. Lett.* **106.** 062001. (2011).

77. STAR Collaboration. “Measurement of Longitudinal Spin Asymmetries for Weak Boson Production in Polarized Proton-Proton Collisions at RHIC”. *Phys. Rev. Lett.* **113.** 072301. (2014).

78. HERMES Collaboration. “Single-Spin Asymmetries in Semi-Inclusive Deep-Inelastic Scattering on a Transversely Polarized Hydrogen Target”. *Physical Review Letters.* **94.** (2005).

79. Collaboration, C. “First Measurement of the Transverse Spin Asymmetries of the Deuteron in Semi-inclusive Deep Inelastic Scattering”. *Physical Review Letters.* **94.** (2005).

80. Adam, J. *et al.* “Measurement of transverse single-spin asymmetries of π^0 and electromagnetic jets at forward rapidity in 200 and 500 GeV transversely polarized proton-proton collisions”. *Phys. Rev. D.* **103.** 092009. (2021).

81. Klem, R. D. *et al.* “Measurement of Asymmetries of Inclusive Pion Production in Proton-Proton Interactions at 6 and 11.8 GeV/c”. *Phys. Rev. Lett.* **36.** 929. (1976).

82. Adams, D. *et al.* “Comparison of spin asymmetries and cross sections in π^0 production by 200 GeV polarized antiprotons and protons”. *Physics Letters B.* **261.** 201. (1991).

83. Akchurin, N. *et al.* “Analyzing power measurement of pp elastic scattering in the Coulomb-nuclear interference region with the 200-GeV/c polarized-proton beam at Fermilab”. *Phys. Rev. D.* **48.** 3026. (1993).

84. E925 Collaboration. “Measurement of analyzing powers of π^+ and π^- produced on a hydrogen and a carbon target with a $22-\mathrm{GeV}/c$ incident polarized proton beam”. *Phys. Rev. D.* **65.** 092008. (2002).

85. Chiu, M. “Single spin transverse asymmetries of neutral pions at forward rapidities in s**(1/2) = 62.4-GeV polarized proton collisions in PHENIX”. *AIP Conf. Proc.* **915.** 539–542. (2007).

86. Adam, J. *et al.* “Measurement of transverse single-spin asymmetries of π^0 and electromagnetic jets at forward rapidity in 200 and 500 GeV transversely polarized proton-proton collisions”. *Phys. Rev. D.* **103.** 092009. (2021).

87. Pappalardo, L. and Schnell, G. “Azimuthal single- and double-spin asymmetries in semi-inclusive deep-inelastic lepton scattering by transversely polarized protons”. *SciPost Physics Proceedings.* (2022).

88. COMPASS Collaboration. “Collins and Sivers asymmetries in muonproduction of pions and kaons off transversely polarised protons”. *Physics Letters B.* **744.** 250. (2015).

89. COMPASS Collaboration. “Collins and Sivers asymmetries for pions and kaons in muon-deuteron DIS”. *Physics Letters B.* **673.** 127. (2009).

90. COMPASS Collaboration. “High-Statistics Measurement of Collins and Sivers Asymmetries for Transversely Polarized Deuterons”. *Phys. Rev. Lett.* **133.** 101903. (2024).

91. Jefferson Lab Hall A Collaboration. “Single Spin Asymmetries in Charged Pion Production from Semi-Inclusive Deep Inelastic Scattering on a Transversely Polarized ^{3}He Target at $Q^2 = 1.4-2.7$ GeV^2”. *Phys. Rev. Lett.* **107.** 072003. (2011).

92. Jefferson Lab Hall A Collaboration. “Single spin asymmetries in charged kaon production from semi-inclusive deep inelastic scattering on a transversely polarized ^{3}He target”. *Phys. Rev. C.* **90.** 055201. (2014).

93. PHENIX Collaboration. “Transverse momentum dependent forward neutron single spin asymmetries in transversely polarized $p+p$ collisions at $\sqrt{s} = 200$ GeV”. *Phys. Rev. D.* **103.** 032007. (2021).

94. COMPASS Collaboration. “Final COMPASS results on the transverse-spin-dependent azimuthal asymmetries in the pion-induced Drell-Yan process”. *Phys. Rev. Lett.* **133.** 071902. (2023).

95. COMPASS Collaboration. “Sivers asymmetry extracted in SIDIS at the hard scales of the Drell-Yan process at COMPASS”. *Physics Letters B.* **770.** 138. (2017).

96. STAR Collaboration. “Measurement of transverse single-spin asymmetries of π^0 and electromagnetic jets at forward rapidity in 200 and 500 GeV transversely polarized proton-proton collisions”. *Phys. Rev. D.* **103.** 092009. (2021).

97. STAR Collaboration. “Measurements of the Z^0/γ^* cross section and transverse single spin asymmetry in 510 GeV p+p collisions”. *Physics Letters B.* **854.** 138715. (2024).

98. Bastami, S. *et al.* “The Drell-Yan process with pions and polarized nucleons”. *Journal of High Energy Physics.* **2021.** (2021).

99. HERMES Collaboration. “Azimuthal distributions of charged hadrons, pions, and kaons produced in deep-inelastic scattering off unpolarized protons and deuterons”. *Phys. Rev. D.* **87.** 012010. (2013).

100. COMPASS Collaboration. “Measurement of azimuthal hadron asymmetries in semi-inclusive deep inelastic scattering off unpolarised nucleons”. *Nuclear Physics B.* **886.** 1046. (2014).

101. Lien, Y.-H. and Chumakov, A. “Measurement of Target Spin (in)dependent Asymmetries in Dimuon Production in Pion-Nucleon Collisions at COMPASS”. *SciPost Phys. Proc.* **8.** 028. (2022).

102. Jaffe, R. L. and Ji, X. “Chiral-odd parton distributions and polarized Drell-Yan process”. *Phys. Rev. Lett.* **67.** 552. (1991).

103. Collins, J. “Fragmentation of transversely polarized quarks probed in transverse momentum distributions”. *Nuclear Physics B.* **396.** 161. (1993).

104. STAR Collaboration. “Azimuthal transverse single-spin asymmetries of inclusive jets and charged pions within jets from polarized-proton collisions at $\sqrt{s} = 500$ GeV”. *Phys. Rev. D.* **97.** 032004. (2018).

105. COMPASS Collaboration. “First Measurement of Transverse-Spin-Dependent Azimuthal Asymmetries in the Drell-Yan Process”. *Phys. Rev. Lett.* **119.** 112002. (2017).

106. Parsamyan, B. “Transverse spin asymmetries at COMPASS: beyond Collins and Sivers effects”. *Proceedings of the XXI International Workshop on Deep-Inelastic Scattering and Related Subject (DIS2013)* (2013).

107. Jefferson Lab Hall A Collaboration. “Measurement of “pretzelosity” asymmetry of charged pion production in semi-inclusive deep inelastic scattering on a polarized ^{3}He target”. *Phys. Rev. C.* **90.** 055209. (2014).

108. Baum, G. *et al.* “COMPASS: A Proposal for a Common Muon and Proton Apparatus for Structure and Spectroscopy”. (1996).

109. Gautheron, F. *et al.* “COMPASS-II Proposal”. (2010).

110. COMPASS Collaboration. “The deuteron spin-dependent structure function g_d^1 and its first moment”. *Physics Letters B.* **647.** 8. (2007).

111. COMPASS Collaboration. “Longitudinal double-spin asymmetry A_1^p and spin-dependent structure function g_1^p of the proton at small values of x and Q^2”. *Physics Letters B.* **781.** 464. (2018).

112. COMPASS Collaboration. “Leading order determination of the gluon polarisation from DIS events with high-P_{T} hadron pairs”. *Physics Letters B.* **718.** 922. (2013).

113. COMPASS Collaboration. “Leading-order determination of the gluon polarisation from semi-inclusive deep inelastic scattering data”. (2017).

114. Collaboration, C. “Collins and Sivers asymmetries in muonproduction of pions and kaons off transversely polarised protons”. *Physics Letters B.* **744.** 250. (2015).

115. COMPASS Collaboration. “Collins and Sivers asymmetries for pions and kaons in muon-deuteron DIS”. *Physics Letters B.* **673.** 127. (2009).

116. COMPASS Collaboration. “Transverse extension of partons in the proton probed in the sea-quark range by measuring the DVCS cross section”. *Physics Letters B.* **793.** 188. (2019).

117. COMPASS Collaboration. “The COMPASS experiment at CERN”. *Nuclear Instruments and Methods in Physics Research Section A: Accelerators, Spectrometers, Detectors and Associated Equipment.* **577.** 455. (2007).

118. COMPASS Collaboration. “The COMPASS setup for physics with hadron beams”. *Nuclear Instruments and Methods in Physics Research Section A: Accelerators, Spectrometers, Detectors and Associated Equipment.* **779.** 69. (2015).

119. Abragam, A. “The principles of nuclear magnetism”. Oxford university press. (1961).

120. Bychkov, V. *et al.* “The large size straw drift chambers of the COMPASS experiment”. *Nuclear Instruments and Methods in Physics Research Section A: Accelerators, Spectrometers, Detectors and Associated Equipment.* **556.** 66. (2006).

121. Hsieh, C.-Y. “Measurement of the differential Drell–Yan cross sections with 190-GeV pion beams in the COMPASS Experiment at CERN”. PhD thesis (National Central University, Taipei, 2021).

122. Bodlak, M. *et al.* “Development of new data acquisition system for COMPASS experiment”. *Nucl. Part. Phys. Proc.* **273-275.** 976. (2016).

123. Bordalo, P., Nunes, A., Pires, C., Quintans, C. and Ramos, S. “Control systems: An application to a high energy physics experiment (COMPASS)”. *Proceedings of 2012 IEEE International Conference on Automation, Quality and Testing, Robotics* 20. (2012).

124. COMPASS Collaboration. “CORAL: COMPASS Reconstruction and Analysis Software”. (2025).

125. COMPASS Collaboration. “PHAST: Physics Analysis Software Tools”. (2025).

126. “PYTHIA: General-Purpose Monte Carlo Event Generator”. (2025).

127. COMPASS Collaboration. “TGEANT: A Geant4-based Monte Carlo simulation for the COMPASS-II experiment”. (2016).

128. Matoušek, J. “Nucleon spin structure studies in Drell-Yan process at COMPASS”. PhD thesis (Charles University, University of Trieste, Prague, 2018).

129. Anselmino, M. *et al.* “Sivers effect for pion and kaon production in semi-inclusive deep inelastic scattering”. *The European Physical Journal A.* **39.** 89. (2008).

130. Anselmino, M. *et al.* “Extracting the Sivers function from polarized semi-inclusive deep inelastic scattering data and making predictions”. *Phys. Rev. D.* **72.** 099903. (2005).

131. COMPASS Collaboration. “Collins and Sivers asymmetries in muonproduction of pions and kaons off transversely polarised protons”. *Physics Letters B.* **744.** 250. (2015).

132. COMPASS Collaboration. “Sivers asymmetry extracted in SIDIS at the hard scales of the Drell-Yan process at COMPASS”. *Physics Letters B.* **770.** 138. (2017).

133. Boughezal, R. *et al.* “Color singlet production at NNLO in MCFM”. *Eur. Phys. J. C.* **77.** 1. (2017).

134. Heinrich, J. G. *et al.* “Measurement of the ratio of sea to valence quarks in the nucleon”. *Phys. Rev. Lett.* **63.** 356. (1989).

135. Eskola, K., Kolhinen, V. and Salgado, C. “The scale dependent nuclear effects in parton distributions for practical applications”. *Eur.Phys.J.C.* **9.** 61. (1999).

136. Alde, D. M. *et al.* “Nuclear dependence of dimuon production at 800 GeV”. *Phys. Rev. Lett.* **64.** 2479. (1990).

137. COMPASS Collaboration. “Measurement of P_{T}-weighted Sivers asymmetries in leptoproduction of hadrons”. *Nuclear Physics B.* **940.** 34. (2019).

138. Martin, A., Bradamante, F. and Barone, V. “Direct extraction of the Sivers distributions from spin asymmetries in pion and kaon leptoproduction”. *Phys. Rev. D.* **95.** 094024. (2017).

139. Lai, H. *et al.* “Global QCD analysis of parton structure of the nucleon: CTEQ5 parton distributions”. *The European Physical Journal C.* **12.** 375. (2000).

140. Bacchetta, A., Delcarro, F., Pisano, C. and Radici, M. “The 3-dimensional distribution of quarks in momentum space”. *Physics Letters B.* **827.** 136961. (2022).

141. COMPASS Collaboration. “High-statistics measurement of Collins and Sivers asymmetries for transversely polarised deuterons”. (2023).

142. Martin, A., Bradamante, F. and Barone, V. “Extracting the transversity distributions from single-hadron and dihadron production”. *Physical Review D.* **91.** (2015).

143. COMPASS Collaboration. “High-Statistics Measurement of Collins and Sivers Asymmetries for Transversely Polarized Deuterons”. *Phys. Rev. Lett.* **133.** 101903. (2024).

144. Bradamante, F., Barone, V., Bressan, A., Kerbizi, A. and Martin, A. "Further direct extractions of the transversity functions". *Proceedings of the 7th International Workshop on Transverse phenomena in hard processes and the transverse structure of the proton (Transversity2024)* 011. (2024).

145. Gluck, M., Reya, E. and Vogt, A. "Pionic parton distributions". *Z. Phys. C.* **53.** 651. (1992).

146. Buckley, A. *et al.* "LHAPDF6: parton density access in the LHC precision era". *The European Physical Journal C.* **75.** (2015).

147. Boer, D. "Investigating the origins of transverse spin asymmetries at BNL RHIC". *Physical Review D.* **60.** (1999).

148. The COMPASS Collaboration. "Extraction of pion Boer-Mulders function from weighted TSA in Drell-Yan". COMPASS Release Note. (2018).

149. Abdul Khalek, R. *et al.* "Science Requirements and Detector Concepts for the Electron-Ion Collider". *Nuclear Physics A.* **1026.** 122447. (2022).

150. Accardi, A. *et al.* "Electron Ion Collider: The Next QCD Frontier - Understanding the glue that binds us all". (2014).

151. Garcia, O. B. *et al.* "High-density gas target at the LHCb experiment". *Phys. Rev. Accel. Beams.* **27.** 111001. (2024).

152. Kikoła, D. *et al.* "Feasibility Studies for Single Transverse-Spin Asymmetry Measurements at a Fixed-Target Experiment Using the LHC Proton and Lead Beams (AFTER@LHC)". *Few-Body Systems.* **58.** (2017).

153. Anselmino, M., D'Alesio, U. and Melis, S. "Transverse Single-Spin Asymmetries in Proton-Proton Collisions at the AFTER@LHC Experiment in a TMD Factorisation Scheme". *Advances in High Energy Physics.* **2015.** 1. (2015).

154. Echevarria, M. G., Idilbi, A., Kang, Z.-B. and Vitev, I. "QCD evolution of the Sivers asymmetry". *Phys. Rev. D.* **89.** 074013. (2014).